

ABSTRACT

Title of Dissertation: COMBINATORIAL INVESTIGATION OF MAGNETIC MATERIALS

Maria A. Aronova, Doctor of Philosophy, 2004

Dissertation directed by: Professor Ichiro Takeuchi
Department of Materials Science and Engineering
Center for Superconductivity Research

Combinatorial synthesis is an efficient tool that can be used to discover new materials. It allows one to systemically study a large number of materials simultaneously as their physical properties change with the varying chemical composition. Using this technique, we study various multifunctional electronic materials. Different designs of libraries, such as discrete libraries and composition spreads, are fabricated and characterized in order to rapidly map composition-structure-property relationships in a variety of systems.

We have made gas sensor device libraries to optimize the performance of gas sensing materials. We have utilized the combinatorial pulsed laser deposition (PLD) flange for fabricating the discrete device library of doped SnO₂ thin films. Several libraries were made with different amounts of dopants such as In₂O₃, WO₃, ZnO, Pt, and Pd. After exposing the whole library to chloroform, formaldehyde, and benzene gases,

the compositions most sensitive to these gases were found. We have also demonstrated the use of a gas sensor library as an electronic nose where responses from different devices are multiplexed to perform pattern recognition for distinguishing different gases at concentrations down to 12.5 ppm with high repeatability of response signals.

Magnetic properties of composition spreads and discrete libraries are analyzed by a scanning SQUID microscope. The in-plane and out-of-plane magnetization distributions are calculated from the magnetic field data using the inversion technique. Various parameters that control the inversion technique are discussed in detail and optimized with the help of simulated data.

By applying the inversion technique to thin-film discrete libraries, we have mapped the functional phase diagram of Ni-Mn-Ga system whose Heusler composition Ni_2MnGa is a well known ferromagnetic shape memory alloys (FSMAs). A large, previously unexplored compositional region of FSMAs outside the Heusler composition is found.

In search for novel multiferroic materials, we have fabricated PbTiO_3 (PTO)- CoFe_2O_4 (CFO) composition spreads using the combinatorial PLD. After calculating the in-plane and out-of-plane remanent magnetization distributions with the help of the inversion technique, it was found that when PTO is added to CFO, CFO's magnetic anisotropy changes. Furthermore, we found that the compositional region between $(\text{PTO})_{0.5}-(\text{CFO})_{0.5}$ and $(\text{PTO})_{0.8}-(\text{CFO})_{0.2}$ exhibits the coexistence of ferroelectricity and ferromagnetism.

COMBINATORIAL INVESTIGATION OF MAGNETIC MATERIALS

by

Maria A. Aronova

Thesis submitted to the Faculty of the Graduate School of the
University of Maryland, College Park in partial fulfillment
of the requirements for the degree of
Doctor of Philosophy
2004

Advisory Committee:

Professor I. Takeuchi, Chairman/Advisor
Professor F. C. Wellstood, co-advisor
Professor C. J. Lobb
Professor R. L. Greene
Professor J. Melngailis

©Copyright by

Maria A. Aronova

2004

DEDICATION

To my family

ACKNOWLEDGEMENTS

I cannot even begin thinking whom I should thank, because there are so many individuals that have helped me in so many different ways. Throughout my stay in the University of Maryland, I have a great number of people that I want to thank both here in Maryland and elsewhere. Each individual has touched me in his or her own way, and made my journey here unforgettable.

I would like to thank my advisor Professor Ichiro Takeuchi for giving me a chance to work in his group and to have a great opportunity to interact with many people in the scientific community. I acquired many skills while working in his group. I am glad that he paid attention to such insignificant persons as myself and gave me a chance to “speak”, because even a little person has something important to say. Thank you for financially supporting me throughout my Ph. D. Thank you for correcting my thesis about a million times for it to become readable, sorry if my writing was painful.

I thank Professor Fred C. Wellstood for agreeing to be my second advisor. Thank you for believing me when I was “playing” in your lab with your equipment, I am thankful that I did not have any major disasters. Thank you for your advice, for teaching me about SQUIDS and for giving me the freedom to do my research even though sometimes I did not know what I was doing.

I would like to thank the committee Professors Richard L. Greene, Christopher J. Lobb, and John Melngailis for taking their time to read and comment on my thesis.

I would like to thank all my group members who treated me with dignity and respect perhaps which I did not deserve. Without their help and inspiration, I probably

would have been insane. I thank Dr. Kao-Shuo Chang for training me in PLD in the beginning, and in assisting me in a number of other things. I thank him for being my first lab partner and the best lab partner that anyone could ask, and for training me to accustom to hard work. Thank you for being my close friend and someone I could always count on for 4 years and hopefully for the rest of my life. To Olugbenga O. Famodu I want to say, “you have the patience” to deal with it all. Thank you for withstanding me and for helping me at anytime I asked. I want to wish him good luck with the rest of graduate school. I would like to thank Dr. Makoto Murakami for being my second lab partner. Thank you for educating me in many experimental aspects, for helping me measure samples, for assisting me in the last year of my lab life and for inspiring me to go on. And of course thank you for being a good friend. I want to thank Jae Hattrick-Simpers, for helping me with programming issues, and overall for keeping me sane with “high class” jokes, that I did not get. To John Read I want to say that you were a great addition to our group when there were so few of us, thank you for great talks. I wish you luck with your Ph. D road, even though I think you are still an artist in your heart. I want to thank Luke “skywalker” Lin for making samples for me and for getting really good deals on many things that I wanted to buy. Thank you Dr. Minghui Yu for educating me about magnetic materials and for great conversations such as “what is a good career for a woman”. I would like to thank Hiroyuki Oguchi, Shige sensei, Chris Long, Peng Zhao, and Richard Cui for interesting discussions about various topics.

I would like to thank Jack Tourt from the Physics Electronics group for helping me with the assembly of the electronic boxes, for teaching me how many things work and

with many more mishaps, I had during my experimental “trials”. I also thank him for having many conversations and for giving me many advices about life issues.

Thank you Russ Wood and David Wenzel for assisting me with many issues about fixing the PLD flange, making my own parts and just advice about mechanical things. In addition, I would like to thank all the machine shop guys: John Cataldi, Mark Vilas (may his soul be saved), Randy, Ernie. Thank you for doing such a great job and making my experiment much easier.

I would like to thank the guys in Prof. F. C. Wellstood’s lab “7581”. Dr. Andrew Berkeley, thank you for helping me with many programming issues, with SQUID controls and electronics and many more things that I asked that I do not even remember now. Thank you Sudeep Dutta for being so kind. Thank you for continuing to help me with programming after Andrew left and for always making me laugh even when I didn’t want to. I wish him good luck with finding what he really wants to do. Thank you Dr. Huizhong Xu, for setting an example of a hard worker and a detached “crazy” scientist. Thank you Hanhee Paik for being a balance in the subbasement by tipping the ratio of guys to girls a little bit more towards girls’ side. Thank you for your care and support and for teaching me about your experiment. I thank Jan Gaudestad, Dr. Erin Fleet, Dr. Guy Chatraphorn and Dr. John Mathews for helping me understand and fix the SQUID microscope located in the subbasement. I thank Dave Tobias and Dr. Roberto Ramos, Dr. Matt Kenyon for having interesting conversations.

I would like to thank people in Neocera Inc. I am grateful that I had a chance to meet you and work with you so closely. First, thank you Dr. Lee Knouse for allowing me to use the scanning SQUID microscope at Neocera. Thank you Dr. Antonio Orozco and

Anders Gilbertson, for assisting me many times in my scans, and for giving me advice on my data. Thank you Steve Garrahan, for helping me with Labview programming for the PLD program. Thank you Nesco Lettsome, for being a great friend and a person whom I always can talk with, thank you for inspiring me to go on in my education. I wish you the best with your endeavors.

I would like to thank Marilyn Kushner at the UC Berkeley Microlab for her kindness and help in making photolithography masks for my thin film samples. Thank you for being patient with me in the beginning, since I didn't know how to properly format the pattern files. Thank you for being so fast in making the masks and for being friendly even though we just communicated by e-mail.

I thank Dr. Leonid Bendersky at NIST for helping us with the TEM analysis and Prof. Samuel Lofland at the Rowan University who helped us with understanding some concepts about magnetic characterizations. Also, thank you Sam for caring for what I was doing, and always asking how things were going.

I would like to thank the group member of Dr. Venky's lab. Thank you, Dr. Sanjay Shinde, Dr. Wei Yang, Dr. Tom Wu, Dr. Bin Ming, Dr. Eric Li, Dr. Supab Choopun, Dr. Z.-Y. Chen, Ram, Betsy Pugel, Alvaro Godinez, for making me feel welcome in your lab, for having interesting conversations and for teaching me many things about experiment. Ming, I especially thank you for spending a long time to teach me how to do lithography and for numerous conversations that we had during our times of difficulty. I wish you all a success in your future life. Thank you Dr. R. D. Vispute, Dr. R. P. Sharma, Dr. S. Ogale, Dr. Rao, Dr. Shiva Hullavarad, for your suggestions about my experiments.

I thank Brian Straughn for teaching me how to use the evaporator, when we first got to know each other and then many more things as we became very good friends. Thank you for many interesting conversations that we had about so many topics. Thank you for helping me at the times when I did not know whom to talk. Thank you for studying with me “Bhagavat Gita” and I hope that you will somehow go on in the future. Thank you Doug Bensen, for helping me to fix many things including my car, and for great conversations. I felt always happy after I talked to you. Thank you, Cleopatra White, Belta Pollard, Brian Barnaby and Grace Sewlall for taking care of all paperwork that I needed, thank you for making it easy.

I would like to thank Jane Hessing for her kindness and care for us graduates students. She has created a very warm and welcoming atmosphere in the department and I thank her for that.

I thank the shipping and receiving office personnel in the physics department Jesse Anderson, Robert Dahms, and Al Godinez for always being kind and patient with me. Al, your dreams came true, you finally will get rid of me.

I thank my classmates in the Physics department. Dr. Matt Sullivan, I hope I answered your question that you ask me every time you saw me. Todd Brintlinger, if I can do it so can you, the time is coming; Josh Higgins, thank you for magnetizing my samples whenever I wanted and for having interesting conversations. “Qman”, thank you for being my first lab partner when we just started the TA training and then during the summer research. You are almost there; I will never forget you. I also thank Dr. Jong-Won Kim, Dr. Seok-Hwan Chung, Dr. Wingshun Lam and Yinggwei Chang for helping me in my class work and for interesting conversations.

I would like to thank Dr. Cohen who didn't let go of me, even though I was hanging on a thread. Thank you for believing in me. Thank you Dr. Ellis for giving me a chance. I also thank Dr. Michael E. Fisher for giving me nice suggestions and for having great conversations.

I would like to thank Dr. Bo for healing me of many problems that I had, may you help many more people. I thank Dr. A. Abdullah for helping me with my major teeth problems, I still can not believe that it is over, sorry for giving you such a difficult challenge. I pray that I never have to go through this again.

Finally, I would like to thank the persons who became my family during the time I was staying here, my spiritual family and my immediate family. I want to thank Dr. Su Young Lee who is my best friend since we met here first time during orientation. We had a common belief, and it bound us forever. I want to thank her for being there for me, for withstanding my difficult personality and for always believing in me. Even though she left to Korea for one year and I was angry with her, I was happy when she came back and gave me a chance to take care of her daughter every weekend for the entire year. I want to especially thank her for giving me another best friend Dr. Youngchan Kim who is as dear to me as she is. Together we have become a very interesting trio. We studied together, we laughed and cried together. I will never forget the times we spent. Also thank you Youngchan for helping me pass the qualifier, without you tutoring me in various subjects, I wouldn't be able to do it. I thank you for being my confidant, and still to this day watch over as I progress. I owe you this degree. I love you both from the bottom of my heart. I also thank both of your families for encouraging me and being very kind to me when I came to visit your homes.

I thank my long time best friend from high school Yann Yi Pan and her family for believing in me. Thank you Yann, for loving me all these years even though we have been separated by continents. Thank you for becoming a doctor, a real one, and for trying to genuinely help people. I wish you to finish all the exams and settle down. And please be happy.

I want to take this chance to thank my spiritual family. I want to pay my humble respects to my spiritual master Tamal Krishna Goswami, Srila Gurudeva. Your instructions are imprinted in my heart and my whole life I am indebted to you. Even though you are no longer here with us physically in this world, I hope that you will still watch over me and be proud of me as you always told me you would when I finish this Ph. D. Thank you for your love and inspiration. I want to thank my Godmother Guru Bhakti for always caring for me, and all my godsisters and godbrothers who will always remind me of Gurudeva and keep me in my lane.

At last, I thank my mom and my dad. I will never be able to repay them for their unselfish love, sacrifice and dedication. You always granted me the freedom to do what I thought was right and I am very grateful for your liberalism. I will always love you and try my best not to disappoint you.

May the Lord bless everyone and I pray that I can be an instrument in His hand to do good for this world. This is just the beginning of my mission.

TABLE OF CONTENTS

LIST OF TABLES.....	xiv
LIST OF FIGURES.....	xv
Chapter 1	1
Introduction.....	1
Chapter 2	4
Combinatorial synthesis.....	4
2.1 Basics of combinatorial synthesis	4
2.2 Combinatorial thin film library fabrication by Pulsed Laser Deposition (PLD).....	10
2.2.1 Basics of PLD	11
2.2.2 Combinatorial PLD flange	15
2.2.3 Automation of all the PLD components.....	21
2.3 Screening of combinatorial libraries	24
Chapter 3	28
Inorganic semiconductor gas sensor libraries: Electronic nose.....	28
3.1 Introduction	28
3.2 How gas sensors work.....	30
3.3 Fabrication of gas sensor libraries.....	35
3.3.1 Photolithography	38
3.3.2 Deposition of the libraries.....	40
3.4 Characterization of gas sensors	43
3.4.1 Basic principle of olfaction	44
3.4.2 Characterization and results	48
3.5 Conclusions	55
Chapter 4	56

SQUID microscopy	56
4.1 Introduction to SQUIDs	56
4.2 SQUID microscopy	58
4.2.1 SQUID fundamentals	60
4.2.2 Fabrication and testing of the SQUID.....	64
4.2.3 The commercial scanning SQUID microscope.....	73
4.3 Conclusions	75
 Chapter 5	76
Characterization techniques of combinatorial libraries of magnetic materials	76
5.1 Introduction	76
5.2 Simulation of uniformly magnetized samples.....	80
5.3 In-plane magnetization	83
5.3.1 Line charge approximation	84
5.3.2 General derivation for the inversion of B_z for in-plane magnetization	93
5.4 Out-of-plane magnetization.....	97
5.4.1 Current loop model	98
5.4.2 General derivation for inversion of B_z for out-of-plane magnetization	104
5.5 Conclusions	106
 Chapter 6	108
Parameter dependence of the inversion technique for calculation of magnetization	108
6.1 General overview	111
6.2 Inversion technique for calculating in-plane magnetization	116
6.2.1 k_w dependence	118
6.2.2 Dependence on integration area	122
6.2.2.1 Varying integration length along magnetization direction	122
6.2.2.2 Varying the dipole width w	124
6.2.3 z and scanning area dependence.....	126
6.3 Inversion technique for calculating the out-of-plane magnetization.....	129

6.3.1	<i>kw</i> dependence	131
6.3.2	Integration area and <i>z</i> dependence	133
6.3.3	Scanning area dependence	134
6.4	Revisiting Chapter 5	144
6.5	Conclusions	144
6.5.1.1	146	
Chapter 7	146
Combinatorial investigation of ferromagnetic shape memory alloys..	146
7.1	Introduction to FSMA	146
7.1.1	Mechanism of shape memory and FSM effect	148
7.1.2	Applications of SM and FSM materials.....	151
7.2	Fabrication of FSMA combinatorial libraries	152
7.3	Characterization of FSMA libraries	156
7.3.1	Composition verification.....	156
7.3.2	Magnetic properties of Ni-Mn-Ga by scanning SQUID	157
7.3.3	Cantilever libraries for SMAs	163
7.3.4	X-ray analysis.....	166
7.4	Mapping of a phase diagram	169
7.5	Conclusions	173
Chapter 8	174
Combinatorial investigation of magnetoelectric materials.....	174
8.1	Introduction to magnetoelectric materials.....	174
8.2	Composition spreads for exploring ME materials.....	177
8.3	Characterization of composition spreads	180
8.3.1	Magnetic properties.....	180
8.3.2	Dielectric properties	188
8.3.3	Structure	192
8.3.3.1	X-ray	192
8.3.3.2	TEM.....	194
8.3.4	Magnetoelectric effect.....	196
8.4	Conclusions	198

APPENDICES.....	199
REFERENCES	224

LIST OF TABLES

Table 3.1 A list of dopant compositions based on SnO ₂ in one library. This was a target library.	42
Table 3.2 Sensors with the highest overall responses from the three initial libraries and the rated responses of individual sensors along with their compositions. In the parentheses are the atomic weight percentages.....	51
Table 5.1 Advantages and disadvantages of various magnetic characterization techniques for measuring and mapping the magnetic properties of combinatorial libraries.....	79

LIST OF FIGURES

Figure 2.1 The correlation between materials complexity (reflected in the number of elements required to form the compounds) and a physical property (T_c) for superconductors.....	6
Figure 2.2 The flow diagram of a representative combinatorial thin film experiment.....	7
Figure 2.3 A schematic of three basic library designs used in our group. (a) Natural composition spread technique. Varying combinations of three different elements (A, B and C) are obtained at different positions on a wafer by co-deposition. (b) A discrete library. Each site has a different composition and can be addressed as C_{xy} . (c) Binary composition spread. The composition across the chip continuously changes from A to B.....	8
Figure 2.4 Schematic drawing of a PLD chamber	12
Figure 2.5 (a) A photograph of the combinatorial thin film deposition 8” flange. (b) A photograph of the combinatorial PLD chamber.....	17
Figure 2.6 A top view photograph of the combinatorial flange showing the shutter assembly and the rotatable heater.....	18
Figure 2.7 A schematic of the top view of the combinatorial shutter assembly. Different aperture layouts are used to fabricate different combinatorial libraries. (a) Set-up for fabricating discrete libraries. (b) Set-up for fabricating composition spreads. The wedge-like thickness profile (Figure 2.8) can be created using this.....	20
Figure 2.8 A schematic side view of a pair of wedge like thin film layers deposited using a moving shutter edge.	21
Figure 2.9 A Simple diagram of one motor connection.....	22
Figure 2.10 Control box and its components for two shutter motors of the PLD.....	23
Figure 3.1 A model of a potential barrier to electronic conduction at grain boundary []. (a) Space charge region is formed on the surfaces of the MOS grains. (b) The resistance of MOS in air is high due to the potential barrier at each grain boundary, when MOS is exposed to gas, the potential barrier height decreases and resistance drops.	31
Figure 3.2 Sensitivity of SnO_2 to 800 ppm H_2 as function of crystallite size D [2].....	32
Figure 3.3 Schematic models for grain size effect. Shaded parts show core region (low resistance), while unshaded show the space-charge region (high resistance). (a) Grain boundary control, (b) neck control and (c) grain control [2].	33

Figure 3.4 Log-log plot of SnO_2 resistivity measured at room temperature as a function of deposition oxygen pressure.	35
Figure 3.5 A schematic of a typical gas sensor electrode pattern of interdigitated fingers. We used thermally evaporated 100 nm thick Au	37
Figure 3.6 A schematic of a complete library of 16 separate sensors.....	38
Figure 3.7 Single mask photolithographic procedure: (a) using lift off, (b) using wet etching	39
Figure 3.8 The schematic of the top view of combinatorial shutter assembly necessary to fabricate gas sensor libraries	41
Figure 3.9 A photograph of a library chip.	43
Figure 3.10 Comparison of the basic elements of an artificial olfactory system with the human olfactory system (from Alpha MOS []).	45
Figure 3.11 Two examples of inorganic electronic noses.....	47
Figure 3.12 A photograph of a gas flow chamber	49
Figure 3.13 The model response of a sensor to the gas flow cycle. R is the resistance in gas, R_0 is the resistance at a fixed reference point prior to flowing gas.....	49
Figure 3.14 Sensor response in resistance change $(R-R_0)/R_0$ at 400 °C for five sensors from the target library. (a) A model response to the flowing of gases and refreshing air introduced in an alternating manner. (b) Each sensor exhibits a different time dependent response pattern for a given gas. The arrows indicate when different gases (F), (B), (C), and (A) were introduced in the chamber.....	52
Figure 3.15 Dependence of time response on gas introduced for two sensors. The responses were found to be reproducible from cycle to cycle.	53
Figure 3.16 A radar plot showing responses of the five sensors for different gases at 400 °C. The normalized resistance change corrected for drift is plotted on each axis for each sensor. Each curve represents a different analyte	54
Figure 4.1 RCSJ model of a Josephson junction connected to a current source.	61
Figure 4.2 (a) A Schematic of a dc SQUID, (b) I-V characteristic curve of a SQUID, (c) periodic relation between V and Φ_a/Φ_0 at a fixed bias current I_{bias}	63
Figure 4.3 (a) Step edge grain boundary Josephson junction, (b) Bicrystal grain boundary Josephson junction (reproduced from Ref. [39]).	65

Figure 4.4 Photolithographic procedures using (a) three masks for making the SQUID chip. First, the chip is covered with a photoresist. (b) Then, the first mask is used to remove the Au and the YBCO from the edges in order to expose the grain boundary area. (c) Then, the second mask is used to remove Au from top of YBCO where the SQUIDs will be located. (d) Finally, the third mask is used to make the SQUIDs pattern. The number of SQUIDs made on one chip is eight.....	67
Figure 4.5 An optical microscope photograph of a successfully fabricated HTS SQUID.	68
Figure 4.6 : I-V characteristic curve of a SQUID at 77 K. The typical values of parameters of interest are: critical current $I_c (= 2I_0) \sim 40 - 120 \mu A$, junction resistance $R_J \sim 2.5-4\Omega$, and voltage modulation depth $\Delta V \sim 40-50 \mu V$	69
Figure 4.7 The copper cold finger. This particular chip had a broken modulation line, so the modulation coil is wound on the sapphire rod itself.....	70
Figure 4.8 The schematic diagram of the flux-locked-loop feedback electronics inside the Berkeley box.	71
Figure 4.9 A photograph of the university scanning SQUID system	72
Figure 4.10 A photograph of a commercial scanning SQUID system, Magma C20.....	74
Figure 5.1 The coordinate system for simulating a sample using the dipole equation (Eq. 5.1).....	81
Figure 5.2 A Labview panel for simulating in-plane magnetized samples. The distribution of magnetic field B_z due to m_x is shown in the window. The sample here is 1 mm x 1 mm x 3000 Å, scanning area 5 mm x 5 mm, $M = 5 \text{ emu/cc}$, step size in x and in y = 50 μm , integration step = 5 μm , scanning height is 150 μm . ..	83
Figure 5.3 The line charge model (a) uniform in-plane magnetization in a thin film in one direction, (b) equivalent magnetic line charge taken to infinity. I will take the B field along the purple dashed line in order to fit the data.....	85
Figure 5.4 The coordinate system to find B_z	86
Figure 5.5 Magnetic field from the magnetic line charge model (solid line) fitted to the simulated data (dotted).	87
Figure 5.6 Variation of maximum B_z as a function of z.	88
Figure 5.7 Variation of M calculated from the line charge model as a function of w for a given $z = 150 \mu m$	89
Figure 5.8 Image of the normal component of magnetic field from a thin-film of SmCo_5 in zero applied field, magnetized with 3T, which is higher than the coercive field.	

The size of the sample is 1.63 mm x 1.7 mm. Black dashed line indicates the boundaries of the substrate, purple dashed line is the field line that I took to fit the data.	91
Figure 5.9 (a) Magnetic field from the magnetic line charge model (solid line) fitted to the experimental data (dotted) from scanning SQUID of SmCo ₅ thin film. (b) The hysteresis loop of the same sample from SQUID magnetometer.	92
Figure 5.10 (a) A schematic diagram of the current loop model for a uniform out-of-plane magnetized sample. The current in this case is flowing in the clockwise direction and produces a magnetic field inside the sample that is going into the plane of the paper (red). (b) One line scan of B_z across the black dotted line of the sample in (a). The profile of B_z is shown.	98
Figure 5.11 The coordinate system for calculating the B_z at a point (x,y,z) from all 4 parts of the wire carrying current I in the clockwise direction. The corners of the loop are labeled as (x ₀₋ , y ₀₋ , 0) and (x ₀₊ , y ₀₊ , 0). The points of x ₀₋ and x ₀₊ are symmetric about the x axis and y ₀₊ and y ₀₋ about the y axis.	99
Figure 5.12 Magnetic field from the current loop model (solid line) fitted to the simulated data (dotted).	100
Figure 5.13 Image of a normal component of magnetic field from the CFO thin film in zero applied field. The size of the substrate and the film is 5.3 mm x 5.1 mm. The yellow dashed line indicates the boundaries of the sample whose magnetization I calculated. The purple dashed line shows the line of B_z that I took to fit the data using the current loop model.	102
Figure 5.14 (a) Magnetic field from the current loop model (solid line) fitted to the experimental data (dotted) from scanning SQUID microscope data of a CFO thin film magnetized out-of-plane. (b) A hysteresis loop in the out-of-plane direction of the same sample from a SQUID magnetometer.	103
Figure 6.1 Schematic for (a) a discrete library and (b) a composition spread.	109
Figure 6.2 (a) A schematic of a composition spread sample with a varying M. The sample is divided into small strips to calculate magnetization for each composition. (b) An example of magnetization distribution for a composition spread.	110
Figure 6.3 Different window functions (a) $f(k)$ in the k space as a function of k/k_w when k_w is the same for all three window functions. (b) $f(k)$ as a function k/k_w when k_w , Gaussian = 0.42 x k_w , Hanning (k_w , Hanning = k_w)	113
Figure 6.4 A simulation of a dipole of 3 mm (l) x 850 μ m (w). (a) The schematic of the simulated data acquisition. The coordinate system shown here denotes the axis directions only. (b) Distribution of the magnetic field due to the in-plane magnetization of a simulated sample. The black dashed line denotes the sample dimensions.	117

Figure 6.5 ρ_m dependence on the k_w value for the simulated data ($z = 150 \mu\text{m}$).....	120
Figure 6.6 Optimum k_w range for in-plane magnetization as a function of $1/z$	121
Figure 6.7 The sample dimensions are 3 mm x 850 μm , and the scanning area is 5 mm x 5 mm (orange dotted line). The integration area is $L \times W$ (purple dashed line)...	123
Figure 6.8 The behavior of M_{in} as a function of the ratio of integration length L over the sample.....	123
Figure 6.9 The dependence of calculated M_{in} on the dipole width w for $z = 150 \mu\text{m}$ when 50 μm strip or the whole sample is selected for integration.....	125
Figure 6.10 The dependence of calculated M on the dipole width w for four different z values.....	128
Figure 6.11 Simulation of an out-of-plane magnetized dipole of 1 mm x 1 mm. (a) Two dimensional image of B_z . (b) Magnetic field along the yellow dashed line in (a) as a function of x	130
Figure 6.12 M_z dependence on the k_w value for the simulated data ($z = 150 \mu\text{m}$).	131
Figure 6.13 Optimum k_w range for the out-of-plane magnetization calculation as a function of $1/z$	133
Figure 6.14 M_z calculated from the current loop model, inversion and the given value dependence on the ratio of scanning area to sample area from the simulated data.	135
Figure 6.15 5 out-of-plane magnetized samples of single composition CoFe_2O_4 thin films of 5 mm x 5 mm (a) 2 mm x 2 mm (b), 1.2 mm (c), 0.6 mm (d), 0.3 mm (e) that were measured using the scanning SQUID microscope. For each sample, two dimensional image of B_z is shown.....	136
Figure 6.16 M_z calculated using the inversion technique, the current loop model and from the SQUID magnetometer as a function of the ratio of scanning area to sample area from the experimental data.....	137
Figure 6.17 For both (a) and (b), the top images are two dimensional magnetization distributions, and the bottom are plots of M_z vs position on the chip taken along the yellow dotted line from the top images. An artificial magnetization generated on the outside of the sample of opposite sign is seen here. In (a) experimental data of the sample 2 mm x 2 mm is shown, in (b) simulated data, as discussed in the text.	138
Figure 6.18 A scan line of B_z of a out-of-plane magnetized sample. When the scanning area (a) is at least 5 times (we will see where this 5 comes from, not drawn to scale)	

the sample area, the field is seen to decay to 0. (b) When the scanning area is smaller than in (a), part of the data is missing: B did not fully decay to 0.	139
Figure 6.19 (a) Adjusted current loop model is used, when the scanning area is not large enough for B_z to completely decay. (b) Comparison of the B field scan line from the first current loop model when the scanning area is sufficiently large (purple). The adjusted model is used when the scanning area is not large enough (blue)...	140
Figure 6.20 $M_z (= M_{z1}+M_{z2})$ dependence on the ratio of the scanning area to the sample size for simulated data and experimental (CFO samples mentioned above) data for $z = 150 \mu\text{m}$ when the inversion is used.	142
Figure 6.21 Propagation of error in M_z as z changes and as the ratio of the scanning area/sample area gets smaller.	143
Figure 7.1 History of discovery of magnetostrictive materials.....	147
Figure 7.2 NiTi wire exhibiting the shape memory effect.....	148
Figure 7.3 An example of transformation of a cubic structure to a tetragonal case: (a) structure of high temperature and low temperature phases, (b) shape memory effect.	149
Figure 7.4 Schematic of FSM effect for a transformation of cubic structure to tetragonal	151
Figure 7.5 Combinatorial co-sputtering UHV chamber (Pbase $\sim 1 \times 10^{-9}$ Torr) system...	153
Figure 7.6 The nonconfocal configuration of the guns. The change in distance x varies the spread profile of the deposited materials.	154
Figure 7.7 An example of FSMA library made with three targets: Ni, Mn, Ni_2Ga_3 on a Si substrate of thickness 5000 \AA , insitu deposited with a physical mask and annealed at a temp 500°C	155
Figure 7.8 An illustration of the use of WDS for mapping a ternary phase diagram A-B-C.	157
Figure 7.9 A scanning SQUID image of Ni-Mn-Ga combinatorial library wafer.....	158
Figure 7.10 Two dimensional image of ρ_m for the same wafer as in Figure 7.9, denoting the most magnetic regions on the wafer.....	159
Figure 7.11 The schematic of a square from a library. Each square is $1.75 \text{ mm} \times 1.75 \text{ mm}$. The spacing between the squares is 0.5 mm	160
Figure 7.12 Distribution of M as a function of position on the physical library.	161

- Figure 7.13 Room temperature magnetic phase diagram of Ni-Mn-Ga. The region inside the blue curve is the compositional region mapped on the spread wafer. The composition where the orange line meets the Ni-Ga line is Ni_2Ga_3 , which is one of the target compositions we used. The circle inside the diagram marks the compositions near the Ni_2MnGa Heusler composition. 162
- Figure 7.14 (a) A photograph of Ni-Mn- Ni_2Ga_3 spread deposited on a cantilever library taken during the temperature-dependent measurement. The lines are a reflection of an image with colored lines held over the wafer. The shifts in the positions of the lines as a function of temperature are used to detect small changes in the local curvature of the cantilever. (b) Zoomed up view of a row of cantilevers that showed martensitic transitions. 164
- Figure 7.15 Mapping of compositional regions on the phase diagram that displayed martensitic transformation. The composition where the orange line meets the Ni-Ga line is Ni_2Ga_3 165
- Figure 7.16 A photograph of the scanning x-ray microdiffractometer. 167
- Figure 7.17 A schematic drawing of diffraction geometry when using a 2-D area detector. A range of 2θ and χ are detected simultaneously. 168
- Figure 7.18 A unit cell of L2_1 structure of an austenite. 168
- Figure 7.19 Scanning X-ray microdiffractogram taken at room temperature along a compositional region marked by the solid black line in Figure 7.15. There are three peaks, two are from a martensite and the middle one is from an austenite. 169
- Figure 7.20 Functional phase diagram deduced from the present experiment. The hatched region has compositions with average electron/atom ratio 7.3–7.8. The dotted line surrounds the region of reversible martensites. In the ferromagnetic region, the red area has the highest magnetization. 170
- Figure 7.21 Martensitic start temperature against room temperature saturation magnetization for data points mapped in Figure 7.15. For this magnetization, cantilevers were measured individually using a vibrating sample magnetometer. The line is a linear fit to the data. 172
- Figure 8.1 A Coupling diagram between ferroelectricity, ferromagnetism and stress. Artificial magnetoelectric composite materials can be made by coupling through the lattice/mechanical property. 175
- Figure 8.2 A schematic of the composition spread where the average composition on the spread is varying continuously from pure CFO at one end to pure PTO at the other end. 178
- Figure 8.3 A schematic of synthesis of a PTO-CFO composition spread. (a) Laser firing, target switching (PTO & CFO) and the shutter motion are synchronized. (b) A

wedge-like thickness gradient is created by the moving shutter during the deposition. (c) The schematic side view of the composition spread, each wedge is 12.6 nm thick.....	179
Figure 8.4 CFO-PTO 15x composition spread in-plane magnetized, outlined by a purple dashed line. (a) Two dimensional B field distribution for the sample (b) calculated ρ_m using the inversion technique. In (a) I denoted the regions of the spread and pure CFO.....	182
Figure 8.5 M_{in} distribution as a function of position on the CFO – PTO composition spread.	183
Figure 8.6 CFO-PTO 15x composition spread out-of-plane magnetized, outlined by a yellow dashed line. Shown is the M_z distribution obtained using the inversion technique. Here, I denoted the regions of the spread and pure CFO.....	184
Figure 8.7 M_z distribution as a function of position on the CFO – PTO composition spread.	185
Figure 8.8 Remanent in-plane and out-of-plane M distribution as a function of composition of CFO – PTO composition spread.	186
Figure 8.9 Hysteresis loop of pure CFO for the in-plane and out-of-plane magnetization measured by the SQUID magnetometer.....	187
Figure 8.10 Hysteresis loop of the out-of-plane magnetization for the single composition thin film of PTO ₈₀ -CFO ₂₀	188
Figure 8.11 A photograph of a scanning tip microwave near-field microscope set-up..	189
Figure 8.12 Linear dielectric constant measured at 1 GHz as a function of average composition across the spread by the microwave microscope. The thickness of the thick end for each wedge layer is ~ 12.6 nm, which corresponds to the 15x unit cell of CFO and the total thickness is ~ 300 nm (the inset). The highest dielectric constant occurs at the composition of (PTO) _{0.8} – (CFO) _{0.2}	190
Figure 8.13 The non-linear dielectric signals measured at 1 GHz as a function of average composition across the PTO – CFO spread by the microwave microscope. The sample under study is the same as shown in the inset of Figure 8.12. The highest non-linear dielectric signal also occurs at the composition (PTO) _{0.8} – (CFO) _{0.2} .	191
Figure 8.14 (a) X-ray diffraction patterns of the (200) and (002) peaks of PTO–CFO composition spread on MgO substrate. The (002) tetragonal PTO shifts to a higher angle of 46° and the (200) tetragonal PTO shifts to a lower angle of 46° as the ratio of PTO decreases. The two peaks (002) and (200) merge when PTO is less than 85%. (b) Phase transition temperature versus the % of PTO in the composition spread.	193

Figure 8.15 (a) A schematic of the composition spread. The thickness of each wedge is 12.6 nm, which corresponds to 15 unit cells of CFO; the total thickness is 300 nm. (b) and (c) show diffraction pattern and an image of cross sectional high-resolution transmission electron micrographs of the $\text{PTO}_{0.8}$ - $\text{CFO}_{0.2}$ film on MgO substrate (incident electron beam is $\langle 100 \rangle$ of MgO).	194
Figure 8.16 (a) and (b) show an image of cross section and a diffraction pattern of high-resolution TEM of the $\text{CFO}_{0.8}$ - $\text{PTO}_{0.2}$ film on MgO substrate (incident electron beam is $\langle 100 \rangle$ of MgO).	195
Figure 8.17 Magnetic and ferroelectric properties of the 15x CFO-PTO composition spread. The circled region corresponds to compositions where we expect to measure magnetoelectric effect.	197

Chapter 1

Introduction

Combinatorial synthesis is a technique that allows one to quickly investigate a large number of previously unexplored materials by fabricating arrays of compositionally varying samples. In combinatorial experimentation, the biggest challenge is often in implementing an effective tool for rapid characterization. To facilitate high-throughput screening of the combinatorial samples, parallel detection schemes and non-destructive scanning probe microscopes are used to identify compositional regions with enhanced physical properties. In our group, we use a number of recently invented scanning probe microscopes that are ideal for scanning the combinatorial libraries and characterizing their electric and magnetic properties. They include the scanning superconducting quantum interference device (SQUID) microscope, scanning microwave and scanning ferromagnetic resonance microscopes.

The focus of this thesis is on the use of combinatorial pulsed laser deposition for synthesis of both discrete libraries and composition spreads, as well as on quantitative analysis of magnetic properties of composition spreads using the scanning SQUID microscope.

In Chapter 2, I introduce the basics of combinatorial synthesis. I discuss the pulsed laser deposition (PLD) technique, and describe the combinatorial PLD system for which I built the automated controls and finalized the software communication. I describe the basic design and operation of the PLD technique used to fabricate

combinatorial libraries. I also briefly introduce the analysis tools that were used to characterize them.

In Chapter 3, I discuss synthesis and operation of gas sensor libraries or electronic noses based on doped semiconducting SnO_2 thin films. I give some background about gas sensing and discuss the mechanism of semiconductor gas sensors. I show how the libraries were fabricated using combinatorial PLD flange and characterized using multiplexing electronics. The gas sensor libraries are an example of discrete library.

A scanning SQUID microscope is a convenient tool for probing magnetic properties of combinatorial libraries and composition spreads. In Chapter 4, I discuss some fundamentals of SQUIDs and the commercial scanning SQUID microscope developed at Neocera, Inc., I then briefly discuss the SQUID fabrication.

In Chapter 5, I introduce simple models, which can be easily adopted to characterize uniformly magnetized thin films. They are the line-charge model for the in-plane magnetization and the current-loop model for the out-of-plane magnetization. These models are discussed in detail, and are applied to experimental and simulated data for obtaining magnetization. For samples with varying magnetization, such as combinatorial libraries and composition spreads, however, the models fail to provide reliable results for magnetization. Therefore, here, I introduce the inversion technique to calculate magnetization. The formal derivation of this technique for the in-plane and out-of-plane magnetization is presented.

In Chapter 6, I examine the role of the parameters that control the inversion technique for calculating the in-plane and out-of-plane magnetization. Understanding their role is important when one wants to obtain reliable and accurate results for

magnetization, in particular, for combinatorial libraries and composition spreads. To this end, I simulate magnetic field for in-plane and out-of-plane magnetized thin films. Using these simulation data, I discuss the effects of the parameters, such as the cut-off-frequency, the distance between the sample and the SQUID, scanning area and integration area on the magnetization. The inversion technique is then applied to experimental data, for uniformly magnetized samples, and the results are compared with the simulated data.

In Chapter 7, I discuss combinatorial investigation of ferromagnetic shape memory alloys (FSMAs), where the inversion technique was applied for calculation of remanent magnetization. I discuss high-throughput synthesis and characterization techniques that were used for this particular system. I show how we have mapped the ternary compositional phase diagram of the Ni-Mn-Ga system, and discuss the results of this investigation, where we extended the known FSMA regions to previously unexplored regions.

In Chapter 8, I discuss magnetoelectric thin film composition spreads. In particular, I discuss on our recent work on the system of PbTiO_3 (PTO) - CoFe_2O_4 (CFO). I focused on magnetic characterization of the composition spreads. Using the optimized parameters of the inversion technique, I calculated in-plane and out-of-plane remanent magnetization distributions for the composition spread. From these distributions, I show that when PTO is added to CFO, and the microstructure of the material changes, and its magnetic anisotropy changes. We found that the compositions between $(\text{PTO})_{0.5} - (\text{CFO})_{0.5}$ and $(\text{PTO})_{0.8} - (\text{CFO})_{0.2}$ exhibit the coexistence of ferroelectricity and ferromagnetism.

Chapter 2

Combinatorial synthesis

In this chapter, the basics of combinatorial synthesis are introduced. I briefly discuss pulsed laser deposition (PLD), and describe the combinatorial PLD system for which I built the automated controls and finalized the software communication. I will describe the fundamental design and operation of the PLD technique used to fabricate combinatorial samples. I will also introduce the analysis tools that were used to characterize the samples.

2.1 Basics of combinatorial synthesis

Throughout history, scientists and engineers have relied on trial-and-error for materials discovery. This process allows only a small number of materials to be examined in a given period of time. Combinatorial synthesis is a technique that allows one to quickly investigate a large number of previously unexplored materials. Within the last two decades, combinatorial chemistry and screening for new drugs and biomolecules have revolutionized the pharmaceutical and DNA-sequencing industries [1]. Its application to inorganic solid-state materials was pioneered at Lawrence Berkeley National Laboratory (LBNL) [2], and the effectiveness of the approach has since been demonstrated in the discoveries of dielectric/ferroelectric materials [3, 4, 5, 6], ferromagnetic materials [7, 8], colossal magnetoresistive materials [9, 10], polymers [11, 12, 13], catalysts [14, 15], and luminescent materials [2, 5].

The combinatorial techniques can be used to address materials issues at different levels in a wide range of topics from semiconductor manufacturing and thin-film smart materials to catalytic powders and biomaterials. It is hoped that the combinatorial approach to materials will lead to accelerated innovation in various industries broadly benefiting our society.

When surveying the history of materials science, one finds that most of the basic binary compounds have been explored, and most of their properties are known. However, the recent discovery of superconductivity in MgB_2 shows that not even this is completely true. However, as soon as one moves to other multi-element compounds such as ternary or quaternary, one finds that a large fraction of all possible compounds (formed by combining different elements) remain unexplored. At the end of 1980s, J. C. Phillips estimated that there were about 24,000 known inorganic materials [16]. Out of these, 16,000 are binary compounds, and only 8,000 are ternary and other multi-element compounds. If one is simply to pick out any three or four elements from the periodic table to form different compounds (there are about 60 non-radioactive and non-gas elements), there are over 30,000 possible ternary compounds and 500,000 possible quaternary compounds. Clearly, an extremely large number of compounds are yet to be explored. Any effort to systematically explore them using the one-by-one traditional approach would take a prohibitively long time. Combinatorial synthesis offers a potential solution to this problem.

The general trend in materials discoveries is that new materials tend to have increasingly complicated structures, often consisting of a large number of elements. Looking at the development of materials, there is also a trend that compounds that are

more complex tend to have physical properties that are more desirable. This is clearly illustrated in the case of high-temperature superconductors, where the highest superconducting transition temperature is currently observed in the $\text{HgBa}_2\text{Ca}_2\text{Cu}_3\text{O}_{8+d}$ compound with a complicated layered structure. Figure 2.1 shows the critical temperature (T_c) of superconductors as a function of number of elements required to form the compound. It suggests that T_c increases as the compounds become more and more complex.

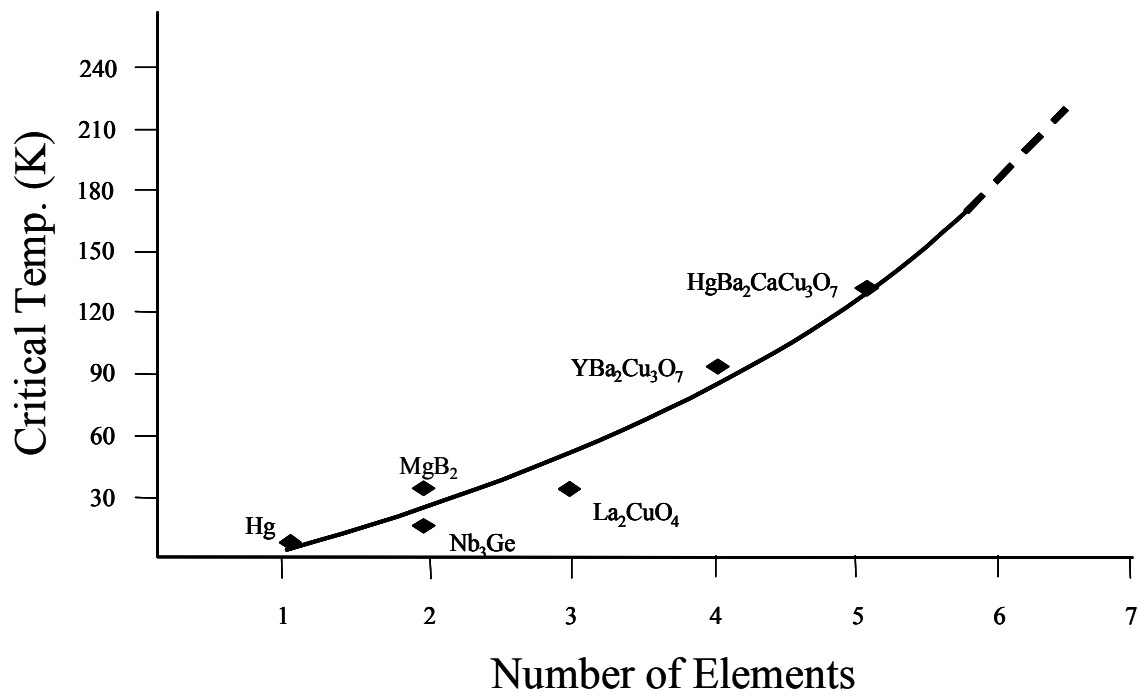


Figure 2.1 The correlation between materials complexity (reflected in the number of elements required to form the compounds) and a physical property (T_c) for superconductors.

The application of the combinatorial approach to technologically relevant electronic materials is best implemented in the form of thin-film libraries. Combinatorial thin-film libraries encompassing large compositional variations can be generated using different thin-film deposition techniques. Figure 2.2 shows the flow process of one

representative combinatorial synthesis thin film experiment. In this scheme, a large collection of compositionally varying samples is synthesized under the same conditions. Each composition, in this case is spatially separated from others by a grid formed by shadow masks. The samples are then processed and screened simultaneously. Different

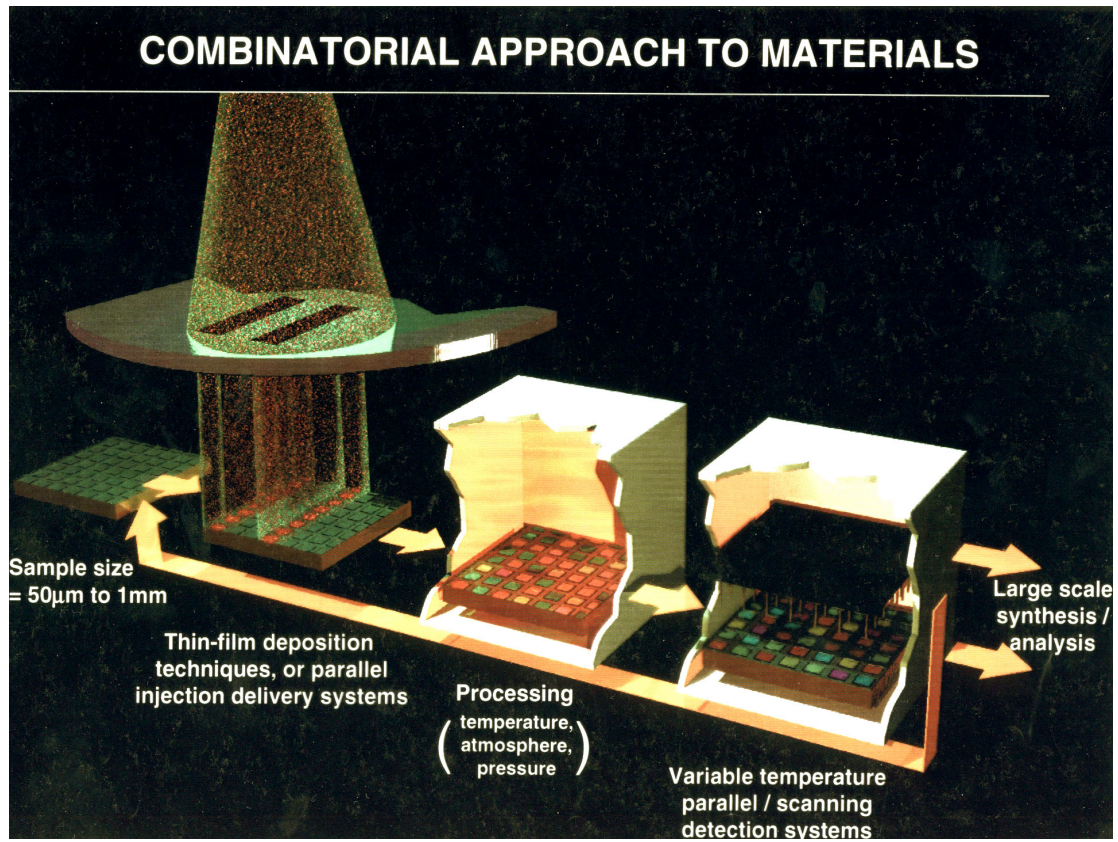


Figure 2.2 The flow diagram of a representative combinatorial thin film experiment.

characterization tools are used depending on the desired application and physical properties of interest. Once compositions with enhanced physical properties are identified, they are analyzed individually in more detail, and subsequently large scale synthesis is pursued. This strategy has the potential to unearth an abundance of useful materials in a single experiment. Materials scientists are increasingly taking advantage of

the efficiency of combinatorial synthesis and extending it to accelerate the discovery of complex compounds in a variety of areas.

In our group, we have developed several new combinatorial deposition chambers. They include versatile pulsed-laser deposition systems with a modular combinatorial flange, a multi-gun ultra-high vacuum sputtering system, and a source dual-gun electron beam evaporating system with a modular combinatorial flange.

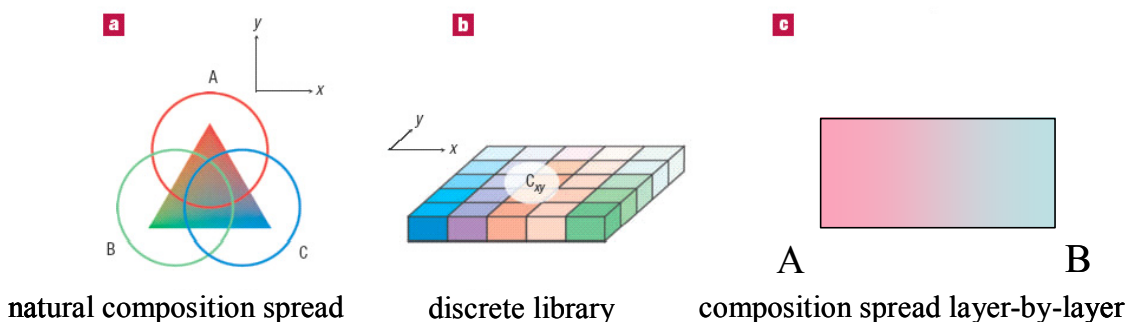


Figure 2.3 A schematic of three basic library designs used in our group. (a) Natural composition spread technique. Varying combinations of three different elements (A, B and C) are obtained at different positions on a wafer by co-deposition. (b) A discrete library. Each site has a different composition and can be addressed as C_{xy} . (c) Binary composition spread. The composition across the chip continuously changes from A to B.

In our group, we utilize several kinds of library designs (Figure 2.3). Figure 2.3 (a) shows the natural composition spread typically made by co-deposition of different elements (A, B, and C). The degree of the intermixing of elements can vary depending on the deposition condition. This technique can be used to map different parts of ternary phase diagrams. This type of library design was employed for the search of new compositions of ferromagnetic shape memory alloys (FSMA) [7], which will be discussed in Chapter 7. The discrete library is shown in Figure 2.2 and Figure 2.3 (b).

Here, each site on the chip is spatially separated from other sites and can be addressed as C_{xy} . Each chip can contain up to thousands of different compositions. This type of library design was used to investigate gas sensor materials [17]. This is discussed in Chapter 3. The last type of combinatorial sample is shown in Figure 2.3 (c), which is a binary composition spread, where the composition across the chip continuously varies from pure A at one end of the chip to pure B at the other. This spread is typically fabricated using a layer-by-layer deposition, which allows one to control the intermixing of the two materials A and B at the nanometer level. Binary phase diagrams can be mapped on individual chips using this technique. An example where the composition spreads were used for the search of magnetoelectric materials (ME) will be discussed in Chapter 8.

Mapping compositional phase diagrams is of paramount importance in materials physics. For instance, establishing the doping phase diagram in cuprate superconductors and perovskite manganites has played a critical role in advancing the understanding of their physical properties [2, 18]. The continuous composition spread techniques (Figure 2.3 (a) and (c)) have proven to be a powerful means to quickly map previously unexplored regions of materials phase-space [7,19, 20]. Such experiments can be used to elucidate the physics of various phenomena.

In combinatorial experimentation, the biggest challenge is often in implementing an effective tool for rapid characterization. Parallel detection schemes and non-destructive scanning probe microscopes are used to facilitate high-throughput screening of the combinatorial libraries and composition spreads in order to identify compositional regions with enhanced physical properties. In our group, we have taken advantage of a

number of recently invented scanning probe microscopes that are ideal for scanning the combinatorial libraries and characterizing their electric and magnetic properties. They include the scanning superconducting quantum interference device (SQUID) microscope, the scanning microwave microscope and the scanning ferromagnetic resonance microscope.

The focus of this thesis is on the use of combinatorial pulsed laser deposition for synthesis of both discrete libraries and composition spreads (Figure 2.3 (b) and (c)), as well as on quantitative analysis of magnetic properties of composition spreads using the scanning SQUID microscope.

2.2 Combinatorial thin film library fabrication by Pulsed Laser Deposition (PLD)

Combinatorial synthesis techniques have been used to make libraries of both bulk materials and thin films. In this thesis, I will mainly discuss thin film library fabrication using PLD. For combinatorial investigation, there are several advantages of thin films over bulk materials. They include the fact that 1) non-equilibrium processes of thin film deposition can lead to the formation of phases unavailable in the bulk and 2) readily available microfabrication techniques can lend themselves to library synthesis techniques. There are two major methods to create large compositional variation in combinatorial libraries and composition spreads: (1) solution-based synthesis [21] and (2) solid-state thin films [22]. The basic premise of library fabrication is that compositional variation is achieved across a library through spatially selective materials deposition and synthesis.

We have used PLD to make different types of combinatorial samples comprised of solid-state thin films.

2.2.1 Basics of PLD

Unlike bulk materials, thin films must be grown on substrates, and the film properties can be highly influenced by the interface between the film and the substrate. Relevant properties of the interface include presence of microstructural defects and strain induced by the substrate. If a film is grown in such a way so that its orientation directly reflects that of the substrate, the growth mode is called epitaxial. When a film is grown on the same material as the substrate (for instance, (100) MgO film on (100) MgO substrate), it is called a homoepitaxial growth. Otherwise, the growths are heteroepitaxial. When there is a lattice mismatch between the film and the substrate, elastic tensile or compressive stresses will occur in the film for thickness less than the critical thickness (h_c) [23]. When the film thickness is larger than h_c , dislocations will start to develop to reduce the stress, and the film gets relaxed. Kinetics of the nucleation mechanism in thin film growth also plays an important role in determining the phase formation and the microstructure of thin films.

Among various thin film deposition schemes, PLD has been embraced as one of the most versatile methods for exploratory research. After the first high-power ruby laser became available, there was a flood of theoretical and experimental studies on the interactions of intense laser beams with solid surfaces, liquids, and gaseous materials. It was seen that vaporizing these materials by the intense laser beam could be achieved without any difficulty. Then the idea of using such intense laser radiation to ablate and

deposit thin films came along and was first demonstrated in 1965 by Smith and Tuner [24]. During the next two decades, however, further investigations were sporadic and slow-paced. The first major breakthrough came in the mid 1970s when an electronic switch was developed to deliver short pulses with very high peak power density. But it was the successful growth of high T_c superconducting films in 1987 that truly lifted PLD off the ground [25]. There have been major advances in the field of metal oxide thin films and devices in general, and this was accomplished with a significant contribution from PLD [26].

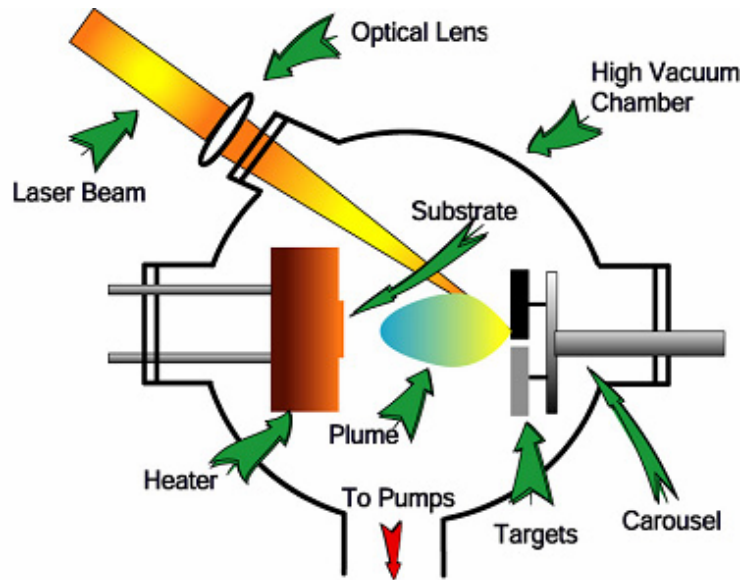


Figure 2.4 Schematic drawing of a PLD chamber

Conceptually and experimentally, PLD is relatively simple. A high-power pulsed laser is used as an external energy source to vaporize a target material and to deposit a thin film of the material on a substrate mounted on a holder inside a vacuum chamber (Figure 2.4). A set of optical components is used to focus and raster the laser beam over the target surface. This technique is flexible and is easily adaptable to different growth

conditions such as substrate temperature variation and the amount and kind of gas injected in the chamber for reactive deposition. The theoretical description of the mechanism that leads to material ablation is somewhat complicated involving equilibrium and nonequilibrium processes and depends on laser beam characteristics as well as optical, topological and thermodynamical properties of the target material.

When the laser radiation is absorbed by a solid surface, electromagnetic energy is first converted into electronic excitation, then into thermal, chemical and mechanical energy to cause evaporation, ablation, excitation and plasma formation. The plume forms from evaporants consisting of a mixture of energized species such as atoms, molecules, electrons, ions, clusters, etc. Since the mean free path inside the dense plume is very short, the plume expands into vacuum to form a hydrodynamic jet from the target surface to the substrate surface. The non-equilibrium mechanism in the plume formation results in the highly stoichiometric transfer mode of materials. The high diffusion mobility of atoms on the substrate surface transferred from the kinetic energy of the plasma plume results in relatively smooth surface of the film.

PLD has many advantages. A single composition film can be made in a relatively short period of time in high vacuum or in low pressure of reactive gases. By monitoring the number of laser pulses, one can control the deposition of materials at atomic layer level, and using a layer-by-layer deposition technique (using more than one target in one set of depositions), one can design and explore novel materials systems that do not exist in bulk forms. Target materials do not need to be biased, and a multiple-target carousel allows deposition of a number of different materials in a single run. PLD systems are relatively inexpensive, and they can be set-up quickly and easily with minimum

maintenance requirements. In addition to metal oxides (and metals), PLD has also been used to fabricate thin films of polymer materials and other organic molecules [27]. However, there are disadvantages of PLD as well. First, the strong directionality of the laser plume results in a pronounced thickness and compositional gradient in deposited film across the substrate. A typical area of uniform thickness and composition under a standard oxide deposition condition (O_2 partial pressure: 100 mTorr, target-substrate distance: ≈ 10 cm and energy density of 1-2 J/cm² focused to a spot of 1mm x 4 mm) is limited to 1 cm x 1 cm. Second, the surface roughness in the deposited film arises from the splashing effect (where particulates are transferred from the target to the substrate) which is enhanced with the increasing laser energy density. The particles produced by splashing can vary in size (sub-micron to micron) and shape (spherical to irregular). This effect can be minimized by the use of velocity selector or by implementing off-axis PLD geometry [28].

Compared to other deposition techniques such as molecular beam epitaxy and chemical vapor deposition, PLD is very flexible in its implementation, and it can be made to be relatively simple in operation. It has proven to be a powerful tool in fabrication of different types of thin films from ultra thin films to complex heteroepitaxial multilayers. From ferroelectricity, piezoelectricity, and optical nonlinearity to magnetism and superconductivity, PLD has become an indispensable tool in exploration of novel functional metal oxide thin films [29].

2.2.2 Combinatorial PLD flange

In order to perform fabrication of combinatorial samples in PLD, the mechanism that allows spatially varying deposition needs to be installed. This could be accomplished in a number of ways. Typically, there are a number of parts in the chamber such as shadow masks and/or movable shutter mechanism that need to be set up. This could result in complex and expensive deposition chamber designs [30, 31]. Our goal in incorporating combinatorial strategy to PLD was to keep its flexibility and to maintain and enhance the versatility. To this end, we have developed a compact combinatorial thin film deposition flange 8 inches in diameter where all the necessary components for creating combinatorial libraries and composition spread of different designs are integrated in a single vacuum flange. It was developed in collaboration with Russ Wood in mechanical development group [32]. Figure 2.5(a) is a photograph of the combinatorial PLD flange. The flange is approximately 19" in height and weighs approximately 25 lbs. The complete mechanism of the flange is entirely modular. Figure 2.5 (b) is a photograph of a PLD system with the combinatorial flange mounted to it. The flange is also applicable to any physical vapor deposition systems involving shadow deposition such as sputtering, evaporation, etc. There is a pending U.S. patent on the flange. Recently, we started using the flange in an electron beam evaporation chamber.

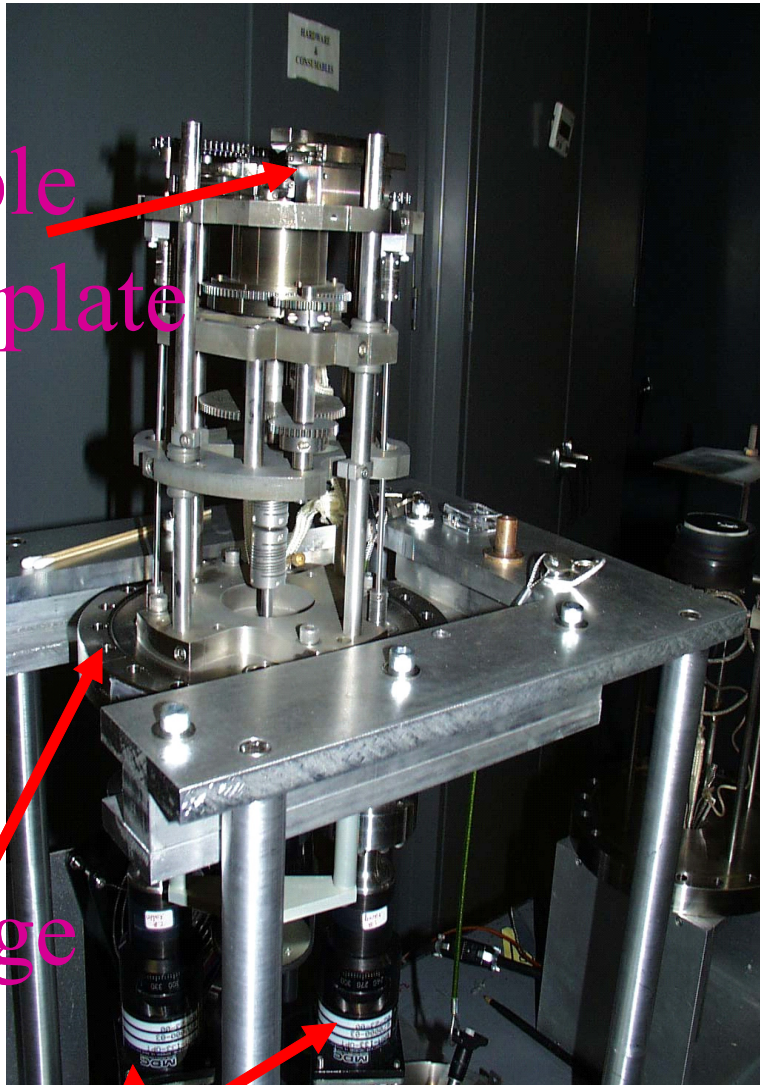
The flange has a 1.5-inch diameter sample-mounting heater plate, attached to a heater housing, which can be raised to a temperature of approximately 800 °C. The heater housing itself is rotatable in an automated manner with an indexed angle. Immediately above the heater plate is an x-y shuttering system, which allows spatially selective shadow deposition of different layouts anywhere on a mounted substrate up to

(a)

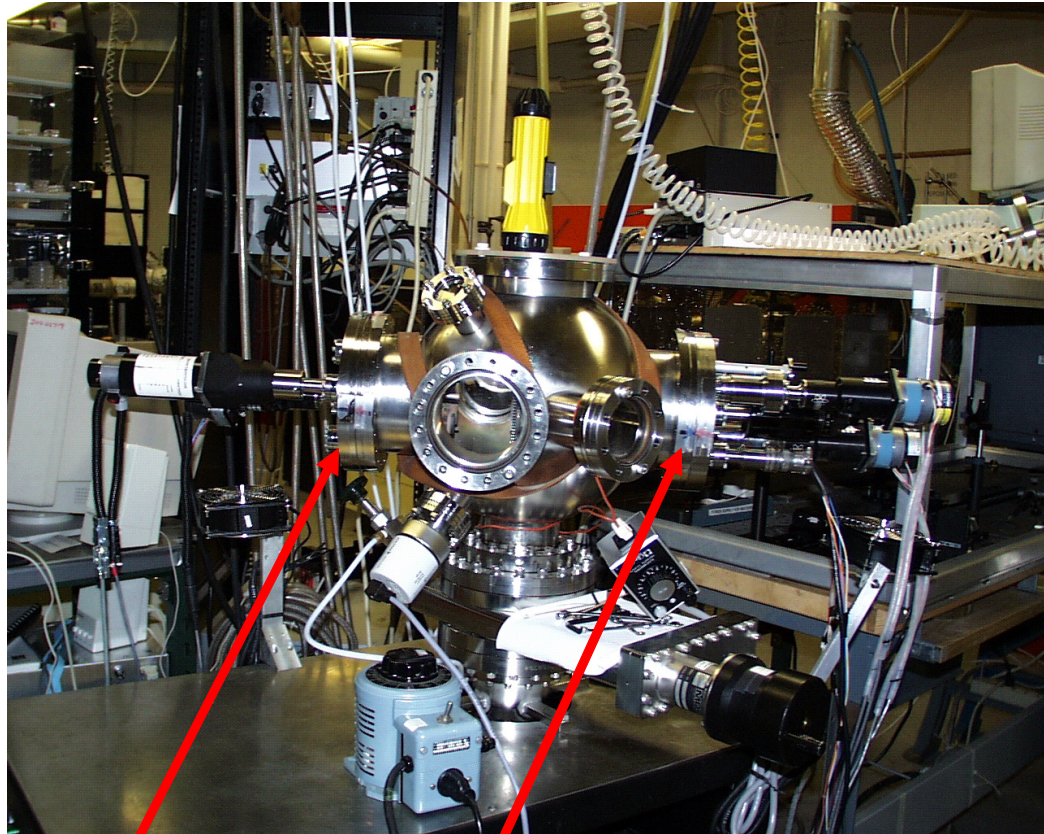
rotatable
heater plate

8" flange

shutter motors



(b)



carousel flange combi flange

Figure 2.5 (a) A photograph of the combinatorial thin film deposition 8" flange. (b) A photograph of the combinatorial PLD chamber.

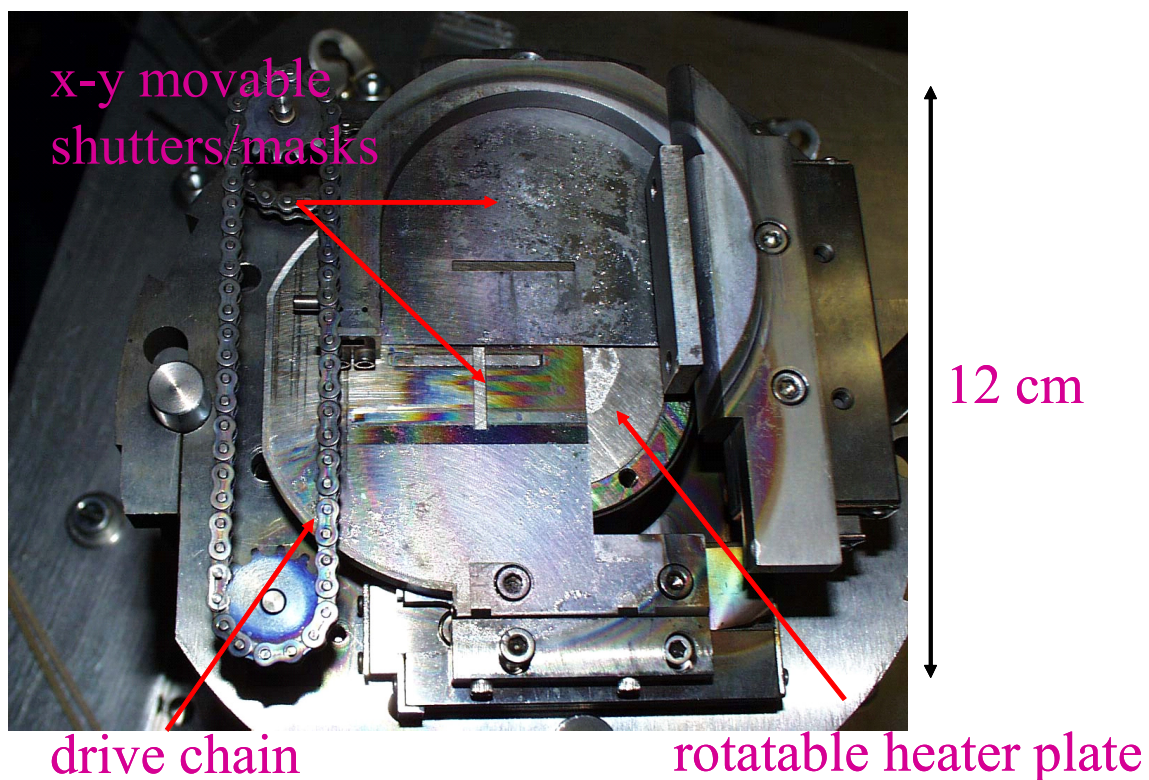


Figure 2.6 A top view photograph of the combinatorial flange showing the shutter assembly and the rotatable heater.

1-inch square in size (Figure 2.6). The shutters motions are automated. The motors drive the shafts transferring the motion to the chains, to which the shutters/masks are connected.

The shutters are about $300\ \mu\text{m}$ thick and are made of stainless steel sheets. The spacing between the heater plate and the shutter plates is adjustable. It can be as close as $100\ \mu\text{m}$, which is often the distance used for room temperature depositions, or as far away as 5 cm, for post deposition anneals at elevated temperatures. For *in-situ* growth of films at elevated temperatures, typically the separation distance is $300\ \mu\text{m}$ which is required for minimizing the heat transfer from the heater to the shutter system and then to

other parts of the mechanical assembly. The shutter plates and the heater plates are replaceable, and they are exchanged in going from experiment to experiment in order to minimize cross-contamination through re-sputtering of materials deposited on them. The shutters can move with variable speeds from 0.18 mm/sec to 1.2 mm/sec. For multilayer depositions, the shutter-driving motors, the target carousel, which fits up to six target materials and laser firing, are all synchronized by a computer and controlled via compiled Labview software.

The combinatorial PLD flange is portable and relatively easy to use. We have found that the two overlapping shutters, which move in orthogonal directions, combined with a rotatable heater allow us to create virtually any type of library/spread designs. I will discuss the details of the electronics and software involved in section 2.2.3.

Depending on the library layout, different shutter designs are required. We create various shapes in stencil masking by cutting different apertures into the shutters. Here, I will discuss two basic designs that I used. The first one is for generating discrete libraries, where thin film samples of different compositions are deposited on separated individual sites of square areas. A schematic of this design is shown in Figure 2.7 (a). For this, two orthogonal slits cut in the x-y shutters are used to position the square opening through which the film is deposited. An example of a library made this way is a gas sensor library with 16 different 50 nm thick sensor films deposited on arrays of two-terminal interdigitated electrodes [17]. The gas sensor library and its fabrication will be discussed in Chapter 3.

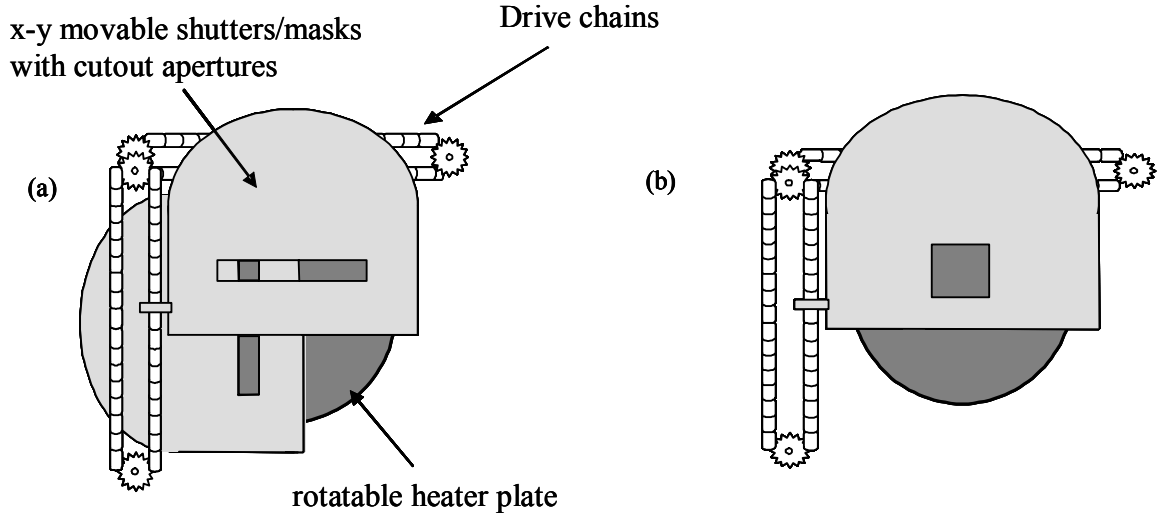


Figure 2.7 A schematic of the top view of the combinatorial shutter assembly. Different aperture layouts are used to fabricate different combinatorial libraries. (a) Set-up for fabricating discrete libraries. (b) Set-up for fabricating composition spreads. The wedge-like thickness profile (Figure 2.8) can be created using this.

The second type of combinatorial samples is composition spreads [32]. The utility of composition spreads has been previously demonstrated in rapid mapping of composition-property phase diagrams [4, 7, 9] as well as for optimizing materials properties [33]. A schematic of aperture design for generating composition spreads is as shown in Figure 2.7 (b). Here, a linear compositional gradient across the spread is created by performing a series of shadow depositions through the rectangular opening in a shutter, which moves back and forth over the substrate during the deposition. The motion of the shutter is synchronized with the firing of the laser in such a way, that for each deposition, a thickness gradient “wedge” is created on a chip.



Figure 2.8 A schematic side view of a pair of wedge like thin film layers deposited using a moving shutter edge.

Figure 2.8 shows a schematic side view of a pair of wedge layers of materials A and B deposited with the moving mask. This technique can be used to make composition spreads where the composition continuously varies from pure material A at one end to pure material B at the other end, and the two materials are intermixed at nanometer level. The utility of this technique in synthesis of PbTiO_3 (PTO)- CoFe_2O_4 (CFO) composition spreads is discussed in Chapter 8.

2.2.3 Automation of all the PLD components

Several components of the combinatorial PLD deposition system are automated. On the flange itself, there are three motors. The first two (motor #1 and motor #2) drive the x-y shutters. The third is a central motor that drives the heater housing. On the target carousel, there are two motors: one drives the main shaft on which the carousel rotates and the other drives each individual target for their rotation. The laser is synchronized with the shutters and the targets. Here in this section, I will describe the controls that I built for the flange motors and the software communication established for the whole system. The motor controls are made of a series of components. Figure 2.9 shows a

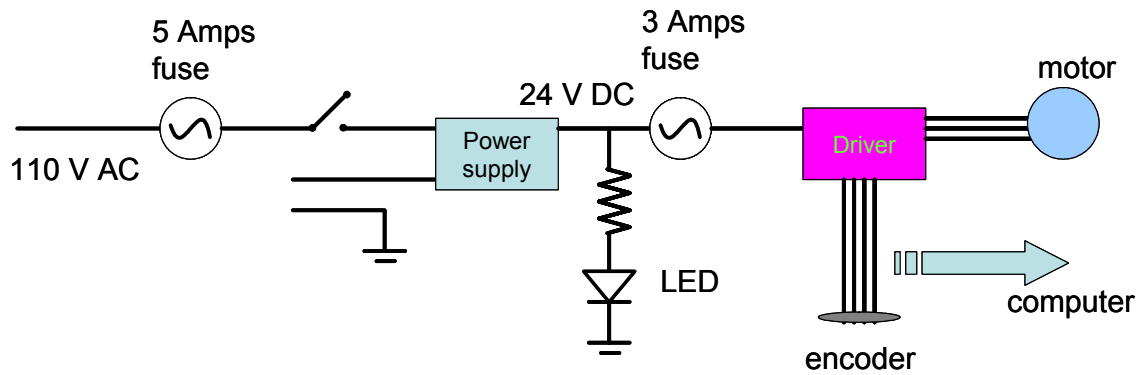


Figure 2.9 A Simple diagram of one motor connection

simple flow diagram of one motor connection. The stepper motor (Slo-syn Inc., Standard 60 mm Frame Size (NEMA Size 23, 200/500 steps/rev) and the encoder (optical encoder 200/500 steps/rev) are connected to the driver (Applied Motion Inc., 3535 Step Motor Drive). They are all powered by a 24 V power supply. As kindly supervised and suggested by Jack Touart of the Physics Electronics group, I incorporated two fuses to protect the driver (3 Amps) and the power supply (5 Amps) from overload current. The driver sends the signals to the control module (PMC Corp., Module DCX-MC360-R) which is mounted on a PCI board (PMC Corp., DCX-PCI300-ATA) which is assembled into the ISA/PCI slot of the computer.

All the connections and the components of the control box for the two motors that drive the two shutters (x and y) are seen in Figure 2.10. In Figure 2.10, the blue and the brown wires are for motor #1 and its encoder, respectively, and the green and orange ones are for motor #2. The black wires are the connections to the two fuses, as discussed above. A separate switch controls each motor, and an LED shows the presence of power. The Wincontrol software (PMC Corp.), supplied with the PCI board, communicates with the encoder via a driver. All the drivers and the .dll files must be installed prior to testing

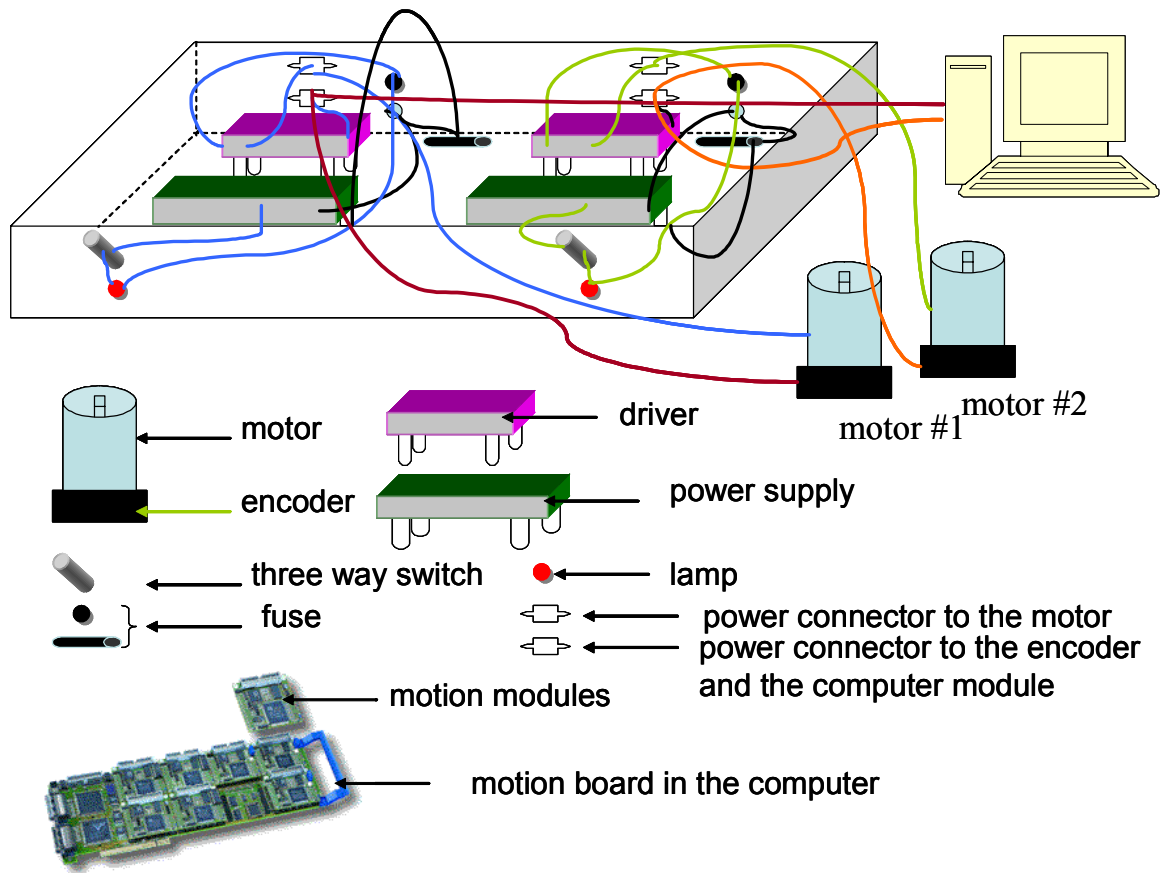


Figure 2.10 Control box and its components for two shutter motors of the PLD

the motion. They can be downloaded from the website of the company that makes the PCI board (www.pmccorp.com). To test the control box and the motion of the motors, I first used Wincontrol commands such as ts33 (tell status), ts34, sv (set velocity), etc. to set up for the desired motion. The velocity and the acceleration are set based on the experimental needs, as well as the trajectory of the velocity curve. However, during experiments, we need to use Labview software. A program that was used was Mask, it was originally written by Dr. Hauyee Chang at UC Berkeley, and modified by me.

There is an additional parameter that we must set in order to have the Labview program work correctly. This program reads the output of the encoder position. In order

for it to work properly, the encoder position must be 10 times the number of steps that one asks the motor to move. So the command to set the ratio of steps to 10 was used. Once this was successful, we connected the masking program to the Laser program. The software engineer Steve Garrahan of Neocera Inc. changed the standard PLD software and integrated his software with our Mask software to synchronize all the moving parts (the two carousel motors, the two shutter motors, the heater motor, and the firing of the laser). The PCI board (Galil Inc.) that controls the carousel motors as well as the driver control box and the power box were bought from Neocera, Inc. The compiled Labview software allowed us to control all the moving components including the firing of the laser. All the parts were incorporated in such a way that we had the freedom to change any relevant parameters (such as velocity and acceleration of the shutters, their repeating motion frequency, the rotation speed and the position of the carousel targets, the frequency and the number of pulses of the laser) in our experiments. The control box for the third motor for the rotary motion of the heater was built using the same design. For this purpose, the Labview program had to be rewritten and set up in such a way so that it was using the compiled software as a subroutine.

2.3 Screening of combinatorial libraries

After combinatorial libraries are made, properties of materials on the libraries need to be measured. In any type of combinatorial investigation, having the appropriate characterization tool is critical. Without a suitable high-speed screening technique, high throughput synthesis serves little purpose. In advanced functional materials, the required performance can be very application-specific. This often translates into having to design,

develop and tailor screening techniques that are specialized for individual applications. For instance, capacitor dielectrics in memory devices and tunable microwave devices using the same class of ferroelectric materials have entirely different sets of performance requirements, necessitating two different screening techniques.

The diverse spectrum of functionalities in materials (ranging from gas sensing and optical nonlinearity to piezoelectricity and magnetoresistance) represents a tremendous challenge in high-throughput screening, often requiring new measurement instruments to be developed. This is in contrast to combinatorial chemistry in life sciences, where the luminescent tagging technique is applicable in a wide range of studies. In many ways, the availability of characterization tools defines the scope of one's combinatorial materials research.

Scanning probe microscopes are often used for rapid characterization of thin film materials. The ability of the scanning probe microscopes to provide non-destructive, spatially resolved mapping makes them the ideal screening tools for a variety of physical properties. For instance, scanning superconducting quantum interference device (SQUID) microscopes have proved essential for investigation of magnetic materials [7, 22]. I will focus on this characterization technique and describe new developments in quantitative analysis of spatially varying magnetic properties from the data acquired from magnetic materials libraries by a scanning SQUID microscope in Chapter 6. Microwave microscopes were born out of the need to carry out non-contact electrical impedance measurements, and they are used for quantitative mapping of dielectric or ferroelectric materials libraries as well as resistance or conductance in thin-film libraries and spreads [3, 4]. Rapid characterization of optical properties (luminescence, transmission and so

on) is relatively straightforward because the necessary components for building the measurement setups are mostly commercially available. On the other hand, there are physical parameters that are more difficult to extract accurately from small volumes of thin-film samples in libraries, such as thermal conductivity and elastic constants.

Aside from scanning probe techniques, methods that allow screening or detection by visual inspection represent some of the most desirable and elegant embodiments of the combinatorial strategy. Investigation of luminescent materials has yielded some striking examples [5], where ‘one look’ can often convey all the information one initially needs about the distribution of emission profiles.

An important new direction in rapid characterization techniques is the incorporation of microelectromechanical systems (MEMS). Arrays of MEMS devices have a natural configuration that enables high-throughput evaluation of materials’ performance. For example, arrays of micro-hotplates have been successfully used for developing libraries of inorganic films for gas sensors with individually addressable sensor elements [34, 35]. Recently, we have demonstrated the utility of an array of micromachined silicon cantilevers to fabricate a ‘self-reporting’ library allowing rapid identification of martensitic transformation of shape-memory alloys by visual inspection [7].

Obtaining accurate mapping of composition and phase distribution is essential for constructing the relationship between composition, structure and properties of materials. It is easy to overlook the importance of materials diagnostics in this field. Even when the composition distribution is clearly laid out in the design of a library, the original

compositional variation may shift or change during the processing, depending on the synthesis procedure of samples.

I will discuss several screening tools used for studies of various functional materials in subsequent chapters. For general microstructure and phase determination, we used a scanning X-ray microdiffractometer and transmission electron microscopy (TEM). For compositional determination and mapping of our library samples, we used wavelength dispersion spectroscopy (WDS). For the dielectric properties of ferroelectric thin films at microwave frequencies, we used a non-destructive scanning near-field microwave microscope to quantitatively measure linear dielectric constants and non-linear dielectric signals. For ferromagnetic properties, a room temperature scanning superconducting quantum interface device (SQUID) microscope was used to measure magnetic field emanating from samples.

In this thesis, there is an emphasis on the application of the scanning SQUID microscopy technique, where I performed quantitative calculation of magnetization of materials in two kinds of libraries: a discrete library of ferromagnetic shape memory alloys and binary composition spreads of multiferroic materials.

Chapter 3

Inorganic semiconductor gas sensor libraries: Electronic nose

In this chapter, I will discuss synthesis and operation of gas sensor libraries based on doped semiconducting SnO₂ thin films. I will give some background about the topic and discuss the mechanism of semiconductor gas sensors. I will show how the libraries were fabricated using the combinatorial PLD flange and how they were characterized using a multiplexing electronics. The gas sensor libraries are an example of discrete libraries I discussed in the previous chapter.

3.1 Introduction

Materials research is often driven by industrial and commercial requirements, particularly in the expanding field of gas sensing and monitoring. The applications in this wide field range from domestic gas alarms and medical diagnostic apparatus to environmental safety and chemical plant instrumentation. There are several ways of manufacturing gas sensors in the form of thin films. Gas sensing materials can be deposited using various techniques including chemical vapor deposition (CVD), electrochemical deposition, solgel, thermal lithography, sputtering, and micropipetting. Here we have used pulsed laser deposition (PLD). There are different types of devices that can be made from gas sensing materials. Much of the past work in this field dealt with surface and bulk acoustic wave (SAW and BAW) devices and quartz microbalances, and organic devices such as lipid layers and conducting polymers. The most common

gas-sensing devices at low cost end of the spectrum are solid state devices, including catalytic and metal oxide semiconductor (MOS) types and electrochemical devices. Here I will discuss MOS type devices.

Electrical properties of some semiconductive metal oxides are sensitive to the surrounding gas atmosphere. In particular, SnO_2 [1, 2, 3, 4, 5] based semiconductors are commonly used for commercial gas sensors. Their low manufacturing cost, low operation power consumption, and high compatibility with microelectronic processing make semiconductive gas sensors ideal in a variety of settings including environmental monitoring, military applications, chemical industrial processes, food processing and biomedical applications [6, 7, 8, 9].

There is a continuing need to improve the sensitivity [10] and selectivity [10, 11] of MOS gas sensors. In particular, selectivity is a critical figure of merit, and ideal sensors would respond differently to different gas species. One strategy in pursuing the development of improved sensors is to systematically study a large number of compositionally varying sensor materials simultaneously. This can be performed using the combinatorial approach where a large number of samples with different compositions as well as samples made with different synthesis parameters can be screened for rapid optimization [12].

An electronic nose is an instrument comprised of an array of different, gas sensors and signal multiplexing electronics, capable of recognizing individual or mixtures of analytes through pattern recognition [13, 14, 15, 16]. It is based on the multisensing principle, in which the distributed response of an array is used to identify the constituents of a gaseous environment, emulating the olfactory sense. Individual sensor elements may

or may not be selective to any one gas. But by using an array of different sensors, gases can be distinguished and identified by a distinct “fingerprint” each gas produces in the form of a pattern of measured electrical responses. Although various electronic noses, mainly composed of organic materials [17, 18, 19], have been demonstrated to date, they have not enjoyed widespread use mainly because of their high cost of fabrication and energy consumption [20,21].

In the next sections, I will discuss rapid fabrication and characterization of thin film combinatorial libraries of gas sensing metal oxides. The utility of combinatorial libraries is two-fold: one is to search and optimize the compositions for high sensitivity and selectivity of gases, and the other is to make use of the natural array geometry of the libraries with different sensor elements for electronic noses. We have measured the library chips using a sensitive wide-ranged balanced-bridge electronics, and demonstrated detection of different gas species by pattern recognition.

3.2 How gas sensors work

Semiconductor sensors detect gases via induced variations in their resistances. The most widely accepted explanation for this is that negatively charged oxygen adsorbates play an important role in detecting inflammable gases such as H_2 and CO . Several kinds of adsorbates such as O^- , O_2^- , and O^{2-} cover the surface of metal oxide semiconductors (MOS) in air. In temperatures of 300-500 °C, at which most MOS are operated, O^- is the most reactive adsorbate with inflammable gases, and eventually the variation in surface coverage of O^- dominates the sensor resistance. The formation of these oxygen adsorbates, in the case of n-type MOS, which I will be discussing, builds up

a space-charge region on the surfaces of MOS grains, resulting in an electron-depleted surface layer. The electron transfer reaction from the grain surfaces to the adsorbates is as shown in Eq. 3.1



The depth of this space-charge layer is a function of the surface coverage of oxygen adsorbates and the intrinsic electron concentration in the bulk. The resistance of the MOS in air is therefore high, due to the development of a potential barrier to the

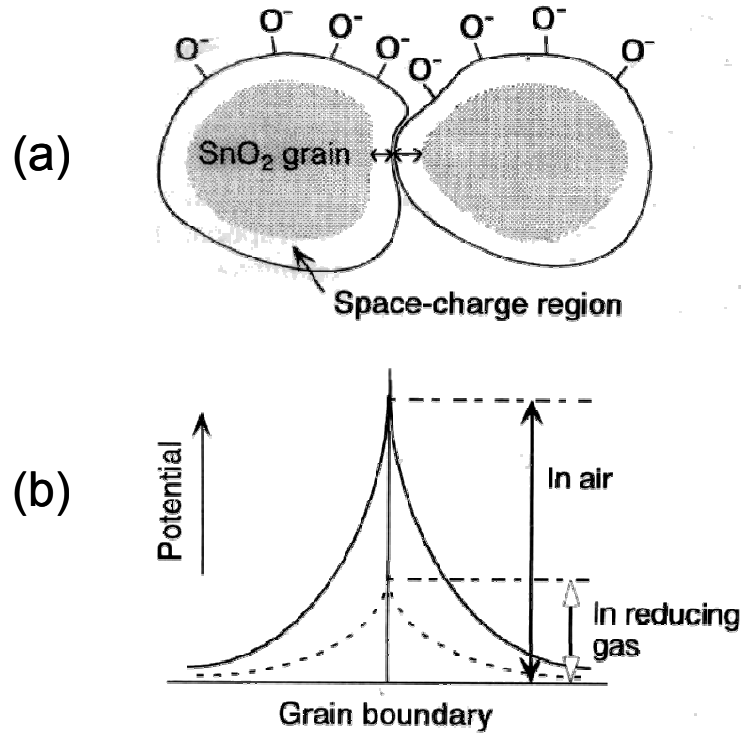


Figure 3.1 A model of a potential barrier to electronic conduction at grain boundary [22]. (a) Space charge region is formed on the surfaces of the MOS grains. (b) The resistance of MOS in air is high due to the potential barrier at each grain boundary, when MOS is exposed to gas, the potential barrier height decreases and resistance drops.

electronic conduction at each grain boundary as shown in Figure 3.1. Thus, one of the most important factors affecting the sensing properties is the actual grain or the crystal

size (D) of the sensor material in comparison with the space charge depth (L). It is reported from the experimental and theoretical results that for the single crystal SnO_2

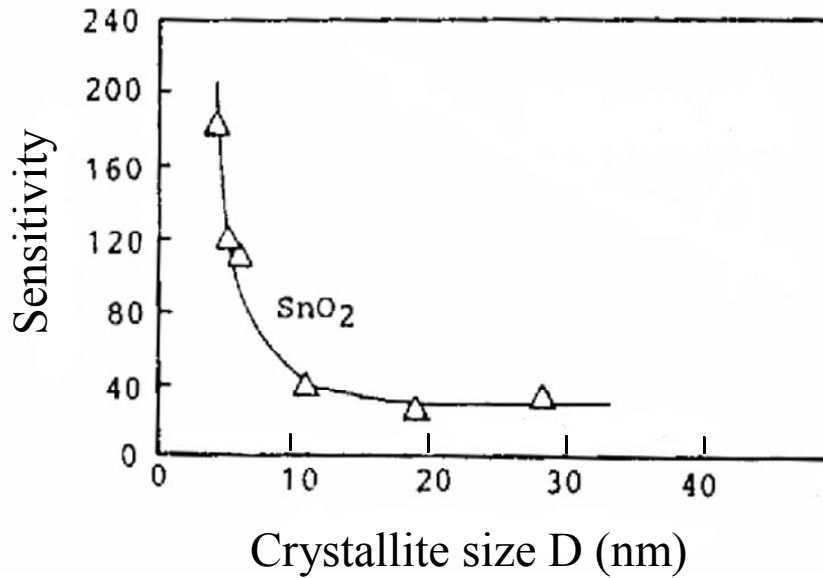


Figure 3.2 Sensitivity of SnO_2 to 800 ppm H_2 as function of crystallite size D [2].

grain, the critical size of D is 6 nm, which means that the sensitivity increases sharply when D decreases below this value (Figure 3.2). Then as D increases, it falls off exponentially leveling off when D is about 25-30 nm. This critical D value is comparable to $2L$ (L is the space-charge depth and is determined by the Debye length and the strength of the oxygen chemisorption). To understand what happens beyond the critical regime, three kinds of resistance control models have been proposed, which are shown in Figure 3.3 [2, 23]. All the models assume that a sensor consists of a chain of uniform crystallites of size D , connected mostly with each other by necks or grain boundaries. When D is much larger than $2L$, the grain boundary contacts are most resistant to electron conduction through the chain, and they govern the electric resistance as well as the gas sensitivity of the chain (grain boundary control, Figure 3.3 (a)). When D is comparable

with $2L$, necks become the most resistant, controlling the gas sensitivity (neck control, Figure 3.3 (b)). Finally, when D is less than $2L$, the grain resistance dominates the resistance of the whole chain and in

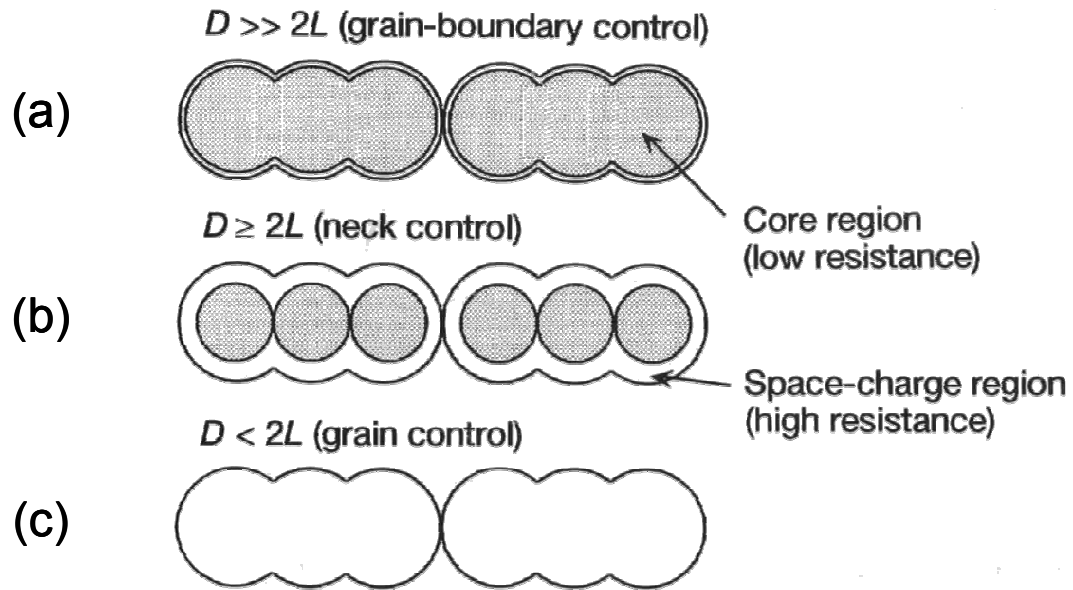


Figure 3.3 Schematic models for grain size effect. Shaded parts show core region (low resistance), while unshaded show the space-charge region (high resistance). (a) Grain boundary control, (b) neck control and (c) grain control [2].

turn the sensor resistance, so the sensitivity is controlled by the grains themselves (grain control, Figure 3.3 (c)). Among the three, grain control is the most sensitive. Theoretical treatments are still awaited for the quantitative analyses of gas sensitivity in the regions of grain-boundary control and grain control. So in the end it is important to have the thickness of the film controlled, so that the sensitivity is optimized. Our films are 50 nm thick, which was shown to be in the optimum sensitivity thickness range of SnO_2 [24, 25]. Here L was calculated to be 3-6 nm and the grain boundary control model (Figure 3.3 (a)) is well adapted for this film thickness.

When the sensor is exposed to an atmosphere containing inflammable gases at elevated temperatures, the oxygen adsorbates are consumed by the subsequent reaction, so the lower steady-state surface coverage of the adsorbates is established. During this process, the electrons trapped by the oxygen adsorbates return to the oxide grains, leading to a decrease in the potential barrier height and a drop in resistance. This resistance change is used as a measurement parameter of a MOS sensor with a sensitivity defined as the ratio of the resistance in air to that in a sample gas containing an inflammable component. Since the reaction of combustion occurs when the sensor is exposed to a gas, the temperature determines how quickly it happens, and therefore, the temperature at which the maximum sensitivity is observed is dependent upon the particular inflammable gas used.

The chemical composition of the MOS is also a key parameter that influences their sensing performance. In fact, composition by itself can affect the microstructure and, thus determine the sensing properties. Tin dioxide-SnO₂ is capable of detecting an extensive range of combustible and toxic gases. It is known that a small amount of dopants such as Pt and Pd can promote the rate of response and boost the sensitivity of SnO₂ gas sensors by increasing the thickness of the space charge layer, which enhances the consumption of oxygen adsorbates on the metal in addition to those on the SnO₂ surface (electronic and chemical sensitization respectively [2]). In addition, it has been shown that the addition of Pd particles lowers the crystallite size of SnO₂, lowering the conductivity of the sensor thus promoting higher sensitivity [26]. Gas sensing characteristics of a number of other metal oxides including In₂O₃, ZnO, and WO₃ have also been previously reported [27, 28, 29, 30].

In section 3.3, I will discuss how we made SnO₂ based gas sensor libraries with various dopants. The utility of the combinatorial flange for making discrete libraries is demonstrated.

3.3 Fabrication of gas sensor libraries

SnO₂ films were deposited by using the combinatorial PLD flange (discussed in section 2.2.2). Since the characterization of the libraries consists of measuring the resistances of the films, before making the complete library it was necessary to get the SnO₂ films in the right resistance range. In order to achieve the measurable resistivity,

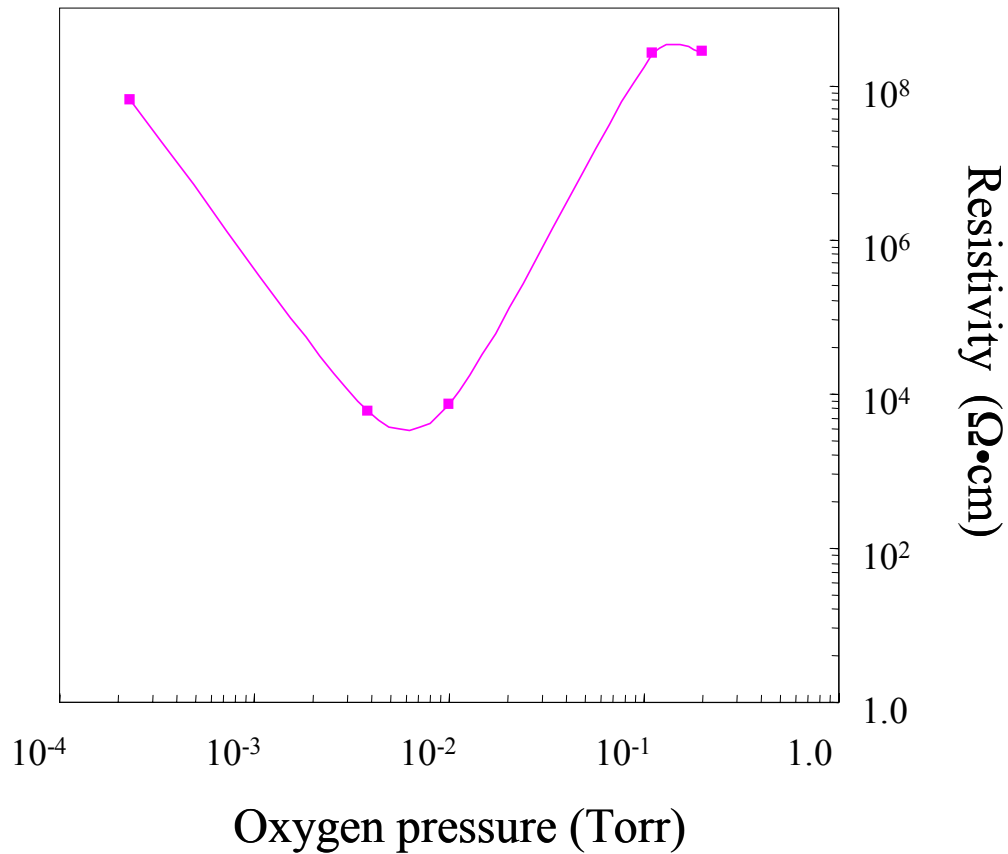


Figure 3.4 Log-log plot of SnO₂ resistivity measured at room temperature as a function of deposition oxygen pressure.

range, I varied the deposition oxygen partial pressure. Figure 3.4 shows the variation of SnO_2 resistance with deposition oxygen pressure. I found that the appropriate resistance range was obtained when partial pressure on the order of 10^{-3} Torr was used.

For this experiment, In_2O_3 , WO_3 , ZnO , Pt, and Pd were chosen as dopants into SnO_2 . These dopants were selected based on previous reports [27, 28, 29, 30]. Although they have been reported, the exact mechanism of how some dopants influence the resistivity is not understood completely. The best way to explore different combinations of dopants in different amounts is through the combinatorial technique [31]. It is important to conduct an experiment systematically, meaning all the deposition processes must take place in more or less the same conditions. Combinatorial PLD allows us to achieve this. A particularly ideal geometry is that of a discrete library. Here, all of the different compositions of gas sensing materials are spatially separated from each other. In this way, each individual device can be characterized separately when the resistive measurement is performed.

A typical sensor device is a thin film with an interdigitated electrode made of Pt/Au, as shown in Figure 3.5. The geometry of this device is very favorable for minimizing the resistance of the film. The gas sensing material between the fingers acts as resistors, connected in parallel, thus the total resistance when measured at the two terminals is smaller than if it was in series. The resistance of sensors at room temperature in air ranges from $800\Omega - 20\text{M}\Omega$. We used the two terminal geometry since the contact resistance was much smaller than these values. We have made the electrode pattern prior to depositing the film. There are several reasons why this was better. First, if the electrodes were deposited after the film deposition, the sensor materials would overheat

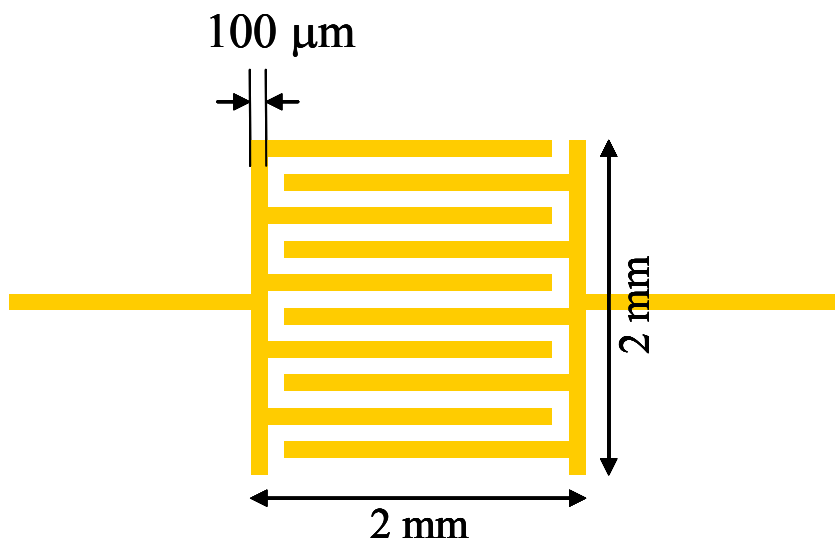


Figure 3.5 A schematic of a typical gas sensor electrode pattern of interdigitated fingers. We used thermally evaporated 100 nm thick Au

and as a result, the sensing properties might change. Second, once the electrodes are deposited on the substrate, it was much easier to align the shutter masks before the deposition of the film using the pattern as a guideline. This was a good demonstration of the use of combinatorial flange for depositing various compositions at different fixed spots dictated by the electrode pattern.

SnO_2 and dopant targets were ablated with an excimer laser (KrF with $\lambda = 248$ nm), and the deposition rates were obtained. The resistivity of each film was measured prior to making a library to make sure that the resistance is not out of the measurable range of the multiplexing electronics ($>200 \text{ k}\Omega$). The substrate material chosen for the library was c- Al_2O_3 (21 mm x 19mm). It is a very common substrate for sensing materials because of its high thermal conductivity and insulating properties. Thus, I made an array of electrodes or 16 sensor elements on a chip. This was done by using the standard photolithography.

3.3.1 Photolithography

To fabricate the interdigitated electrode pattern for 16 sensor elements (Figure 3.6) prior to the deposition of gas sensor libraries, I used the standard photolithography. It is a process of transferring a pattern from the mask to the surface of the substrate/film. I made a pattern using the ICE ED software and mailed it to Berkeley to a development engineer Marylin Kushner who makes Cr masks. I used a positive resist (Shipley 1813) for patterning. There are two ways of making this pattern, which give the same result: one is using wet etching and the second is by lift off. They are illustrated in Figure 3.7 (a) and (b). I found that it was cleaner and easier to use the lift-off technique. Figure 3.7 (a) shows the schematic and the processing steps needed for this process.

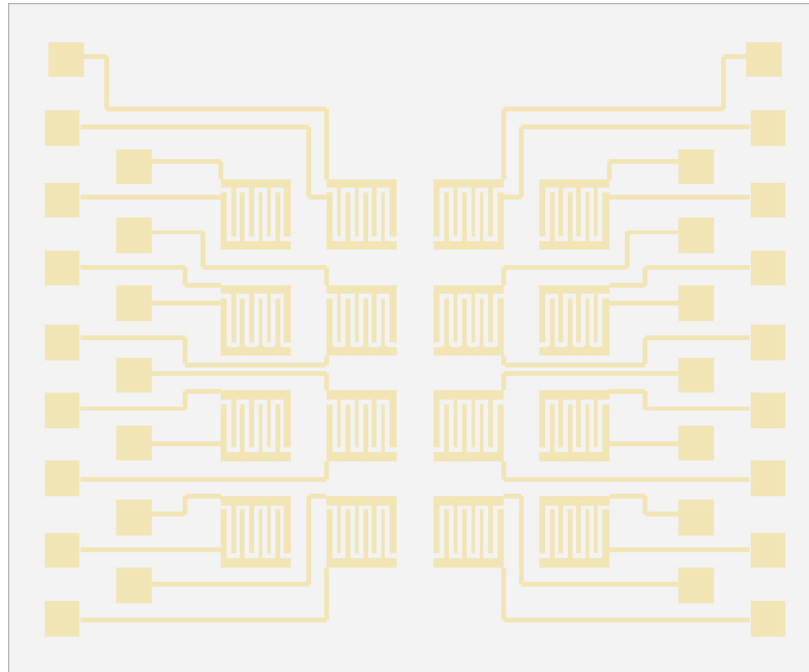


Figure 3.6 A schematic of a complete library of 16 separate sensors

The first step is to clean the surface of the Al_2O_3 substrate with acetone followed by methanol in the ultrasonic bath and dry it with nitrogen gas. I then placed the

substrate on the resist spinner to apply the photoresist for 40 seconds at 4000 RPM. This allows a formation of a uniform layer of photoresist of 1400 nm on the surface. Then I baked the resist on a hotplate at 90°C for 2 minutes (or baked it in the oven at 110°C for 15 minutes). The second step is the mask alignment and exposure of the photoresist. I used a Cr-mask for positive resist. The pattern of the library is not very complicated, with the smallest feature being 100 microns. I used the contact method with the exposure of 11 seconds of UV light (8mW/cm^2 , $\lambda=365\text{ nm}$) on a Karl Ziess MJB3 mask aligner.

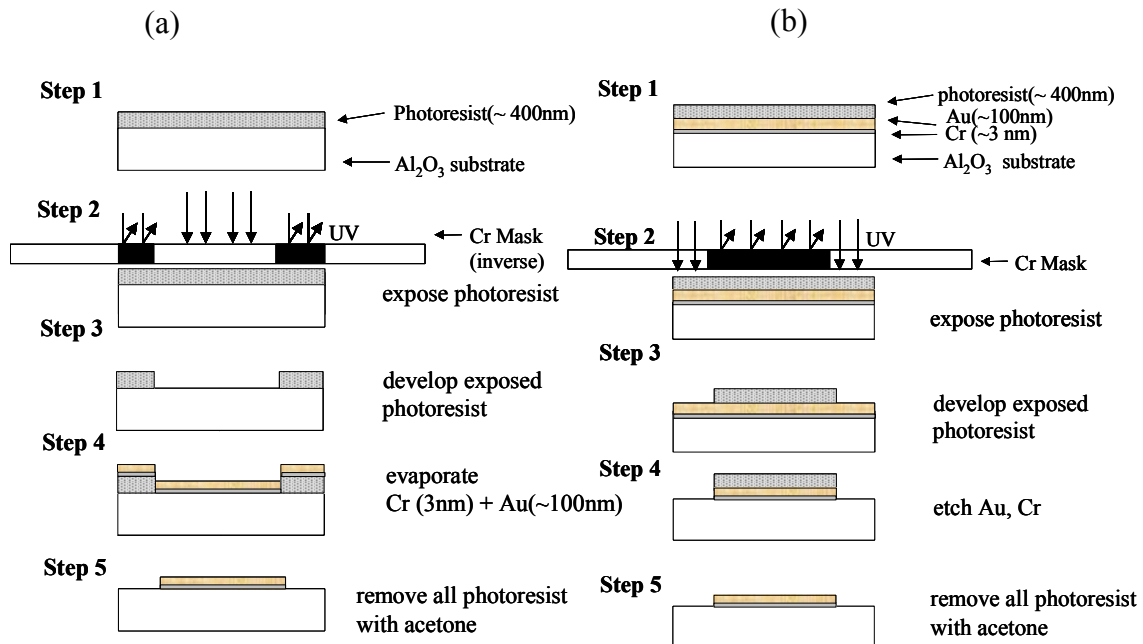


Figure 3.7 Single mask photolithographic procedure: (a) using lift off, (b) using wet etching

The third step was to develop the exposed photoresist. To do this I dipped the substrate into the developer (Shipley Microposit CD 30) for 40 seconds and rinsed with DI water. In the next step, I thermally evaporated the Au metal for contacts. This step was tricky because in the beginning the gold would not directly stick to the sapphire substrate. It

was important to add a buffer layer, 3 nm of Cr, prior to depositing 100 nm of Au. The final step was to remove the excess metal to obtain the desired pattern. This step was important in determining whether the pattern would stay or peel off. I either left the sample sitting in acetone for 5-10 minutes or put the sample into the ultrasonic. When I used the ultrasonic I placed the sample there periodically for 1 second. If the pattern stayed, it was ready for deposition of sensor materials. Figure 3.7 (b) shows the schematic of wet etching. I will not discuss the details, but the process is the same, except for the fact that photolithography is done after the metal deposition and the metal is etched afterwards.

3.3.2 Deposition of the libraries

Figure 3.8 shows the schematic of the shutters used to make gas sensor libraries. When the two shutter slits overlap, they make a square aperture through which film, when deposited, has the dimensions similar to these of the interdigitated electrode pattern, namely a 2 mm x 2 mm square (Figure 3.8). The shutters can be moved to place the square opening at other positions. The positions of all the interdigitated patterns were recorded in terms of encoder counts of the motors, which move the shutters. In this way, I had a preprogrammed routine that I must follow during the course of deposition of 16 different sensor materials. Because the substrate was larger (21 mm x 19 mm, this size as determined by the measurement setup), than the PLD plume size (10 mm x 10 mm) I deposited a quarter of the chip at a time and then rotated the heater plate 90

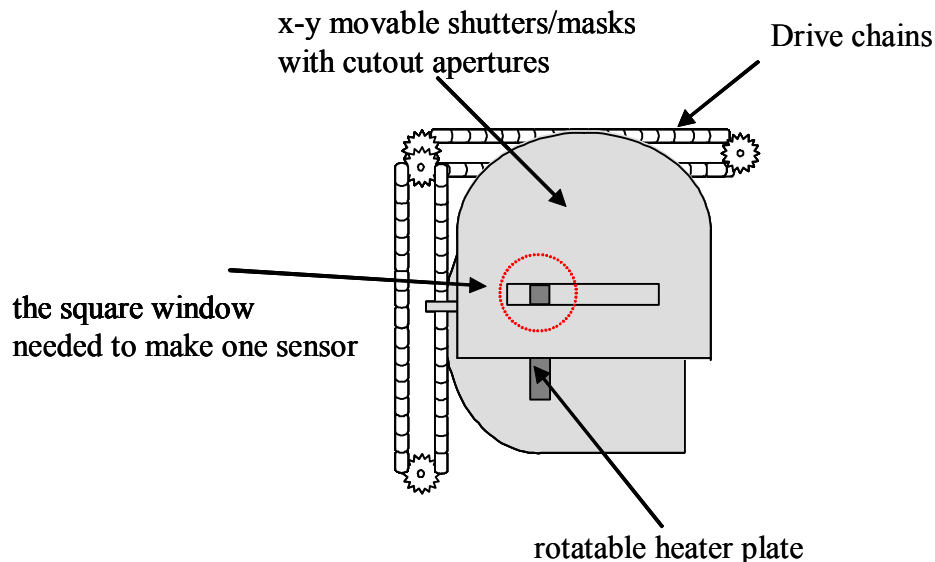


Figure 3.8 The schematic of the top view of combinatorial shutter assembly necessary to fabricate gas sensor libraries

degrees in between sets of depositions. It was the practical design of the flange that allowed us to overcome the limits of the deposition in PLD and make a library without breaking the vacuum.

All of the libraries were SnO_2 based and different amounts of In_2O_3 , WO_3 , ZnO , Pt , and Pd were varied from one chip to another. To create thin films of selected chemical compositions, I deposited materials using a layer-by-layer process [32, 33] where SnO_2 and other layers were deposited in an alternating manner. Each repeating layer of SnO_2 and its dopant material was less than 4 Å thick (lattice constant of SnO_2) so that dopants were intimately mixed at a sub-nanometer level. The typical distance between the shutter plane and the substrates was 500 μm during the deposition. The deposition substrate temperature was 550°C, and the oxygen partial pressure was 1×10^{-3} Torr. The ablation energy was approximately 1 J/cm², and the total thickness of each sensor element was 500 Å. As I mentioned earlier, the thickness of the film will

influence the crystallite size of the sensor material, and in turn the sensitivity of the sensor. The closer the crystallites size D is to $2L$ (L is space charge depth), the more sensitive the sensor is. Sixteen sensors were deposited one after another on the electrode pattern at desired interdigitated locations, and the total fabrication time of one library was ≤ 3 hours.

A photograph of one of the libraries is shown in Figure 3.9, and the compositions of the 16 sensors on one chip are listed in Table 3.1. I will refer to this library later. Although 16 is not such a large number, if one were to synthesize 16 different sensors one by one, it would require many days, since one must spend at least 4-5 hours for one deposition, from pump down to taking the chips out of the chamber. In addition, even if one were to make 16 different films in 16 different runs, the conditions in the chamber might slightly change and alter the results. Also, if one were to do photolithography of individual sensors one at a time, there can be subtle differences in the processing conditions that could preclude one from truly comparing the performance of the sensors.

None	In ₂ O ₃ (5wt%)	ZnO (5wt%)	WO ₃ (50wt%)
Pt (2.5wt%)	In ₂ O ₃ (5wt%) + Pt (2.5wt%)	ZnO (5wt%) + Pt (2.5wt%)	WO ₃ (50wt%) + Pt (2.5wt%)
Pd (2.8wt%)	In ₂ O ₃ (5wt%) + Pd (2.8wt%)	ZnO (5wt%) + Pd (2.8wt%)	WO ₃ (50wt%) + Pd (2.8wt%)
Pt (2.5wt%) + Pd (2.5wt%)	In ₂ O ₃ (5wt%) + Pt (2.5wt%) + Pd (2.5wt%)	ZnO (5wt%) + Pt (2.5wt%) + Pd (2.5wt%)	WO ₃ (50wt%) + Pt (2.5wt%) + Pd (2.5wt%)

Table 3.1 A list of dopant compositions based on SnO₂ in one library. This was a target library.

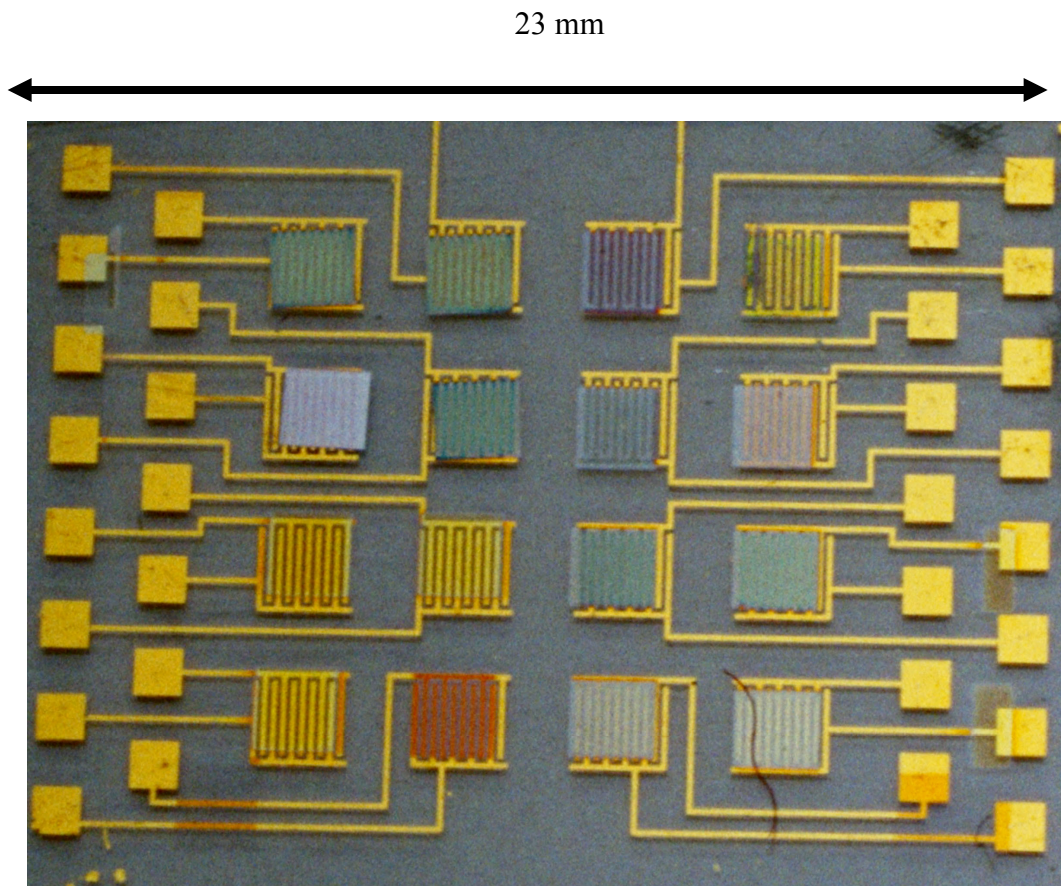


Figure 3.9 A photograph of a library chip.

3.4 Characterization of gas sensors

We perceive coffee for example, as having an easily distinguishable and unmistakable odor, but the aroma actually consists of hundreds of different odorous molecules. They are generally small and polar and can be detected by humans at levels below 1 ppb (parts per billion). In recent years, significant interest in the use of sensor arrays to discriminate between odors has arisen. The term “electronic nose” is applied to such an array of chemical sensors, where each sensor has partial specificity to a wide range of odorant molecules, coupled with a suitable pattern recognition system. A sensory array for discrimination between odors was first demonstrated in 1982 [34].

Subsequent improvements in both sensors and data analysis methods has led to the appearance of several commercial electronic noses. Combinatorial libraries of discrete separate gas sensor elements have the form of sensor arrays. Thus, we can operate our libraries as electronic noses. Indeed, it was in this capacity that our libraries proved to be most useful. Previous work on combinatorial libraries as electronic noses includes work by S. Semancik and R. Cavicchi from NIST [35, 36] and R.A. Potyrailo from GE [37]. There is a need for low cost fabrication and low energy consumption devices that are flexible and compact; our technique fulfills many of these requirements.

Before describing how we characterized the libraries and operated them as electronic noses, I will explain the basic principle of how the sensors should work together as an electronic nose and how it compares to the human olfactory system. Then I will discuss our results and analysis.

3.4.1 Basic principle of olfaction

To appreciate the operation of an electronic nose, it is necessary to have a basic understanding of the principles behind the human olfactory system. Figure 3.10 illustrates the basic components of the human olfactory system and relates these to the corresponding components of an electronic nose. The sensation of smell is dependent upon the interaction of odorant molecules with a group of specialized nerve cells, the olfactory receptors, which are situated just above the bridge of the nose out of the main air stream. Each olfactory cell has a number of cilia, which contain different binding proteins (about 1000 genes encode 1000 different odor receptors) [38, 39]. After the excitation of the receptor cell, (the exact nature of the interaction between the odor

molecule and a receptor cell has not been unambiguously established), a cascade of reactions occurs where an electrical signal passes along the axon to the olfactory bulb. The signals are then processed and sent to the brain, where they are amplified increasing both sensitivity and selectivity of the system. The final stage is in the cerebral cortex of the brain, which classifies and memorizes the odors [40]. The human olfactory system is quite remarkable in its ability. Even though the number of binding proteins is 1,000, the number of olfactory cells is 100 million, which means the same proteins are present in many different olfactory cells. Humans can detect at least 10,000 different odors [41]

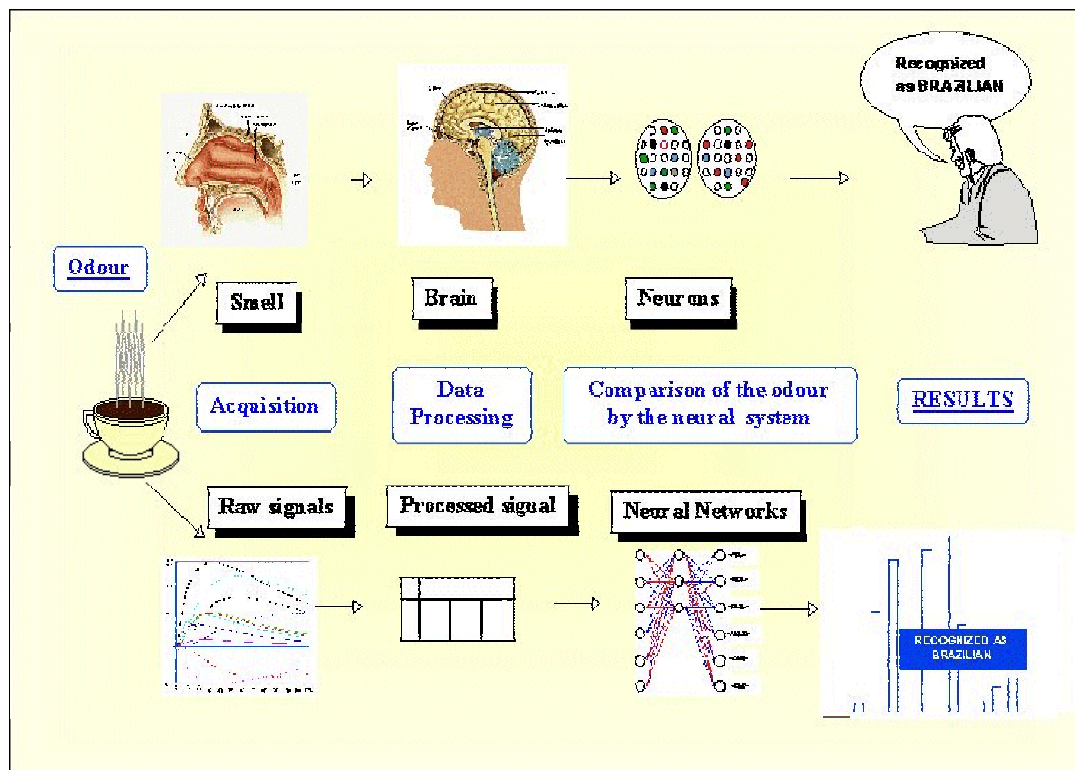


Figure 3.10 Comparison of the basic elements of an artificial olfactory system with the human olfactory system (from Alpha MOS [42]).

and only this year in October, a Nobel prize in medicine was awarded to Axel and Buck for their discoveries of odorant receptors and the organization of the olfactory system and

exactly how these odors can be recognized [43]. However, the number of identifiable odors is approximately 50, each odor binds to several receptors with partially overlapping sensitivities.

An electronic nose system is made to mirror the human olfactory system. Each chemical sensor represents a group of olfactory receptors and produces a time dependent electrical signal in response to an odor. The noise and the drift may be reduced by using signal-preprocessing techniques. In the final stage in the artificial nose, the pattern recognition software is used, which performs the process equivalent to the human olfactory process in the brain [41].

There are a number of electronic nose instruments available on the market today. The website <http://www.nose-network.org/review/> shows major companies and universities that participate in this project. I will give several examples here. One is an electronic nose made by RST-Rostock (Germany) (Figure 3.11 (a)) which is composed of 10 MOS sensors. It has been successfully used in quality control in the food industry, controlling of odors and harmful substances in the consumer industry, evaluation of the room air or quality of breath, and in the automobile industry. Another example of the electronic nose is the one from Alpha MOS-Multi-Organoleptic Systems, Prometheus (Figure 3.11 (b)). It has an array of MOS type devices, and is one of the first odor and volatile organic compounds (VOC) analyzers that combines a highly sensitive fingerprint mass spectrometer with a large choice of patented multi-sensor array technologies to create an extremely flexible analysis platform. Even though these advanced tools are useful, they are very expensive. The typical prices are in 10's and 100's thousands of

(a)



Electronic nose made of 10 MOS sensors (RST-Rostock-Germany)

power Supply: 230 V(50Hz)

Power Consumption: approx. 200 W

Dimensions: 460 x 410 x 270 mm

(WxDxH) Weight: 17,5 kg

Operating Conditions: 0° C to +40° C
up to 95% relative Humidity
(not condensing)

(b)



Electronic nose made of 6-18 MOS/SAW sensors (Alpha MOS-Multi Organoleptic Systems-France)

Large choice of sampling methods
(static, dynamic, manual) and vial
capacity

High throughput capability (up to 96
samples)

No special sample preparation
required

Figure 3.11 Two examples of inorganic electronic noses.

dollars. As a result, they are predominantly used in laboratories. Although technical details of the commercial instruments are not available, for making the sensor array chips, we believe that the combinatorial approach is very practical and inexpensive, and can be easily employed for this technology. Next, I will discuss how we characterize our gas sensor libraries.

3.4.2 Characterization and results

The testing of the chips was performed at Lynntech Inc., located in College Station, Texas. This company develops innovative solutions to different kinds of technological barriers for public and private sectors, their expertise ranges from engineering and physical sciences to biological sciences. The idea for the project was to develop an inexpensive portable inorganic electronic nose that is sensitive to various volatile organic compounds (VOC's) such as benzene, chloroform, formaldehyde, etc., that can be used in our daily life. Our way of fabricating the electronic noses, using the combinatorial technique was very suitable for this. They built a testing chamber, specifically for our library chips. It is a cylindrical gas flow chamber (5 cm in diameter, 3.5 cm in height and 2 ml in inside volume) where a chip could be heated up to 400°C during measurements, spring loaded pins are used to make electrical contacts to all the sensors. The setup is shown in Figure 3.12. The fact that the sensors can be tested at different temperatures is important, because the performance of the sensors can drastically change (as discussed in section 3.2), and some sensors are best operated at high temperatures (200°C -400 °C). All sensors were connected to the outside electronics to monitor their resistance change. Gases studied were chloroform (C), formaldehyde (F), and benzene (B), at concentrations of 100 ppm, 50 ppm, 25 ppm, and 12.5 ppm in air. The sequences of testing were run at 200°C, 300°C and 400°C. To test the reproducibility and recovery of the sensor performance, responses of the sensors to multiple periods of a fixed gas flowing cycle were monitored. For each segment within a cycle, a gas was introduced in the chamber continuously for 300 seconds at 24 ml/min, and then air (A) was introduced for the same period of time (Figure 3.13).

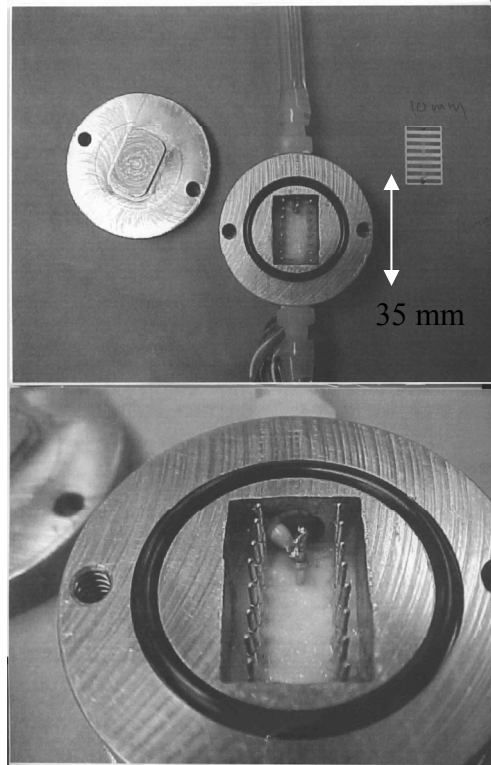


Figure 3.12 A photograph of a gas flow chamber

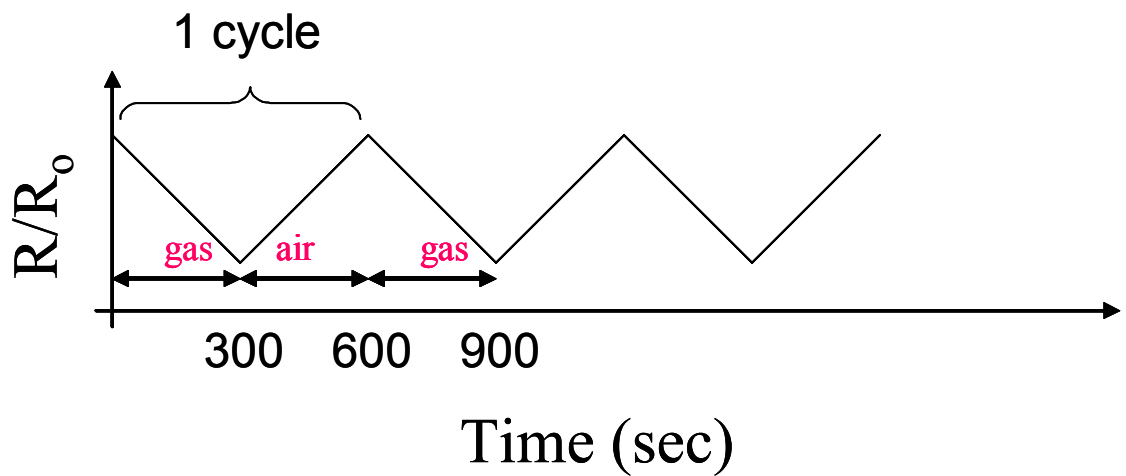


Figure 3.13 The model response of a sensor to the gas flow cycle. R is the resistance in gas, R_0 is the resistance at a fixed reference point prior to flowing gas.

Depending on the dopant composition, the resistances R of the sensors in air, measured before exposing the chip to gases, were in the range of $1\ \Omega$ to $20\ \text{M}\Omega$, which corresponded to the resistivity in the range of $10^{-3}\ \Omega\text{cm}$ to $10\ \Omega\text{cm}$.

We have made several libraries at the first stage. Table 3.2 summarizes the results from the first three libraries. The results indicate that Pt and Pd have the largest effect in enhancing the response, whereas oxide dopants did comparatively less. From all three libraries, a number of sensors had resistances out of range ($> 200\ \text{k}\Omega$) and/or had open circuits. For those compositions, we were not able to acquire any data. Based on the results from the first three libraries, I have selected compositions for the target library (Table 3.1), which were focused down to different doping concentrations of Pt, Pd and ZnO only. Every sensor on the target library was found to display significant responses to all gases. Here I will discuss five sensors whose responses were the most pronounced.

Figure 3.14 shows a plot of $(R-R_0)/R_0$, where R_0 is the resistance at a fixed reference point prior to the gas flowing cycle, for the five sensors from the target library measured at $400\ ^\circ\text{C}$. The compositions of the five sensors were $\text{SnO}_2 + \text{Pd}$ (6wt%) (sensor 1), $\text{SnO}_2 + \text{Pd}$ (8wt%) (sensor 2), $\text{SnO}_2 + \text{Pt}$ (8wt%) (sensor 3), $\text{SnO}_2 + \text{ZnO}$ (5wt%) + Pt (2wt%) (sensor 4), and $\text{SnO}_2 + \text{Pt}$ (8wt%) + Pd (8wt%) (sensor 5). Different gas species (at the concentration of 100 ppm) and refreshing air were introduced in an alternating manner as shown in Figure 3.14(a). It can be seen that the sensors exhibit dissimilar time dependent responses for different gases, and the responses are reproducible from cycle to cycle. To further illustrate the dependence of the response time on the chemical composition of the sensors, I replot data in Figure 3.15 (from Figure 3.14) for two of the sensors from one gas flow cycle.

Sensor-rating	Library #1
Best responder	SnO ₂ + Pt (2.5 %)
2 nd best	SnO ₂ + Pd (2.5 %)
3 rd best	SnO ₂ + In ₂ O ₃ (2.8 %)
4 th best	SnO ₂
Sensor- rating	Library #2
Best responder	SnO ₂ + Pt (2.5 %) + Pd (2.5 %)
2 nd best	SnO ₂
3 rd best	SnO ₂ + ZnO (5 %) + Pt (2.5 %) + Pd (2.5 %)
Sensor- rating	Library #3
Best responder	SnO ₂ + WO ₃ (5 %)
2 nd best	SnO ₂ + ZnO (5 %) + Pt (2.5 %) + Pd (2.5 %)
3 rd best	SnO ₂ + ZnO (10 %) + Pt (2.5 %)
4 th best	SnO ₂ + Pt (2.5 %) + Pd (2.5 %)

Table 3.2 Sensors with the highest overall responses from the three initial libraries and the rated responses of individual sensors along with their compositions. In the parentheses are the atomic weight percentages.

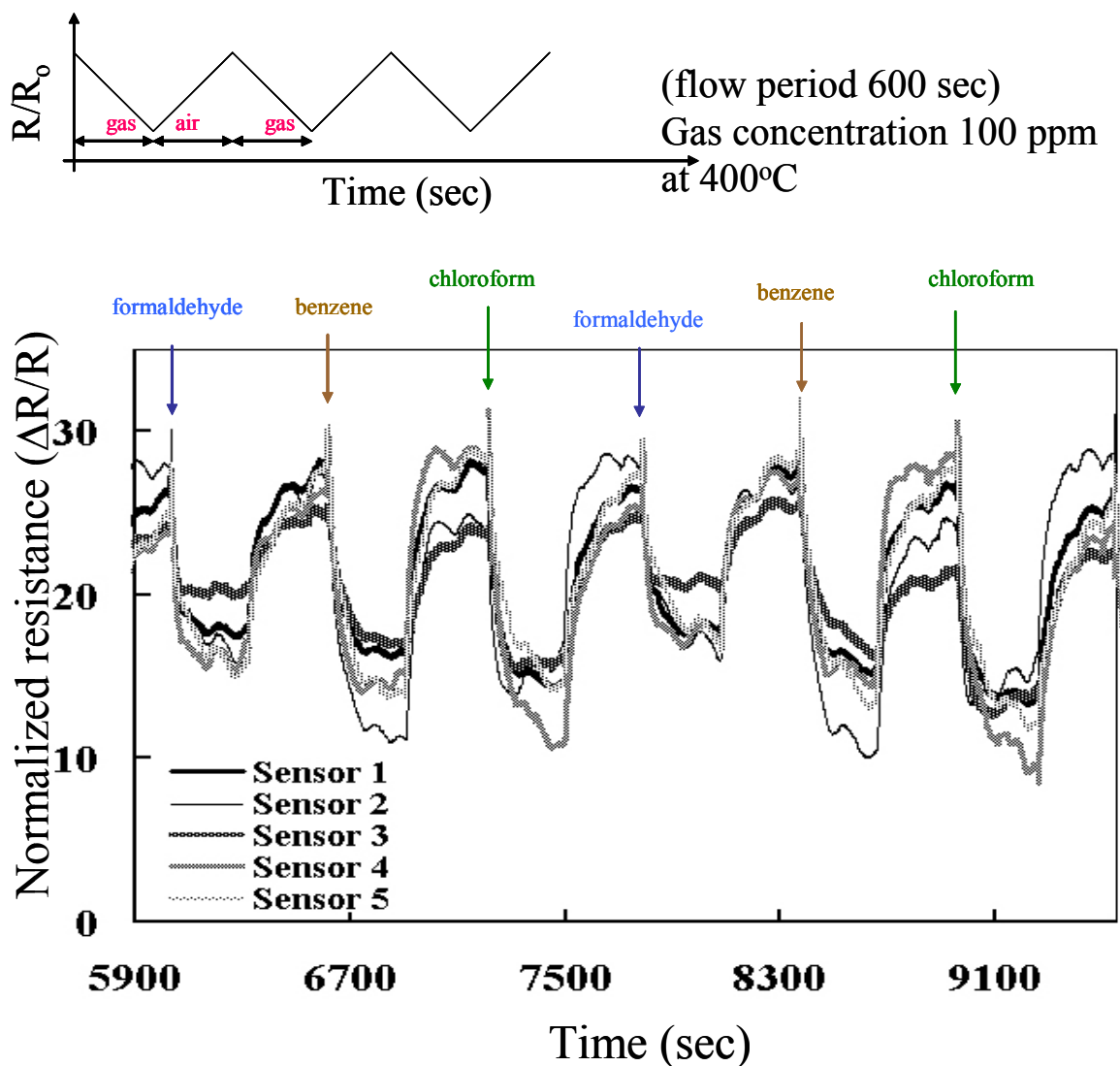


Figure 3.14 Sensor response in resistance change $(R-R_0)/R_0$ at 400 °C for five sensors from the target library. (a) A model response to the flowing of gases and refreshing air introduced in an alternating manner. (b) Each sensor exhibits a different time dependent response pattern for a given gas. The arrows indicate when different gases (F), (B), (C), and (A) were introduced in the chamber.

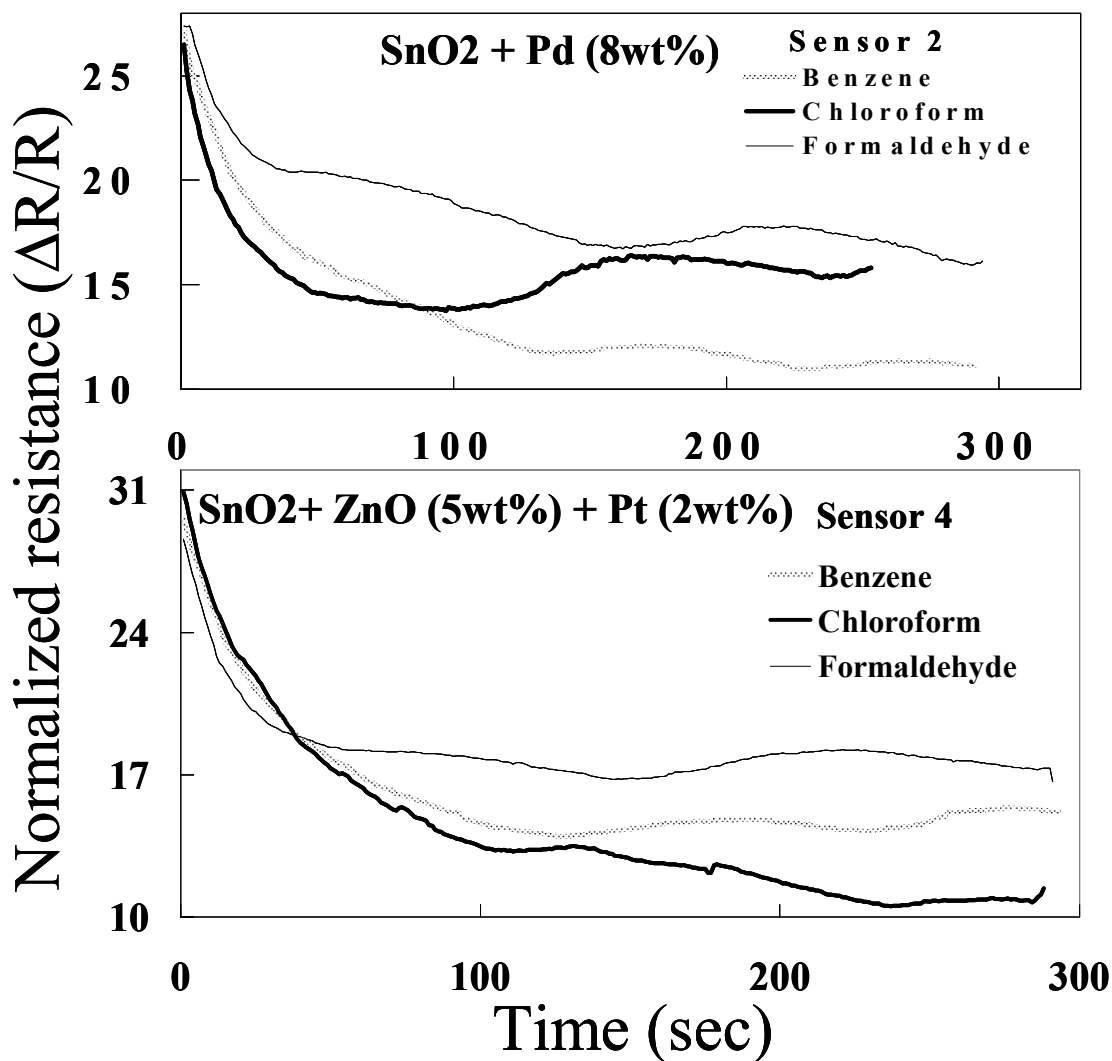


Figure 3.15 Dependence of time response on gas introduced for two sensors. The responses were found to be reproducible from cycle to cycle.

While the overall responses are similar, the details of the responses are different. What is important is the shape of the response and how fast it levels off.

In order to demonstrate the ability of sensor arrays to distinguish different gas species through a multi-channel pattern recognition, averaged normalized responses at 400 °C from the five sensors were plotted in a radar plot. 100 ppm of chloroform, formaldehyde, and benzene were used (Figure 3.16). Each curve in the plot represents

data for one gas. It is clear that each gas produces a different response pattern with the five sensors. The variation of sensor responses to the same analyte was found to range typically from 0.3% to 1.6% from the average value, attesting to a high repeatability of the response and yielding a well-defined pattern for each curve. The size of the response signal was found to be roughly proportional to the concentration of the analytes. We

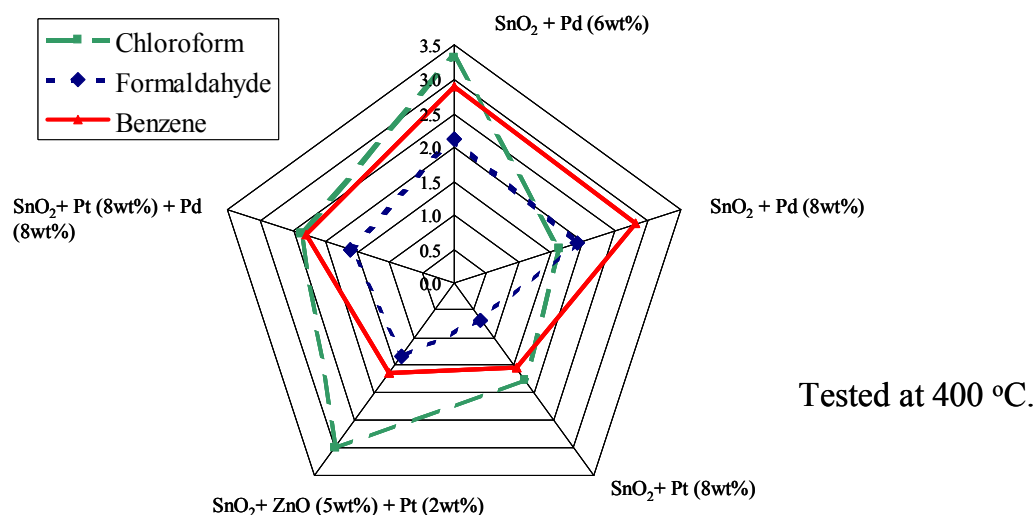


Figure 3.16 A radar plot showing responses of the five sensors for different gases at 400 °C. The normalized resistance change corrected for drift is plotted on each axis for each sensor. Each curve represents a different analyte

were able to discern response patterns for different gases down to 12.5 ppm. The sensors did not exhibit a "memory" of prior exposure to various analytes: refreshing in air always brought the sensors back to approximately the same resistance. The average response times of the sensors were 600 sec, 300 sec and 50 sec for operation temperatures of 200 °C, 300 °C and 400 °C, respectively. Thus, using these patterns we can distinguish the gases.

3.5 Conclusions

I have utilized combinatorial PLD flange for fabricating the discrete gas sensor libraries of doped SnO₂ thin films. Since all the sensors are spatially separated from each other on one chip, each one can react to all the gases at the same time, which is a characteristic of the electronic nose. We have fabricated several libraries with different amounts of dopants of In₂O₃, WO₃, ZnO, Pt, and Pd. After testing them as electronic noses, we narrowed down the compositions that were the most sensitive to chloroform, formaldehyde, and benzene. Compositions were then selected for a target library, which only had Pt, Pd and ZnO as dopants. The target library showed its ability to distinguish different analytes by showing different responses with concentrations down to 12.5 ppm with high repeatability of response signals. Thus, we have demonstrated that the present method of creating electronic noses allows a fast and relatively inexpensive way of fabricating compact electronic nose devices.

Chapter 4

SQUID microscopy

In this chapter, I will introduce the basics of SQUIDs. I will discuss the fabrication of SQUIDs and the fundamentals of SQUID microscopy.

4.1 Introduction to SQUIDs

In 1962, Brian D. Josephson predicted that cooper pairs would "tunnel" through a narrow non-superconducting region [1], and that this would produce some surprising phenomena which we now call the dc and ac "Josephson effects". The Josephson effects were soon used by Jaklevic, Lambe, Silver, and Mercereau to develop the first SQUID (Superconducting QUantum Interference Device) [2]. A SQUID is an electrical device that is extremely sensitive to weak magnetic fields. There are two kinds of SQUIDs. One is a dc SQUID [3], which consists of two Josephson junctions in a loop and the other is the rf SQUID [4], which consists of a single Josephson junction in a loop and is operated with a radio-frequency flux bias. It turns out that, with proper circuits, SQUIDs can be used as magnetic flux meters, magnetometers, gradiometers, voltmeters, susceptometers, rf amplifiers, current comparators, and even quantum bits. The main difference between these applications is in the nature of the input signal and the input circuit that is used to couple the input signal to the SQUID. One of the great merits of the SQUID in an application is that it can have extremely high sensitivity or low noise. Depending on the application, a specific circuit optimization is required to achieve the

best performance (highest signal-to-noise ratio). The main difficulty has been the need to cool devices to cryogenic temperatures. Even in the case of high- T_c superconductors, the temperature to operate the device must be below 77K.

Since SQUIDs are small and extremely sensitive to magnetic field, they can be a very powerful tool for imaging magnetic fields. Many techniques have been used for imaging magnetic fields, including Hall microscopy [5], scanning magnetoresistive microscopy [6], magnetic force microscopy [7], magneto-optical imaging [8], and electron beam holography.

The first SQUID microscopes, which were developed in 1990's, had the sample and the SQUID cooled by liquid cryogens in a vacuum environment [9, 10, 11]. Some of these systems were used for investigating the properties of the superconducting order parameters in high- T_c materials [12] and vortices [13], and some were used to demonstrate nondestructive evaluation (NDE) in metallic structures [14,15]. Even though there was a history of using SQUIDs for imaging NDE samples, there were sample limitations and difficulties with sample loadings. In mid-1990's R. Black, Y. Gim, and F. Wellstood built the first high- T_c (HTS) "room temperature" scanning SQUID microscope[16]. In their system, the SQUID was in vacuum at 77 K, and the sample was in air at room temperature. The SQUID to sample separation was the thickness of a sapphire window [17,18] of $25\mu\text{m}$, plus a distance between the window and the sample, which result in a minimum sensor-to-sample distance of about $100\mu\text{m}$. A patent for the idea and technology of the scanning SQUID microscope was granted to Wellstood, Gim, and Black [16]. This patent was licensed by Neocera, Inc., which proceeded to commercialize the scanning SQUID microscope. In collaboration with the

Wellstood group, they modified the cooling system to use closed-cycle refrigeration rather than liquid nitrogen, and made other improvements to make the system user friendly. Even though this scanning SQUID microscope was primarily built for failure analysis and fault isolation in integrated circuits and multi-chip modules [19, 20], I primarily used this system to screen our combinatorial libraries and obtain quantitative magnetization values. Several other groups have developed their own SQUID microscopes. L. N. Morgan et al. built HTS SQUID system for room temperature NDE [21, 22]. J. Clarke et al. built a HTS SQUID system with a SiN window for bio-magnetic samples [23]. Wikswo et al. [24] and Decert et al. [25] have built low- T_c (LTS) SQUID systems for room temperature NDE of samples.

In this chapter, I will discuss some fundamentals of SQUIDs and the commercial scanning SQUID microscope. I will briefly discuss the SQUID fabrication, since I made several SQUIDs for the university system in Prof. Wellstood's lab before I could use Neocera's system. Since I focused on characterization of magnetic materials, in Chapter 5, I will introduce the analysis techniques that I used to calculate magnetization for our libraries with data obtained with a scanning SQUID microscope.

4.2 SQUID microscopy

In order for a SQUID to work, it must be cooled below the superconducting transition temperature. For the work described in this thesis, I used high- T_c $\text{YBa}_2\text{Cu}_3\text{O}_{7-x}$ (YBCO) SQUID, which works at temperatures below about 80 K. The microscopes in Wellstood's lab and the commercial one keep the SQUID cold by using a mixture of circulating gases. To obtain a high spatial resolution in a SQUID microscope, the

SQUID and the sample must be placed very close to each other, even though the SQUID is in vacuum and cold, and the sample is in air at room-temperature. This is made possible by placing the SQUID in vacuum to provide thermal insulation and using a 25 μm thick window to separate the SQUID from air. In order to ensure that the SQUID is completely parallel to the surface of the window, the window can be manipulated and brought close to the SQUID. By adjusting the bias current and the ac and dc flux modulation, the optimal operating set point of the SQUID can be found. To take magnetic images of the samples, the sample rather than the SQUID itself is moved. The scanning process and data acquisition are controlled by a personal computer. The details of these processes for the commercial system will be described in section 4.2.3. For the microscope in the Wellstood lab, the details can be found elsewhere [17, 18].

There are many advantages of using a room temperature scanning SQUID microscope as opposed to microscopes that have the sample and the SQUID at cryogenic temperatures in a dewar. The SQUID can remain cold for a long period of time without being exposed to air or thermal cycling to change samples. Many types of samples such as liquid-biological samples, integrated circuits and electronics circuits are not able to withstand cryogenic temperature or vacuum. Sample exchange for a room temperature scanning SQUID, and sample preparation are faster and easier, and the scanning range is not limited by the size of the dewar. It is relatively simple to add electrical connections, control lines or cables as needed to operate a test sample. To this date, the room temperature scanning SQUID microscopes have been used in a variety of applications ranging from failure analysis of the integrated circuits, localizing the defects in the computer chips or multi-chip modules, to corrosion studies (very weak magnetic fields

from hidden active corrosion [26] can be detected) to biomagnetic [27, 28, 29, 30] and geophysical studies [31].

4.2.1 SQUID fundamentals

Before going into details of SQUID microscopy, it is worthwhile to understand what a dc SQUID is and how it works. A dc SQUID consists of a superconducting loop interrupted by two Josephson junctions [32]. An ideal Josephson tunnel junction consists of two weakly coupled superconductors separated by a thin insulating layer through which Cooper pairs can tunnel. Many characteristics of Josephson junctions can be explained by the resistively and capacitively shunted junction model (RCSJ) [33, 34]. Figure 4.1 shows the basic components of this model: the critical current I_0 , which is the maximum supercurrent the junction can support, the capacitance C of the junction, and the junction resistance R .

We can find the equations of motion of an RCSJ by considering the current flow in each arm of the circuit. Current I_c through the capacitor is given by

$$I_c = C \frac{dV}{dt} \quad \text{Equation 4.1}$$

where $C = \epsilon A/a$, is the parallel plate capacitance of a junction with an insulating barrier of thickness a , an area A , and permittivity ϵ . The current through the resistor R is

$$I_r = \frac{V}{R} \quad \text{Equation 4.2}$$

Also, the ac Josephson relation [35] tells us that

$$V = \frac{\Phi_0}{2\pi} \frac{d\delta}{dt} \quad \text{Equation 4.3}$$

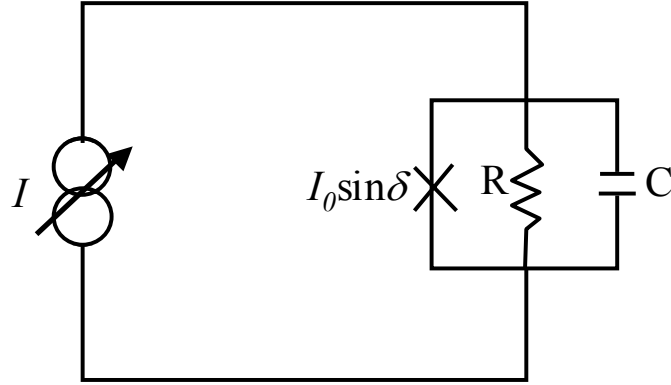


Figure 4.1 RCSJ model of a Josephson junction connected to a current source.

where $\Phi_0 \equiv h/2e = 2.07 \times 10^{-15} \text{ T} \cdot \text{m}^2$ is the flux quantum and δ is the gauge-invariant superconducting phase difference between the two superconductors. Finally, the current through the junction is given by the dc Josephson relation,

$$I_j = I_0 \sin \delta, \quad \text{Equation 4.4}$$

where I_0 is the critical current of the junction. The total current I flowing through the three arms of the resistively and capacitively shunted junction will be,

$$I = \frac{C\Phi_0}{2\pi} \frac{d^2\delta}{dt^2} + \frac{\Phi_0}{2\pi R} \frac{d\delta}{dt} + I_0 \sin \delta. \quad \text{Equation 4.5}$$

A dc SQUID consists of a superconducting loop which is broken by two Josephson junctions, as shown in Figure 4.2 (a). When the Josephson junctions are non-hysteretic, the capacitance can be neglected, and the total current flowing through the SQUID is the sum of the currents flowing through each junction and each parallel shunting resistor. From Eq. 4.5, the total current I is given by

$$I = I_1(t) + I_2(t) = I_0 \sin \delta_1 + I_0 \sin \delta_2 + \frac{\Phi_0}{2\pi R_1} \frac{d\delta_1}{dt} + \frac{\Phi_0}{2\pi R_2} \frac{d\delta_2}{dt}, \quad \text{Equation 4.6}$$

where the index $i = 1, 2$ represent the left and right arm of the SQUID, respectively. The circulating current $J(t)$ that flows around the loop is then just:

$$J(t) = \frac{(I_2(t) - I_1(t))}{2} \quad \text{Equation 4.7}$$

The flux-phase relation tells us furthermore that the total flux in the loop is related to the junction phases by [36]:

$$\delta_1 - \delta_2 = 2\pi(\Phi_a + LJ) / \Phi_0 \quad \text{Equation 4.8}$$

where L is the total loop inductance and Φ_a is the external applied flux. The term $(\Phi_a + LJ) = \Phi_T$ is the total flux threading the superconducting ring. With some additional calculations and simplifications [37] one can obtain the time averaged voltage,

$$V = \frac{IR}{2} \sqrt{1 - \left[\frac{2I_0}{I} \cos \left(\pi \left(\frac{\Phi_a}{\Phi_0} + \beta j / 2 \right) \right) \right]^2} \quad \text{Equation 4.9}$$

where modulation parameter β is defined as $2I_0L/\Phi_0$, and the circulating current $j \equiv J/I_0$. From this expression, it is clear that the I-V curve depends on the applied flux, j , and β . β is determined during the fabrication process.

For $\beta \ll 1$, the effect of j can be clearly neglected, and we see that V is periodic in Φ_a/Φ_0 . This is the most important property of a dc SQUID. As flux is applied, the I-V curve will modulate between the curves at integer external field ($\Phi_a = n\Phi_0$) and that at half-integer external field ($\Phi_a = (n+1/2)\Phi_0$), as shown in Figure 4.2 (b). For β not small compared to 1, the equation for the I-V curve is not simple because of the circulating current J term, but the relation between the voltage

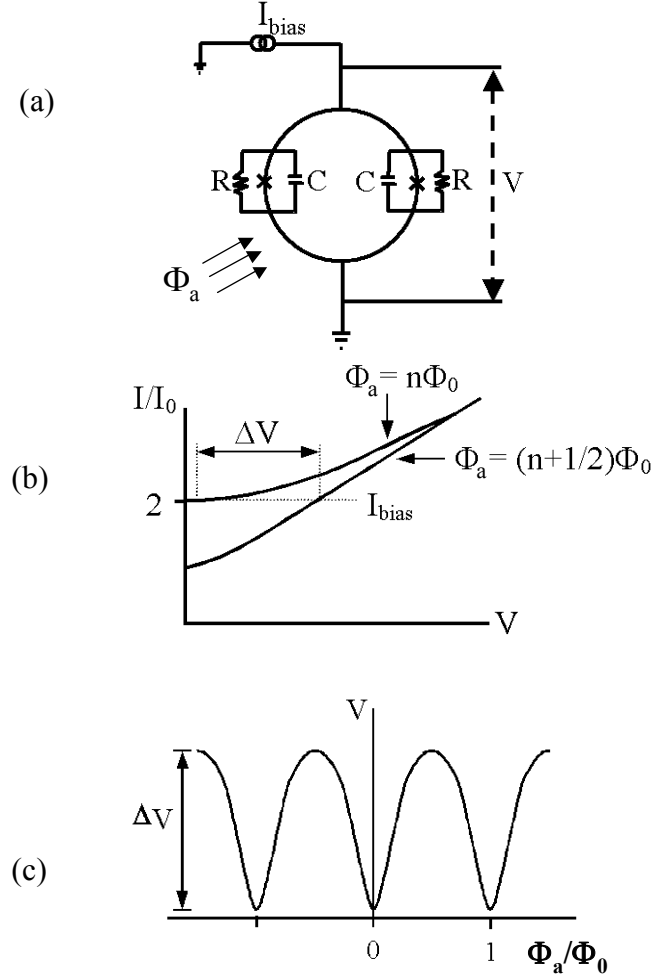


Figure 4.2 (a) A Schematic of a dc SQUID, (b) I-V characteristic curve of a SQUID, (c) periodic relation between V and Φ_a/Φ_0 at a fixed bias current I_{bias} .

and the applied flux will still be periodic. When the SQUID is biased at $I = 2I_0$, the modulation of voltage is a maximum. The relation between the voltage and external flux is shown schematically in Figure 4.2 (b) for this bias current. When the SQUID is biased with a current, which exceeds the critical current of the device, the voltage drop across the SQUID depends on the applied flux and oscillates with a period of Φ_0 , as seen in Figure 4.2 (c). Since the response of the SQUID is non-linear, it is difficult to use it as a measuring device by itself because its response is very sensitive to the operating point.

To linearize the response of the SQUID, it is a standard practice to use a negative feedback loop or “flux-locked loop”.

The ability of a SQUID to detect small magnetic flux or field is ultimately limited by the noise in the SQUID itself. This noise can be separated into two distinct types. One is the white noise or the broad-band noise that arises from the resistive shunts in the SQUID. This noise does not depend on frequency, hence the term “white”. The other is the $1/f$ noise, which increases with decreasing frequency. Typically, $1/f$ noise in SQUIDs is only visible below 10 Hz to 103 Hz. Depending on the film quality, the flux noise can change dramatically, from $10^{-5} \Phi_0/\text{Hz}^{1/2}$ to $10^{-2} \Phi_0/\text{Hz}^{1/2}$ at 1 Hz and 77 K in HTS SQUIDs [38]. I will not discuss about the noise since I did not consider it in my calculations, for more extensive discussion about noise in the SQUID, one can refer to [19, 37].

4.2.2 Fabrication and testing of the SQUID

There are several known ways to fabricate Josephson junctions for high- T_c SQUIDs. The most common are step-edge junctions and bicrystal grain boundary junctions. For the step edge junction, the first step is to ion-mill photoresist-masked SrTiO_3 substrate to produce a step on the substrate with a step angle of $65\text{-}75^\circ$ (see Figure 4.3). An HTS film is then deposited over this step and patterned into a line, forming a junction where the line goes over the step (see Figure 4.3 (a) [39]). By using standard photolithography and ion-milling, the step edge can be placed anywhere. This can be advantageous when making gradiometers [40] or multiple devices. A bicrystal grain boundary junction is produced by growing an HTS film on a specially

manufactured bicrystal substrate - two pieces of substrates are fused together with an in-plane crystal misalignment of 24° and 30° , as shown in see Figure 4.3 (b) [39]. Weak-link Josephson junctions are formed at the grain boundary in the film, which is grown over the fused line. For minimizing the noise and increasing the sensitivity [41], it has been demonstrated that 30° bicrystals produce the best junctions. Because junctions are

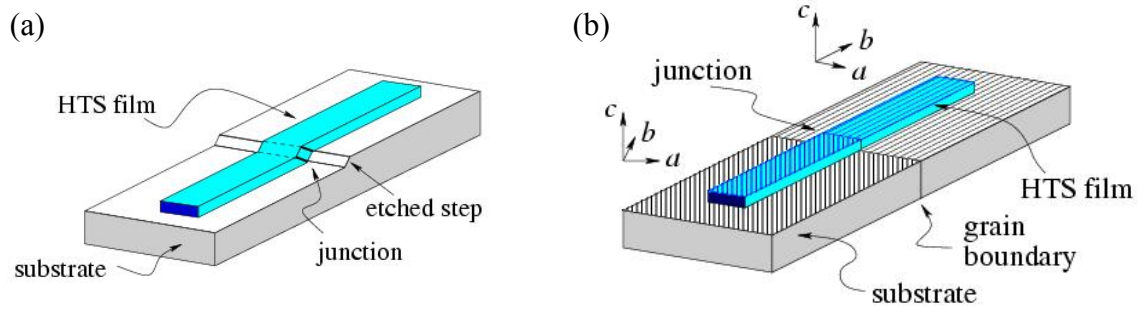


Figure 4.3 (a) Step edge grain boundary Josephson junction, (b) Bicrystal grain boundary Josephson junction (reproduced from Ref. [39]).

only formed along this fused line, there is a significant restriction on the design of the devices. However, their fabrication is very straightforward and reliable.

Several methods have been used to grow high- T_c superconducting thin films. Popular methods include co-evaporation, pulsed laser deposition (PLD), and sputtering. I have used films deposited by PLD. PLD is relatively simple and tends to have a high success rate compared to other growth techniques, making it ideal for prototyping new materials (Sec. 2.1). The process of growth of YBCO films for the SQUID fabrication is thoroughly discussed in [17, 18, 23]. The YBCO and Au layer (for making good ohmic contact) film were deposited on a one-side polished bicrystal SrTiO_3 (STO) substrate [42] that was $10 \text{ mm} \times 10 \text{ mm}$ in size with a 30° grain boundary mismatch.

After deposition, several tools can be used to see if the YBCO film has grown well. The most powerful diagnostic is a measurement of the transition temperature using non-

contact AC susceptibility. Another useful check is to look through an optical microscope with reflected light and direct light to check the surface of the film for large particles or empty holes in the film. X-ray diffraction is also important for checking the crystal structure.

I used standard photolithography (Sec. 3.3.1) to make SQUIDS from YBCO films. The process that I followed is described in [37]. For SQUID fabrication, I had to repeat four basic steps for every chip that was made, which are shown in Figure 4.4.

The first mask was used to remove the Au and the YBCO from the edges, in order to expose the grain boundary area (Figure 4.4 (b)). The second mask (Figure 4.4 (c)) was used to remove Au on top of YBCO where the SQUIDS will be located, while keeping Au everywhere else. In this procedure, it is very important to etch the gold but not YBCO. The procedure with the third mask (Figure 4.4 (d)) is the most delicate and very important. Through the optical microscope in the mask aligner, I have to find the bicrystal line and align the line very accurately so that the bicrystal line is within the 3 μm of the junction area of all 8 SQUIDS. The final step is covering the SQUID chip with photoresist in order to protect the YBCO from water and prevent O_2 from escaping the YBCO film. Since each substrate is expensive and the SQUIDS can be easily damaged during the processing or dicing, I have eight SQUIDS on one substrate. Because of this, it was hard to etch all the SQUIDS and modulation lines using the same time interval. A longer etching time could be used to fine-tune one device, but in doing so, the other devices might be overetched and possibly destroyed. It is critical to have a uniform thin film deposited on the substrate. Of course, it is important to use clean beakers, pure chemicals, and fresh photoresist for photolithography.

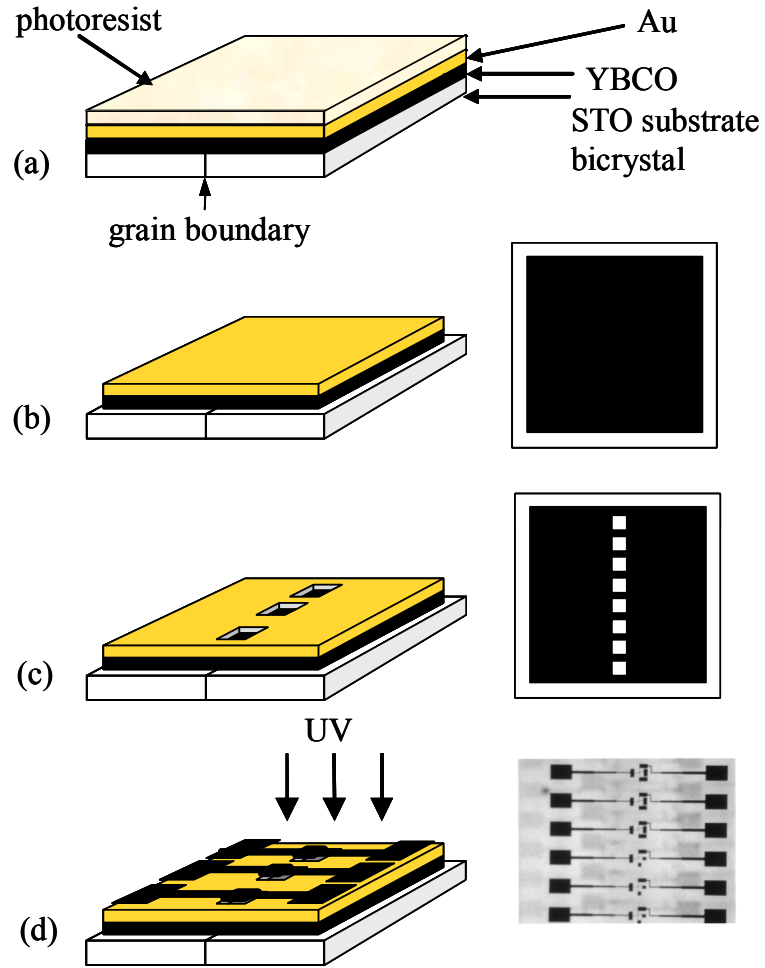


Figure 4.4 Photolithographic procedures using (a) three masks for making the SQUID chip. First, the chip is covered with a photoresist. (b) Then, the first mask is used to remove the Au and the YBCO from the edges in order to expose the grain boundary area. (c) Then, the second mask is used to remove Au from top of YBCO where the SQUIDs will be located. (d) Finally, the third mask is used to make the SQUIDs pattern. The number of SQUIDs made on one chip is eight.

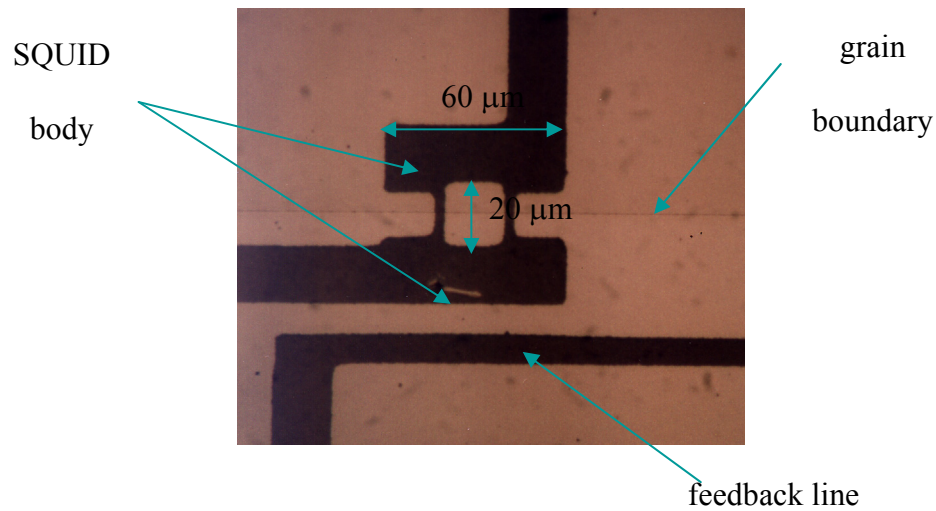


Figure 4.5 An optical microscope photograph of a successfully fabricated HTS SQUID.

A photograph of a successful SQUID device is shown in Figure 4.5. The size of the SQUID area is $20\ \mu\text{m} \times 60\ \mu\text{m}$. On this chip, the feedback line is patterned adjacent to the SQUID. Sometimes the patterning would fail, due to overetching or cracks in the photoresist that would allow the bridges or modulation line to be etched in some places. When that happened and the modulation line was ruined, I had to wind the modulation line (wire) on the sapphire rod on which the SQUID chip is mounted.

To check the quality of a SQUID, one must measure the I-V characteristics. As I explained earlier in this chapter, the junctions of high- T_c SQUIDs are resistively and capacitively shunted, and the I-V curve is non-hysteretic. When the external flux is changed continuously, the I-V curve should modulate periodically. I used a standard 4-

point probe method for the I-V measurement. I used a function generator and a 1 k Ω resistor to supply current to one SQUID at a time.

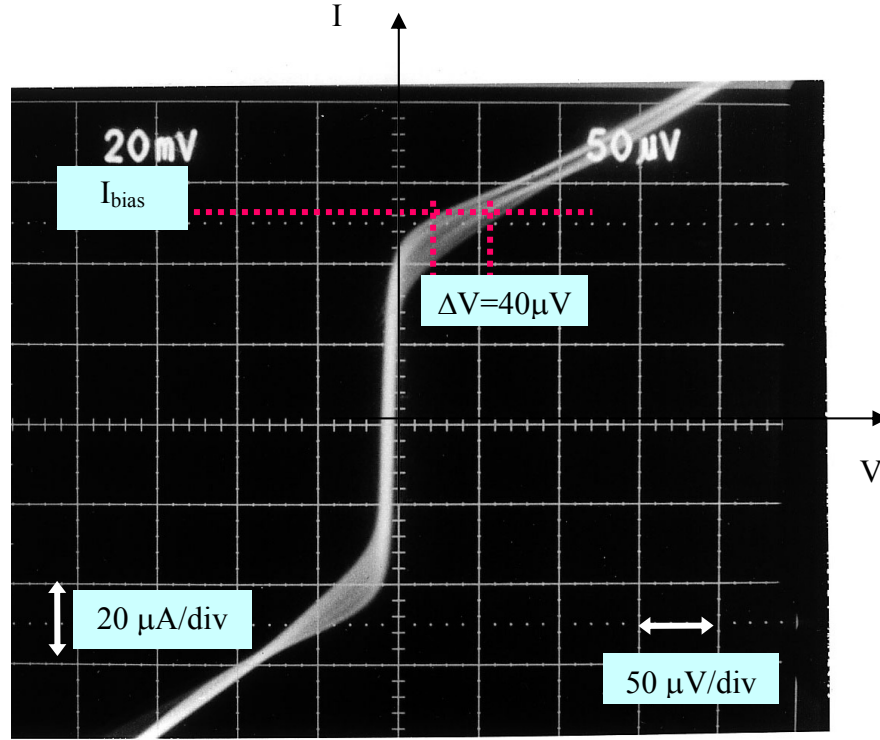


Figure 4.6 : I-V characteristic curve of a SQUID at 77 K. The typical values of parameters of interest are: critical current $I_c (= 2I_0) \sim 40 - 120 \mu$ A, junction resistance $R_J \sim 2.5-4 \Omega$, and voltage modulation depth $\Delta V \sim 40-50 \mu$ V.

From the I-V curve, I can find the critical current, junction resistance, and voltage modulation depth of each SQUID. In particular, it is important to make sure that the critical current and the junction resistances are not beyond the operational ranges of the microscope electronics. Figure 4.6 shows the I-V curve of one of the SQUIDS. I note that the critical currents of the SQUIDS varied from 40~120 μ A, R_J varied from 2.5~4 Ω and ΔV varied from 40~50 μ V, even though the SQUIDS were on the same chip. Once the SQUIDS are tested, they are diced and sanded. One undamaged SQUID picked from

the batch is then mounted on a sapphire rod and then on a cold finger. After assembling the cold finger (Figure 4.7), the SQUID is tested again. The cold finger must be assembled with great care, making sure everything is grounded while assembling. The details of these procedures can be found elsewhere [17, 18, 37]. After going through the different stages of assembly, the SQUID can alter, and can even become non functional.

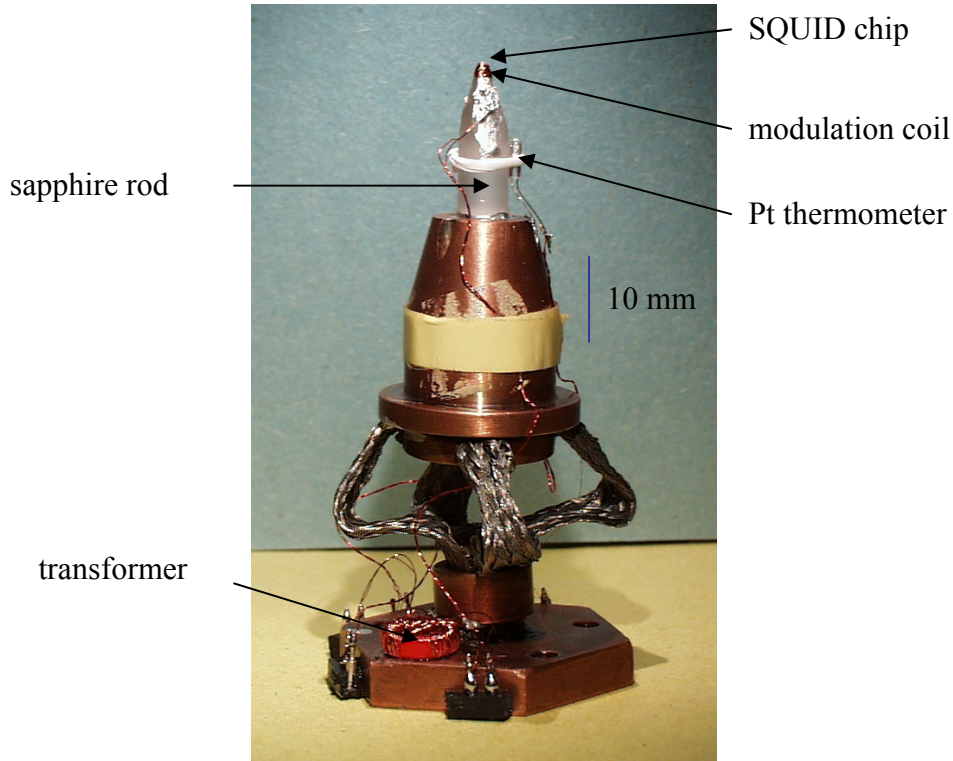


Figure 4.7 The copper cold finger. This particular chip had a broken modulation line, so the modulation coil is wound on the sapphire rod itself.

During the second testing, it is often found that the SQUID critical current and resistance had become larger than previously tested, but are still in the operational ranges. After testing the cold finger, it is ready to be mounted into the microscope. As I mentioned earlier, the SQUID is a non-linear device, therefore there is a need of electronics to linearize the response of the SQUID to changes in applied magnetic flux. This is done by flux-locked-loop (FLL) feedback electronics all assembled in a box,

which was made by the Physics Dept. Electronics group [43], originally adapted from J. Clarke's group in Berkeley. It is called the Berkeley box. The basic concept of the FLL is that it keeps the flux in the SQUID constant. Figure 4.8 shows the overall layout of the SQUID electronics. The electronics dc current biases the SQUID and using feedback coil, a 100 kHz square wave modulation flux is applied. The output voltage from the SQUID is stepped up by a transformer and then amplified by a preamp and two

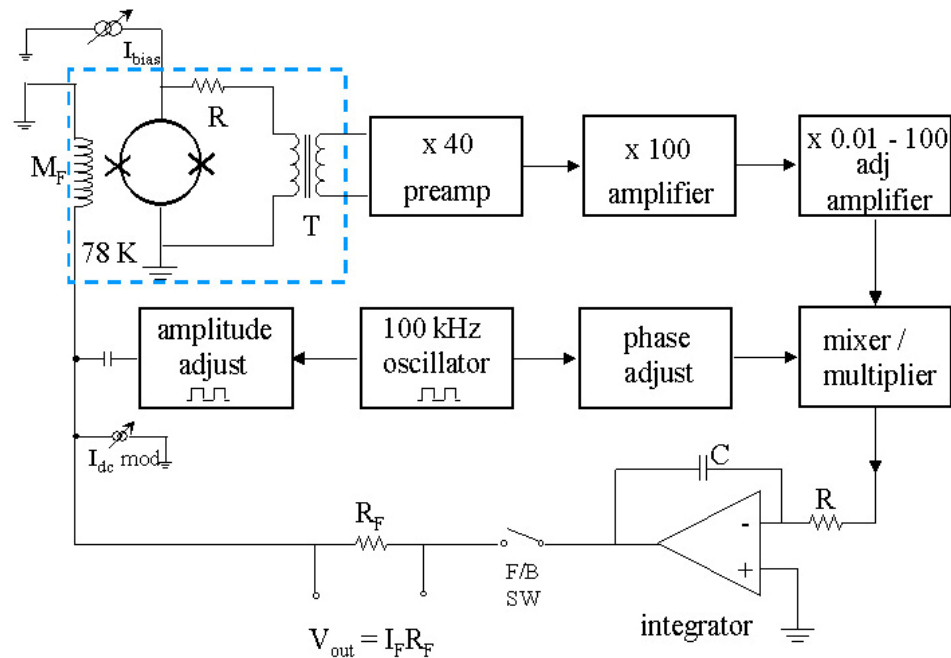


Figure 4.8 The schematic diagram of the flux-locked-loop feedback electronics inside the Berkeley box.

amplifiers. This signal is mixed with a 100 kHz reference signal and integrated. Then it is fed back as a correction flux to the SQUID. As shown in Figure 4.8, the area inside the blue dotted line encloses all the circuit components that are kept at 77 K. They are the modulation coil and the transformer, which is mounted on the cold finger, as shown in Figure 4.7.

Several times, there were shorts either in the electronic box, or among the wires going from room temperature to 77 K. Therefore, I decided to rewire all the SQUID connections to the Berkeley electronic box and make a vacuum connector fitting to make the wiring more accessible and easily replaceable when needed. When all the shorts were eliminated, the SQUID microscope was ready to be used. However, due to all the temperature and vacuum cycling, the critical current became even larger, and the Berkeley box was no longer a sufficient supply of current. There were three 3 k Ω

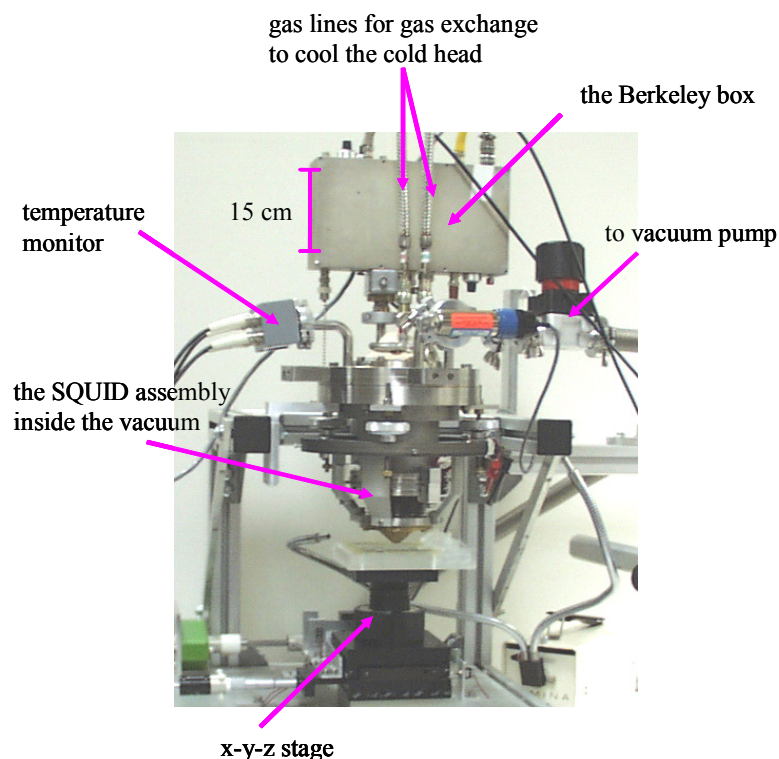


Figure 4.9 A photograph of the university scanning SQUID system

resistors connected in parallel that control the current that goes to the SQUID. So we replaced them with lower value resistors: 1kOhm, 600 Ohm and finally 300 Ohm. Subsequently, the current that was biasing the SQUID was sufficient, and the microscope

was used. A photograph of the entire scanning SQUID system located in the subbasement of the center for superconductivity research at the university is shown in Figure 4.9. The details of this SQUID system can be found in Erin Fleet's thesis [18].

Even though I had used this system in the beginning of my research, most of the time, I used the commercial system at Neocera. In the beginning, I used Magma C1, which is discussed elsewhere [18, 19], later I used the upgraded microscope Magma C20, which I will discuss in the next section.

4.2.3 The commercial scanning SQUID microscope

The idea and the technology of the scanning SQUID microscope was first conceived in Prof. Wellstood's group at the University of Maryland. I had the privilege to use Neocera's next generation scanning SQUID microscope to characterize our samples. I will briefly describe the system and point out some of its features that were necessary for my analysis.

Figure 4.10 shows a photograph of the entire Magma C20 system. The SQUID assembly inside the vacuum chamber, the LCD display, the stage equipment, the camera and the leveling probe are all located inside of the shielded mount. The computer and the instruments' racks are next to the shield but far enough so that the electronics' noise will not interfere with the signal from the sample. As in the university system, the SQUID cold finger and the cold head are mounted inside the vacuum chamber. The SQUID is cooled by a circulating mixture of gases; the compressor and the vacuum pump are neatly fixed in the instrument rack. The x-y-z stage, the probe, the camera, and the lowering/raising of the SQUID window are all automatic, controlled by the compiled

Labview software. The procedure of setting up the scan of a sample and some of the key features, which were very advantageous to our research, are described in Appendix A.

The basic function of Magma C20 is the same as the university's system. It is the z-SQUID system, which means that it is sensitive only to the z component of the B field. The sample is scanned on the x - y - z stage, while the SQUID itself does not move. Even though the electronics of the Magma C20 is different, it plays the same role as the Berkeley box. The FLL loop maintains the constant flux in the SQUID, and while the sample is scanned, the change in voltage is recorded by the DAQ board.

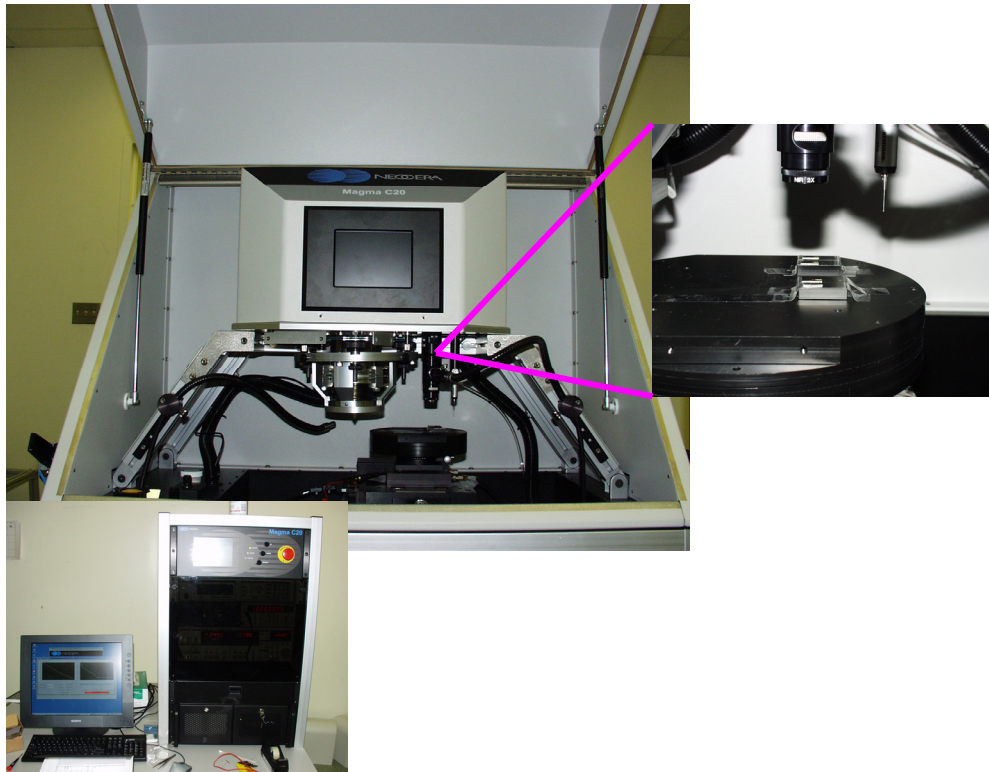


Figure 4.10 A photograph of a commercial scanning SQUID system, Magma C20

4.3 Conclusions

I discussed dc SQUIDs and their function as sensors for magnetic fields. I described how I fabricated the SQUIDs and tested them to be used in the scanning SQUID microscope. I introduced scanning SQUID microscopy and described the commercial system that I have used to characterize my samples. In the next Chapter, I will discuss how the data are treated in order to extract magnetization. I will use simulated results to derive the conditions for the techniques to calculate magnetization.

Chapter 5

Characterization techniques of combinatorial libraries of magnetic materials

In this chapter, I will introduce different techniques for characterizing combinatorial libraries of magnetic materials. I will discuss various methods for calculating magnetization of thin film samples from data obtained using the scanning SQUID microscope. Then, I will show how I simulated the magnetic field data to be used in studying the inversion technique in calculating magnetization. This is continued in Chapter 6 where I discuss various parameters that control the inversion technique. In this chapter, I discuss several simple models for calculating in-plane and out-of-plane magnetization from the magnetic field data.

5.1 Introduction

Magnetic materials serve a rich variety of functions in various technologies in our society and are important topics for combinatorial investigation. Some magnetic materials for which the combinatorial approach has been successfully applied are ferromagnetic shape memory alloys (FSMA) which can be used for sensors and actuators [1], magnetic semiconductors for spintronics devices [2, 3], permanent magnets [4] and magnetoelectric (ME) materials for memory and sensor device application [5, 6]. As discussed in Chapter 2, for screening combinatorial libraries, the use of rapid characterization tools is essential. In the case of magnetic materials, it is important to quickly scan the library and assess various magnetic properties of the materials in the

library. For instance, one property of immediate interest is magnetization. To date, several techniques have been developed which enable one to scan a library and directly or indirectly obtain the magnetization distribution of samples in the library. Some of the examples of these techniques include low/room temperature scanning SQUID microscopes, low/room temperature Magneto-Optical Kerr effect (MOKE), X-ray magnetic circular dichroism (XMCD), and scanning hall probe microscopy (SHPM).

MOKE is a technique that uses a laser beam to probe magnetization of the top surface layers of a material [7]. The laser intensity variation detected by the photodiode, is due to the polarization change of the reflected light induced by the magnetization of the material. By applying magnetic field, one can obtain a hysteresis loop from a localized spot on a sample using MOKE. The smallest sampling size is determined by the aperture size through which the laser passes and by the lens used to focus the beam. Using a calibrated sample, quantitative mapping of the hysteresis loop can be obtained. Its only drawback is that it only probes top 20 nm of the sample [8]. XMCD is similar in practice to MOKE, but instead of the laser, it utilizes the synchrotron x-ray beam [9]. The spatial resolution of XMCD depends on the aperture and the focusing lens, and it can range from 1 nm to 100 nm. The XMCD signal represents the difference between the absorption of left and right circularly polarized x-rays, which effectively measures the populations of the up and down spin orientations [10]. The probing depth is much deeper than MOKE, and it can be up to 1000 nm [11]. XMCD is element-specific, and thus it can provide the magnetic behavior of different elements inside the material. SHPM is another noninvasive instrument with which one can perform quantitative measurements of the surface magnetic field profiles under variable temperature and magnetic field [12]. Its

spatial resolution is higher than the other techniques discussed above, and it is about 1 μm . Its magnetic field sensitivity is $2.9 \times 10^{-8} \text{ T}/\sqrt{\text{Hz}}$. SHPM uses a microfabricated semiconductor Hall sensor and a positioning technique. The scanning SQUID microscopes use the SQUID device (low T_c or high T_c superconductors) as a sensor to map the distribution of the magnetic field emanating from the sample. The sensitivity of now commercially available SQUIDs is unmatched, and it is better than $20 \times 10^{-15} \text{ T}/\sqrt{\text{Hz}}$ for high T_c SQUIDs and better than $1 \times 10^{-15} \text{ T}/\sqrt{\text{Hz}}$ for low T_c SQUIDs [13]. One major drawback of SQUID microscopes is that one cannot apply magnetic field during the measurement. Because of this, we can only obtain remanent magnetization of the sample. Fabrication of high T_c SQUIDs and their properties were discussed in the previous chapter. Table 5.1 summarizes the advantages and the disadvantages of the various techniques discussed above.

For combinatorial study of FSMA and ME materials, we have used the room temperature scanning SQUID microscope. When measured, these samples were in ambient at room temperature. In some instances, the libraries were patterned into grids, and in others, unpatterned composition spreads were measured. The scan itself does not take a long time (typically 1 hour for a 3" diameter wafer library), and the scanning stage travel limits are large enough to scan the entire 3" silicon wafer (for FSMA libraries) at a time. The results are very reproducible and reliable.

A scanning SQUID microscope can be used to measure magnetic field emanating from a sample at a fixed distance, and one should be able to extract the value of remanent magnetization of magnetized materials without calibration. While this is true in principle, obtaining the accurate value of remanent magnetization turned out to be a

nontrivial task. In particular, I have found that there are many caveats to arriving at the correct value of the remanent magnetization from scanned data. Because ability to map accurate values of remanent magnetization is crucial for combinatorial investigation, I

Scanning Tool	Advantages	Disadvantages
Room Temp. Scanning SQUID	rapid visualization of the B field distribution on the library, which can be converted to remanent M using several calculation techniques; the sample is at RT, no special preparation.	do not have a direct measure of magnetization, but can calculate remanent magnetization from B field; can not apply field and thus cannot do hysteresis loop.
Low Temp. Scanning SQUID	higher resolution than RT; lower device noise.	Must wait to cool the sample; cannot measure RT properties needed for the RT devices; do not have a direct measure of magnetization, but can calculate remanent magnetization from B field; can not apply field and thus cannot do hysteresis loop.
Magneto-Optical Kerr effect (MOKE) (Low/Rm Temp)	can quickly obtain hysteresis loop of a single spot when saturating field is less than the maximum field of the magnet used for the measurement.	surface effect, penetration depth of the laser is limited; need to calibrate each sample separately to convert to M, difficult to obtain an accurate qualitative result for M.
X-ray magnetic circular dichroism (XMCD)	can quickly obtain hysteresis loop of a single spot; elementally selective	the resolution is not readily available; need to calibrate each sample as in MOKE to convert to M
scanning hall probe microscopy (SHPM)	sensitivity is great when measuring strongly magnetic materials	small scanning and imaging area

Table 5.1 Advantages and disadvantages of various magnetic characterization techniques for measuring and mapping the magnetic properties of combinatorial libraries.

have looked into this issue in details. I will be addressing it in this and in the next chapter. I used the scanning SQUID microscope located in Prof. Wellstood's lab and the one at Neocera, Inc.

5.2 Simulation of uniformly magnetized samples

In calculating the magnetization from the experimental data of magnetized samples, I will use the inversion technique, which has been broadly used in the past. However, in order to apply this technique, it is necessary to understand how it works and how accurately it calculates the magnetization. For this purpose, I will use simulated magnetic field data, which are, unaffected by any noise or any experimental errors. In this section, details of the simulation are presented.

To obtain \vec{B} in three dimensional space from magnetized sample, one can integrate the dipole equation [14] given by

$$\vec{B}(\vec{r}) = \frac{\mu_0}{4\pi} \int_V \left(\frac{3\vec{m}(\vec{r}') \cdot (\vec{r} - \vec{r}')}{|\vec{r} - \vec{r}'|^5} (\vec{r} - \vec{r}') - \frac{\vec{m}(\vec{r}')}{|\vec{r} - \vec{r}'|^3} \right) d^3r' \quad \text{Equation 5.1}$$

An object with local magnetization $\vec{m}(\vec{r}')$ produces magnetic field at a distance \vec{r} as shown in Eq. 5.1.

I have used the scanning SQUID, which has the SQUID mounted in such a way so that the SQUID loop lies in the plane of the scanning stage and thus the SQUID is sensitive to the z component of the field- B_z . In general, when measuring only one component of the magnetic field, one can not determine the magnetization \vec{M} of the sample uniquely. If no additional constraints can be placed on \vec{M} , then the problem is insoluble. However, there are some special situations where one can obtain the

magnetization value by fitting to Eq. 5.1. These are the cases when the magnetization is uniform. In the case of in-plane magnetization samples, one can approximate the magnetization as arising from two parallel magnetic line charges, which will be discussed in Sec 5.3.1. On the other hand, for out-of-plane magnetization, the situation is equivalent to a loop of constant current (which can be related to M) surrounding the sample. This is discussed in section 5.4.1.

The coordinate system that I used here is shown in Figure 5.1. Here the point where the B field is measured is denoted by (x, y, z) , and the point on the sample is (x', y', z') . The thin film sample dimensions are $l \times w \times d$, and z is the perpendicular distance from the measuring point to the plane of the sample. \vec{m} is a function of position (x', y', z') . One can obtain the expression for B_z for given $\vec{m}(\vec{r}')$ via Eq. 5.1.

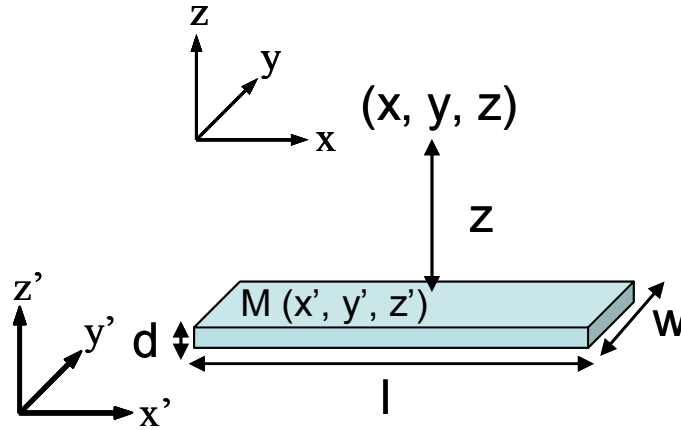


Figure 5.1 The coordinate system for simulating a sample using the dipole equation (Eq. 5.1)

When the sample thickness d is much smaller than z (which is the typical case in thin film experiments), one can approximate the three dimensional integral to the two

dimensional one. In the case of a sample with uniform in-plane magnetization, the equation for B_z is given by

$$B_z(x, y, z) = \frac{3\mu_0 d}{4\pi} \iint \frac{z[m_x(x-x') + m_y(y-y')]}{[(x-x')^2 + (y-y')^2 + z^2]^{5/2}} dx' dy' \quad \text{Equation 5.2}$$

Here, m_x and m_y are the in-plane components of \vec{m} which are constants and where magnitude m is $\sqrt{(m_x^2 + m_y^2)}$. On the other hand, for uniform out-of-plane magnetization, one obtains

$$B_z(x, y, z) = \frac{\mu_0 d}{4\pi} \iint m_z \left\{ \frac{3z^2}{[(x-x')^2 + (y-y')^2 + z^2]^{5/2}} - \frac{1}{[(x-x')^2 + (y-y')^2 + z^2]^{3/2}} \right\} dx' dy' \quad \text{Equation 5.3}$$

Here, m_z is the out-of-plane component of \vec{m} which is a constant.

In order for me to perform the simulation, Equations 5.2 and 5.3 were integrated numerically in x' and y' to obtain the distribution of B_z for both in-plane and out-of-plane magnetized samples, respectively. For simplicity, in the case of the in-plane magnetization, I set $m_y=0$. In all the simulations performed, I used the simplest way to integrate, which is just a summation with small integration intervals dx' and dy' . It is important to make sure the values of dx' and dy' are small enough so that the integral value does not change as dx' and dy' change. It was checked that the interval of $5 \mu\text{m}$ in x' and y' was sufficiently small to obtain accurate results. The scanning step size (which is the distance between the nearest data points) is $50 \mu\text{m}$ in the x and y directions. For the simulations, initially I was helped with the Labview programming by Dr. John

Mathews and Dr. Su Young Lee. The panel of the software for the in-plane magnetization case can be seen in Figure 5.2.

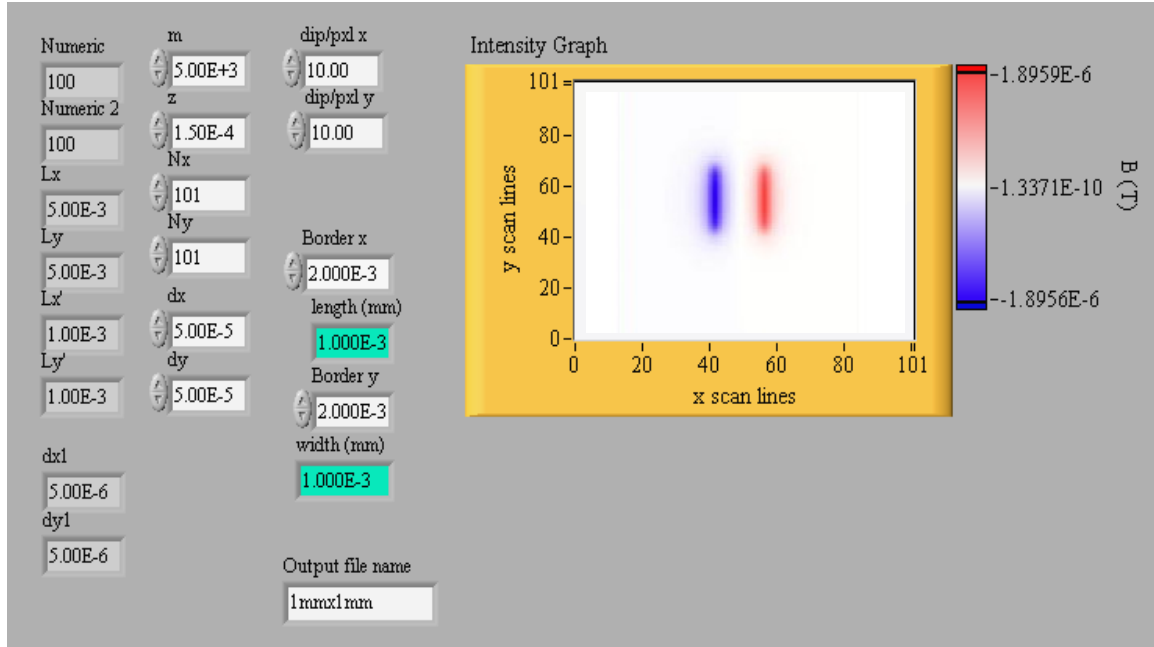


Figure 5.2 A Labview panel for simulating in-plane magnetized samples. The distribution of magnetic field B_z due to m_x is shown in the window. The sample here is 1 mm x 1 mm x 3000 Å, scanning area 5 mm x 5 mm, $M = 5$ emu/cc, step size in x and in y = 50 μm , integration step = 5 μm , scanning height is 150 μm .

5.3 In-plane magnetization

The scanning SQUID microscope has a wide variety of applications. The research of magnetic thin film combinatorial libraries is the area that I focus on in this thesis. The task at hand is to obtain accurate values of remanent magnetization of thin film samples given the distribution of B_z measured by the scanning SQUID microscope. To quantitatively characterize the samples, one must develop the analysis tools for interpreting the data from the scanning SQUID microscope. For the out-of-plane magnetization (see section 5.4 below), a unique solution already had been reported [15], which allows accurate determination of the remanent magnetization value. The out-of-

plane problem is solvable because there is only one component of the magnetization. However, for general two-dimensional in-plane magnetization, there is no unique solution given only B_z measured by the scanning SQUID microscope. In principle, we can think of this problem as having an infinite number of solutions. I will discuss several methods for deducing the in-plane remanent magnetization value, using reasonable assumptions about the magnetization of the sample.

5.3.1 Line charge approximation

In some instances, one can use simple models to fit the acquired magnetic field data. The first model I use is the line charge model. This generalized approach can be found in literature [16]. There are several approximations needed for this model. The first approximation is that the sample is uniformly magnetized along one side of the sample. For a thin film of thickness d , length l and width w , (as shown in Figure 5.3 (a)), one can use a general definition of a surface magnetic charge density σ_m as

$$\sigma_m = \hat{n} \cdot \vec{M}, \quad \text{Equation 5.4}$$

where \hat{n} is a unit vector in the direction of M , which is parallel to l . This can be mapped into two parallel magnetic line charges of density σ_m , and length w as shown in Figure 5.3 (b). Now if the length w is sufficiently large, one can approximate it to be infinite. This is the second approximation that I will use. Note however, that for finite line charges one is able to calculate the field exactly only on the plane which cuts the line charge perpendicularly in the middle, shown as the purple dashed line in Figure 5.3 (b), since the sample is symmetric about this plane. The relationship between the magnetic charge per unit length λ_m and the magnetization M can be expressed as

$$\sigma_m = \frac{Q_m}{w \cdot d} = \frac{\lambda_m}{d} = M$$

Equation 5.5

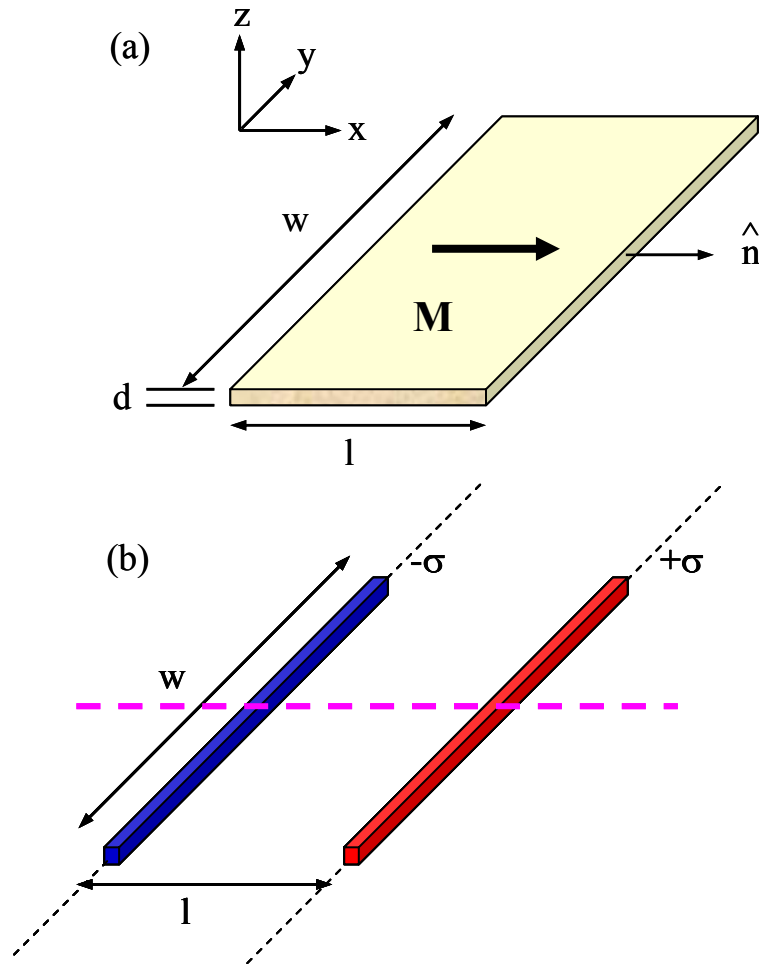


Figure 5.3 The line charge model (a) uniform in-plane magnetization in a thin film in one direction, (b) equivalent magnetic line charge taken to infinity. I will take the B field along the purple dashed line in order to fit the data.

To calculate the magnetic field \vec{B} (in Tesla) at a distance r from one of the line-charges one can simply consider the magnetic field \vec{B} that is produced by a magnetic

charge Q_m . Using the formulation from the electric field due to the electric charge Q , \vec{B} is expressed as

$$\vec{B} = \frac{\mu_0 Q_m}{4\pi r^2} \hat{r} \quad \text{Equation 5.6}$$

To calculate B_z from Eq. 5.6, I need to define the coordinate system as shown in Figure 5.4.

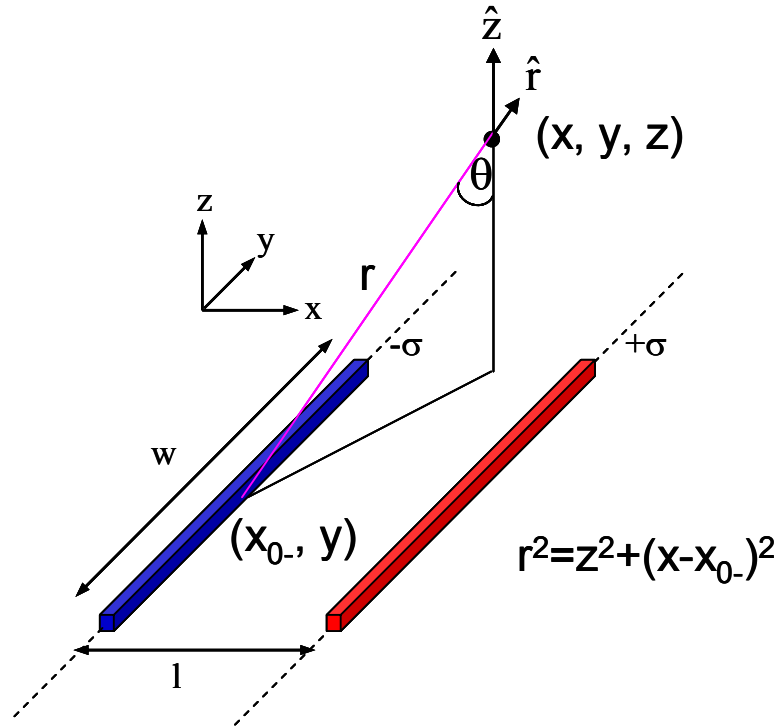


Figure 5.4 The coordinate system to find B_z .

Then after the integration over the line, B_z for an infinite line charge will be expressed as,

$$B_z = \frac{\mu_0 \lambda_m}{2\pi r} \hat{r} \cdot \hat{z} = \frac{\mu_0 \lambda_m}{2\pi r} \cos \theta = \frac{\mu_0 \lambda_m}{2\pi r^2} z. \quad \text{Equation 5.7}$$

Then by using Eq. 5.5 to express λ_m in terms of M , the two magnetic line charges yield

$$B_z = \frac{\mu_0 M d}{2\pi} \left(\frac{z}{(x - x_{0-})^2 + z^2} - \frac{z}{(x - x_{0+})^2 + z^2} \right) \quad \text{Equation 5.8}$$

where x_{0+} and x_{0-} are the locations in the x -axis of the positive and negative line charges, respectively, and the other parameters such as d and z are known to very good accuracy from the measurement. Therefore, knowing all these parameters and having the data for B_z , M can be fitted easily using Mathematica (see Appendix D.1) or any other software.

To check this model, I used simulated data first. I took a simulation of a sample of 4 mm x 4 mm with $M = 5$ emu/cc, $\Delta x = \Delta y = 50 \mu\text{m}$ (scanning step size), and

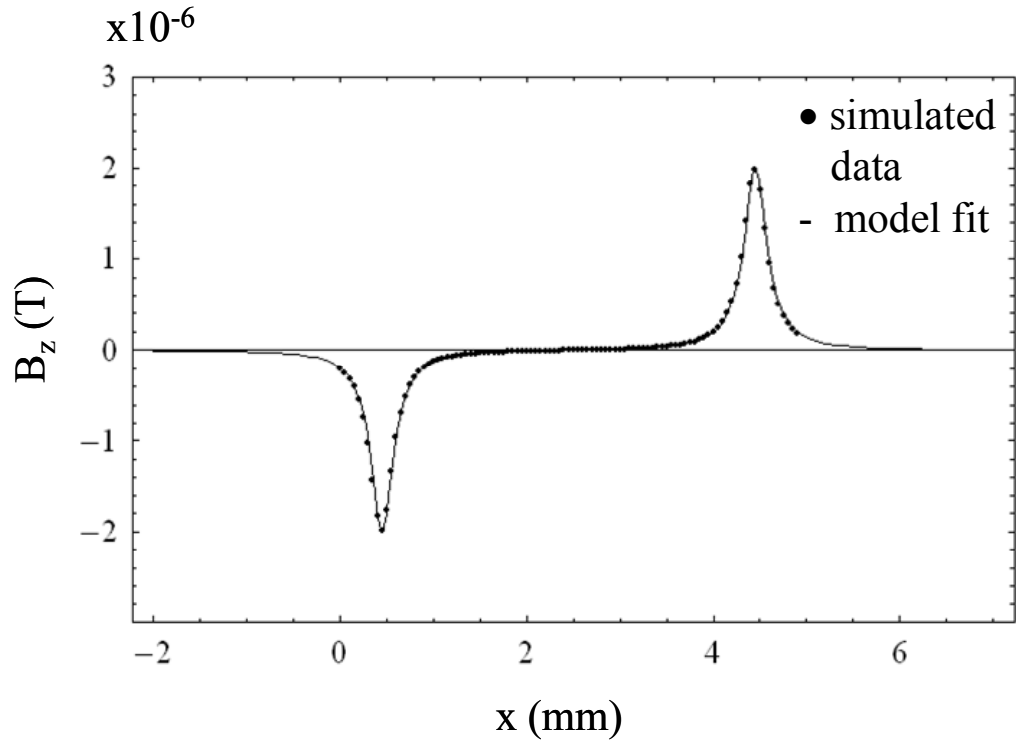


Figure 5.5 Magnetic field from the magnetic line charge model (solid line) fitted to the simulated data (dotted).

$z = 150 \mu\text{m}$ and using Eq. 5.2 calculated the B_z distribution. I took one line scan in the middle of the sample along the purple dotted line of Figure 5.3 (b), and fitted it with all the known parameters to Eq. 5.8 in order to find M . Figure 5.5 shows the fitted curve (solid line) and the original data (dotted) from the simulated scan. From the fitting, we

obtain the correct M value. However, it is clear that when the sample width w becomes smaller, the infinite-line charge approximation begins to fail. A question then arises: when does the approximation fail?

To address this question, in Figure 5.6, I look at the maximum of B_z as a function of the ratio of w to z in a log-log plot. One sees a transition in the changing behavior of

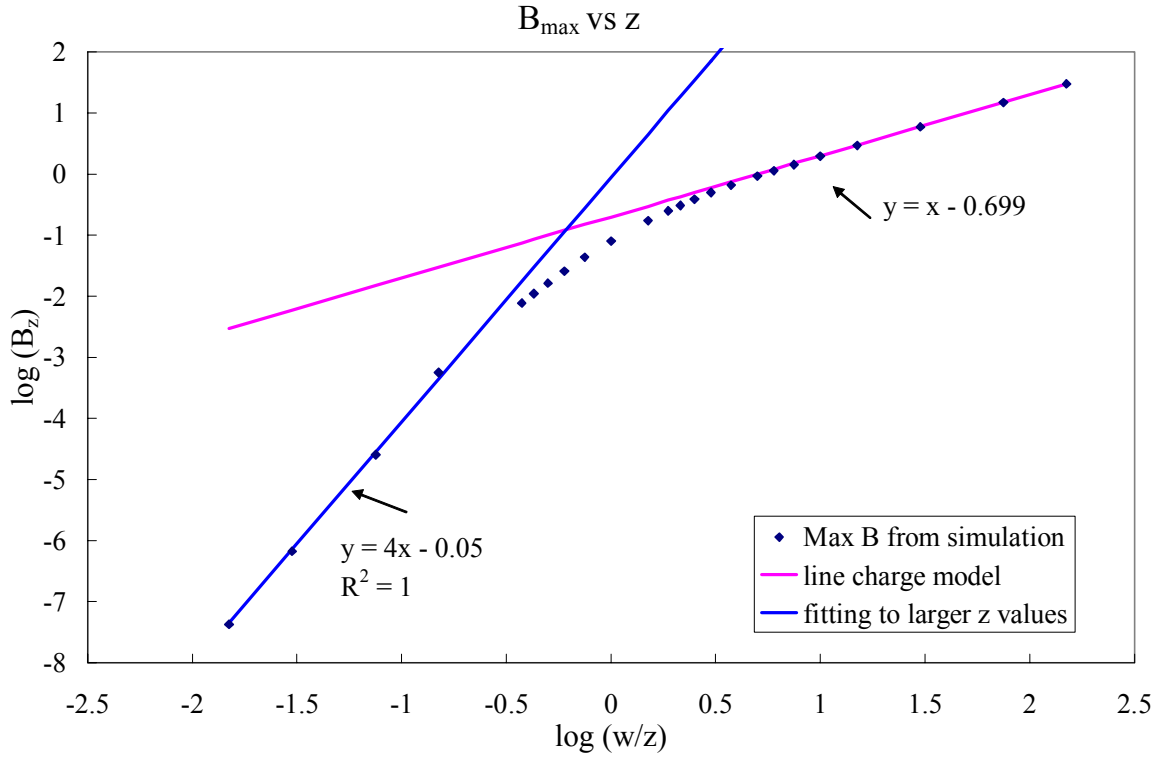


Figure 5.6 Variation of maximum B_z as a function of z .

the maximum B_z , which varies as $1/z$ for small z , while for larger z , the maximum decays as $1/z^4$. To understand the behavior of B_z at small z , one may consider Eq. 5.8 from the infinite-line charge approximation. From this equation, one can obtain the maximum value of B_z as

$$B_z = \frac{C}{z} \quad \text{Equation 5.9}$$

where C is $\frac{\mu_0 M d}{2\pi}$. The purple line in Figure 5.6 represents this limit. On the other hand, when z becomes large, one can see from Eq. 5.2 that the maximum B_z will vary as $1/z^4$. This is shown as the blue line in Figure 5.6. As one can see from the figure, as the ratio $\log(w/z)$ becomes smaller than 0.5, the maximum B_z clearly deviates from the infinite-line charge approximation. Therefore, the line charge approximation fails in this regime.

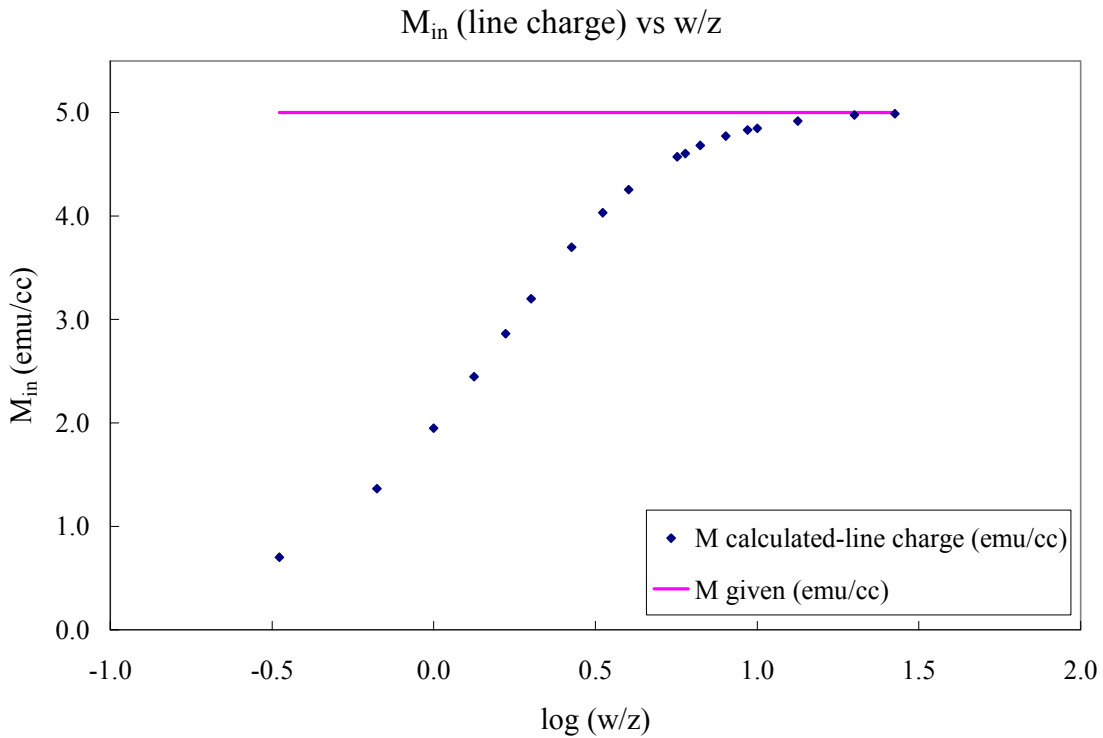


Figure 5.7 Variation of M calculated from the line charge model as a function of w for a given $z = 150 \mu\text{m}$.

To check this more quantitatively, I fitted the simulated data of different w at $z = 150 \mu\text{m}$ to Eq. 5.8 as before to calculate the magnetization. The results are plotted in Figure 5.7.

As expected, the magnetization calculated from the line charge approximation gives already 10% error from the given value even when $\log(w/z)$ is smaller than 0.7. From these calculations, it is then evident that to obtain the accurate magnetization from the line charge approximation, one needs to have the ratio w/z at least larger than 10. When the sample is such that w is smaller than $10z$, it is then necessary to use other methods to calculate magnetization. In special instances, however, it is useful to use the line-charge model, because it is simple and quick to adapt.

Now I am going to demonstrate the same technique on a thin film sample. Dr. Minghui Yu grew a 150 nm thick film of SmCo_5 on a silicon wafer and capped it with a thin layer of Fe and Pt by magnetron sputtering. This composition has ferromagnetic properties at room temperature [4]. Therefore, I should be able to see remanent magnetization due to ferromagnetism exhibited in the sample as I scan it using the scanning SQUID microscope. The silicon wafer was patterned into a grid, therefore, I broke off one square 1.63 mm x 1.7 mm ($l \times w$) and magnetized it in the in-plane direction using a commercial SQUID magnetometer (Quantum Design Inc.). Then I scanned the sample in zero field with the distance z of 300 μm . Figure 5.8 shows the magnetic field B_z from the remanent magnetization of the sample. The field ranges from -15 μT (blue) to 15 μT (red), and the sample is seen to be magnetized in-plane in one direction.

I took the magnetic field data along a line parallel to the magnetization direction (purple dotted line) from the scanned data and did the same fitting as discussed earlier for the simulated data with Eq. 5.8. The plot of data scanned along the middle line and its fitting is shown in Figure 5.9. The fitting then yields 204.6 emu/cc for the in-plane

magnetization. This value is about 10 % lower than the remanent magnetization value measured with the SQUID, which is 227.9 emu/cc. The sample size was 1.63 mm x

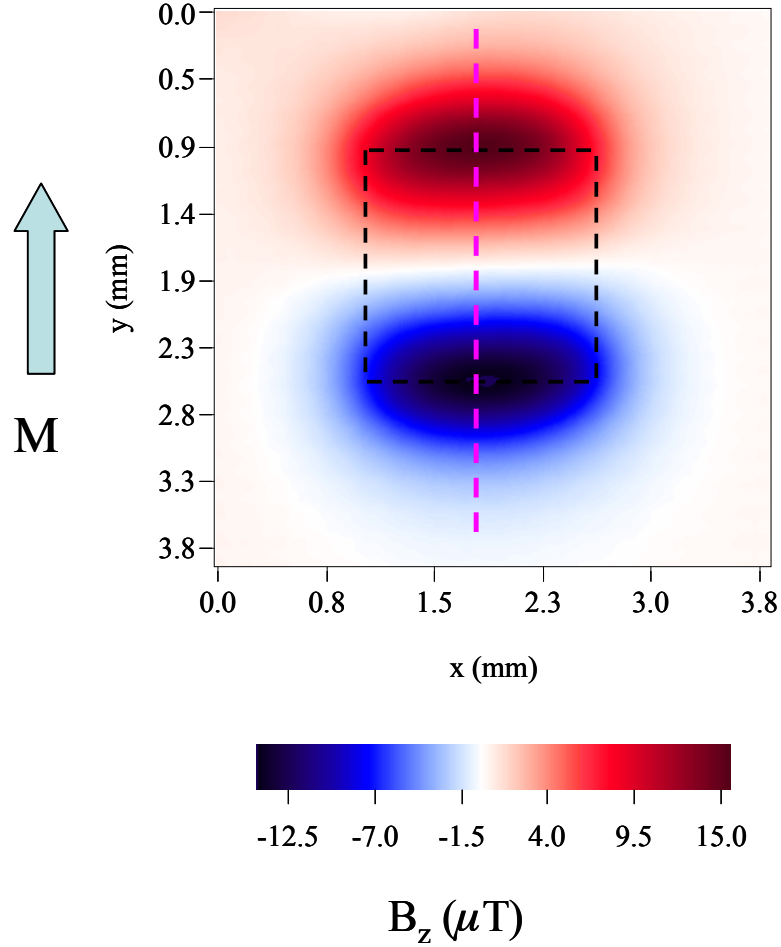


Figure 5.8 Image of the normal component of magnetic field from a thin-film of SmCo_5 in zero applied field, magnetized with 3T, which is higher than the coercive field. The size of the sample is 1.63 mm x 1.7 mm. Black dashed line indicates the boundaries of the substrate, purple dashed line is the field line that I took to fit the data.

1.7 mm while z was 300 μm , which yields the $\log(w/z)$ ratio of 0.753. If one looks at Figure 5.7 (which shows the fitted magnetization of the simulation data as a function of $\log(w/z)$), one finds that at the value 0.735 of $\log(w/z)$ the fitting gives an error of 9.5 % for M . This then agrees well with 10 % deviation of the measured magnetization of the

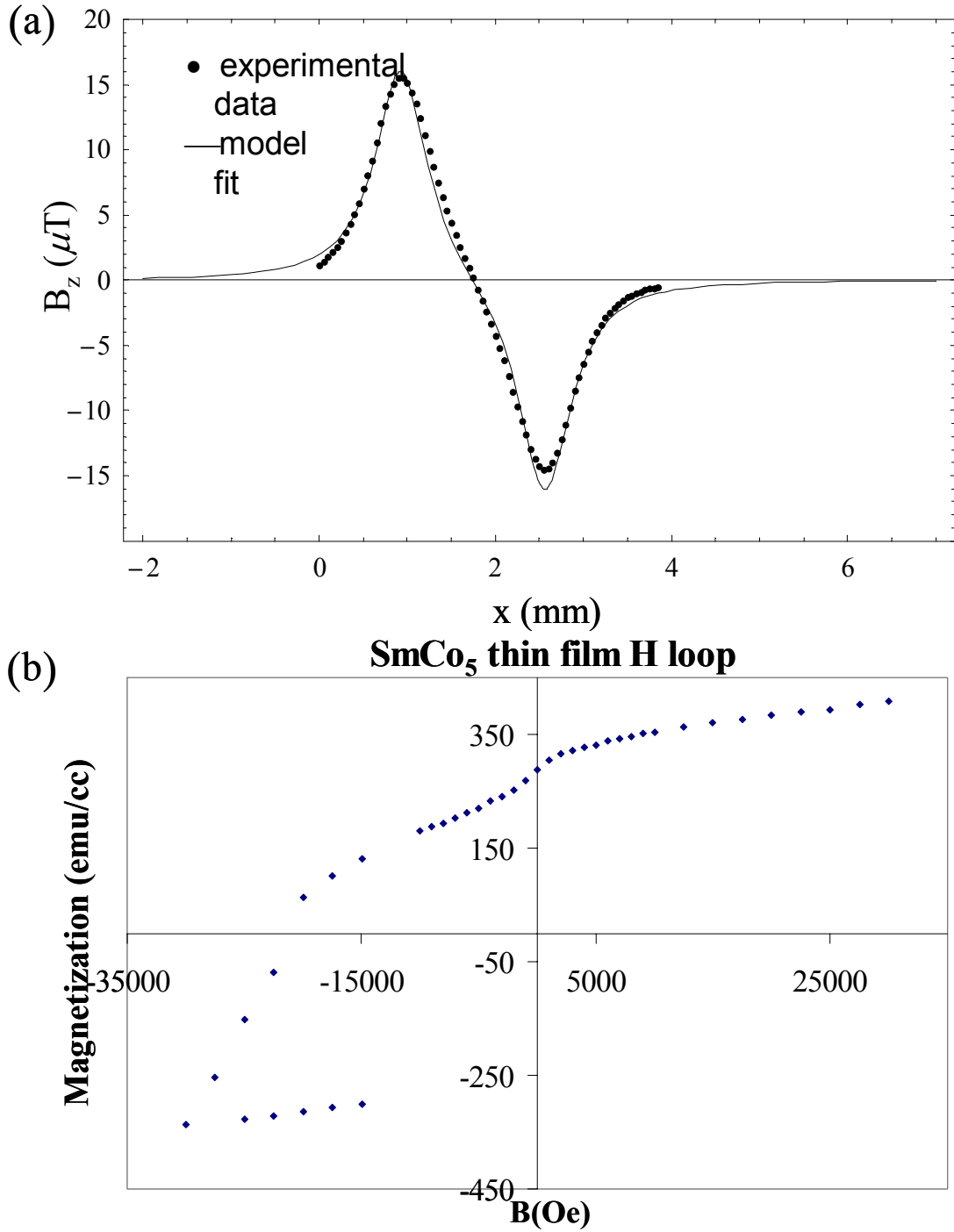


Figure 5.9 (a) Magnetic field from the magnetic line charge model (solid line) fitted to the experimental data (dotted) from scanning SQUID of SmCo_5 thin film. (b) The hysteresis loop of the same sample from SQUID magnetometer.

sample via fitting. The inset of Figure 5.9 shows the hysteresis loop taken from commercial SQUID magnetometer on the same sample. The saturated magnetization was 340 emu/cc at 3 T and the remanent magnetization (after it is saturated) is, as mentioned, 227.9 emu/cc. Overall, the fitting to the line-charge model is a very good technique to calculate uniform magnetization and all one needs is one scan line of B_z data instead of the entire mapping; however, one must keep in mind the limitation associated with sample dimension w , the distance z , and the uniformity of M .

On the other hand, what we are often interested in are the samples that have spatially varying magnetization. This is because we fabricate combinatorial samples with varying compositions, which lead to varying magnetic properties across a single substrate. In such instances, this technique is inaccurate and difficult to apply. In the next section, I will introduce the inversion technique for calculating the in-plane magnetization.

5.3.2 General derivation for the inversion of B_z for in-plane magnetization

The technique of inverting magnetic field B is widely used and has been previously reported [15]. Here I will review some of the formulation of extracting magnetization from magnetic field obtained from a scanning SQUID, which was discussed extensively in the dissertations of S. Chatrathorn and E. F. Fleet [16, 17,]. I will introduce the inversion technique, which allows us to calculate M at every point on the sample. This technique uses the entire two dimensional data from B field instead of just fitting a line. I will also point out some of the limitations of this technique and

dependence of results on several parameters, which will be discussed in more details in Chapter 6.

The local magnetization $\vec{M}(x', y', z')$, of a sample, where m_x and $m_y \neq 0$ with thickness d as shown in Figure 5.1, can be related to B_z through the following equations assuming the surface term is negligible [14]:

$$\rho_m(x', y', z') = -\vec{\nabla} \cdot \vec{M}(x', y', z') \quad \text{Equation 5.10}$$

$$B_z(x, y, z) = \frac{\mu_0}{4\pi} \iiint \frac{z \rho_m(x', y', z')}{[(x-x')^2 + (y-y')^2 + (z-z')^2]^{3/2}} dx' dy' dz' \quad \text{Equation 5.11}$$

where $\mu_0 = 4\pi \times 10^{-7}$ Tm/A is the permeability of free space and $\rho_m(x', y', z')$ is the magnetic pole density with the following condition:

$$\rho_m(x', y', z') = \begin{cases} \rho_m(x', y') & \text{for } d/2 \leq z' \leq d/2 \\ 0 & |z'| > d/2 \end{cases} \quad \text{Equation 5.12}$$

If z (scanning distance) $\gg d$, one may set $z'=0$. This then leads the dz integral in Eq. 5.11 to a value of d . Thus, one arrives at

$$B_z(x, y, z) \approx \frac{\mu_0}{4\pi} \iint \frac{\rho_m(x', y', z')}{[(x-x')^2 + (y-y')^2 + z^2]^{3/2}} dx' dy' \quad \text{Equation 5.13}$$

which is a convolution integral. This can be written in Fourier space as

$$b_z(k_x, k_y, z) = g(k_x, k_y, z) \tilde{\rho}_m(k_x, k_y) \quad \text{Equation 5.14}$$

where $g(k_x, k_y, z)$ is a Fourier transform of a Green's function,

$$G(x-x', y-y', z) = \frac{\mu_0 d}{4\pi} \frac{z}{[(x-x')^2 + (y-y')^2 + z^2]^{3/2}}, \quad \text{Equation 5.15}$$

while $\tilde{\rho}_m$ is the Fourier transform of the magnetic pole density. By Fourier transforming Eq. 5.15, one simply obtains

$$g(k_x, k_y, z) = \frac{\mu_0 d}{2} e^{-kz} \quad \text{Equation 5.16}$$

Hence, b_z of Eq. 5.14 in Fourier space is expressed as

$$b_z(k_x, k_y, z) = \frac{\mu_0 d}{2} e^{-kz} \tilde{\rho}_m(k_x, k_y) \quad \text{Equation 5.17}$$

Therefore, to calculate ρ_m in real space, one needs to solve for $\tilde{\rho}_m$ in the k space from Eq.

5.17, and inverse Fourier transform it to real space as

$$\rho_m(x, y) = FT^{-1}[\tilde{\rho}_m] = FT^{-1}\left[\frac{2}{\mu_0 d} e^{kz} b_z(k_x, k_y, z)\right] \quad \text{Equation 5.18}$$

where FT^{-1} is the inverse Fourier transform.

There is an exponential factor in Eq. 5.18 that is very important for analyzing the data. This factor exponentially increases the large k (small x) features in the data, thus improving the spatial resolution of the image acquired from the microscope. On the other hand, the microscope is not noiseless, and thus not every feature can be recovered with Eq. 5.18. Typically this noise is independent of x , y , and z and appears at all k . So at large enough k , the signal will be dominated by noise and will be obscured. This means that the smaller features at higher k values will be obscured quicker than the larger features, and trying to recover them will simply introduce large noise in the resulting ρ_m in the x space. Therefore, the solution from Eq. 5.18 must be windowed [18], such that all data above some chosen cut-off frequency k_w are discarded. I primarily used two functions for windowing data in the frequency space. These are:

Hanning window

$$f(k) = \begin{cases} 0.5[1 + \cos(\pi \frac{k}{k_w})] & ; |k| \leq k_w \\ 0 & ; |k| > k_w \end{cases} \quad \text{Equation 5.19}$$

Gaussian window

$$f(k) = \frac{1}{\sqrt{2\pi}k_w} e^{-\frac{k^2}{2k_w^2}} \quad \text{Equation 5.20}$$

In the next sections, I will discuss how this k_w should be chosen to obtain the maximum spatial resolution, which for our purpose should provide reasonably accurate magnetization values.

So rewriting Eq. 5.18 including the window filter function $f(k)$ in terms of the known parameters, I obtain

$$\rho_m(x, y) = FT^{-1}(\tilde{\rho}_M(k_x, k_y)) = FT^{-1}\left(\frac{2}{\mu_0 d} e^{kz} \cdot f(k) \cdot FT[B_z(x, y)]\right) \quad \text{Equation 5.21}$$

Extracting \vec{M} from a relationship of \vec{M} and ρ_m in Eq. 5.10, in general, is not a solvable problem, since $\vec{\nabla} \times \vec{M}$ is unknown. Erin Fleet [17] has shown that, in general, the total magnetic dipole \vec{m} can be obtained as:

$$\vec{m} = d \int_A (x\hat{x} + y\hat{y}) \rho_m(x, y) dx dy. \quad \text{Equation 5.22}$$

Here the surface term is ignored, and the sample is considered to be two-dimensional with thickness d where ρ_m is uniform in z . From Eq. 5.22 one can calculate m_x and m_y , the x and y components of \vec{m} . The average in-plane magnetization M_{in} per unit volume can be calculated from

$$M_{in} = \left(\frac{\sqrt{m_x^2 + m_y^2}}{V} \right) \quad \text{Equation 5.23}$$

From this point when I am referring to the value of in-plane magnetization, I will use M_{in} as the notation.

All the calculations for the inversion technique are done using the Transform software. The programming code for the in-plane calculations can be found in Appendix C.1 and C.2.

I will calculate M_{in} using the inversion technique for the sample shown in Figure 5.8 in Chapter 6.

5.4 Out-of-plane magnetization

As I mentioned earlier in this chapter a unique solution to the out-of-plane magnetization, using the inversion technique, already has been reported [15]. Because there is only one component of magnetization that we are trying to solve using B_z acquired from the scanning SQUID, the problem is solvable. Here I will discuss two ways of solving for out-of-plane magnetization from B_z distribution obtained from the SQUID microscope. One is the current loop model, which is a straightforward, exact calculation using the Biot-Savart law and the other is the inversion technique using Fourier transform. Although the current loop model can be used to calculate the uniform out-of-plane magnetization exactly, it is difficult to employ for the nonuniform case, which is often the case. In this case, the inversion technique can be applied to calculate the magnetization.

5.4.1 Current loop model

Here I will propose a simple model to calculate the out-of-plane magnetization from a uniformly out-of-plane magnetized sample. The uniform out-of-plane magnetization of a sample can be modeled by a current loop of constant current flowing around the edge of the sample. Figure 5.10 shows the schematic diagram of a current

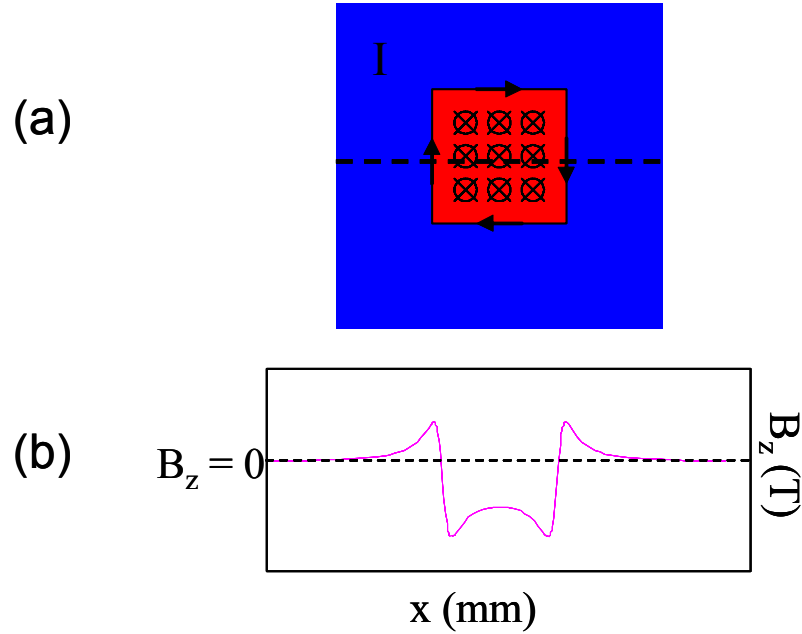


Figure 5.10 (a) A schematic diagram of the current loop model for a uniform out-of-plane magnetized sample. The current in this case is flowing in the clockwise direction and produces a magnetic field inside the sample that is going into the plane of the paper (red). (b) One line scan of B_z across the black dotted line of the sample in (a). The profile of B_z is shown.

loop. The constant current in the loop then produces the magnetic field, which is equivalent to the field generated by a uniform magnetization M_z inside the sample. One can calculate the magnetic field of the current loop by using the Bio-Savart Law. Magnetization can be related to the current in the following relation

$$I = M_z \cdot d, \quad \text{Equation 5.24}$$

where d is the thickness of the sample while I is the current in the loop. Since the wire has finite dimensions and has a geometrical shape, the calculation becomes a little more complicated, since one has to consider the limits of integration. But it is still manageable. I will take the coordinate system, which is shown in Figure 5.11. To calculate the B_z of the sample measured at point (x, y, z) I need to include the contribution from all four parts of the current carrying wires. The integration limits are set by the dimension of the sample, as shown in Figure 5.11. The Bio-Savart Law equation is

$$\vec{B} = \frac{\mu_0 I}{4\pi} \int \frac{d\vec{l} \times \vec{r}}{r^3} \quad \text{Equation 5.25}$$

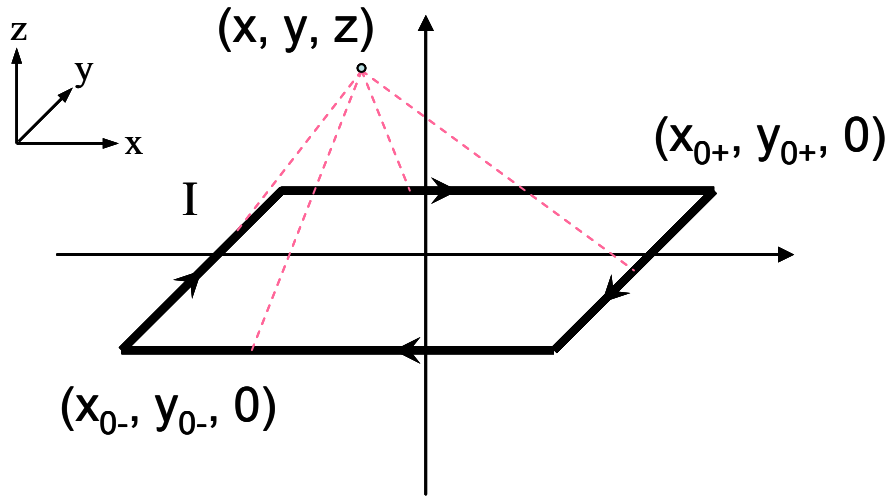


Figure 5.11 The coordinate system for calculating the B_z at a point (x,y,z) from all 4 parts of the wire carrying current I in the clockwise direction. The corners of the loop are labeled as $(x_{0-}, y_{0-}, 0)$ and $(x_{0+}, y_{0+}, 0)$. The points of x_{0-} and x_{0+} are symmetric about the x axis and y_{0+} and y_{0-} about the y axis.

I will demonstrate how to get an expression for B_z for one part of the wire, namely the left hand side wire, where $d\vec{l} = dy \hat{j}$ and $\vec{r} = (x - x_{0-}) \hat{i} + (y - y_{0-}) \hat{j} + z \hat{k}$. Here, the corners of the loop are labeled as $(x_{0-}, y_{0-}, 0)$, $(x_{0+}, y_{0+}, 0)$, etc. So the z component of magnetic

field produced by a segment (located at x_{0-}) of the wire as a function of M , using Eq. 5.24,

$$\text{is } B_z = \frac{\mu_0 M d}{4\pi} \int_{y_{0-}}^{y_{0+}} - \frac{(x - x_{0-}) dy}{\left((x - x_{0-})^2 + (y - y_{0-})^2 + z^2\right)^{3/2}} \quad \text{Equation 5.26}$$

This integral gives

$$B_z = \frac{\mu_0 M d}{4\pi} (x - x_{0-}) \left[\frac{(y - y_{0+})}{(x - x_{0-})^2 + z^2} \cdot \frac{1}{\left((x - x_{0-})^2 + (y - y_{0+})^2 + z^2\right)^{1/2}} - \frac{(y - y_{0-})}{(x - x_{0-})^2 + z^2} \cdot \frac{1}{\left((x - x_{0-})^2 + (y - y_{0-})^2 + z^2\right)^{1/2}} \right] \quad \text{Equation 5.27}$$

Similarly, one can obtain the expression for B_z for every segment of the wire loop and add them together. I then used the Mathematica software to fit the equation for all the wire parts using all the parameters that are known from the data acquired (see

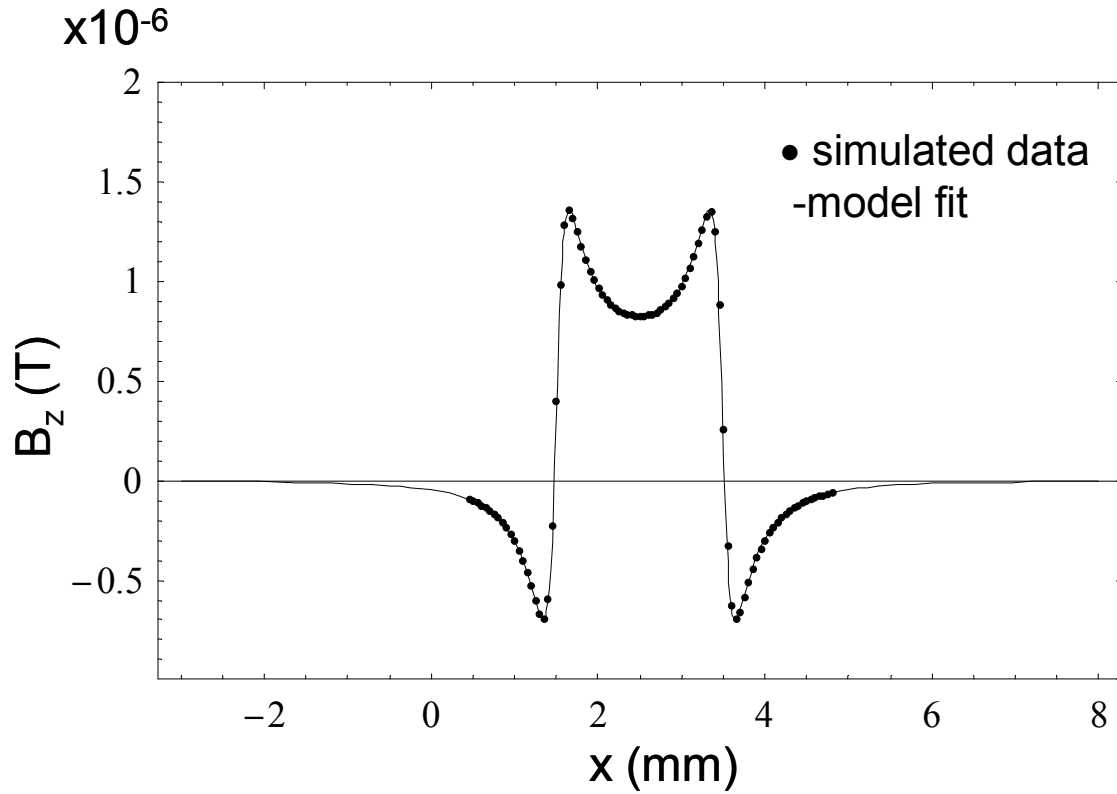


Figure 5.12 Magnetic field from the current loop model (solid line) fitted to the simulated data (dotted).

Appendix D.2). To demonstrate the validity of my calculation, I took a simulation of a sample of 2 mm x 2 mm with $M = 5$ emu/cc, $\Delta x = \Delta y = 50 \mu\text{m}$, and $z = 150 \mu\text{m}$ and calculated B_z using Eq. 5.3. I took one line scan of B_z in the middle of the sample (as shown in Figure 5.10 along the black dashed line) and entered the known parameters to the total equation of B_z (4 equations as the Eq 5.26) in order to find M . Figure 5.12 shows the fitted function (solid line) and the original data (dotted) from the simulated scan. From the fitting result, I got the same value of M as the assigned value in the simulation.

Now I used this model to calculate M for a single composition thin film. The film that I used was a 300 nm thick film of CoFe_2O_4 on a 10 mm x 10 mm MgO substrate grown by pulsed laser deposition [19, 20]. I cut the sample into 4 squares and patterned them into strips of several sizes. Here I will only consider a sample of dimension 5 mm x 5 mm. CoFe_2O_4 has a Curie temperature T_c of 790K, and it has an out-of-plane easy axis magnetization. Therefore, I expect to see out-of-plane remanent magnetization due to ferromagnetism exhibited in the sample as I scan it using the scanning SQUID microscope. I magnetized the sample in the out-of-plane direction with field of 3 T, using a commercial SQUID magnetometer. The sample was scanned in zero field with the distance z from the SQUID sensor to the sample of $150 \mu\text{m}$. Figure 5.13 shows the false color image of magnetic field B_z due to the remanent magnetization of the sample. The field ranges from $-48 \mu\text{T}$ (blue) to $30 \mu\text{T}$ (red), and the sample appears to be magnetized out-of-plane. I took one line of B_z from this scan (across the purple dashed line in Figure 5.13) and did the same fitting as for the simulated data. The plot of the data and the model fit are shown in Figure 5.14 (a).

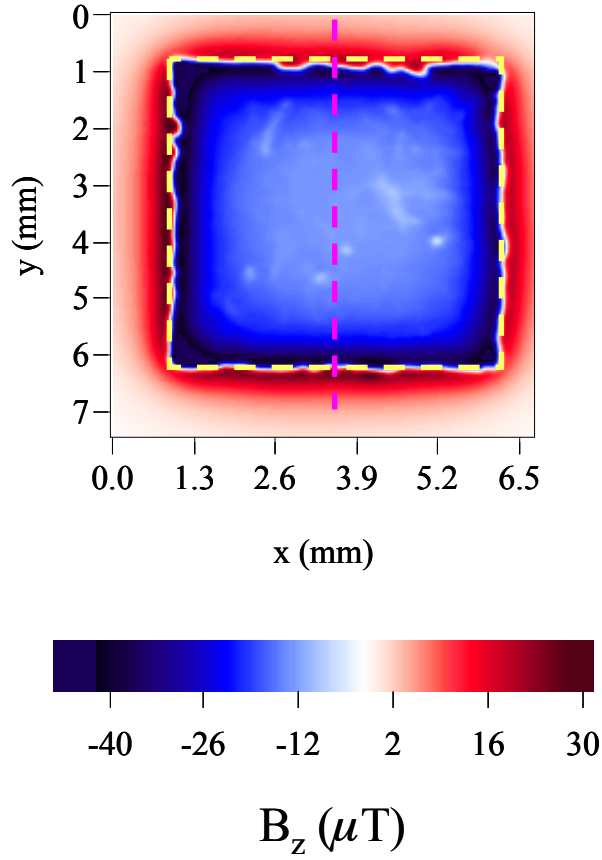


Figure 5.13 Image of a normal component of magnetic field from the CFO thin film in zero applied field. The size of the substrate and the film is 5.3 mm x 5.1 mm. The yellow dashed line indicates the boundaries of the sample whose magnetization I calculated. The purple dashed line shows the line of B_z that I took to fit the data using the current loop model

Here the quality of the fit is still good, although it is seen that one of the edges is not fully recovered. The value of the remanent magnetization that I obtained from the current loop model using the fitting was 153.6 emu/cc. Figure 5.14 (b) shows the hysteresis loop taken from a commercial SQUID magnetometer on the same sample. The saturated out-of-plane magnetization is 350 emu/cc at 2.5 T and the remanent magnetization (after it is saturated) is 156.7 emu/cc.

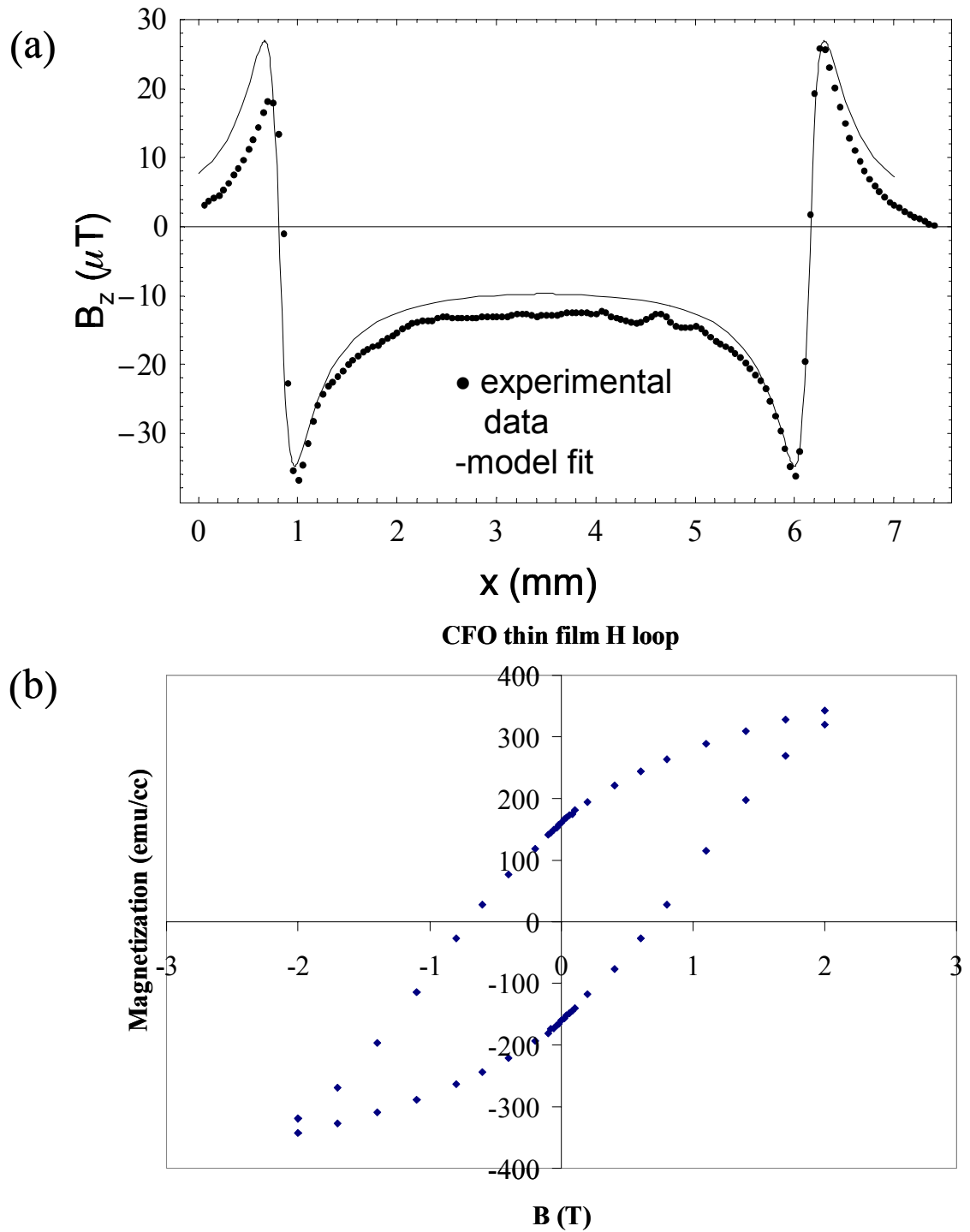


Figure 5.14 (a) Magnetic field from the current loop model (solid line) fitted to the experimental data (dotted) from scanning SQUID microscope data of a CFO thin film magnetized out-of-plane. (b) A hysteresis loop in the out-of-plane direction of the same sample from a SQUID magnetometer.

The value for M_z that I obtained from the sample via the fitting to the current-loop model is in very good agreement (less than 2 % error) with the value from the SQUID measurement. Therefore, the current loop model is a very good technique if the sample is a single composition thin film with a uniform out-of-plane magnetization. However, it is often necessary for us to accurately calculate the out-of-plane magnetization of sample where the composition is varying inside the sample. In this case, the magnetization will be varying throughout the sample, and thus, the current loop model becomes difficult to apply. Therefore, I will introduce the inversion technique for calculating the out-of-plane magnetization, which can be employed in the case of varying magnetization. Note, however, that for a simple uniform case, where magnetization is not changing the current loop model is easier to adapt than using the inversion technique.

5.4.2 General derivation for inversion of B_z for out-of-plane magnetization

In section 5.3.2 I gave a general derivation of the inversion of B_z for the in-plane magnetized sample. Here in this section I will derive the inversion of B_z for the out-of-plane magnetized sample.

Now for the case of the out-of-plane magnetization, it is straightforward to use Eq. 5.1 and apply the inversion. For this calculation of M I assume that $M_x = M_y = 0$, and $M_z \neq 0$. Note that M_z needs not be a constant. The coordinate system is the same as in Figure 5.1. The z component of the magnetic field B_z produced by M_z from Eq. 5.1 is expressed as

$$B_z(x, y, z) \approx \frac{\mu_0 d}{4\pi} \iint m_z(x', y') \left\{ \frac{3z^2}{[(x-x')^2 + (y-y')^2 + z^2]^{5/2}} - \frac{1}{[(x-x')^2 + (y-y')^2 + z^2]^{3/2}} \right\} dx' dy' \quad \text{Equation 5.28}$$

Note that by assuming that $z \gg z'$ as in section 5.3.2 (in-plane case), the dz integral is reduced to d , which is the thickness of the sample. Now Eq. 5.28 is a convolution of two functions: the magnetization $m_z(x', y')$ and the Green's function, which is given by

$$G(x-x', y-y', z) = \frac{\mu_0 d}{4\pi} \left\{ \frac{3z^2}{[(x-x')^2 + (y-y')^2 + z^2]^{5/2}} - \frac{1}{[(x-x')^2 + (y-y')^2 + z^2]^{3/2}} \right\} \quad \text{Equation 5.29}$$

The Fourier transform of $G(x-x', y-y', z)$ in the two-dimensions is simply

$$g(k_x, k_y, z) = \frac{\mu_0 d}{2} k e^{-kz} \quad \text{Equation 5.30}$$

Thus, using the result from Eq. 5.30, one obtains the Fourier transform of the magnetization as

$$\tilde{m}_z(k_x, k_y) = \frac{2}{\mu_0 d} \frac{e^{kz}}{k} \cdot b_z(k_x, k_y, z). \quad \text{Equation 5.31}$$

Here as in the case of the in-plane magnetization, there is an exponential factor that amplifies the large k (small x) features in the data. This can increase the spatial resolution. On the other hand, noise is also amplified and the signal can be lost when the values of k are too large. Hence as in the in-plane case, in practice it is important to window the data with properly chosen range of k values. Multiplying by a window function in k space then yields

$$\tilde{m}_z(k_x, k_y) = \frac{2}{\mu_0 d} \frac{e^{kz}}{k} \cdot b_z(k_x, k_y, z) \cdot f(k) \quad \text{Equation 5.32}$$

where $f(k)$ is a window filter function. The windows, which I used, are Hanning and Gaussian. Now notice that when k goes to zero, m_z in the k space diverges to infinity, i.e. an infinitely large sheet of dipoles does not produce B_z . Thus to prevent this anomaly, one should set $b_z(k_x = 0, k_y = 0, z) = 0$. The two-dimensional image of the magnetization in real space can be obtained from the inverse Fourier transform of Eq. 5.31 as

$$m_z(x, y) = FT^{-1} \left(\frac{2}{\mu_0 d} \frac{e^{kz}}{k} \cdot f(k) \cdot FT[B_z(x, y, z)] \right) \quad \text{Equation 5.33}$$

To calculate M_z , magnetization per unit volume in real space over a certain area, one can integrate in a manner similar to the in-plane case

$$M_z = \frac{1}{V} d \int_A m_z(x, y) dx dy, \quad \text{Equation 5.34.}$$

From now on, whenever I refer to the out-of-plane magnetization of the sample, I will use M_z as the notation. The programming code for the out-of-plane calculations is given in Appendix C.3 and C.4. Again as in the in-plane case for the experimental data, I will use the inversion technique once several parameters of the inversion are optimized.

5.5 Conclusions

In this chapter, I introduced different analysis tools that can be used to characterize magnetic properties of combinatorial libraries. I derived several techniques for calculating the in-plane and out-of-plane magnetization. For the in-plane case, I described the line charge approximation and the inversion technique. For the out-of-plane magnetization, I introduced the current loop model as well as the inversion technique.

I used the calculations from both models, the line charge model and the current loop model to compare the experimental results and the simulated results. However, I did

not compare them to the inversion calculation. This will be discussed in the next chapter. For both in-plane and out-of-plane magnetization the inversion technique has several parameters that control the calculation. Thus, in order to implement the technique, these parameters such as the cut off frequency k_w , the scanning area, the integration area and the z value that can greatly alter the result of the inversion technique must be known. This is discussed in the next chapter.

Chapter 6

Parameter dependence of the inversion technique for calculation of magnetization

In Chapter 5, the line-charge model and the current-loop model were introduced to calculate the in-plane and the out-of-plane magnetization, respectively. The magnetization values were obtained by using these models via fitting with the magnetization M as the only parameter. It was found that when the sample size is large enough compared to the scanning distance from the sample and when the sample is uniformly magnetized, these models could be applied easily to obtain the accurate values of magnetization. However, as I discussed in Chapter 5, the models cannot be used effectively when the magnetization is not uniform, which is often the case for combinatorial libraries.

In Chapter 2, I introduced two kinds of libraries that are investigated for their magnetic properties. They are the discrete libraries and the continuous composition spreads. Schematics of a typical discrete library and a typical composition spread are shown in Figure 6.1 (a) and Figure 6.1 (b) respectively.

In a discrete library, individual samples with different compositions are created. In the example shown in Figure 6.1 (a), samples are patterned into a square grid. Every square has a different composition and can have a different magnetic property. Each square with a magnetic material acts as its own dipole and one needs to be able to distinguish each square separately. For discrete libraries of magnetic materials, one can calculate M for each composition separately using a simple model introduced in Chapter 5. However, it is inefficient and impractical to do the same calculation for a large

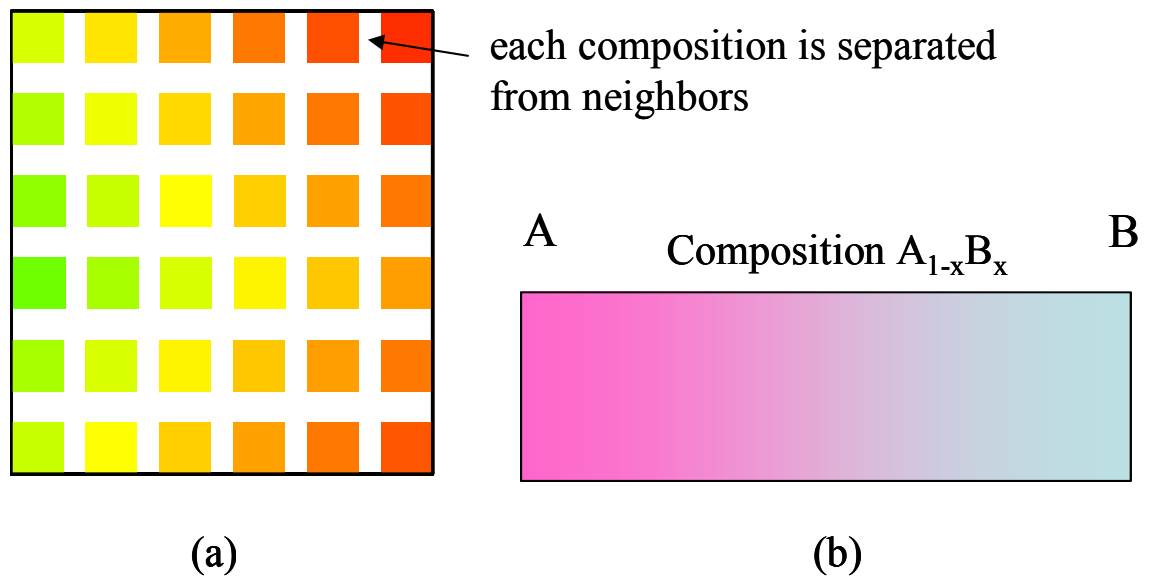


Figure 6.1 Schematic for (a) a discrete library and (b) a composition spread.

number of samples. In addition, there are necessary conditions on the spacing between the squares and on the size of the squares in order to apply the line charge model, and some of these conditions are difficult to implement in libraries. For instance, as discussed in Chapter 5, the dimension of the sample in magnetization direction must be at least 10 times the z value. Thus, we use the inversion in mapping magnetization from actual discrete libraries. This is discussed in Chapter 7.

In a composition spread sample, the composition is continuously changing across a contiguous sample. Thus, in a composition spread of magnetic materials, magnetization has a continuous distribution. Figure 6.2 (a) shows a simple schematic for a composition spread in which the composition and thus the magnetization varies continuously along the horizontal direction. An example of magnetization distribution is shown in Figure 6.2 (b). To calculate magnetization in such cases, one cannot apply the simple models discussed in Chapter 5. First, the magnetization is continuously changing;

the basic assumption for the models to work is for magnetization to be uniform. Second, even if one breaks the sample into strips, one still cannot use the simple model, because

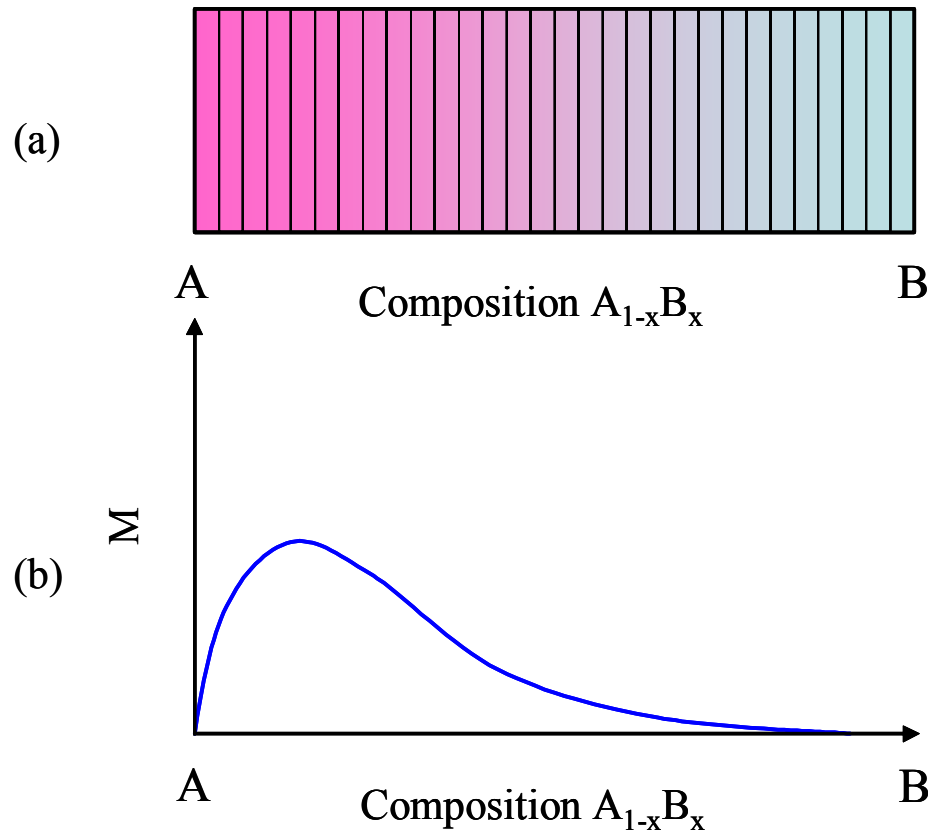


Figure 6.2 (a) A schematic of a composition spread sample with a varying M . The sample is divided into small strips to calculate magnetization for each composition. (b) An example of magnetization distribution for a composition spread.

there is error associated with the sample size and one would have to consider contributions from neighboring strips.

Obtaining accurate values of magnetization is very important for combinatorial samples. However, this is a challenge for composition spreads. Since the composition is continuously varying, it is necessary to divide the sample into strips as shown in Figure 6.2 (a). For each strip, data from the area are integrated and M can be obtained. As we will see later in this chapter, the integration area will be one of the parameters that I will

carefully consider which influences the value of M . In Chapter 5 (5.3.2 and 5.4.2) I presented some theoretical background for the inversion technique. In this chapter, I will discuss the effects of several parameters for calculating magnetization of combinatorial libraries.

6.1 General overview

In order to apply the inversion techniques for calculating magnetization, it is necessary to examine the role of the parameters that control the calculations. Here, I revisit two main equations from Chapter 5. The equation to calculate ρ_m for the in-plane magnetization case is given by (p. 95, p. 106, in Chapter 5)

$$\rho_m(x, y) = FT^{-1}(\tilde{\rho}_M(k_x, k_y)) = FT^{-1}\left(\frac{2}{\mu_0 d} e^{kz} \cdot f(k) \cdot FT[B_z(x, y,)]\right), \quad \text{Equation 6.1}$$

while for the out-of-plane magnetization case, it is given by

$$m_z(x, y) = FT^{-1}\left(\frac{2}{\mu_0 d} \frac{e^{kz}}{k} \cdot f(k)\right) \cdot FT[b_z(k_x, k_y, z)]. \quad \text{Equation 6.2}$$

Note that in these equations z is the distance between the sample and the SQUID, while d is the thickness of the sample. The function $f(k)$ is a windowing function that contains a cut-off frequency k_w . This means that when the Fourier transform is applied, all the amplitudes of B_z in the k space at k values higher than k_w are discarded. It is clear that the type of windowing function used will affect the calculations in the inversion technique.

As I mentioned in the previous chapter, a proper filter window must be used to correctly handle the ρ_m data. Initially, I considered two windows, namely Gaussian and Hanning windows [1, 2]. They are given in Eqs. 5.19 and 5.20 (Ch. 5) and shown in

Figure 6.3. Previously, Erin Fleet [3] had considered three types of windows (Gaussian, Hanning and square (Figure 6.3)) for his analysis of the field emanating from a current flowing in a sample. He considered two infinite line charges, and these three windows were used to calculate magnetization. He then concluded that the best result was provided by the Gaussian window. However, in his analysis of the Gaussian window he did not consider any cut-off in the Fourier space in order to do the integral exactly and to obtain the analytical result. On the other hand, for the other windows he introduced the cut-off. When the cut-off frequency k_w is also considered in the case of the Gaussian window, it is actually the square window that provides the best analytical result. This is because the square window preserves the function in the k space within the cut-off frequency (since the window filter is equal to one), while the other windows (Gaussian and Hanning) reduce the amplitudes of the B field in the k space.

For the analysis of the combinatorial libraries, one must consider a finite-size sample, and in this case, analytical study of window selection, similar to E. Fleet's, is not feasible. When magnetization is distributed throughout the finite-size sample, it is not obvious which window function is optimal. Figure 6.3 (a) shows the three window functions with the same cut-off frequency k_w in terms of the normalized wave vector k/k_w . One can see from this figure that these window functions will produce different results when the inversion technique is used, since they treat the amplitudes at k values near the cut-off frequency differently. It is clear that the square window is the worst when one

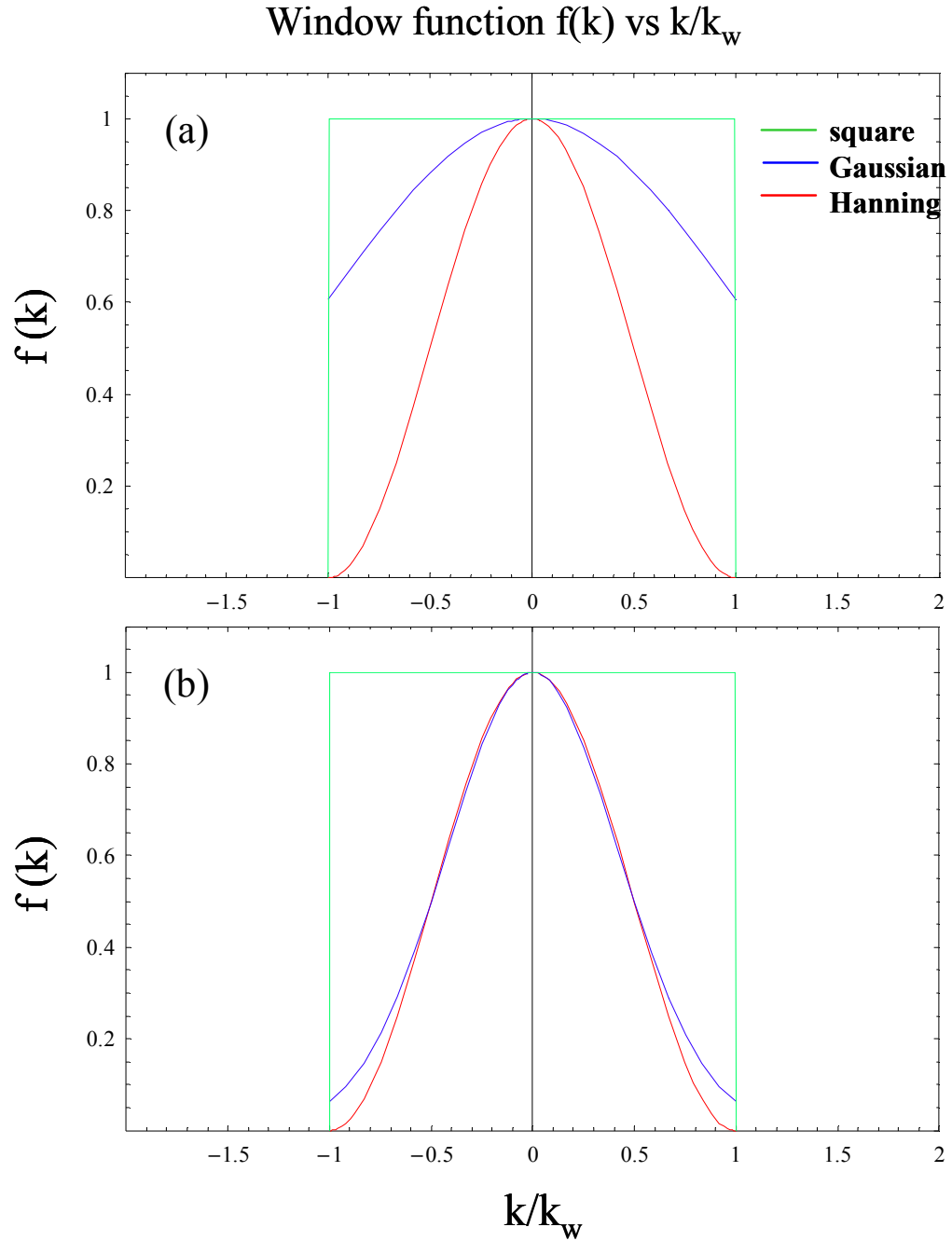


Figure 6.3 Different window functions (a) $f(k)$ in the k space as a function of k/k_w when k_w is the same for all three window functions. (b) $f(k)$ as a function k/k_w when $k_{w, \text{Gaussian}} = 0.42 \times k_{w, \text{Hanning}}$ ($k_{w, \text{Hanning}} = k_w$)

handles finite data, since it amplifies noise due to the amplitudes at high k values. On the other hand, one can see that the Gaussian and Hanning windows have similar shapes

when different cut-off frequencies are chosen. If we set, $k_{w,Gaussian} = 0.42 k_{w,Hanning}$ one obtains the same half-decay width. This can be seen in Figure 6.3 (b). Therefore, one can guess easily that choosing such cut-off frequencies for the two windows may yield almost the same results. This assumption has been verified with the simulation data, and no noticeable dependence of the magnetization on the window functions was observed. However, one may notice that the Gaussian window has a discontinuity at $k=k_w$, as can be seen in Figure 6.3. This discontinuity in the Fourier space may generate undesired errors when it is applied to the data from combinatorial libraries. Hence, throughout this and following chapters, I will use the Hanning window.

Once the window function is chosen, it is now important to understand the roles of various parameters, especially the cut-off frequency k_w , and the distance z contained in the equation. As studied previously, the value of k_w is very important for calculating ρ_m and determining the spatial resolution. One can see that if k_w is too large, then the inversion technique amplifies the noise. On the other hand, when k_w is too small, one cannot capture fully the shape of the magnetic field. Thus, it is important to choose the correct values for k_w when the inversion technique is used to calculate magnetization accurately. In Secs. 6.2.1 and 6.3.1, I discuss the effects of k_w and obtain its optimal values for the in-plane and out-of-plane magnetization cases, respectively.

In Eq. 6.1, the exponential factor has a parameter z (coupled to the wave vector k), which is the distance between the SQUID sensor and the sample. Since z is multiplied by k , it is clear that the value of z will affect the choice of k_w . In typical experiments, the scanning distance z varies from 150 μm to 500 μm . Thus, I will explore this range of z in studying the inversion technique. Secs. 6.2.1 and 6.3.1 present the variations of the k_w

optimal values as a function of z , while in Secs. 6.2.3 and 6.3.2 more elaborate discussion of the z dependence of the magnetization is presented for the in-plane and out-of-plane cases.

Another parameter, which is not apparently present in Eq. 6.1 but influences the results of the inversion technique, is the scanning area. When the scanning area is large enough, one is able to obtain the accurate magnetization via the inversion technique, while if the scanning area is too small, the lack of the magnetic field data hampers calculating magnetization. One then asks: how large of a scanning area should one consider in order to obtain reliable and accurate values of M ? The relevant parameter in this case is then the ratio of the scanning area to either the sample area or the distance z . In Secs. 6.2.3 and 6.3.3, I will discuss the dependence of the magnetization on this parameter.

To calculate the in-plane magnetization from ρ_m one needs to integrate the density over a certain area using the following equation:

$$\vec{m} = d \int_A (x\hat{x} + y\hat{y}) \rho_m(x, y) dx dy \quad \text{Equation 6.3}$$

This value is then divided by the volume of the sample to obtain M . For the out-of-plane case, the integration does not have the r vector multiplying the ρ_m (Eq. 5.40). In an ideal situation, the magnetization should not depend on the area A of the integration. However, in real experiments one has only limited amount of the magnetic field data inside the scanning area. This limitation diminishes the magnetic pole density by introducing noisy oscillations. In this case, one may think that considering the entire available area for integration is natural. However, as one will see in this chapter, integrating over the entire scanning area does not provide an accurate M . This effect arises from the noisy behavior

of the density near the edges of the scanning area. Furthermore, because our goal is to apply the inversion technique to continuous composition spread samples, where magnetization is spatially varying, it is important to be able to divide the sample into strips (Figure 6.2) and integrate each strip separately. Thus, it is essential to understand how the integration area affects the result of the magnetization. In fact, as we will see later in this chapter, the area of integration can play a big role in determining magnetization values. I will discuss in detail how one should select the integration area in order to obtain the magnetization accurately, for different values of z and the sample size.

To understand the roles of these parameters and to optimize them in the inversion technique, I will use simulated data obtained by integrating the dipole equation, Eq. 5.2 in Chapter 5, numerically. For details of the simulation, one can refer to Sec. 5.3. Once the effects of the various parameters are understood and their optimal values are chosen, one can apply the inversion technique for the analysis of the measured experimental data. In Chapter 7 and Chapter 8, these optimal values of the parameters will be used to calculate the magnetization of actual combinatorial samples.

6.2 Inversion technique for calculating in-plane magnetization

In this section, I will discuss how the parameters introduced in Sec. 6.1 will affect the calculation of the inversion technique for the in-plane magnetization. For this purpose, four different values of z will be considered throughout the calculation and analysis. In order to perform this analysis, I use a sample large enough (larger than z) so that the errors due to the small sample size can be avoided. In particular, I will address

the questions: how accurately can one obtain the magnetization when the position of the SQUID is far from the sample? How small can the sample be and one can still obtain accurate values of magnetization? To answer these questions, I will consider various sample sizes. These important questions are relevant to the limit of the utility of the scanning SQUID microscope to characterizing combinatorial samples.

For all of the discussion and optimizations of the parameters, I have used simulation data generated by a Labview program discussed in Chapter 5 (Figure 5.2). In Figure 6.4 (a), I define the sample configuration and dimensions. The distance between

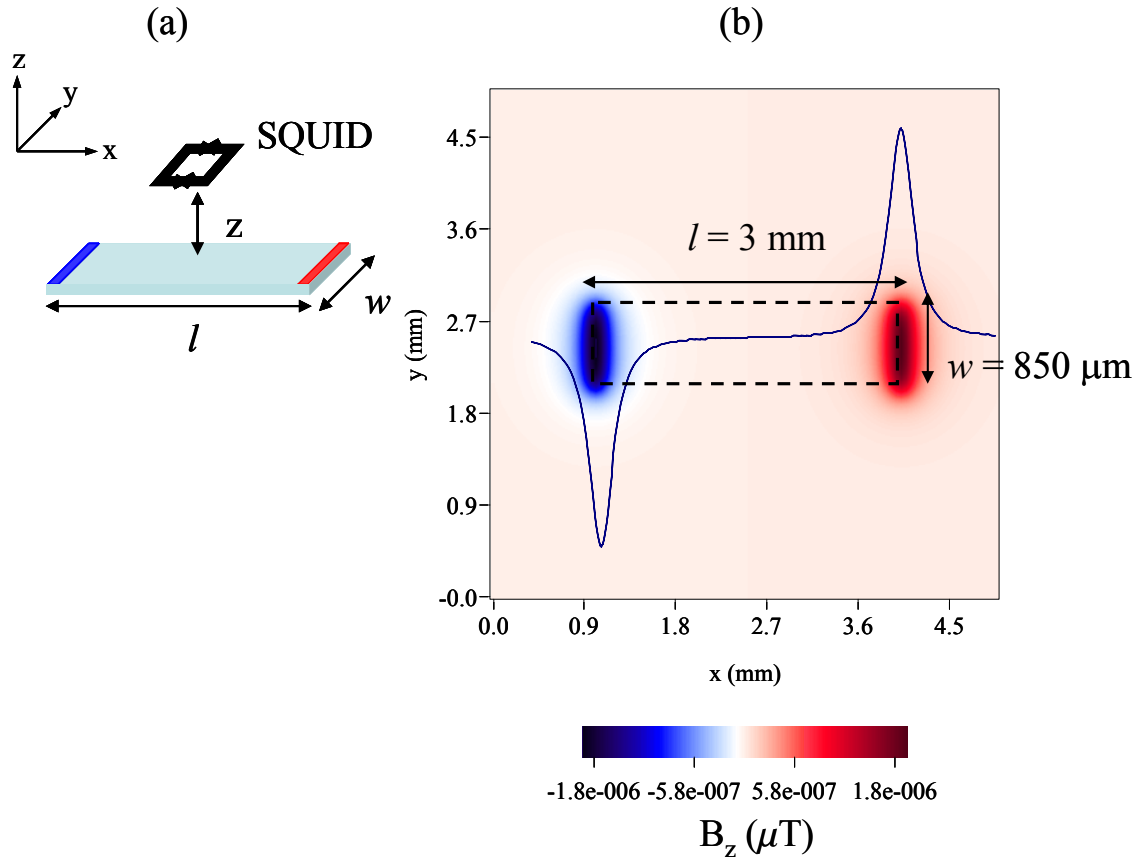


Figure 6.4 A simulation of a dipole of 3 mm (l) x 850 μm (w). (a) The schematic of the simulated data acquisition. The coordinate system shown here denotes the axis directions only. (b) Distribution of the magnetic field due to the in-plane magnetization of a simulated sample. The black dashed line denotes the sample dimensions.

the poles is l (which is parallel to magnetization direction), while the length perpendicular to the magnetization direction is defined as w . When I varied the dipole size, I changed the w dimension, keeping l constant. The scanning area used was always a square. For calculating the magnetization, the dimensions of the integration area is $L \times W$ (where the integration length L and width W are parallel to l and w of the sample, respectively, as shown in Figure 6.7 of Sec. 6.2.2). For the dependence of magnetization on k_w , scanning area, and the area of integration, I have used simulated data of a uniformly magnetized sample of 3 mm (l) \times 850 μm (w). The schematic of the sample and the simulated field distribution from the dipole are shown in Figure 6.4 (a) and (b).

6.2.1 k_w dependence

For the analysis of data on current carrying wires on chips, the relationship between spatial resolution and k_w was discussed in Ref. [4]. However, for the ρ_m analysis, the influence of k_w on the spatial resolution has not been studied. As k_w is increased, the spatial resolution is undoubtedly improved. However, it becomes more difficult to calculate magnetization, when the noise becomes more pronounced and dominates the signal. Therefore, there is a trade-off between the spatial resolution and the accuracy of the calculated value of magnetization. For our purpose of characterizing combinatorial libraries, it is actually more important to calculate magnetization accurately than to obtain the ultimate spatial resolution. This is because each individual sample in combinatorial libraries is typically much bigger than the spatial resolution of the scanning SQUID. It is the magnetization trend of the samples that we are most interested in. Keeping this in mind, I will determine what the limits for k_w are.

Initially I simulated data from the sample of 3 mm x 850 μm at four different z values (which are smaller than 850 μm , as mentioned below) by integrating Eq. 5.2 numerically to avoid an error associated with the sample size. To collect the magnetic field data for the analysis, I adopted a scanning area of 5 mm x 5 mm, which is large enough (about 10 times larger than the sample area) so that the error due to the limited scanning area may also be small and could be ignored. There were four sets of data generated, one for each z . The z values were 150 μm , 200 μm , 250 μm and 300 μm , which are smaller than the w (=850 μm) and l (=3 mm) of the sample. For all the simulations, the samples were in-plane magnetized along the l (=3 mm) direction with a given fixed M_{in} value of 5 emu/cc. The scanning step size of the simulation data was 50 μm in x and y , where x and y are the directions parallel to l and w , respectively.

For each simulated data at a given z value, I calculated ρ_m with k_w ranging from 1 to a value that makes the data look very noisy. Then I integrated ρ_m initially over a 50 μm strip in the middle of the sample to find the value of magnetization. Note that as we will see in the next section, this choice of the integration area provides reliable values for the magnetization when the distance z is smaller than the sample size (w). Based on the magnetization value calculated, I determined what the lower and upper boundaries are for k_w . Figure 6.5 shows the variation of ρ_m as k_w changes. One can see that as k_w gets larger and larger, more and more ripples are introduced in the data. I calculated M_{in} for each k_w and determined how far M_{in} deviated from the given M_{in} value. In the inset the black square denotes the result with the upper bound k_w value of 11 that I used for the case of $z = 150 \mu\text{m}$. Next, I performed the same calculations for the other z values.

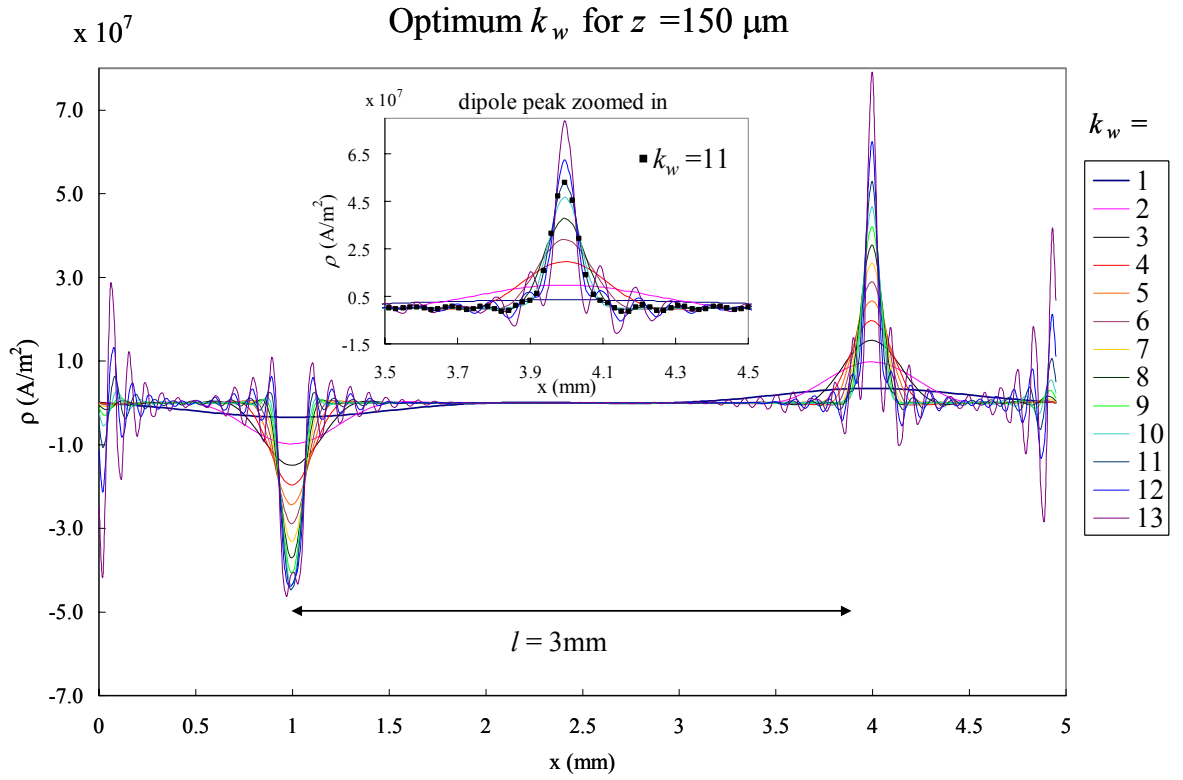


Figure 6.5 ρ_m dependence on the k_w value for the simulated data ($z = 150 \mu\text{m}$).

Figure 6.6 shows the optimum k_w range for the 4 z values. Here I plot k_w as a function of $1/z$, since dimensionally k_w and $1/z$ are the same, and one would expect that k_w should decrease as z increases. From this plot, one can see that the further the sample is from the SQUID sensor, the narrower the range of the k_w values that one can choose is. This makes sense, because when z increases, the magnetic field at a distance z becomes broad and remains significant outside the scanning area. Thus, cutting the magnetic field outside the scanning area causes enhanced sensitivity to the cut-off frequency, k_w . In real experiments, this can cause a further problem due to the noise in the data, which may dominate the magnetic field data for large z . In addition, if one looks at the upper bound

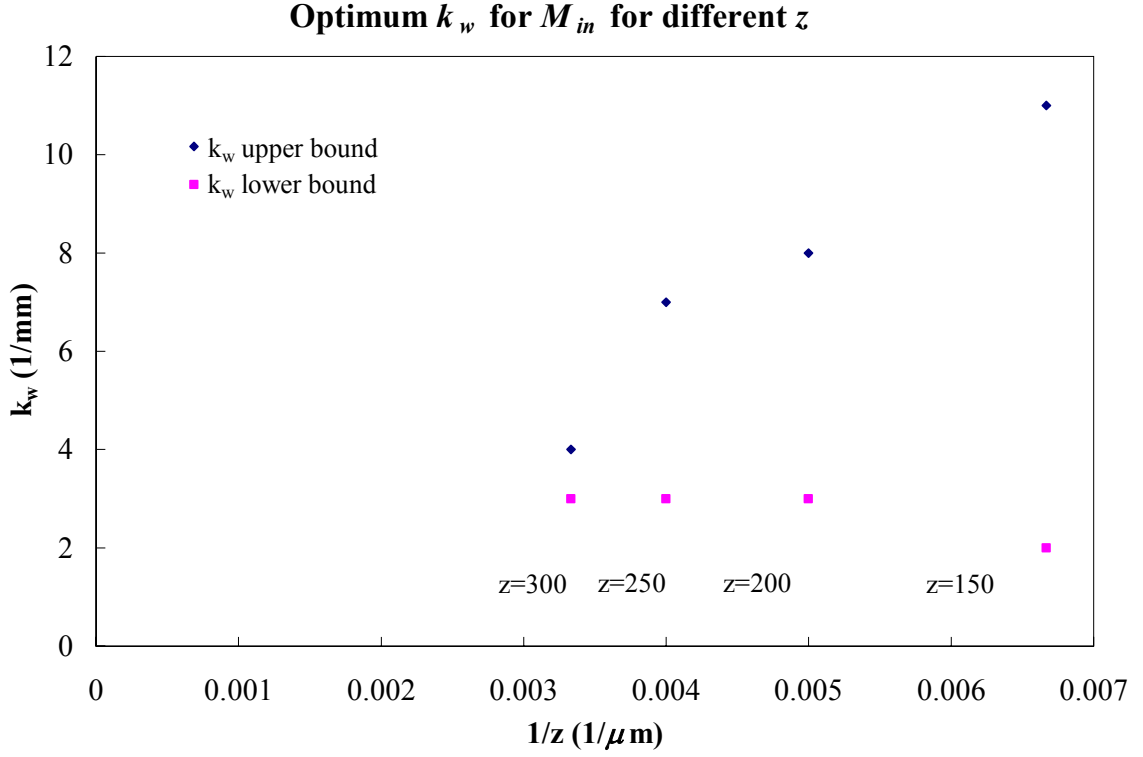


Figure 6.6 Optimum k_w range for in-plane magnetization as a function of $1/z$.

curve, one can see that the relationship between k_w and $1/z$ appears to have an almost linear relationship. One might expect the linear relationship from the inversion equation for the density given in Eq. 6.1, since the exponential factor in the Green's function contains kz and as z increases k_w should decrease inversely with z to prevent the amplitudes of high wave vectors (near k_w) from growing exponentially. Note that the other parameters such as the scanning area or the size of the sample may also influence the optimum value of k_w .

6.2.2 Dependence on integration area

To calculate magnetization of the sample from a magnetic pole density ρ_m , one needs to integrate it (multiplied by the r vector) over a certain area as seen in Eq. 6.3. To study how the integration area influences the value of magnetization, I used simulated data of the 3 mm x 850 μm sized sample ($l = 3 \text{ mm} \times w = 850 \mu\text{m}$), with a scanning area of 5 mm x 5 mm with an assigned $M_{in} = 5 \text{ emu/cc}$, at $z = 150 \mu\text{m}$. Once ρ_m is obtained via the inversion technique by using optimal k_w values (Sec. 6.2.1), I integrated it over different integration area $L \times W$, as shown in Figure 6.7. First, I will discuss the dependence of M_{in} on the integration length L while keeping W constant, equal to 50 μm . Then the dependence of M_{in} on W is discussed.

6.2.2.1 Varying integration length along magnetization direction

In order to understand the dependence of the magnetization on the integration length L , I first fixed the integration width $W = 50 \mu\text{m}$ and varied the integration length L from 2.9 mm (slightly less than the sample length $l = 3 \text{ mm}$) to 5 mm (which is the scanning length). As was shown earlier, in Figure 6.2, and Sec. 6.1, the reason why I used a strip of $W = 50 \mu\text{m}$ (in the y direction) and not the entire sample is that for the combinatorial sample of spatially varying magnetization, I need to divide the sample into strips and then calculate M_{in} for each strip that I select. The example of this will be discussed in Chapter 8.

The result of the calculations is shown in Figure 6.8. Here, one can see first that the integration length L must be at least larger than 1.1 times the sample length l .

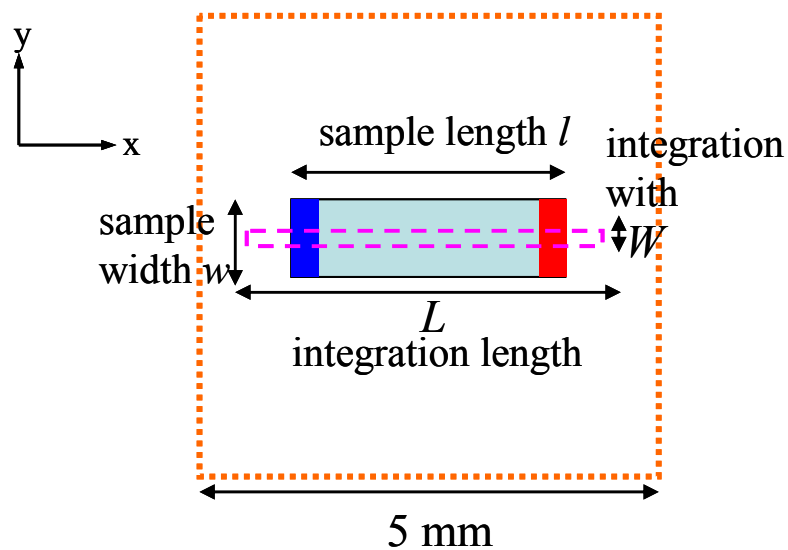


Figure 6.7 The sample dimensions are $3\text{ mm} \times 850\text{ }\mu\text{m}$, and the scanning area is $5\text{ mm} \times 5\text{ mm}$ (orange dotted line). The integration area is $L \times W$ (purple dashed line).

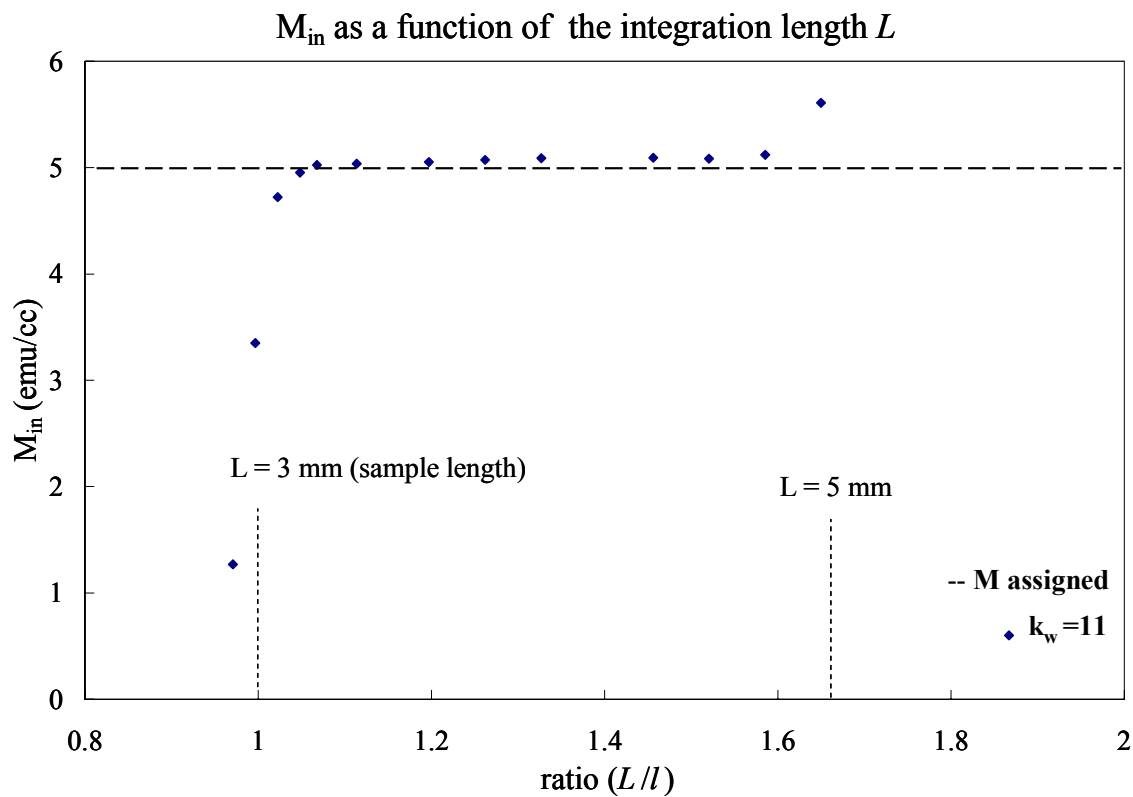


Figure 6.8 The behavior of M_{in} as a function of the ratio of integration length L over the sample.

On the other hand, if one chooses L equal to the total scanning length of 5 mm to integrate over, the calculated magnetization deviates from the given value due to the noise at or near the edges of the scanning area. Thus, one must choose the integration area, which includes at most the scanning length minus $\sim 300 \mu\text{m}$.

6.2.2.2 Varying the dipole width w

In the present analysis, the sample width w ($=850 \mu\text{m}$) and length l ($=3 \text{ mm}$) are larger than the distance z between the sample and the scanning position. It was found that in this case, the calculated value for M_{in} is insensitive to the integration width W . It is due to the fact that the magnetic pole density ρ_m is almost flat inside the sample along the W direction perpendicular to the magnetization direction. It is then interesting to see how the sample size (especially, the width w) affects the proper choice of integration width W . This issue is important for calculating magnetization of composition spread samples.

To this end, I simulated different sample sizes at the same distance $z = 150 \mu\text{m}$. In particular, I varied the sample width w from $50 \mu\text{m}$ to $450 \mu\text{m}$ with $50 \mu\text{m}$ interval (but keeping the sample length l at 3 mm). I then integrated the density ρ_m over the area of $L = 4 \text{ mm} \times W = 50 \mu\text{m}$. The value of M_{in} as a function of the sample width w is plotted in Figure 6.9. As one can see in this figure, when the sample width w is smaller than the z value (in this case $z = 150 \mu\text{m}$), M_{in} is substantially reduced (blue squares). This is because in the sample with smaller w , the variation in ρ_m amplitude (along the w direction) is so large that it is difficult to get an accurate answer while integrating a small

strip. Depending on where the strip is chosen on the sample, the value of M_{in} is different.

In order to obtain an accurate M_{in} value, one then needs to choose an integration area,

M_{in} dependence on sample width for $z = 150 \mu\text{m}$

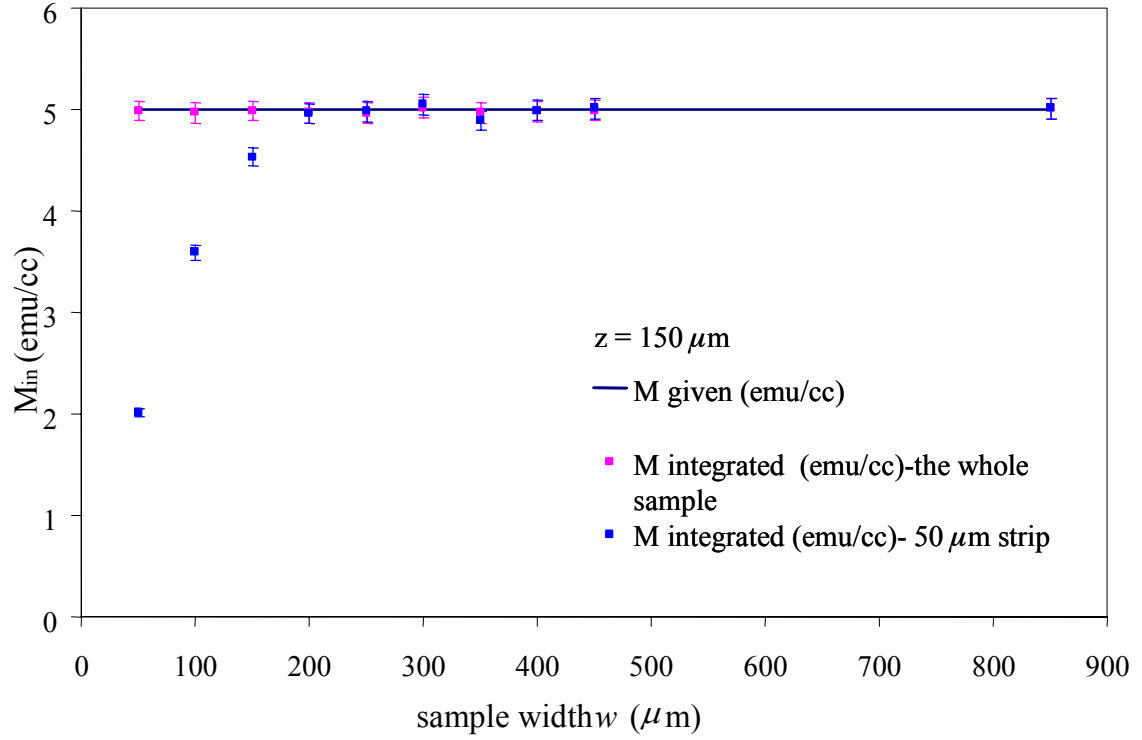


Figure 6.9 The dependence of calculated M_{in} on the dipole width w for $z = 150 \mu\text{m}$ when $50 \mu\text{m}$ strip or the whole sample is selected for integration.

which includes the whole sample (but less than the scanning area as discussed above). This data is plotted in Figure 6.9 as purple squares. On the other hand, when the sample width w is larger than the distance z , one can obtain magnetization accurately, although the width of integration W is $50 \mu\text{m}$. Thus, one has to keep in mind that another restriction for the integration area is that if the sample is smaller than z in the w dimension, one needs to integrate ρ over the entire sample.

From the above analysis, one can conclude that when the magnetization varies slowly in the range smaller than the scanning distance z , it is safe to use the integration width smaller than the sample width, e.g., $50\ \mu\text{m}$, for calculating the magnetization. Since the scanning step size is $50\ \mu\text{m}$, the least possible width of the strip that I can chose is $50\ \mu\text{m}$. On the other hand, when the magnetization varies rapidly over the same range, integrating over a $50\ \mu\text{m}$ width yields a substantial error in the calculated value of magnetization. Thus, for the analysis of the combinatorial samples, it is important that the magnetization changes gradually in the integration space.

6.2.3 z and scanning area dependence

Finally, in this section I consider the dependence on the parameter z , which is the distance between the SQUID sensor and the sample and the scanning area. One should notice from Eq. 6.1, that z enters the exponent of the Fourier transform of the Green's function. Thus, even a small error in z may amplify the error in the final results.

One may naively think that as the value of z becomes larger, the minimum size of the sample that can be resolved while obtaining an accurate value of M_{in} increases. This would imply that for a sample size smaller than the z value, magnetization would have a large error. To look at this issue closely, I performed simulations with different sample sizes. I fixed $l = 3\ \text{mm}$ and varied w from $50\ \mu\text{m}$ to $4\ \text{mm}$ with in-plane magnetization of $5\ \text{emu/cc}$, and the scan step size of $50\ \mu\text{m}$ in x and in y . Note, again, that x and y are directions along the sample length l and width w , respectively. In the simulations, four different values of z , namely, $150\ \mu\text{m}$, $200\ \mu\text{m}$, $250\ \mu\text{m}$ and $300\ \mu\text{m}$, are used.

In Sec. 6.2.2, it was found that when the sample was simulated at $z = 150 \mu\text{m}$, the magnetization value could be obtained accurately even for a relatively small sample width w ($< 150 \mu\text{m}$) with the scanning area of $5 \text{ mm} \times 5 \text{ mm}$. Notice, however, that when the sample width w was smaller than the distance z , the magnetization was sensitive to the selection of the integration area. In fact, to get the accurate magnetization for w smaller than z , it was necessary to choose the integration area larger than the sample area. Now when z is much larger than w , say 10 times or more, the peaks of the magnetic field broaden; scanning the same area as above will have an error in the calculated magnetization. It is then important to establish how large the scanning area must be for such a large distance z to calculate M_{in} accurately.

Before I discuss this issue, I turn to how the magnetization will vary with the dipole width w for different z . Figure 6.10 shows the M_{in} dependence on the dipole width w for four different z values. The error associated with the calculation was roughly 2% of the given value of 5 emu/cc . Note that in calculating M_{in} , I chose the integration area larger than the sample to avoid any error due to the integration area, especially for w smaller than z . Here it is obvious that M_{in} does not depend on the dipole width w . I stress here that for all the simulations a fixed scanning area of $5 \text{ mm} \times 5 \text{ mm}$ was adopted.

Now I consider the question addressed above, namely, how large the scanning area must be to accurately calculate the magnetization, when z increases. From Eq. 5.2 of Chapter 5, one can see that when the magnetization is along the l direction (i.e., $m_y = 0$), which is the case in this simulation, the magnetic field decays as $1/x^4$ along the x direction, while it decays as $1/y^5$ along the y direction (perpendicular to the magnetization): the field decays more slowly along the magnetization direction.

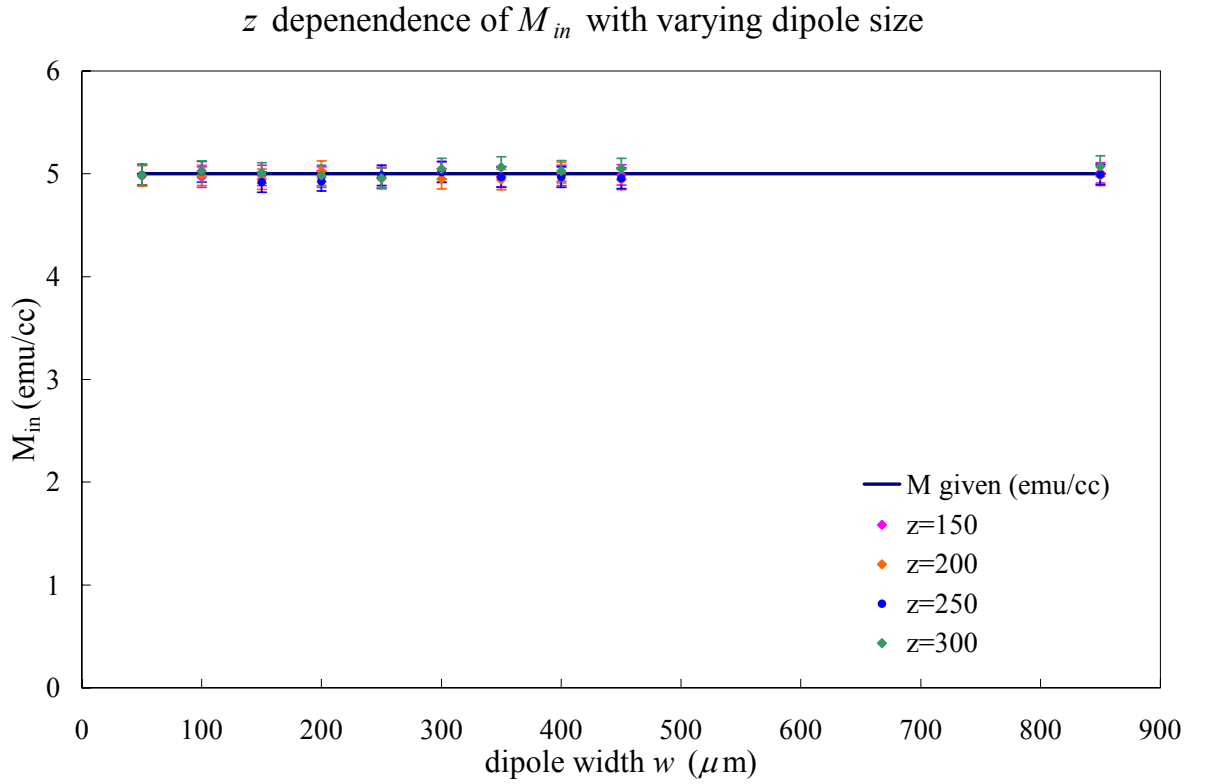


Figure 6.10 The dependence of calculated M on the dipole width w for four different z values.

Therefore, the ratio of the scanning length to the sample length parallel to the magnetization direction will be more important in selecting the scanning area in order to obtain accurate value of the in-plane magnetization. In order to obtain an accurate value for M_{in} it is crucial to have the scanning length at least 1.2 times larger than the sample length, when z is of the same order as the sample width w , as shown in Appendix E. It is also observed in Appendix E that when the ratio of the scanning length to the sample length is smaller than 1.2, the calculated M_{in} becomes sensitive to the choice of k_w . However, it is found (not shown) that when z is very large, even on the order of millimeters (much larger than the sample size), the scanning area plays an important role.

To obtain the accurate magnetization in such a case, it is then important to scan a large enough area of each side length at least five times larger than z to include all the variation in B_z . Only then, there will be no problem of the spatial resolution.

The calculated M value always remain the same, no matter how far one scans and no matter how small the size of the sample is, as long as one chooses an appropriate k_w , scanning area and the integration area. In practice, it is often not possible to satisfy all the requirements, and certainly, there is noise in the experimental data. In addition, it is good to scan with the SQUID sample distance z as small as possible.

6.3 Inversion technique for calculating the out-of-plane magnetization

The inversion technique is also applied for calculating the out-of-plane magnetization. As in the case of in-plane magnetization, there are parameters that influence the results of the inversion technique. As for the in-plane magnetization, they are the distance, z , between the SQUID sensor and the sample, the cut-off frequency, k_w , the scanning area, and the integration area to obtain the magnetization. For the out-of-plane magnetization calculation, the Hanning window is also used.

First I will consider the cut-off frequency k_w and optimize it for each value of z . There are four values of z considered as in the in-plane case. With the optimized k_w , I will consider samples of different sizes and find how the out-of-plane magnetization changes with z . Then I will use a sample large enough to find the dependence of magnetization on a selected integration area. After this I will show how M_z varies with the scanning area for a given sample size for each z value. As in the in-plane case, simulation is performed to generate the data for B_z and to optimize all the parameters.

The dipole and the scanning area were square; therefore, for varying the dipole size, I changed both the length and the width of the sample. For the k_w , scanning area, and the area of selection dependence, I will use simulated data of a sample of 1 mm x 1 mm, which is shown in Figure 6.11.

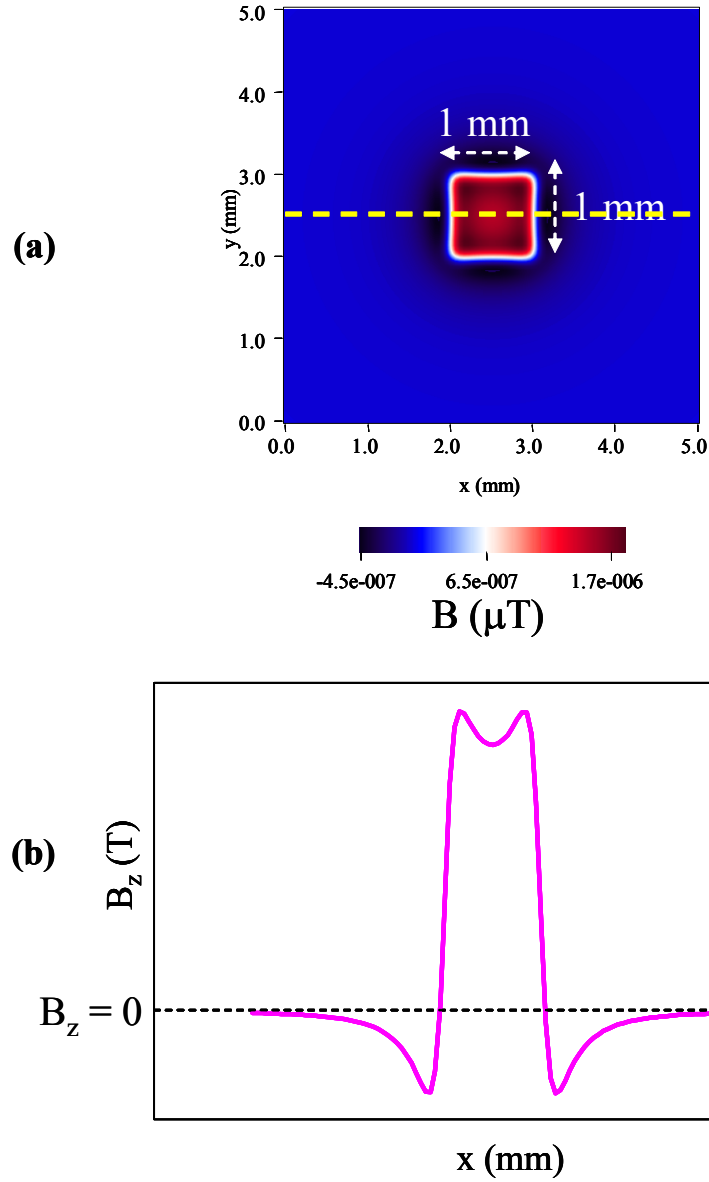


Figure 6.11 Simulation of an out-of-plane magnetized dipole of 1 mm x 1 mm. (a) Two dimensional image of B_z . (b) Magnetic field along the yellow dashed line in (a) as a function of x .

6.3.1 k_w dependence

To find the limits of k_w , I simulated a sample of 1 mm x 1 mm, which is larger than the scanning distance z (Figure 6.11), by integrating Eq. 5.3 (as explained in Chapter 5) with a scanning area of 5 mm x 5 mm, which is large enough to avoid error associated with the sample size and the scanning area. There are four sets of data generated, one for each z . For all the simulations, the samples are out-of-plane magnetized with the M_z value of 5 emu/cc. The scanning step size of the simulation data is 50 μm in the x and y directions.

For each simulated data at a given z value, I calculate ρ_m with k_w ranging from 1 to a value that makes the data look very noisy and the sample boundary is no longer visible.

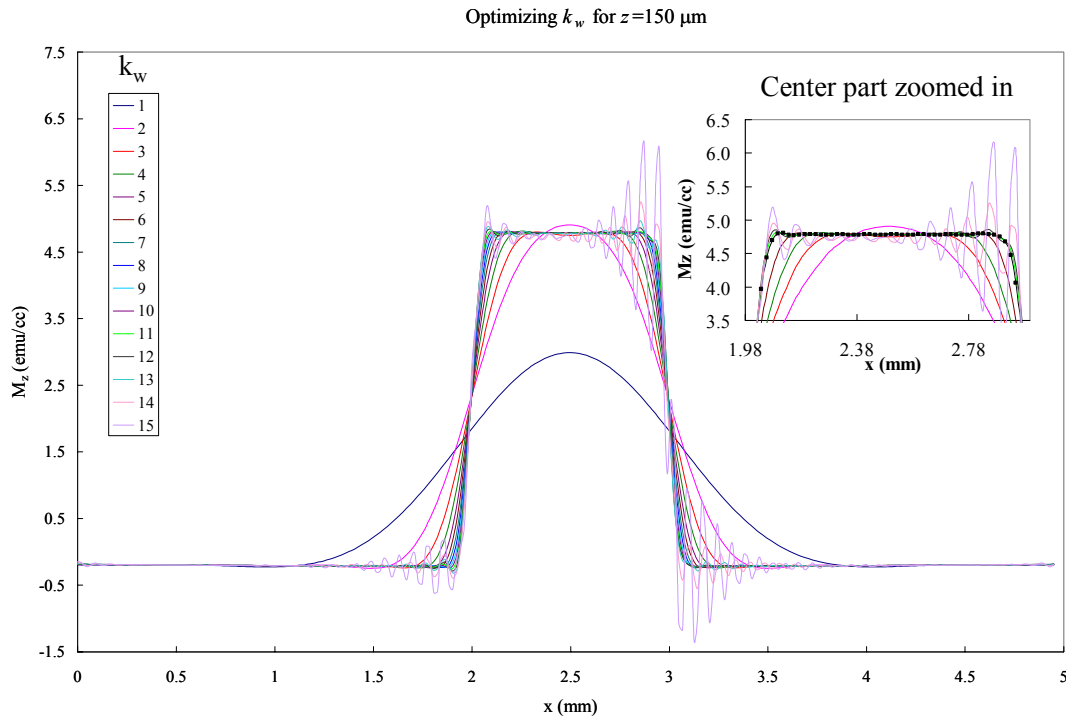


Figure 6.12 M_z dependence on the k_w value for the simulated data ($z = 150 \mu\text{m}$).

Figure 6.12 shows the optimization of k_w for $z = 150 \mu\text{m}$. Here one can see that when k_w is very small or very large, the sample shape is not well reproduced. For the small values, the data do not give the correct shape and for the large values, there is noise associated with large k -oscillations. Therefore, it is important to pick a k_w value such that these problems are not present. For upper k_w , I picked the value before the data become noisy, as seen in

Figure 6.12, and for the lower k_w , I picked the value when the shape of the magnetization curve matched the sample dimensions closely enough. The inset shows the zoomed-in central region of the plot, and the line with the black squares denotes the upper bound value of $k_w = 10$, that I used for $z = 150 \mu\text{m}$. To find the out-of-plane magnetization I integrated the data over an area inside the sample, since the magnetization starts to decay inside the sample as shown in

Figure 6.12

Figure 6.13 shows the optimum k_w range for calculating the out-of-plane magnetization as a function of $1/z$. One can see that for z values of $200 \mu\text{m}$, $250 \mu\text{m}$ and $300 \mu\text{m}$ both upper and lower bounds of optimum k_w values appear to increase linearly with $1/z$. Similar to the in-plane case, $1/z$ and k_w have a linear relationship. A reason may be that when z changes, k_w must be adjusted so that the exponential factor of the Green's function k^*z , remains constant. On the other hand, when z approaches $150 \mu\text{m}$ and smaller, optimum k_w values are no longer determined by z alone. In this region, the optimum k_w value shows a saturated behavior. Note that in this region other parameters such as the scanning step size and the sample size affect the calculations.

6.3.2 Integration area and z dependence

Unlike in the in-plane magnetization case, in order to calculate the out-of-plane magnetization M_z one must average ρ_m over a certain area, instead of integrating the

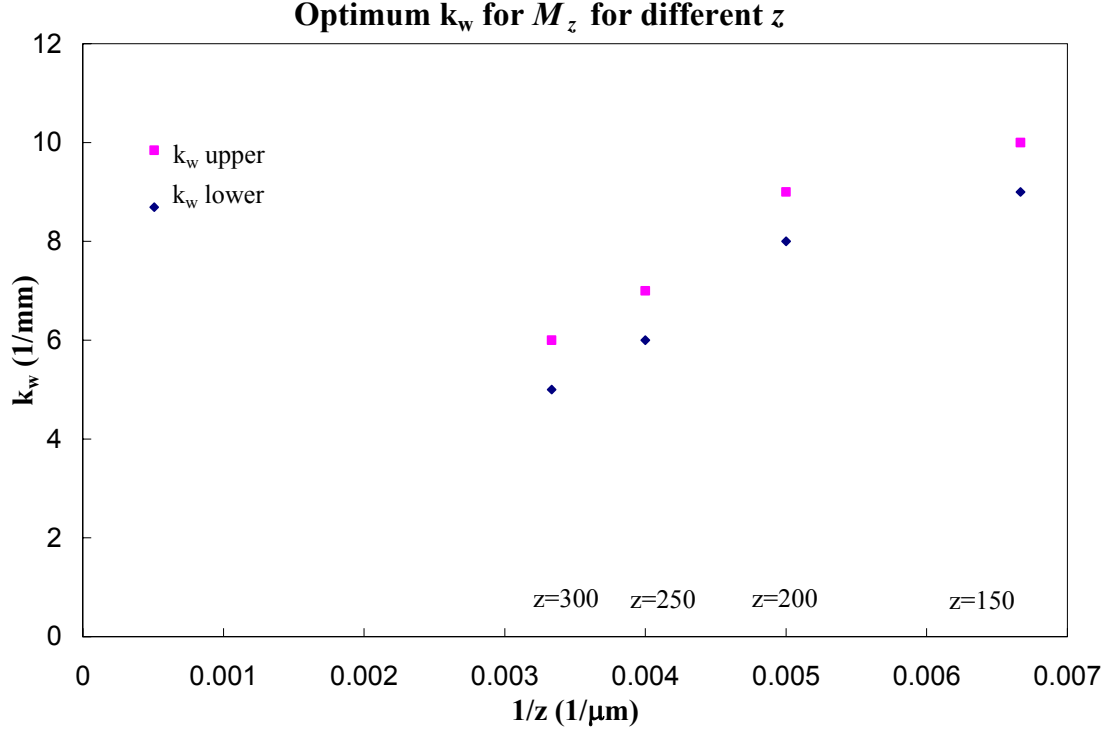


Figure 6.13 Optimum k_w range for the out-of-plane magnetization calculation as a function of $1/z$.

density multiplied by the r vector (Appendix C.4). Therefore, there is not much dependence of M_z on the area of integration, except for the fact that one must select the area well inside the sample, and not include the edges of the sample (

Figure 6.12). If one includes the edges, then the decreasing values along the edges will be included in the calculation and will decrease the total magnetization value.

It was observed that there is no z dependence of the out-of-plane magnetization when the ratio of the scanning area to the sample area is large enough, as presented in the

next section. With a proper k_w and the proper area of integration there was no apparent z variation of M_z for the samples that are out-of-plane magnetized. However, when the ratio of the scanning area to the sample size approaches 1, then z becomes an important factor in determining the M_z . This is discussed in the next section.

6.3.3 Scanning area dependence

For the in-plane magnetization case, to see the scanning area dependence I varied the scanning area and took the ratio of scanning length to the sample length, and examined the dependence of M_{in} on this ratio (Sec. 6.2.3). For the out-of-plane magnetization, the magnetic field decays in the same rate along both the x and y directions unlike in the in-plane magnetization case. Since there is no preferred in-plane direction for the out-of-plane magnetized sample, I will use the ratio of the scanning area to the sample area.

Now to see what happens with the out-of-plane magnetization I performed the same calculation. I simulated five samples (the dimensions are the same as the experimental samples, described below), with the same scanning area of 7 mm x 7 mm, with $M_z = 5$ emu/cc and calculated their out-of-plane magnetization. I plot the calculated M_z using the inversion technique and the current loop model for the simulated data vs the ratio of the scanning area to sample area in Figure 6.14. Note again that the out-of-plane magnetization is obtained by integrating the density inside the sample. The current loop model yields results with excellent agreement to the given M_z , while the inversion technique gives a much larger deviations from the given M_z value even for the large ratio (>10). One might then ask: where do such large deviations come from?

To observe this experimentally, I scanned different sample sizes with the same scanning area. There were 5 sample sizes of single composition CoFe_2O_4 thin films (first

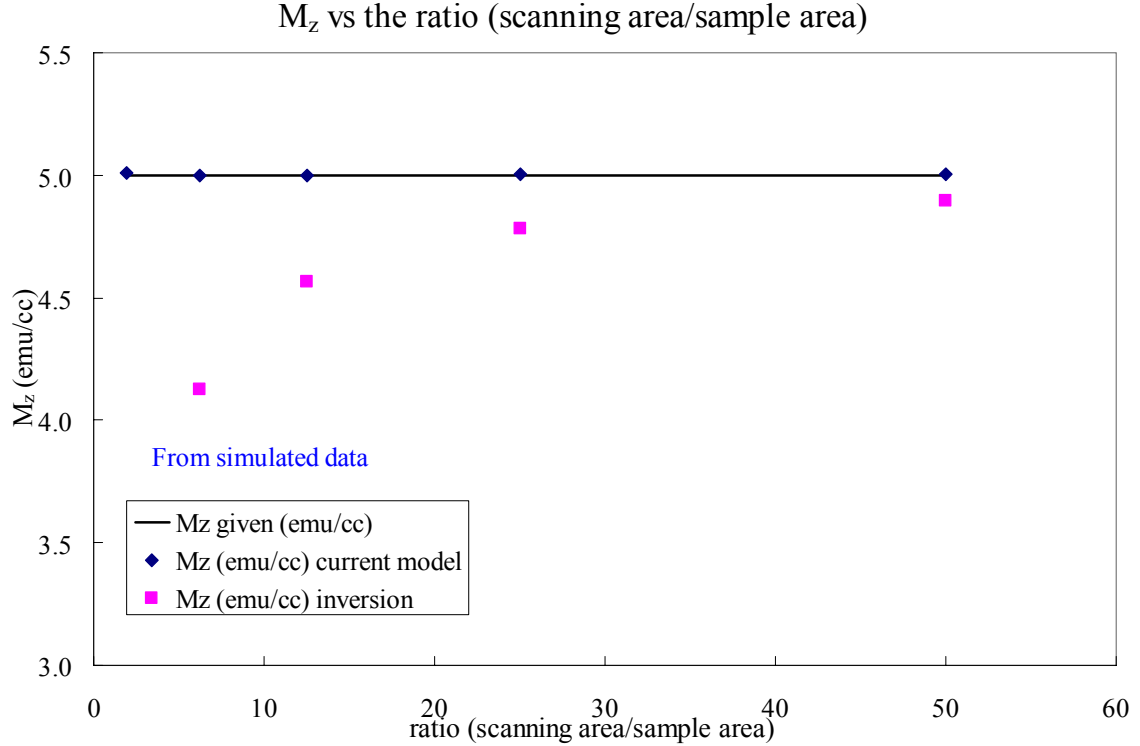


Figure 6.14 M_z calculated from the current loop model, inversion and the given value dependence on the ratio of scanning area to sample area from the simulated data.

introduced in Chapter 5) of 2 mm x 0.3 mm, 0.6 mm, 1.2 mm, 2 mm, and 5 mm x 5 mm. All the samples, shown in Figure 6.15, were made of the same material, uniformly magnetized with 3T magnetic field, and scanned using the scanning SQUID microscope with the scanning area of 6.5 mm x 6.5 mm and the scanning step size of 50 μm in the x and y directions at a z distance of 150 μm . I will refer to this data throughout this section. When I calculated M_z , it varied just as in the simulated data as the ratio of the scanning area to the sample area approached unity. The values of M_z calculated from the inversion

technique were smaller than those obtained from the current loop model. This is shown in Figure 6.16. The result is consistent with the simulation analysis.

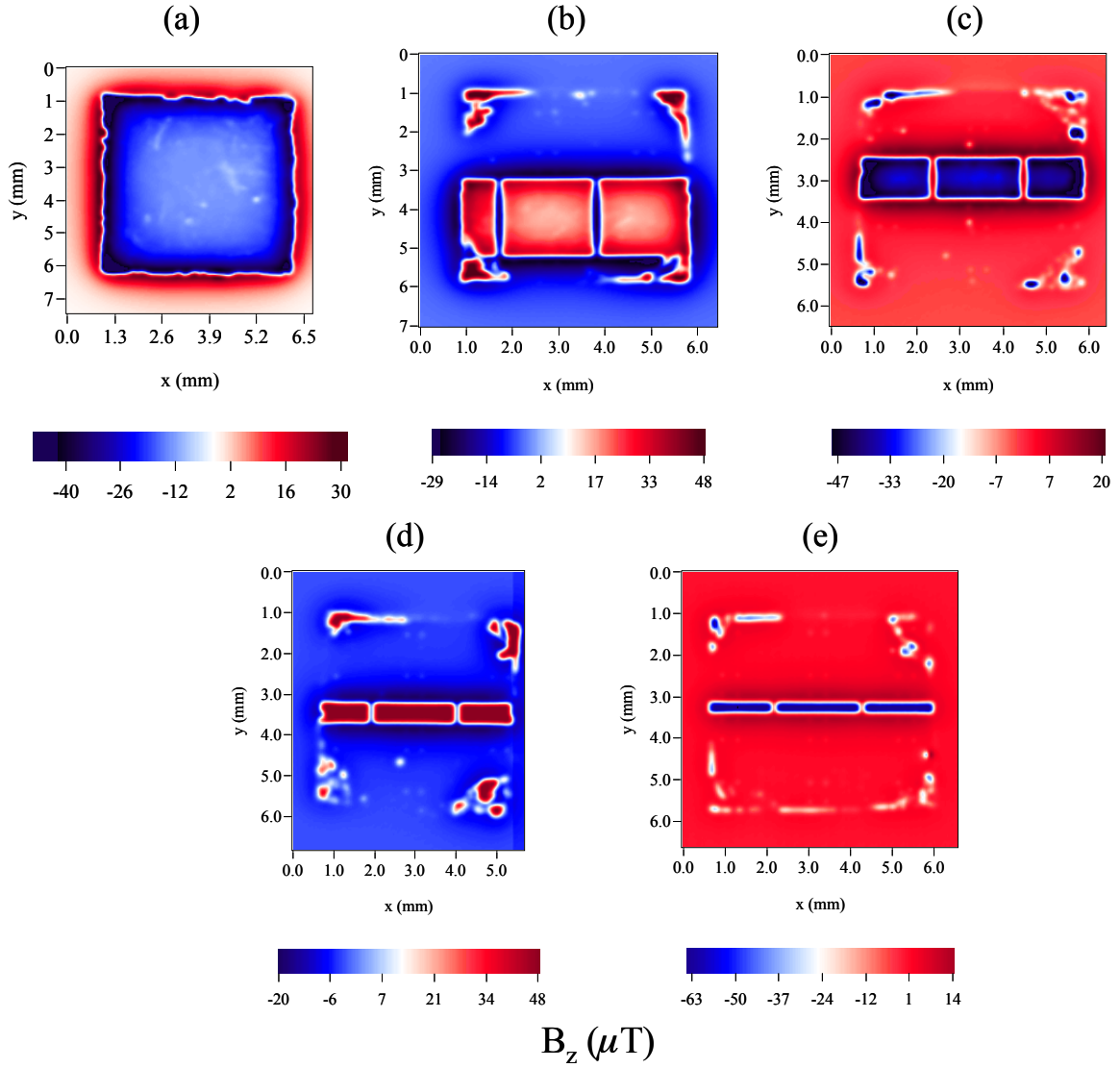


Figure 6.15 5 out-of-plane magnetized samples of single composition CoFe_2O_4 thin films of 5 mm x 5 mm (a) 2 mm x 2 mm (b), 1.2 mm (c), 0.6 mm (d), 0.3 mm (e) that were measured using the scanning SQUID microscope. For each sample, two dimensional image of B_z is shown.

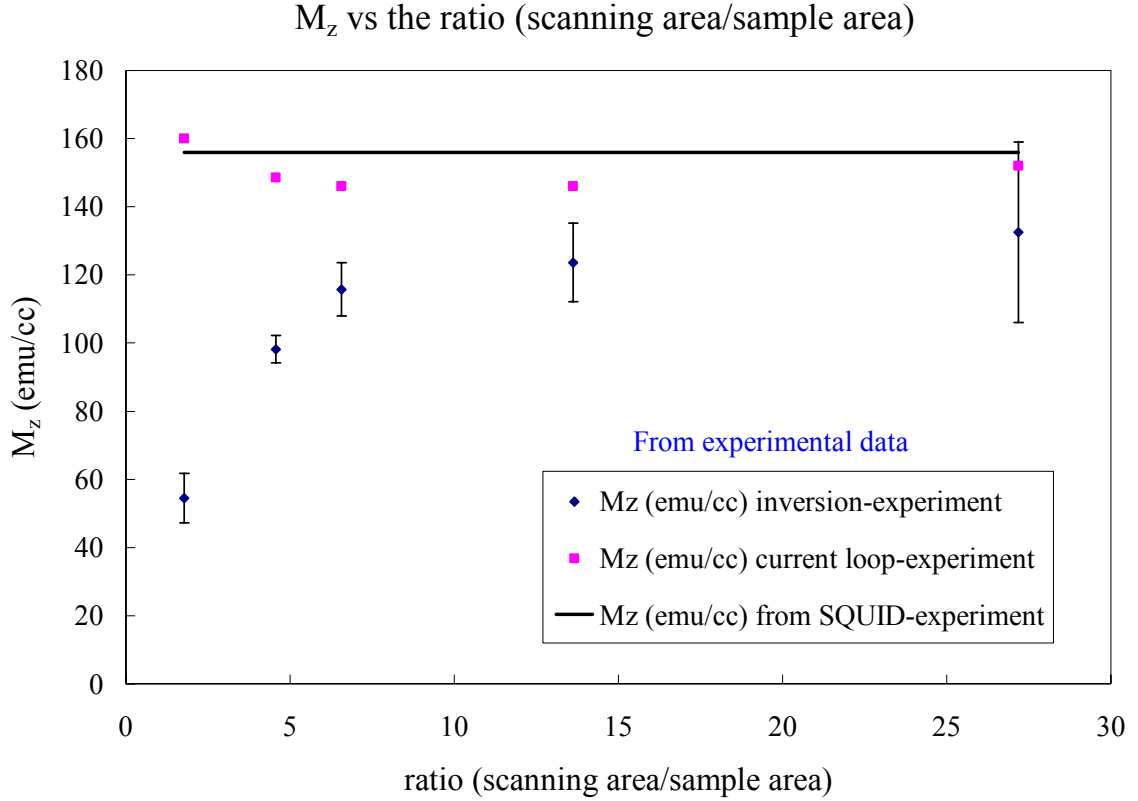


Figure 6.16 M_z calculated using the inversion technique, the current loop model and from the SQUID magnetometer as a function of the ratio of scanning area to sample area from the experimental data.

Now to understand what causes such deviations/errors in calculating the out-of-plane magnetization from the inversion technique and possibly to find a way to improve the calculations, I looked at the data closely, especially for the sample whose area is not much larger than the scanning area. I found that the area outside the sample has a large M_z value of an opposite sign after the inversion technique is applied. Figure 6.17 shows a two dimensional M_z image of the simulated and experimental 2 mm x 2 mm sample. Also it shows the line scan in the region along the yellow dotted line. Figure 6.17 clearly indicates that when the inversion technique is used, an artificial magnetization of

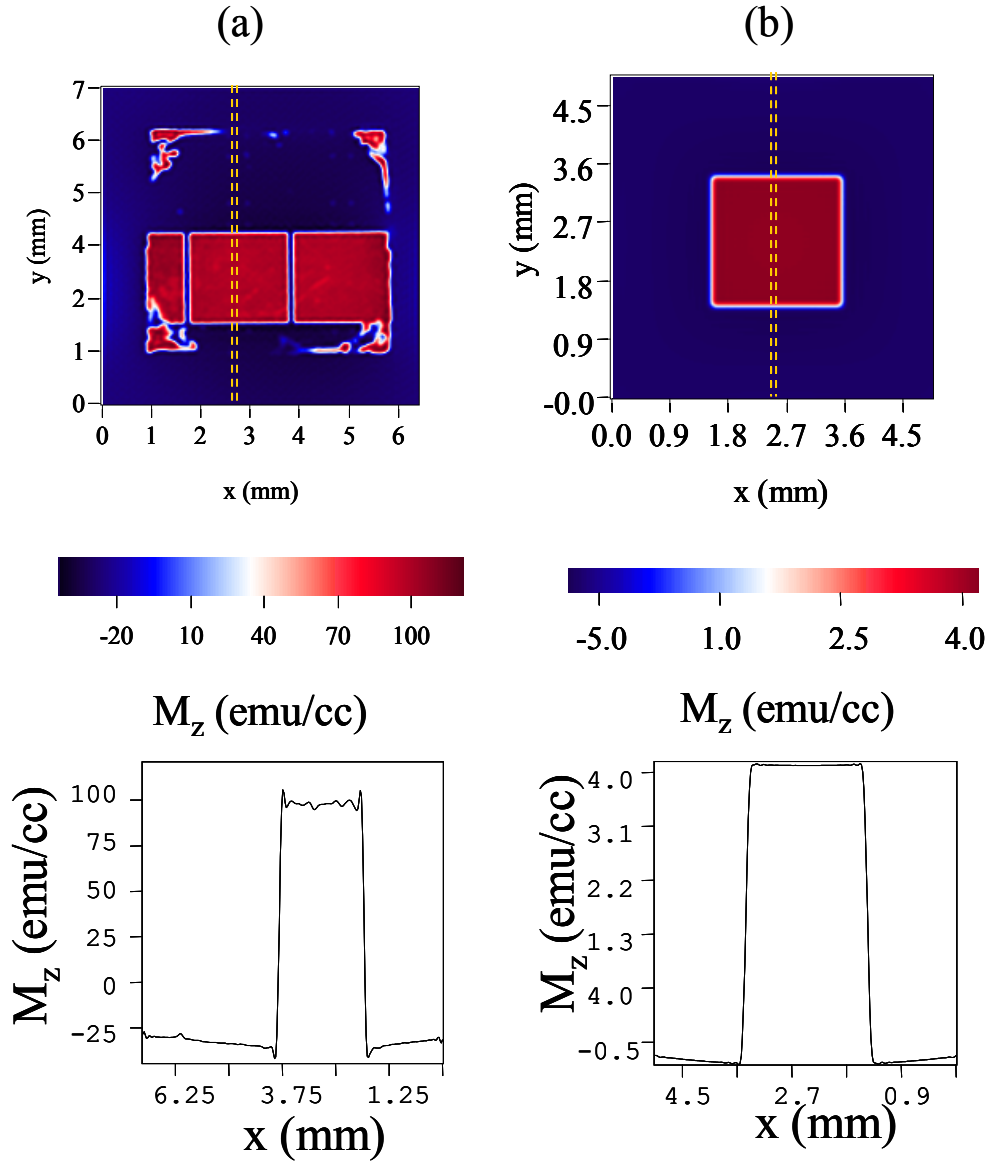


Figure 6.17 For both (a) and (b), the top images are two dimensional magnetization distributions, and the bottom are plots of M_z vs position on the chip taken along the yellow dotted line from the top images. An artificial magnetization generated on the outside of the sample of opposite sign is seen here. In (a) experimental data of the sample 2 mm x 2 mm is shown, in (b) simulated data, as discussed in the text.

opposite sign is generated outside the sample. This happens when the scanning area is small compared to the sample area. Because the field from the sample does not decay

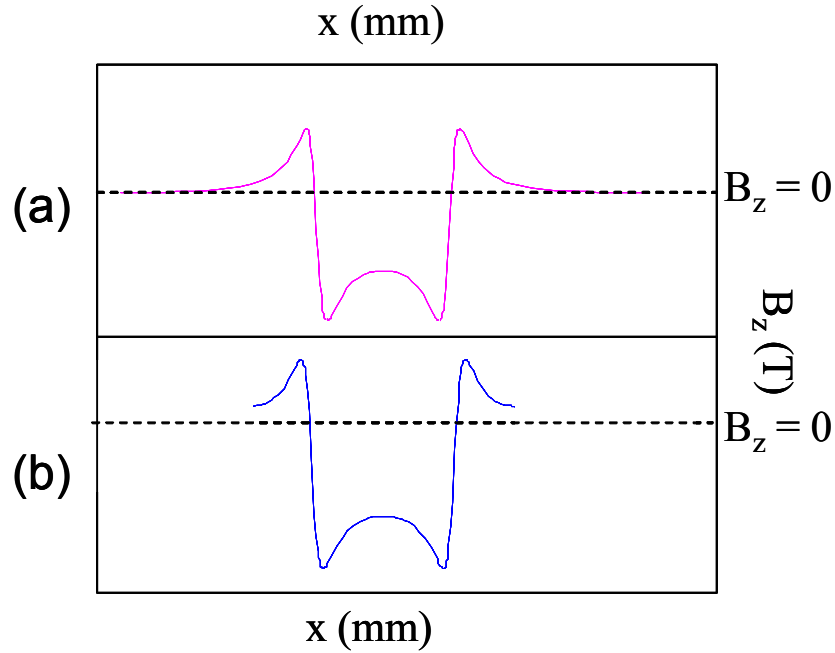


Figure 6.18 A scan line of B_z of a out-of-plane magnetized sample. When the scanning area (a) is at least 5 times (we will see where this 5 comes from, not drawn to scale) the sample area, the field is seen to decay to 0. (b) When the scanning area is smaller than in (a), part of the data is missing: B did not fully decay to 0.

enough at the edge of the scanning area, such an artificial magnetization may be generated by the magnetic field cutoff outside the scanning area. In chapter 5, Figure 5.13, I showed the field distribution of out-of-plane magnetized CFO thin film of size 5 mm x 5 mm. One can see that outside the sample, the field is not zero. The scan line of B_z across the sample for two scanning areas is shown in Figure 6.18 (a) when the scanning area is large enough, and (b) when the field did not decay to zero because of insufficient scanning area. Therefore, in order to obtain an accurate M_z value of the sample, one must consider the magnetization outside the sample.

To understand why the inversion technique produces an artificial magnetization outside the sample, why it gives a lower value for the magnetization inside the sample,

and how to obtain the correct value of magnetization of the sample, let us consider an adjusted current loop model as shown in Figure 6.19 (a). In this figure, magnetization distribution obtained from the inversion technique is drawn schematically. The technique yields a value M_{z1} for the magnetization inside the sample, while it gives magnetization $-M_{z2}$ for outside the sample. This is equivalent to the sum of magnetization $M_{z1}+M_{z2}$ inside the sample and $-M_{z2}$ inside the scanning area as seen in Figure 6.19 (a).

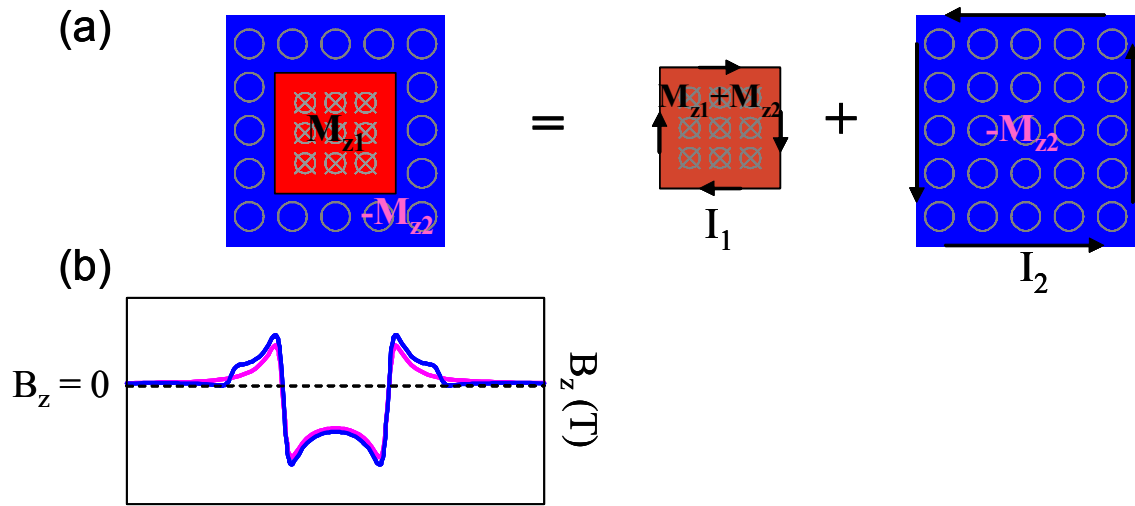


Figure 6.19 (a) Adjusted current loop model is used, when the scanning area is not large enough for B_z to completely decay. (b) Comparison of the B field scan line from the first current loop model when the scanning area is sufficiently large (purple). The adjusted model is used when the scanning area is not large enough (blue).

Now I will show that $M_{z1}+M_{z2}$ is the actual magnetization inside the sample which produces the actual magnetic field as shown in Figure 6.18 (b), namely the magnetic field which is cut off at the edges of the scanning area. In order to calculate the magnetic field due to the magnetization distribution in Figure 6.19 (a), one can break it down into two current loops surrounding the sample and the scanning area, flowing in the opposite direction. The currents I_1 and I_2 are given by $I_1 = (M_{z1}+M_{z2})d$ and $I_2 = M_{z2}d$, where d is the sample thickness. The magnetic field B_z outside the scanning area

produced by I_2 then has the opposite sign to the B field due to the current I_1 . Thus, proper magnitudes for I_1 and I_2 cancel the field outside the sample as shown schematically in Figure 6.19 (b). In addition to this, inside the sample, the dominant contribution to the magnetic field comes from I_1 , since the magnetic field due to I_2 decays very rapidly inside the sample. Therefore, the magnetic field observed in the sample is produced by the magnetization $M_{z1}+M_{z2}$. Thus, when calculating the out-of-plane magnetization using the inversion technique, the magnitudes of M_{z1} and M_{z2} should be added to improve the accuracy.

Now I repeated the calculation of M_z for the samples that I simulated and the samples that I scanned using the inversion technique, keeping in mind the above mentioned points about the area of integration and the scanning area with M_{z1} and M_{z2} added. Figure 6.20 shows the result of this calculation. Here in order to plot the experimental data and the simulated data on the same scale, I normalized M_z values to their respective maximum. Now we can see that the M_z does not change very drastically when the ratio of the scanning area to the sample area is varied. Notice that there is a deviation and a bent feature that is seen when the ratio of scanning area to the sample area is around 5. To understand this, we return to the adjusted current loop model. As the scanning area decreases and approaches the sample area, it is clear that the current I_2 or M_{z2} should increase in order to cancel the magnetic field outside the scanning area. In addition, I_2 will affect the total magnetic field substantially inside the sample, and thus reduce I_1 or $M_{z1}+M_{z2}$ in order to match the given magnetic field data. Because of this, one can see a general trend of decreasing magnetization M_{z1} as shown in Figure 6.14 and Figure 6.16, and of $M_{z1} + M_{z2}$ as shown in Figure 6.20. Therefore, one must use a

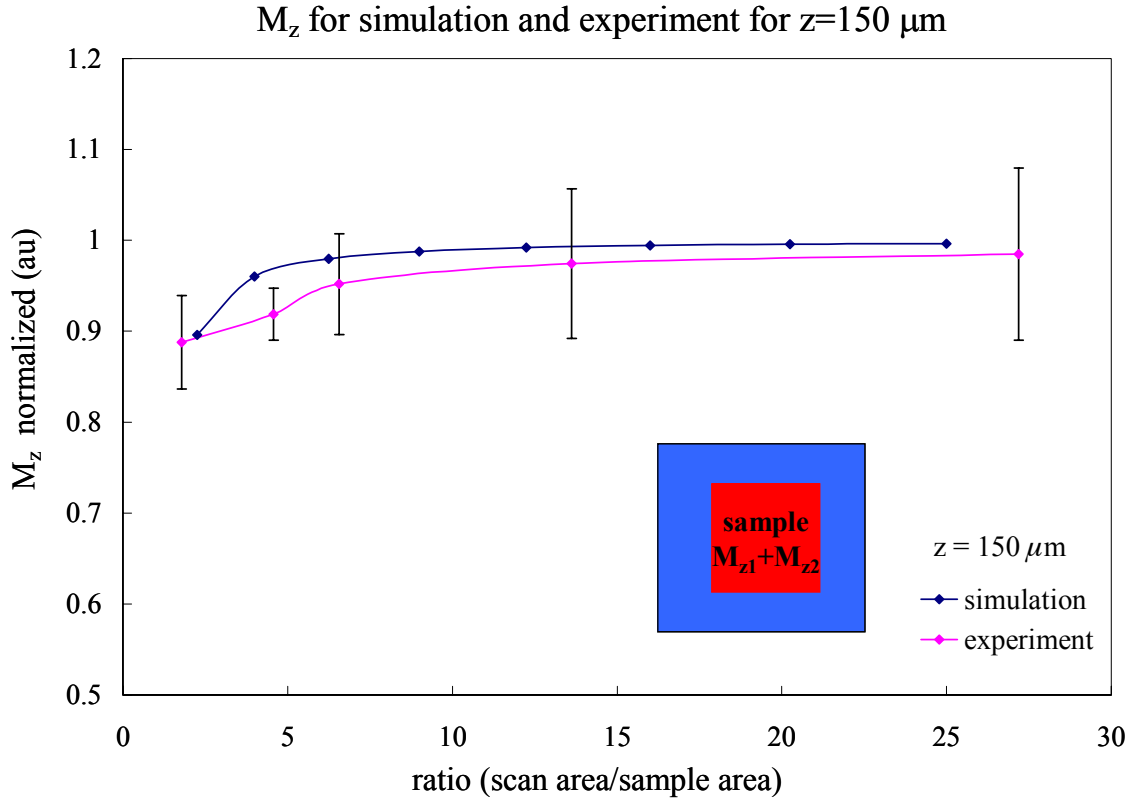


Figure 6.20 M_z ($= M_{z1}+M_{z2}$) dependence on the ratio of the scanning area to the sample size for simulated data and experimental (CFO samples mentioned above) data for $z = 150 \mu\text{m}$ when the inversion is used.

scanning area that is at least 5 times larger than the sample area to get an accurate value of M_z .

To see how this error propagates as z increases, I performed the same calculation for the simulated data for other z values. I simulated the data for additional z values of $200 \mu\text{m}$, $250 \mu\text{m}$, $300 \mu\text{m}$ while keeping the other parameters the same. For these simulations, the sample size was kept the same, namely $1 \text{ mm} \times 1 \text{ mm}$ (Figure 6.11) and the scanning area was varied from $5 \text{ mm} \times 5 \text{ mm}$ to $1.2 \text{ mm} \times 1.2 \text{ mm}$. I calculated M_z using the inversion technique and accounted for the scanning area, with M_{z1} and M_{z2}

added. Figure 6.21 shows the result. Note that the bent feature is present for all z values. On the other hand, one can see that as z increases, the error in M_z gets larger as the ratio of the scanning area to the sample area approaches 1. This is happening

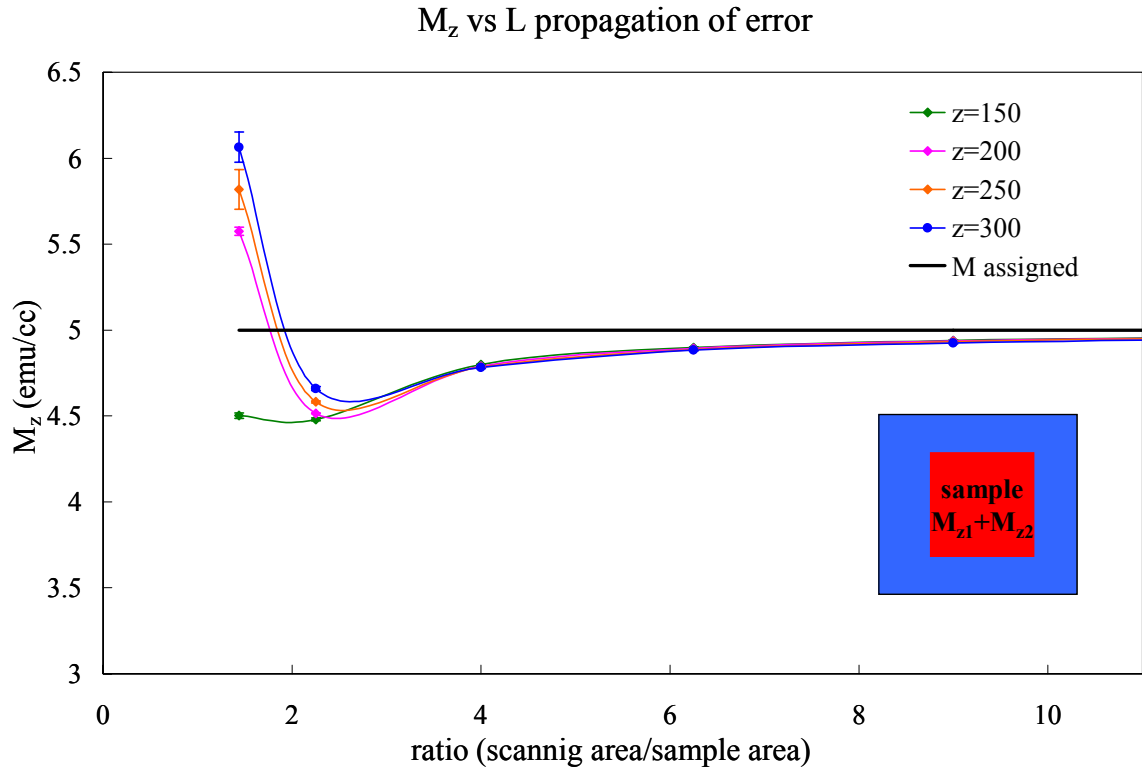


Figure 6.21 Propagation of error in M_z as z changes and as the ratio of the scanning area/sample area gets smaller.

because the error is amplified near the scanning edges when the scanning area is too small. Therefore, to calculate M_z accurately one must take into account the scanning distance z as well as the ratio of the scanning area to the sample area.

6.4 Revisiting Chapter 5

Now that I have optimized all the parameters of the inversion technique, I can use it to calculate M of the samples that I introduced in Chapter 5. For the in-plane case, the value of calculated remanent M_{in} of a SmCo_5 thin film sample using the line charge model was 224 emu/cc, and the inversion technique gave a value of 229 emu/cc, while the SQUID remanent magnetization from the hysteresis loop gave 227.4 emu/cc. For the out-of-plane case, the value of M_z for a CFO thin film that I calculated from the current loop model was 153.6 emu/cc, as was shown in Chapter 5. Using the inversion technique with all the optimizations, the M_z of this sample is 141 ± 10 emu/cc, while from the SQUID remanent magnetization of the same sample was 156.7 emu/cc. Note that the error estimation for M_z from the inversion technique is the standard deviation of the average M_z inside the sample, and it does not take into account the noise in the field data or any other source.

6.5 Conclusions

In this chapter, I discussed and optimized the parameters that control the inversion technique for calculating the in-plane and out-of-plane magnetization. I found that for the in-plane magnetization with the proper choice of k_w value it is the relationship between z , the scanning area and the sample area that matter the most in calculating M_{in} . When the sample size (along the magnetization direction) is smaller than the z value, it is the ratio of the scanning area to z that is important for the calculation of M_{in} . However, when the sample size is larger than z , it is the ratio of the scanning area to the sample area, which is important.

For the out-of-plane calculation, the most important parameters that determine the accuracy of M_z value, is the ratio of the scanning area to the sample area together with the z value. Because of the insufficient scanning area, one must add the outside M to the inside M to get M_z of the sample. It is seen from both the experiment and simulation that the ratio of scanning area to the sample area must be at least 5 in order for M_z to have a value with less than 10 % in error.

6.5.1.1

Chapter 7

Combinatorial investigation of ferromagnetic shape memory alloys

In this chapter, I will discuss combinatorial investigation of ferromagnetic shape memory alloys (FSMA). I will first introduce FSMA and their applications. I will then discuss high-throughput synthesis and characterization techniques that we used for this particular system. We have mapped the ternary compositional phase diagram of the Ni-Mn-Ga system. I will discuss the results of this investigation, where we extended the known FSMA regions to previously unexplored regions. Magnetic properties were mapped by applying the inversion technique on the magnetic field data, obtained from the scanning SQUID microscope, to the entire library.

7.1 Introduction to FSMA

Smart materials are a class of materials that function as both sensors and actuators [1]. They respond to external fields, such as stress, electric and magnetic fields and display field induced strain. Piezoelectric materials, magnetostrictive materials and shape memory alloys (SMA) are examples of smart materials. When stress is applied to a piezoelectric material, there is a change in the electric polarization. When the electric field is applied to a piezoelectric material, there is a change in polarization as strain is induced. Magnetostrictive materials behave similarly to the piezoelectric, except it is the magnetic field that induces strain. Shape memory alloys (SMA) are sensitive to

temperature and stress instead of electric or magnetic field. Changes in temperature and stress will induce strain or volume change in these materials.

Ferromagnetic shape memory alloys (FSMAs) are a class of smart materials, and they have two properties that coexist together. They are ferromagnetic and shape memory alloys: they are ferromagnetic materials that undergo reversible martensitic transformation. Strong magnetoelastic coupling in FSMAs results in enormous magnetic field induced strain. Strain as large as 8 % has been reported for applied field of about 1T [2].

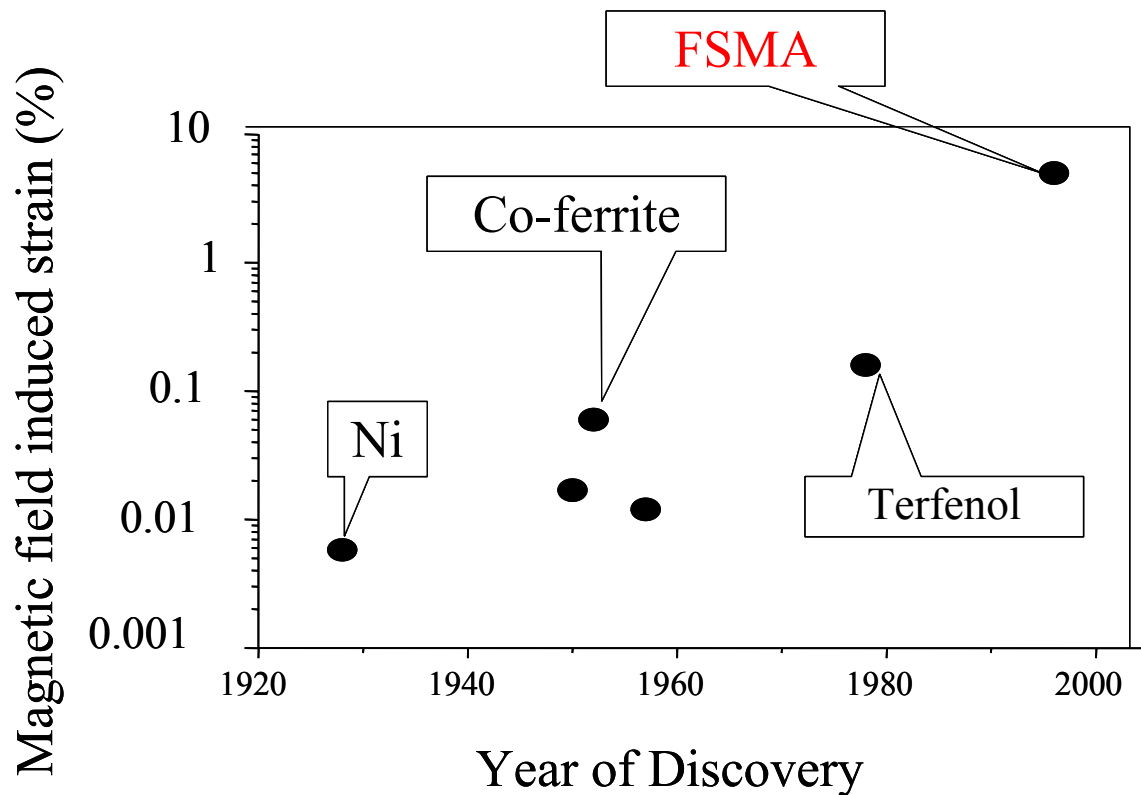


Figure 7.1 History of discovery of magnetostrictive materials.

If one looks at the development of magnetostrictive materials as presented in Figure 7.1, one can see that recently discovered FSMA have magnetic field induced

strain of two orders of magnitude higher than terfenol. In the next section, I briefly discuss the mechanism of field induced strain in FSMAs. We used the combinatorial method to explore FSMAs in order to find new compositions of FSMAs and understand their composition-structure property relationship.

7.1.1 Mechanism of shape memory and FSM effect

In order to discuss how an FSMA functions, I want to introduce first the SMA effect. The SMA effect can be seen below in Figure 7.2 when a NiTi (nitinol) wire is

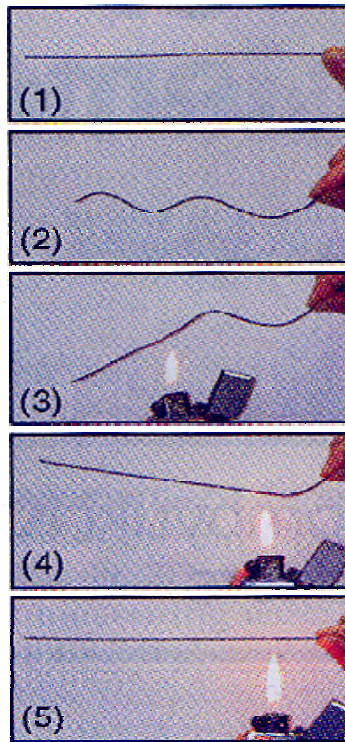


Figure 7.2 NiTi wire exhibiting the shape memory effect.

heated after it has been distorted. NiTi is a known SMA that has up to 8% induced strain when heated. Figure 7.2 shows the step-by-step change in the wire after it is bent. First

it is seen in (1) that a straight NiTi wire is bent to a different shape (2), then as it is heated (3, 4) it straightens out “remembering its shape” in (5).

To explain this, one must consider a change in the crystal structure of the material. I will look at an example of a simple case where there is a transformation from a cubic structure (which is a parent high temperature phase) to a tetragonal low temperature phase. Figure 7.3 shows an example of this transformation. For clarity, I first define the two phases that I will consider as shown in Figure 7.3 (a). The first phase

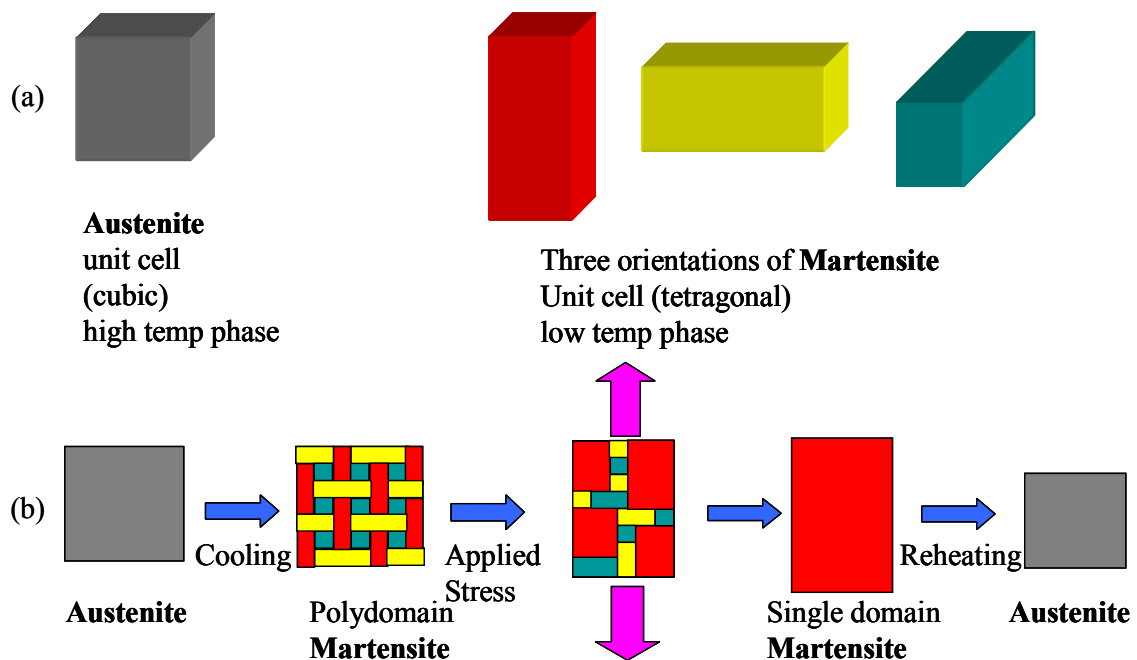


Figure 7.3 An example of transformation of a cubic structure to a tetragonal case: (a) structure of high temperature and low temperature phases, (b) shape memory effect.

is a cubic phase that is called an austenite. It is a high temperature and high symmetry phase and has only one orientation. The second phase is a tetragonal phase and is called a martensite. It is a low temperature and a lower symmetry phase and has three orientations or variants (domains), as shown in Figure 7.3 (a).

Several transition temperatures are associated with this phase transformation. When an austenite is cooled to the temperature M_s , the martensitic phase starts to form. It then continues to form until the temperature reaches M_f or the martensite-finish temperature. In the martensitic phase, three different orientations are possible, shown in red, yellow and blue in the figure. The two neighboring variants are twin-related to each other and may contribute to deformation if the interface is mobile under stress. Thus, when stress is applied to the polydomain martensite (Figure 7.3 (b)), deformation proceeds by twin boundary movement and a single-domain martensite is formed. Now when this single-variant martensite is heated, an austenite phase starts to form at the temperature A_s . The transition is completed at the temperature A_f . Above A_f , the martensite variant has all transformed back to the parent (cubic) phase. This transformation is crystallographically reversible.

Now, let us look back at Figure 7.2, when a NiTi wire was exhibiting the SMA effect. The wire is straight in the initial martensite phase (Figure 7.2 (1)). It was made straight at temperature above A_f in the austenite phase. The wire is then deformed in the martensitic state (see Figure 7.2 (2)). Room temperature is below M_f . Then as the wire is heated, it reverts back to its original shape as shown in Figure 7.2 (3-5). Temperature is above A_f .

Once the SMA effect is understood, we can look at the mechanism of magnetic field induced strain in FSMAs. The difference between FSMAs and SMAs is that in FSMAs, ferromagnetism is coupled to the SMA effect. Figure 7.4 shows the similar schematic as in Figure 7.3 (b) for the transformation of cubic phase to tetragonal. The magnetic domains are directly coupled to and incident with the martensitic variants.

Thus, instead of applied stress to deform the martensites, the magnetic field, B , is controlling the twin boundary motion. The FSMA is an SMA and thus goes through the

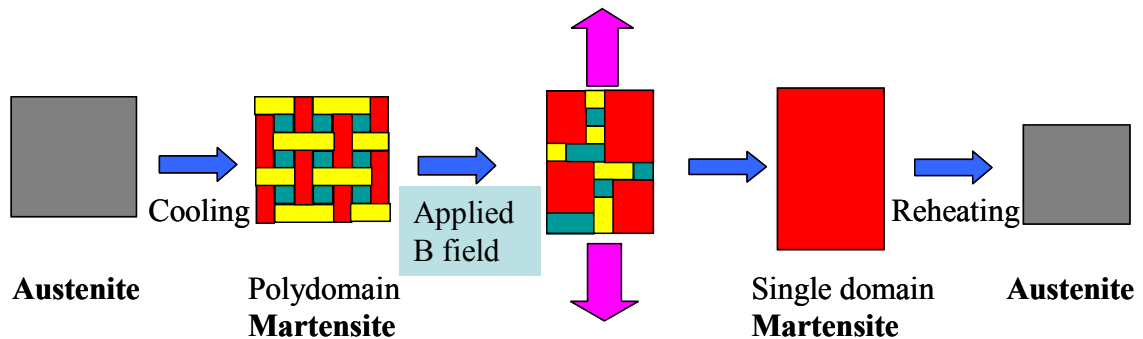


Figure 7.4 Schematic of FSM effect for a transformation of cubic structure to tetragonal

same reversible crystallographic transformation as discussed above. An ideal FSMA possesses high room-temperature magnetization, which results in high magnetostatic energy (so that it is not necessary to apply a large B field to rotate the domain and induce strain) and a high martensitic transition temperature so that the martensite material is stable at room temperature.

7.1.2 Applications of SM and FSM materials

SMA's are commonly used already. The first successful application of SMA's was made by Raychem Corp. for fasteners and tube couplings [3]. These couplings are also used for the hydraulic systems of jet fighters. Then SMA's are used in heat engines, where thermal energy is converted to mechanical work. This is an example of an environmentally-oriented application. Various thermal actuators and thermostatic mixing valves [4] also use SMA's. Furthermore, in biomedical fields, they are used as minimally invasive devices [5] and surgical anchors [6], since the temperature of the human body is

enough to induce transformation and leads to actuation. FSMAs are not used in practical applications yet. But there has been significant progress in materials development in the FSMA field, and their application in sensors and actuators are being pursued by many groups around the world [7]. In some applications, not only bulk FSMAs but also thin films FSMAs are important. In our group, we focused on the thin films of FSMAs. In the next sections, I describe how we fabricate and characterize our combinatorial libraries.

7.2 Fabrication of FSMA combinatorial libraries

So far, I have given a general description of FSMAs, and their properties. From here on, I will primarily focus on the Ni-Mn-Ga system. We have started with this system because there is a well-known composition of Ni_2MnGa , which is an FSMA. Prior to our investigation, there were limited studies of other Ni-Mn-Ga compositions. Thus, the purpose of our study was two fold: 1) to see if there are other compositions which are FSMAs in this ternary system; 2) to map the composition-property (magnetic and martensitic) relationship in this system in order to better understand the co-occurrence of ferromagnetic and shape memory effect. We note that our phase-diagram mapping experiments are performed entirely with thin film samples. It is well known that thin films and bulk samples can in general exhibit different properties. In particular, thin film FSMAs can display significantly reduced strain because of the clamping effect of the substrate. On the other hand, there have been reports that thin films FSMAs show similar magnetic properties as bulk samples (such as saturation magnetization) [8]. It has also been reported that martensitic transitions in thin film FSMAs occurs at roughly the

same temperature as the transition temperature range in bulk samples [9]. Thus, it is justified to use thin film libraries to obtain the correct trend in the composition-property relationship.

The composition spread libraries were deposited in an ultra-high-vacuum magnetron co-sputtering system with a base pressure in the range of 10^{-9} Torr (Figure 7.5). Three 1.5-inch-diameter guns were placed parallel and adjacent to each other in a triangular configuration (Figure 7.6). This allows natural mixing of the materials from

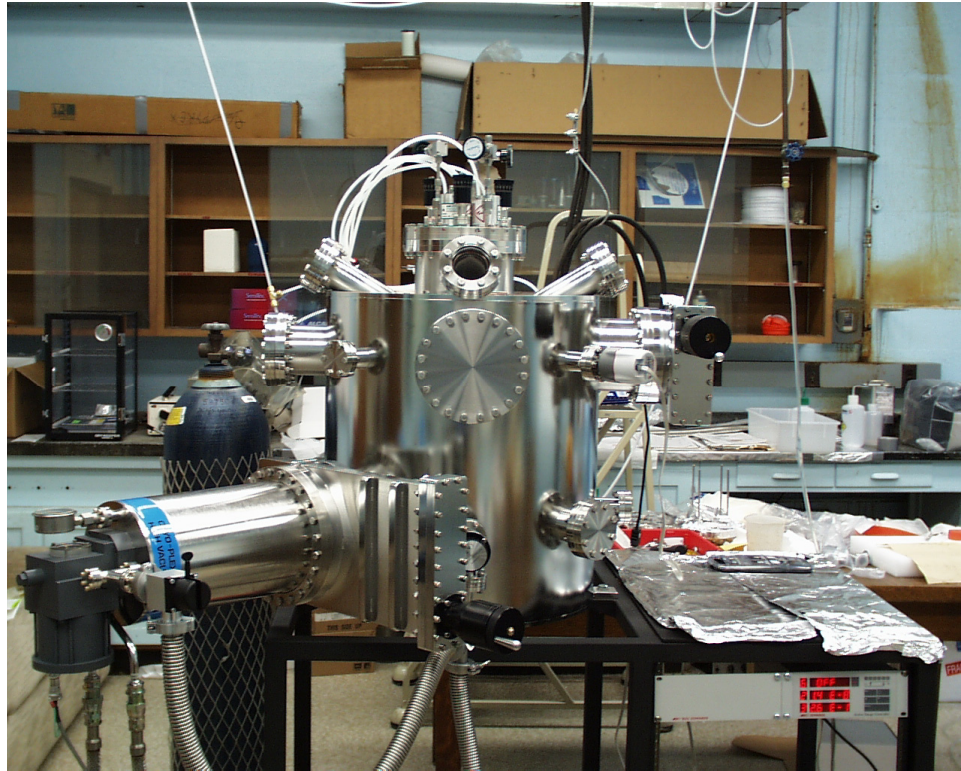


Figure 7.5 Combinatorial co-sputtering UHV chamber (Pbase $\sim 1 \times 10^{-9}$ Torr) system

three guns through codeposition, and a natural composition variation is created on deposited wafers. Depending on the distance between the guns and the substrate, the

profile of mixture of the three elements varies. This is illustrated in Figure 7.6. When the distance between guns and the substrate, z , is small there is less intermixing between

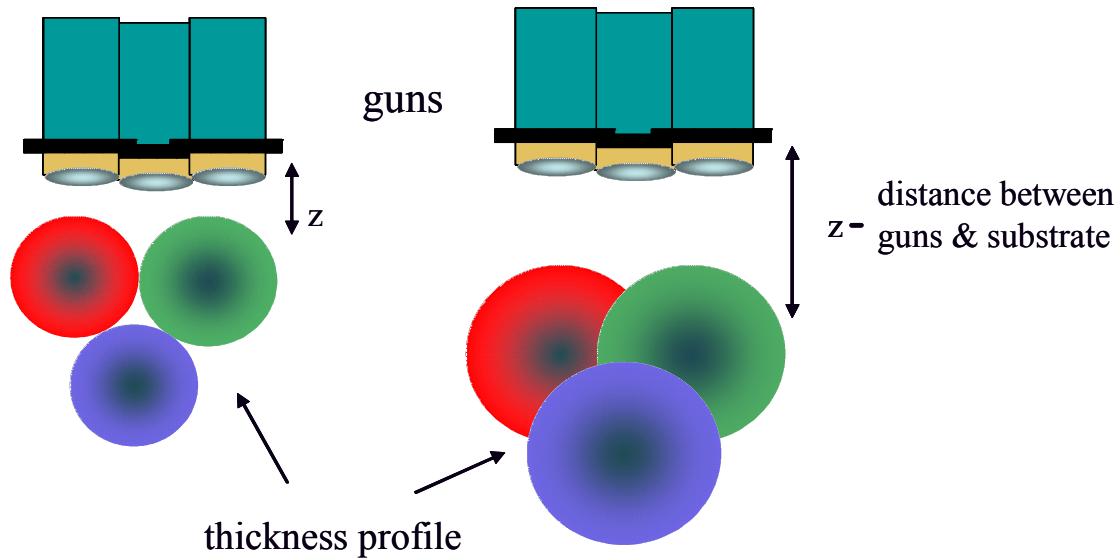


Figure 7.6 The nonconfocal configuration of the guns. The change in distance x varies the spread profile of the deposited materials.

the materials and less overlapping of regions. When z is large, there is more mixing and thus less variation in thickness and in composition, since the three materials are more intimately mixed. We have confirmed that, by adjusting the power applied to each gun and the distance between the guns and the substrate (typically 12 cm), different regions of the ternary phase diagram can be mapped out. Each gun is housed in a 2-inch-long chimney, which helps to minimize the cross-contamination of the guns. The three targets used in this experiment were Ni, Mn and Ni_2Ga_3 , and both AC and RF sputtering were used.

The substrates that we used were 3-inch-diameter (100) Si wafers. Sometimes we prepatterned them and other times we deposited the composition spread through a shadow mask to make a discrete library (as discussed in Chapter 2). An example of one

of the wafers is shown in Figure 7.7. The regions of the target materials are marked as areas

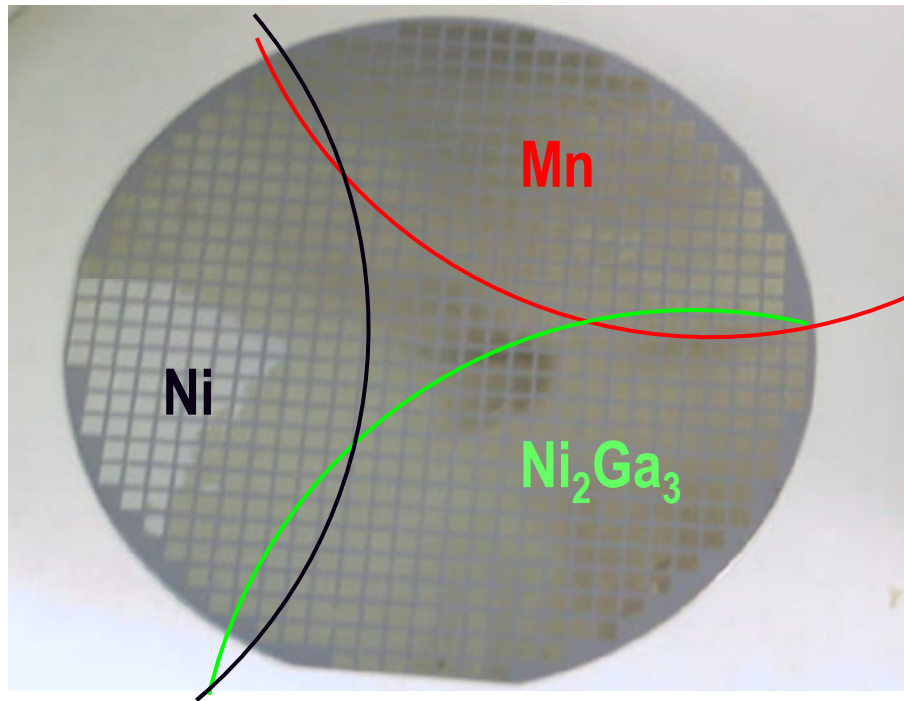


Figure 7.7 An example of FSMA library made with three targets: Ni, Mn, Ni₂Ga₃ on a Si substrate of thickness 5000 Å, insitu deposited with a physical mask and annealed at a temp 500 °C

directly under 3 sputtering guns.

We used two deposition conditions that produced similar results. In the first, we deposited the spread at room temperature followed by annealing the wafer in situ at 550 °C for 2 hours in vacuum, and in the second, we directly deposited it on a wafer heated to 500 °C. The typical gun power was 50–100 watts, and spread films with thicknesses in the range of 500 nm to 1 μm were deposited in 1–2 hours. The films were fiber-textured with predominantly (110) orientation normal to the substrate (as revealed by x-ray

diffraction). After fabricating the libraries, we characterized them for their ferromagnetic and SMA properties.

7.3 Characterization of FSMA libraries

The FSMA effect occurs in materials that are simultaneously ferromagnetic and reversible martensites, which make them shape-memory alloys. This defines our strategy for high-throughput screening: search for compositions that show both properties. First, we measure the composition of our libraries at each square. This is done by wavelength-dispersive spectroscopy (WDS). For ferromagnetic properties, we used the scanning SQUID microscope. For detecting reversible martensites, we made micromachined cantilever libraries. We used scanning x-ray diffraction to track the structure change as the composition changed in some regions of the spread. These characterization techniques are discussed in the next section.

7.3.1 Composition verification

To accurately map the exact composition distribution of the combinatorial samples, wavelength-dispersive spectroscopy (WDS) was used for every discrete and cantilever library (discussed in Sec. 7.3.3). It is a widely used micro-probe technique for obtaining composition distribution information. The principle of this technique is that when an electron beam strikes the sample, x-rays emitted will have different wavelengths depending on the element present. By detecting characteristic wavelengths of different elements, qualitative and quantitative identifications of elements can be performed. An illustration of the use of WDS to map regions of a ternary system can be seen in Figure

7.8, where A, B, and C are three elements. Here each point on the composition spread A-B-C has a different atomic percentage. It is then converted to a point on a ternary A-B-C diagram. Phase diagram plots allow us to visualize the data such as the values of magnetization and martensitic transformation.

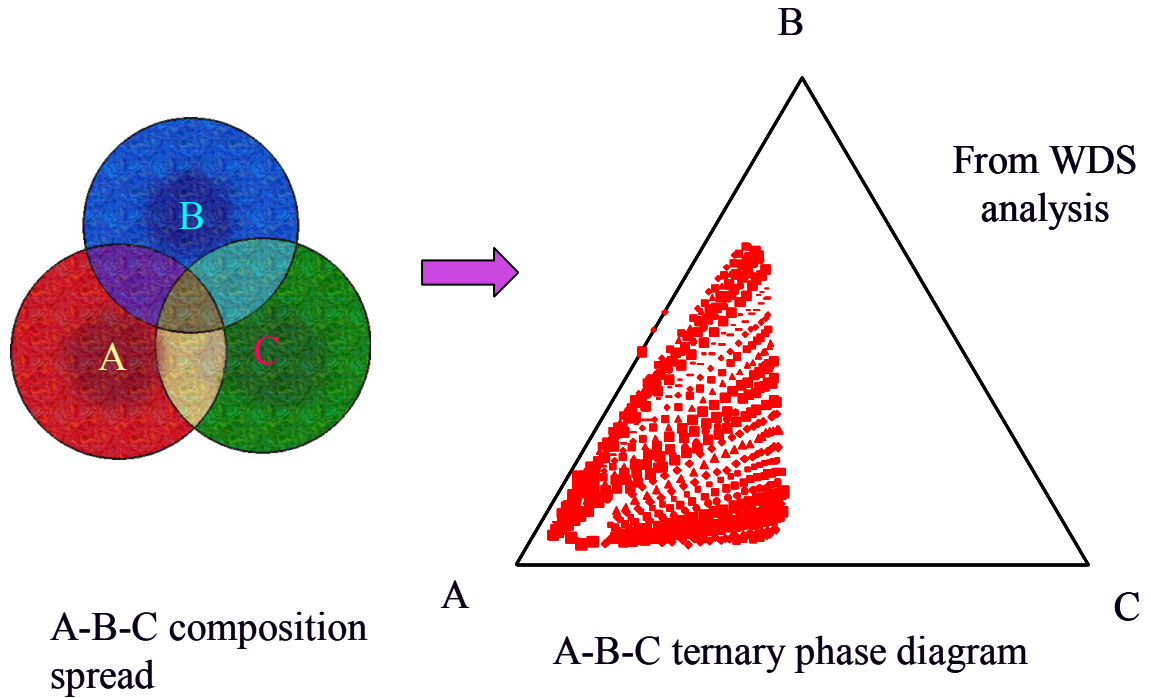


Figure 7.8 An illustration of the use of WDS for mapping a ternary phase diagram A-B-C.

7.3.2 Magnetic properties of Ni-Mn-Ga by scanning SQUID

For rapid characterization of magnetic properties, we used a room temperature scanning SQUID microscope, as mentioned in the previous chapters. After the fabrication of the sample, the sample is magnetized in-plane uniformly with a 1 T permanent magnet. We have found that our textured films always have the in-plane direction as the easy axis due to the shape anisotropy of the film. Figure 7.9 shows a magnetic field image of a spread wafer, which covers a large fraction of the Ni-Mn-Ga

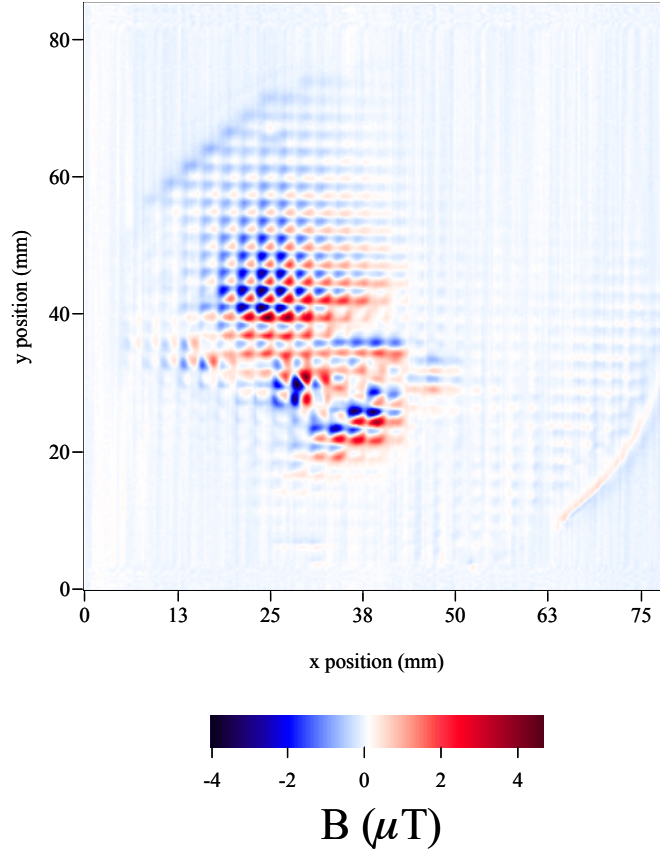


Figure 7.9 A scanning SQUID image of Ni-Mn-Ga combinatorial library wafer.

ternary system. This wafer was scanned at $z = 300 \mu\text{m}$, with a step size of $300 \mu\text{m}$ in x and in y .

Variation in the strength of the magnetic field as a function of composition is evident. As discussed in Chapters 5 and 6, it is easier and more practical to use the inversion technique on the entire library at once to calculate remanent magnetization from the magnetic field distribution data. Using the optimized parameters discussed in Chapter 6, I calculated ρ_m using the Transform software. I used Hanning window with $k_w = 4$. The code for ρ_m to run the calculation can be found in Appendix C.1. From ρ_m I calculated remanent in-plane magnetization for each square, since each square is a dipole.

The plot of ρ_m of the entire data and the most magnetic regions can be seen in Figure 7.10.

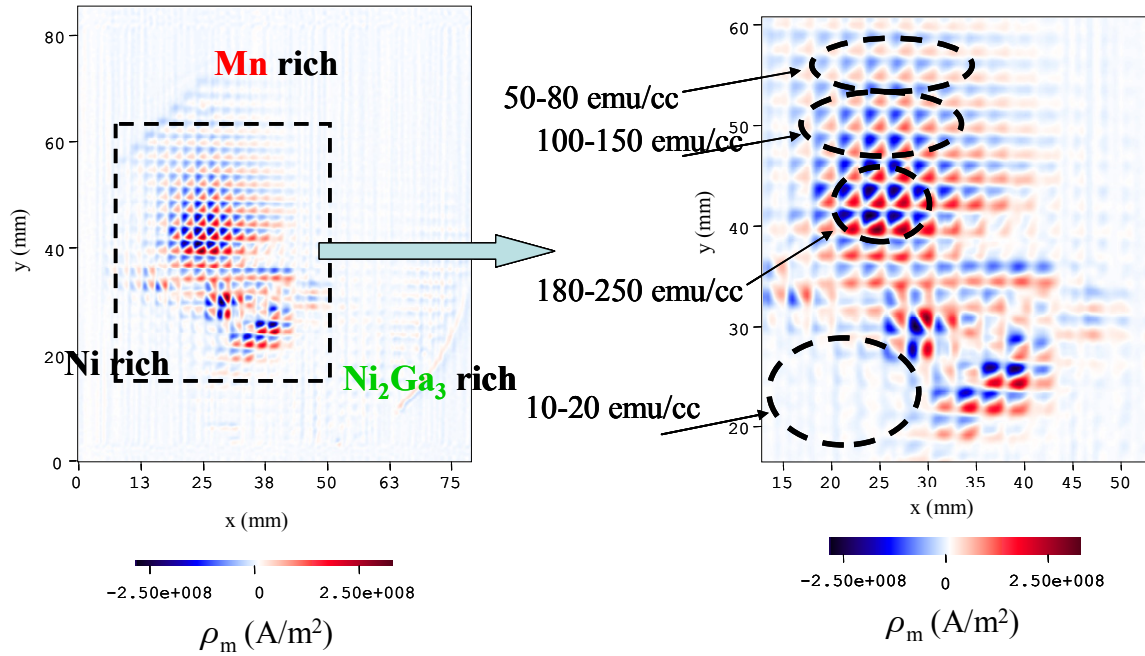


Figure 7.10 Two dimensional image of ρ_m for the same wafer as in Figure 7.9, denoting the most magnetic regions on the wafer.

With the help of Dr. Andrew Berkley, we wrote a program using Matlab software that would automate the integration to calculate the magnetization for each dipole (a small square). The code for the program can be seen in Appendix B. The software takes the data for ρ_m and plots it in two dimensions (as in the software Transform, as shown in Figure 7.10). Then after entering the parameters for the length and the width of a single square, I apply a grid of many squares on the sample. This grid must be carefully matched to the physical grid of the sample as seen in Figure 7.7. If there is a tilt in the scan or in the pattern, the data need to be divided into several parts. What is important is

that the integration area for each square should be accurate; otherwise, there will be an error in M (as discussed in section 6.2.2).

The space between the squares must be large enough for ρ_m to decay; we adjusted the size of the squares and the space between the squares as we learned about this. For the library shown above, the size of each square is 1.75mm x 1.75 mm (Figure 7.11), and the spacing between each square is 0.5 mm. The size of the square and the spacing defined the integration area. Each area of integration area is from 1.75 mm - 2 mm x 1.75 mm - 2 mm, in this way all the data for each square is included in the integration area.

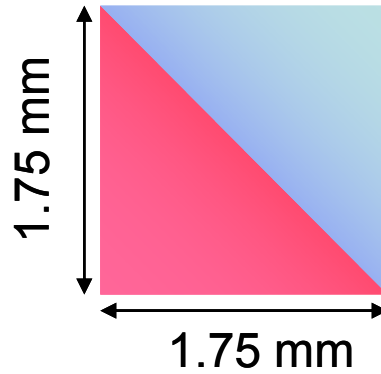


Figure 7.11 The schematic of a square from a library. Each square is 1.75 mm x 1.75 mm. The spacing between the squares is 0.5 mm.

The grid sets up an integration area for each square in the entire library wafer. Then the program calculates M for each square, by integrating ρ_m as discussed earlier. The result is given in the form of a matrix: x , y and M for each square. Figure 7.12 shows the plot of this matrix in Matlab. Here the color denotes the value of M calculated from the magnetic field data, x and y are the position of the midpoint of each square on the wafer. The orientation of the wafer is the same as in Figure 7.10

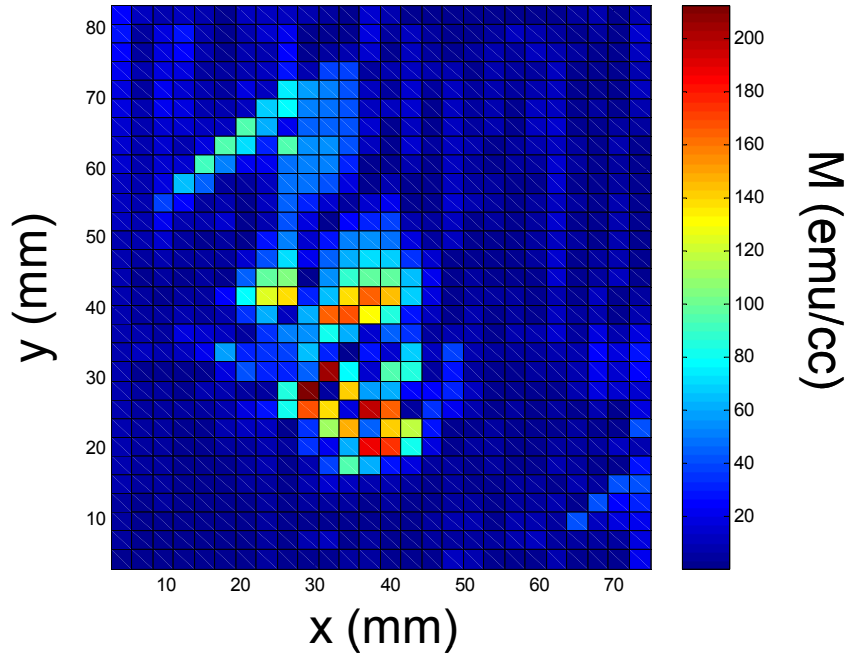


Figure 7.12 Distribution of M as a function of position on the physical library.

Then, this result is combined with the composition mapping from WDS to construct a mapping of the remanent magnetization as a function of composition (Figure 7.13). Remanent magnetization is one measure of the strength of magnetism, and thus, we call this a magnetic phase diagram. In this figure, the blue curve is the compositional region mapped on this particular wafer. It is clear that the most strongly magnetic region stretches from near the middle of the phase diagram towards slightly Ni-rich composition. The black circle indicates the region surrounding the Heusler composition, Ni_2MnGa , which has been extensively studied [10, 11, 12, 13] and which lies near one end of this highly magnetic region. As one moves away from this region, the magnetization becomes smaller. Nickel is strongly magnetic, but its moment decreases

rapidly as it is diluted with other elements, and in the Ni-rich region covered in this spread, the composition is already only weakly magnetic. On the other hand,

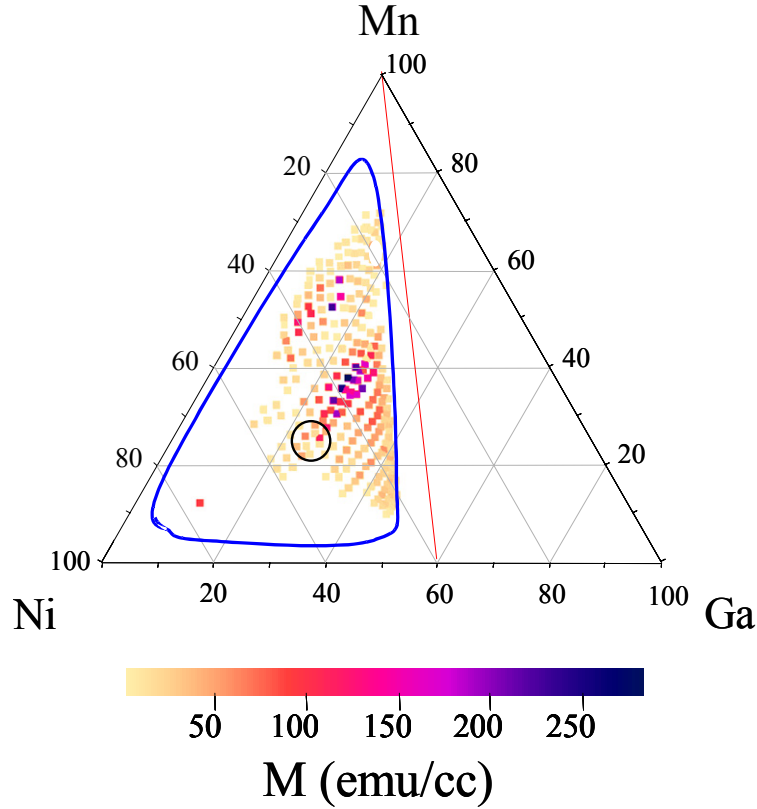


Figure 7.13 Room temperature magnetic phase diagram of Ni-Mn-Ga. The region inside the blue curve is the compositional region mapped on the spread wafer. The composition where the orange line meets the Ni-Ga line is Ni_2Ga_3 , which is one of the target compositions we used. The circle inside the diagram marks the compositions near the Ni_2MnGa Heusler composition.

Manganese is antiferromagnetic, and this is not detectable by SQUID.

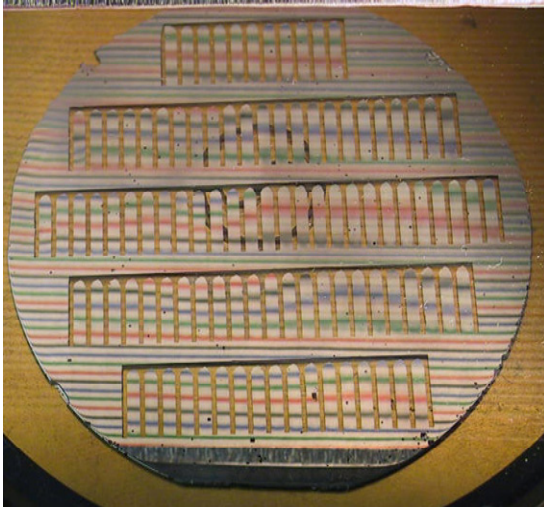
The peak in magnetization is observed near the center of the phase diagram around the half-Heusler composition, NiMnGa . Several spread wafers fabricated under slightly different conditions (annealing temperatures) were all found to result in the similar phase diagram pattern. The values of magnetization extracted here are consistent with those of magnetization obtained by a vibrating sample magnetometer on separate

individual composition samples at room temperature. Ferromagnetic resonance measurements of the individual samples showed a very narrow line width (as low as 70 Oe) as well as well-defined spin resonance waves, indicating that the films are generally of very high quality and magnetically very homogeneous [14].

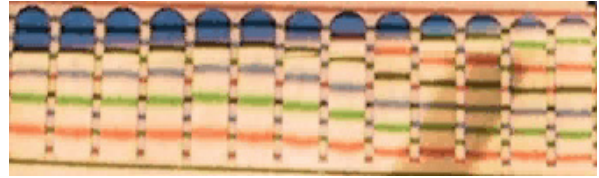
7.3.3 Cantilever libraries for SMAs

Properties of thin-film SMAs can be studied by depositing them on micromachined Si cantilevers [8]. By monitoring the reversible thermally induced actuation of such SMA film/Si cantilever bimorphs, martensitic transformation temperatures can be detected [8]. For individual cantilevers, actuation is typically measured using a capacitance formed between the end of the cantilever and a separate electrode. To map the regions of SMAs and their transition temperatures for the entire spread, we have micromachined arrays of cantilevers, and deposited the composition spreads directly on the array wafers. Each cantilever is 8.5 mm long, 2 mm wide and 60 μm -100 μm thick, and one wafer has 90-100 cantilevers on it. To study thermally induced actuation of the entire cantilever array simultaneously by visual inspection, we have developed a method that works on the simple principle that individual cantilevers with metallic films deposited on them behave as concave mirrors. During a transition, stress-induced actuation of a cantilever results in a sudden change in the radius of curvature of the ‘mirror’, and an image reflected off the cantilevers responds very sensitively as the concavity of the mirrors change. By monitoring the change in the image as a function of temperature, we can readily discern composition regions undergoing a transition. In this manner, a cantilever array serves as a ‘self-reporting’

combinatorial library for detection of structural phase transitions. Figure 7.14 (a) is a photograph of a spread deposited on a cantilever array that is reflecting an image (a series



(a)



(b)

Figure 7.14 (a) A photograph of Ni-Mn-Ni₂Ga₃ spread deposited on a cantilever library taken during the temperature-dependent measurement. The lines are a reflection of an image with colored lines held over the wafer. The shifts in the positions of the lines as a function of temperature are used to detect small changes in the local curvature of the cantilever. (b) Zoomed up view of a row of cantilevers that showed martensitic transitions.

of colored lines). The measurement consists of recording the image projected on cantilever arrays as the temperature is varied. Figure 7.14 (b) shows a row of cantilevers. All transitions observed here were found to be reversible. From the cantilevers displaying transitions, another phase diagram is constructed (Figure 7.15), which shows the composition regions that undergo a martensitic transition and the corresponding transition temperature. Because of the finite size of individual cantilevers, there is compositional variation on each cantilever. A typical thermal hysteresis width is about 50 K, and this is partly attributed to the compositional variation within each cantilever.

WDS was done at three positions along the length of each cantilever. For mapping, we have labeled these three compositions

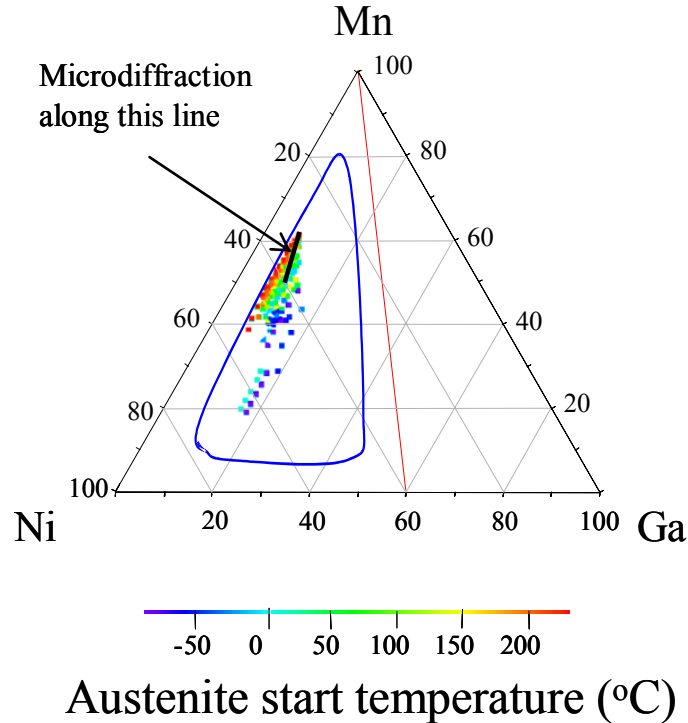


Figure 7.15 Mapping of compositional regions on the phase diagram that displayed martensitic transformation. The composition where the orange line meets the Ni-Ga line is Ni_2Ga_3 .

with one transition temperature observed for the cantilever. A large region previously unexplored was found to be SMAs.

Because of the layout of the cantilever libraries, there are regions of the spread not covered by active areas on cantilevers. We therefore compiled data from several spread wafers deposited at slightly different relative orientation of the sputtering guns with respect to the cantilever wafers. A clear trend emerges, and the general region that undergoes martensitic transitions can be easily seen from the phase diagram. The exact

martensitic transition temperatures are known to depend on many factors such as atomic ordering, microstructure and the residual stress [9, 15, 16]. Reported values of the martensitic transition temperature of nominally Ni_2MnGa samples vary widely, and in one study [12] it was found to range from 113 K to 298 K. Naturally, we expect to have regions that undergo transitions at temperatures out of the range of our measurements (150–570 K), and we believe this is the reason we do not see Ni_2MnGa transforming in our measurement range in this particular experiment.

Rather than focusing on the exact transition temperature, we discuss the trend as a function of compositional variation. There are reversible martensites in large compositional regions previously not reported. This region stretches from near Ni_2MnGa to Ga-deficient, Mn-rich regions. The transition temperature increases as the molecular percentage of Ga is decreased. A typical composition here is $\text{Ni}_{43}\text{Mn}_{47}\text{Ga}_{10}$, whose martensite start temperature was found to be 400 K. In much of the newly discovered region, the martensitic transformation temperature is near room temperature or above, which is desirable for practical applications.

7.3.4 X-ray analysis

An X-ray diffractometer is used to characterize the structure of materials. Using Bragg's law $n\lambda = 2d \sin\theta$, where n is integer, λ wavelength of the incident beam, d spacing between two atomic planes, and θ reflection angle, one can calculate the spacing d or the lattice constant of the material. X-ray diffraction patterns are obtained as a result of atoms scattering from different planes thus revealing the atomic arrangement of a material. Figure 7.16 shows a scanning X-ray microdiffractometer, D8 DISCOVER with

GADDS by Bruker-AXS, equipped with a two-dimensional (2-D) area detector (diameter: 11.5 cm) and an x-y-z stage for combinatorial screening of out-of-plane lattice constant.

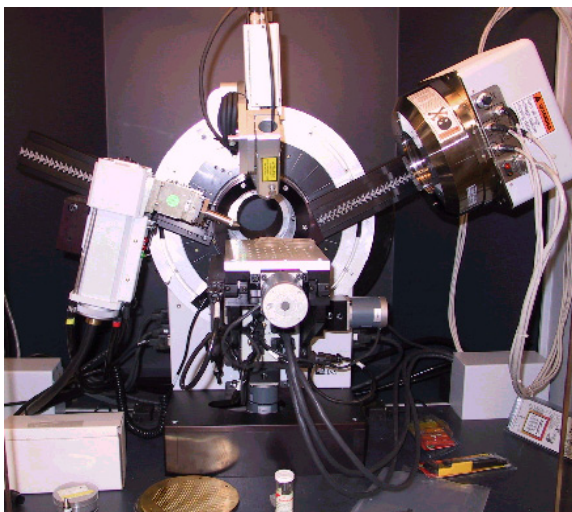


Figure 7.16 A photograph of the scanning x-ray microdiffractometer.

A schematic drawing of the diffraction geometry in the 2-D area detector is shown in Figure 7.17. When one uses the traditional point detector, only the diffracted beam in the detection plane can be detected. The plane along z-direction cannot be measured. In contrast, the area detector can pick up photon signals ranging along the z-direction. As a result, χ information is also obtained. The range of 2θ depends on the distance between the detector and the sample. By integrating intensities in the χ plane, a spectrum that resembles a regular θ - 2θ diffraction pattern can be obtained.

The X-ray beam size can be adjusted and it is in the range from 50 μm to 500 μm . The beam size used for individual spots of discrete libraries was 500 μm . The microdiffractometer is fully automated and controlled by a computer. Scanning across a combinatorial sample is relatively easy and efficient.

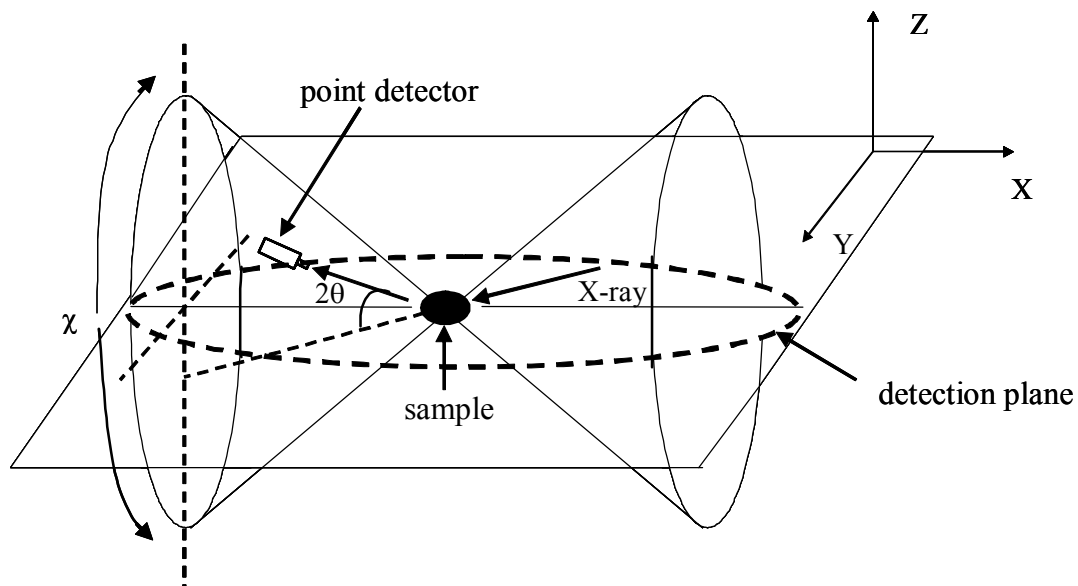


Figure 7.17 A schematic drawing of diffraction geometry when using a 2-D area detector. A range of 2θ and χ are detected simultaneously.

Scanning X-ray microbeam diffraction of the spread indicates that most of the composition regions mapped on our composition spreads have the diffraction pattern consistent with the $L2_1$ structure, (Figure 7.18), of the Heusler composition or a tetragonally distorted $L2_1$ structure (for the martensite). Figure 7.19 shows a scanning

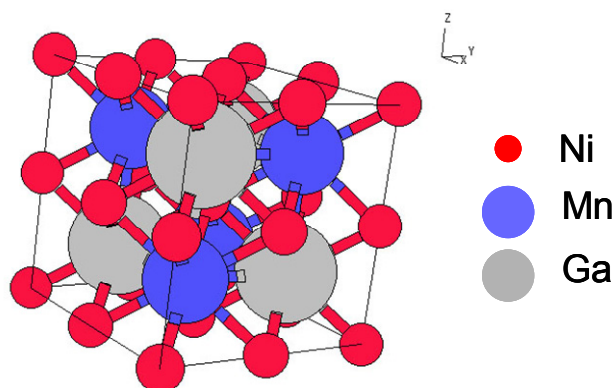


Figure 7.18 A unit cell of $L2_1$ structure of an austenite.

diffractogram taken at room temperature along the black line region in Figure 7.15. In this region, the composition goes from the mixed phase displaying three peaks (two from the martensite and one from the austenite) to a region where it is mostly austenite. This verifies that the new region we found must be SMAs and indeed martensites.

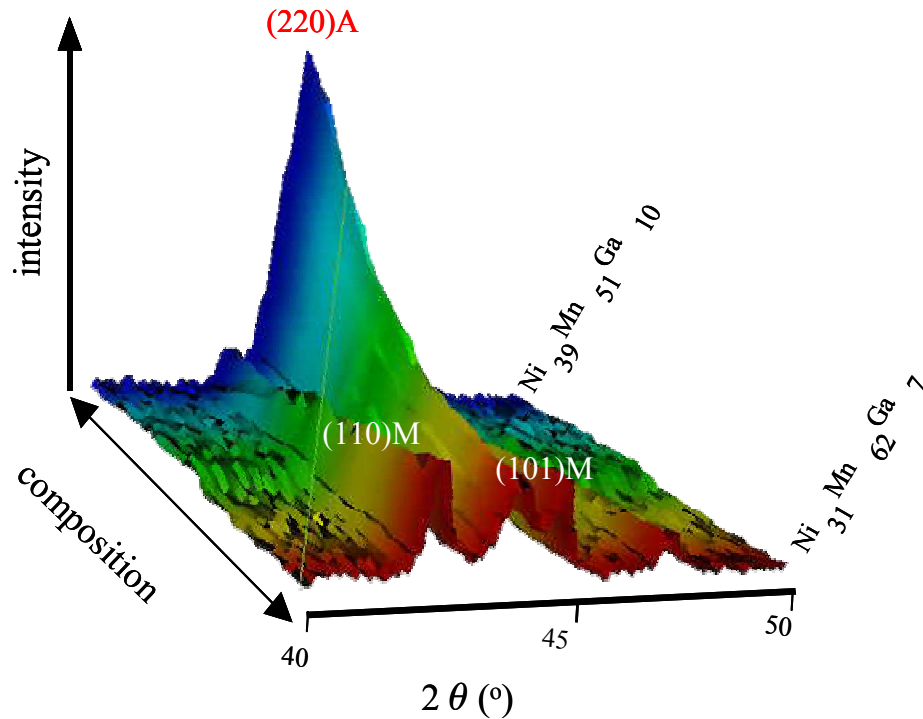


Figure 7.19 Scanning X-ray microdiffractogram taken at room temperature along a compositional region marked by the solid black line in Figure 7.15. There are three peaks, two are from a martensite and the middle one is from an austenite.

7.4 Mapping of a phase diagram

Figure 7.20 summarizes the magnetic and the martensite phase diagrams deduced from the obtained data. To date overwhelming majority of reported work had focused on regions inside the blue circle whose composition is close to the Heusler alloy. It is

evident that there is a large region well outside the near- Heusler composition that contains ferromagnetic, reversible martensites. It has been shown [17, 18] that this class of material displays martensitic instability for stoichiometries where the average number of electrons per atom is ~ 7.4 . The green hatched area in Figure 7.20 covers the region where the average number of electrons per

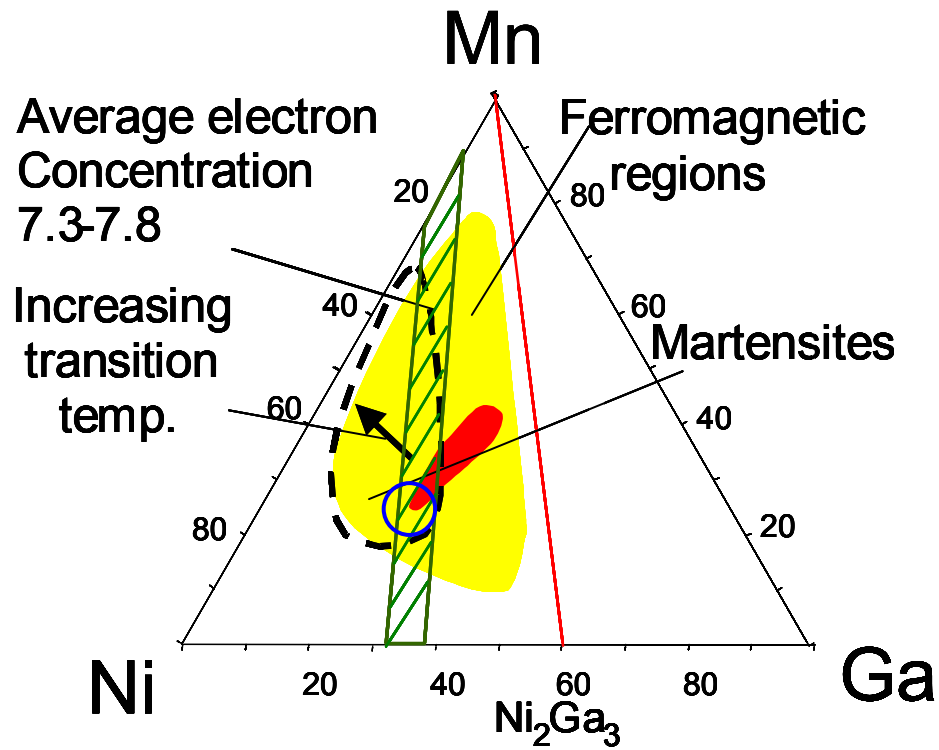


Figure 7.20 Functional phase diagram deduced from the present experiment. The hatched region has compositions with average electron/atom ratio 7.3–7.8. The dotted line surrounds the region of reversible martensites. In the ferromagnetic region, the red area has the highest magnetization.

atom is 7.3–7.8. There is a large overlap between this region and the observed reversible martensite region. Because the electron/atom ratio rule is expected to apply strictly in the L_{21} structure, the overlap is perhaps an indication that the structure in the region is indeed L_{21} or one close to it.

The closer the composition is to the $\text{Ni}_{1-x}\text{Mn}_x$ line of the phase diagram, the lower the magnetization becomes. A separately prepared $\text{Ni}_{1-x}\text{Mn}_x$ spread did not show any indication of reversible martensites. $\text{Ni}_{1-x}\text{Mn}_x$ is known to be ferromagnetic for $x < 0.25$ – 0.4 and antiferromagnetic for greater x , and the actual value of x where the transition takes place is dependent on atomic ordering [19, 20]. Martensitic instabilities are often associated with magnetic transitions [21]. We speculate that it is the ferromagnetic–antiferromagnetic transition or competition in $\text{Ni}_{1-x}\text{Mn}_x$ that is serving as the precursor to the martensites in the Ni–Mn–Ga system. The martensitic instability is perhaps set off by introduction of a small Ga concentration. The robustness of the martensite associated with the L2_1 phase may be reflecting the large solid-solution region in the $\text{Ni}_{1-x}\text{Mn}_x$ phase diagram near the Ni end.

The room-temperature magnetization is plotted against the martensitic start temperature in Figure 7.21 for the compositions studied here. There is a clear relationship between the two parameters: the higher the magnetization, the lower the transformation temperature. We have confirmed that, for different samples, the magnetization at room temperature is roughly proportional to the Curie temperature. For this, we measured individual cantilevers using a vibrating sample magnetometer. The plot points to a strong thermodynamic magneto-structural coupling in this system. Such a coupling has previously been observed in a limited range of composition near Ni_2MnGa (inside the circle in Figure 7.13) [13], and a Ginzburg–Landau model has been used to explain the influence of the magnetic order on the martensitic transition [13, 22]. Our experiment shows that the same coupling behavior holds for a much wider compositional range. A phenomenological interpretation of this is that magnetism tends to stabilize the

austenite structure of the alloy, and this necessarily lowers the structural transformation temperature. It is interesting that a first-principles calculation has suggested [23] that a cubic to tetragonal change would actually result in a slight increase in the total magnetic moment in Ni_2MnGa . The seeming discrepancy may indicate the importance of a magneto-elastic coupling term in the free energy, which gives rise to the observed trend.

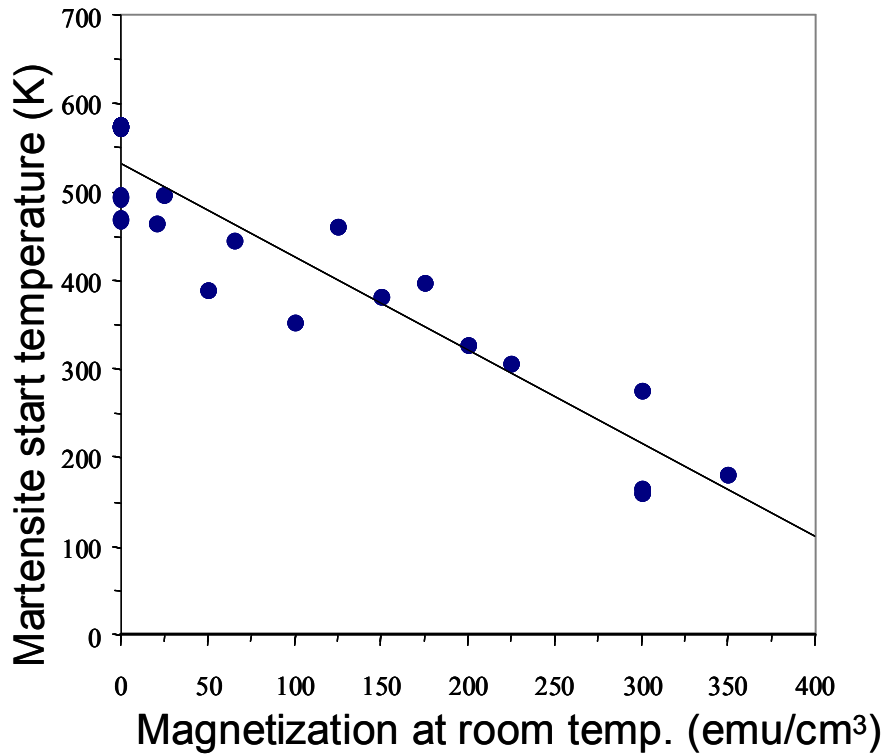


Figure 7.21 Martensitic start temperature against room temperature saturation magnetization for data points mapped in Figure 7.15. For this magnetization, cantilevers were measured individually using a vibrating sample magnetometer. The line is a linear fit to the data.

For applications, the goal when searching for new FSMAs is to find compositions with (1) high Curie temperature, and thus increased room-temperature magnetization, which in turn results in increased magnetostatic energy necessary for rotating the

magneto-elastic domains, and (2) high martensitic transition temperatures. Our results clearly indicate an intrinsic trade-off between the two in a given system. Also, within a given ternary system, the Heusler composition does not necessarily provide the optimized functionality. This may also be the case for other properties such as complete spin polarization, which has been predicted in some Heusler compounds but not yet unambiguously established [24]. Perhaps exploration is warranted outside the Heusler composition in the ternary phase diagram for high spin polarization.

7.5 Conclusions

Here, using thin-film composition spread libraries, we have mapped the functional phase diagram of Ni-Mn-Ga system whose Heusler composition Ni_2MnGa is a well-known FSMA. A characterization technique that allows detection of martensitic transitions by visual inspection was combined with quantitative magnetization mapping using scanning SQUID microscopy. We found that a large, previously unexplored region outside the Heusler composition contains reversible martensites that are also ferromagnetic. A clear relationship between magnetization and the martensitic transition temperature was observed, revealing a strong thermodynamical coupling between magnetism and martensitic instability across a large fraction of the phase diagram.

Our work reinforces the importance of systematically exploring structural transitions in looking for novel ferroic materials as well as understanding their physical origin. Guided by techniques such as the ones described here, it would also be possible to make a systematic search and survey of functional correlations of other multiferroic materials.

Chapter 8

Combinatorial investigation of magnetoelectric materials

In this chapter, I will discuss combinatorial investigation of magnetoelectric (ME) thin film materials. ME materials are a new type of smart materials. I will introduce their properties and potential applications. I will discuss our investigation of the PbTiO_3 (PTO) - CoFe_2O_4 (CFO) system using composition spreads. The emphasis is on the magnetic properties of the composition spreads. Finally, I will present the results of this investigation, where we have identified new compositions of thin film magnetoelectric materials from the composition spreads.

8.1 Introduction to magnetoelectric materials

Magnetoelectric materials [1] are a class of multiferroics where ferroelectricity and magnetization co-exist and are coupled to each other. Such materials display the magnetoelectric effect, where changes in magnetization are induced by an applied electric field, and the electric polarization is modulated by an applied magnetic field. They are described by the second terms in Equation 8.1 and 8.2.

$$P_i = (\chi_e)_{ij} E_j + \alpha_{ij} H_i \quad \text{Equation 8.1}$$

$$M_i = (\chi_m)_{ij} H_j + (\alpha_{ij} / \mu_0) E_j \quad \text{Equation 8.2}$$

Here, P is the polarization, χ_e and χ_m are the electric and magnetic susceptibility respectively, H and E are the magnetic and electric field, respectively, α_{ij} is the magnetoelectric coefficient and μ_0 is the magnetic permeability in vacuum.

There are two ways to obtain magnetoelectric materials. One is to look for materials where there is a natural coexistence of ferroelectricity and ferromagnetism, and the other is to create composite materials artificially to indirectly couple ferroelectricity and ferromagnetism. This is schematically shown in Figure 8.1.

Multiferroicity and multiferroic materials

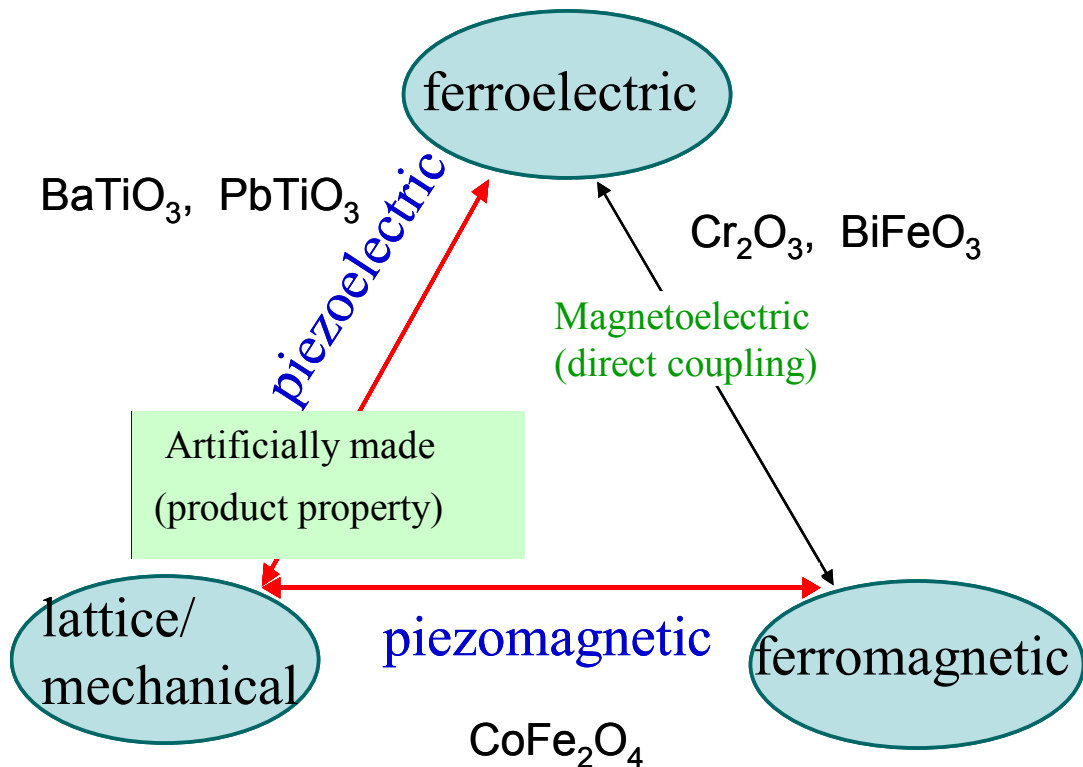


Figure 8.1 A Coupling diagram between ferroelectricity, ferromagnetism and stress. Artificial magnetoelectric composite materials can be made by coupling through the lattice/mechanical property.

There are very few natural single phase ME materials, such as Cr_2O_3 and BiFeO_3 , which were discovered in the last three decades [2, 3, 4, 5]. The scarcity of such materials is believed to be due to the contradiction of the general principles of ferroelectricity and ferromagnetism. The contradiction comes from the fact that there are

no 3d-orbital electrons in the B-site atoms for most ferroelectric perovskite oxides. This facilitates spontaneous polarization in ferroelectric materials. However, 3d-orbital electrons are necessary for ferromagnetic materials to create spin polarization. N. A. Hill *et al.* have used the first-principle density functional theory (DFT) to show that the d-orbital electrons in transition metals essential for magnetism reduce the tendency for off-center ferroelectric distortion [6, 7]. This indicates that additional electronic or structural driving forces are necessary to have ferroelectric and ferromagnetic properties coexisting together. In addition, the magnetoelectric effect in these single phase materials was found to be generally very weak, which limits their applications in devices, or strong but only at low temperature and under high field [8].

The other way to obtain magnetoelectric materials is by synthesizing composites, combining materials with different ferroic properties. For example, J. Van Den Boomgaard *et al* [9, 10, 11, 12, 13] made the first artificial magnetoelectric material by combining a ferroelectric (piezoelectric) BaTiO₃ (BTO) and a ferromagnetic (piezomagnetic) CoFeO₄ (CFO) in an eutectic sintered composite. In such a composite system, the magnetoelectric effect occurs via the product property (Figure 8.1) [11], i.e. piezoelectric and piezomagnetic properties are coupled through the lattice/mechanical property of the material. Here we can define the magnetoelectric coefficient as $\alpha = \partial e / \partial H * \partial P / \partial e$, where e is the induced strain, H is the magnetic field, and P is the polarization. This indicates that by applying a magnetic or electric field to this composite, one can induce a change in polarization or magnetization through strain.

Harshe *et al* proposed bilayered or multilayered composite structures held by epoxy in order to enhance the magnetoelectric effect [14]. The layered composites were

expected to have a higher magnetoelectric effect than bulk eutectic composites due to two main reasons. First, the piezoelectric layers are easily poled, thus improving piezoelectricity and second, the piezoelectricity is not suppressed by the piezomagnetic material. There have been reports of many magnetoelectric effects in layered composites such as $(\text{Pb,Zr})\text{TiO}_3$ (PZT) – $\text{Tb}_{0.3}\text{Dy}_{0.7}\text{Fe}_{1.92}$ (Terfenol-D), PZT- NiFeO_4 , Polyvinylidene fluoride (PVDF) – Terfenol-D, etc. [15, 16, 17, 18].

To date, the composite magnetoelectric effect has been exclusively studied in bulk composite materials. In the present work, we explored the possibility of fabricating such materials in thin film forms using the combinatorial approach.

8.2 Composition spreads for exploring ME materials

Thin films have several advantages over bulk. First, magnetoelectric thin film heterostructures can be fabricated by alternating piezoelectric and piezomagnetic layers, where one can investigate coupling of the two properties at nanometer level. Second, one can pursue fabrication of compact thin film magnetoelectric devices.

Our initial idea was to combine ferroelectric and ferromagnetic materials together using combinatorial PLD. We create gradual mixing of ferroelectric and ferromagnetic materials in the composition spread. Our goal is to couple ferroelectric and ferromagnetic properties through the lattice/mechanical property (Figure 8.1) to see if we can obtain multiferroic materials somewhere in the middle of the composition spread. The schematic is shown in Figure 8.2. The criteria for choosing the ferroelectric and ferromagnetic materials are that the ferromagnetic material needs to be an insulator and should have a high magnetostriction coefficient. The ferroelectric material must possess

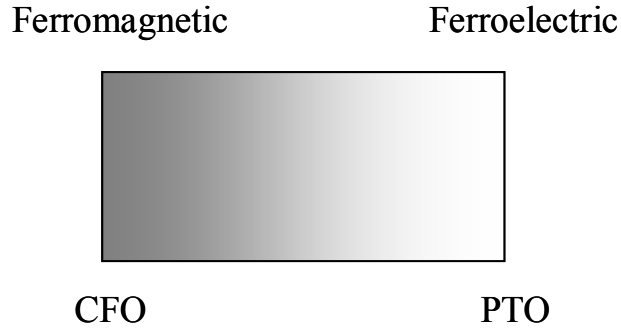


Figure 8.2 A schematic of the composition spread where the average composition on the spread is varying continuously from pure CFO at one end to pure PTO at the other end.

a high piezoelectric coefficient. Keeping this in mind, we decided to try PbTiO_3 (PTO) as the ferroelectric material and CoFe_2O_4 (CFO) as the ferromagnetic material.

To synthesize *in-situ* PTO-CFO composition spreads, two ceramic targets, PbTiO_3 (PTO) and CoFe_2O_4 (CFO), were ablated in an alternating manner with an excimer laser (KrF with $\lambda = 248$ nm) and deposited onto an (100) MgO substrate. CFO is cubic with a lattice constant $a = 0.839$ nm, and as it is grown on (100) MgO it is c-oriented. On the other hand, PTO is tetragonal with $a = b = 0.390$ nm, $c = 0.415$ nm and when it is grown on MgO it has a mixture of c- and a-oriented growth as confirmed from the x-ray and TEM studies. For more details, refer to section 8.3.3.2.

Linear compositional gradient across the spread is created by performing a series of shadow depositions through a rectangular opening of the automated shutter in our combinatorial PLD flange. This was first discussed in Chapter 2. The shutter is glided back and forth over the substrate during the deposition; see Figure 8.3 (a). The typical distance between the shutter plane and the substrates is $300\text{ }\mu\text{m}$. The motion of the shutter is synchronized with the firing of the laser in such a way that for each deposition,

a thickness wedge-like gradient is created on a chip as shown in Figure 8.3 (b). We fabricate this superlattice-like spread by depositing a layer of PTO and CFO in an alternating manner until we reached the desired thickness of 300nm. The thickness of each wedge varied from 1 times the CFO unit cell of 0.8 nm (1x) to 15 times CFO unit cell (15x). In this chapter, I will focus only on the 15x composition spread where the thickest part of the wedge is 12.6 nm, since this particular layering gave the best result in

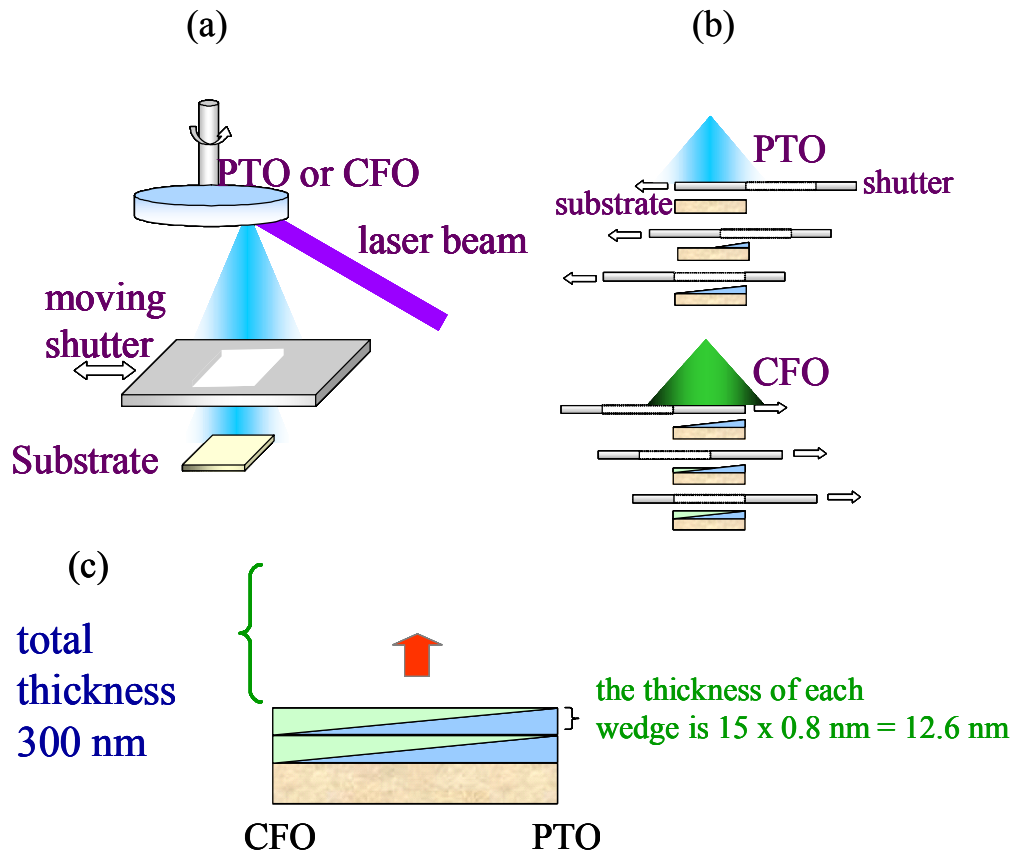


Figure 8.3 A schematic of synthesis of a PTO-CFO composition spread. (a) Laser firing, target switching (PTO & CFO) and the shutter motion are synchronized. (b) A wedge-like thickness gradient is created by the moving shutter during the deposition. (c) The schematic side view of the composition spread, each wedge is 12.6 nm thick.

terms of ferroelectric and magnetic properties. The schematic of the 15x CFO-PTO spread is shown in Figure 8.3 (c). The average composition on the spread is varying

continuously from pure PTO at one end to pure CFO at the other end. The substrate temperature during the deposition was 600 °C, and the oxygen partial pressure was 200 mTorr. The ablation energy was approximately 2 J/cm², and the total thickness at each position on the spread was 300 nm. The spread sample was approximately 6 mm long in the spread direction. Once the samples are fabricated, we first look for regions that are simultaneously ferromagnetic and ferroelectric, then we try to see if we can measure ME effect.

8.3 Characterization of composition spreads

To characterize the CFO-PTO composition spreads we analyzed the magnetic properties using a room temperature scanning SQUID in Neocera Inc., ferroelectric properties using scanning microwave microscopy and structure using a scanning x-ray diffractometer and transmission electron microscopy (TEM). We have also obtained preliminary results on the magnetoelectric effect.

The composition distribution is obtained via WDS (as discussed in Chapter 7). We found that average composition was linearly varying along the spread as designed.

8.3.1 Magnetic properties

Magnetic properties of the composition spreads are analyzed by using a scanning SQUID microscope with the aid of the inversion technique, which was discussed thoroughly in Chapters 5 and 6. As in the case for the FSMA libraries, I used Transform and Matlab software to calculate the magnetic pole density, ρ_m , and to finally obtain the magnetization by integrating ρ_m . Here I will focus on the 15x CFO-PTO composition

spreads. Unlike in the FSMA libraries, in these samples, both in-plane and out-of-plane remanent magnetization were analyzed.

The CFO-PTO composition spread was deposited on a 10 mm x 10 mm substrate. The length of the spread is 6 mm, on one edge there is 2 mm of pure CFO and on the other edge, there is 2 mm of pure PTO. The pure CFO and PTO regions were made for reference. I cut the sample into 4 pieces along the spread direction, so that we have 4 nominally same samples of the same composition spread. I used two pieces, one was magnetized in-plane, and the other was out-of-plane. As I first introduced in Chapter 6, I will use M_{in} as the remanent magnetization of the in-plane magnetized sample, and M_z as the remanent magnetization of out-of-plane sample.

Two samples were scanned at 150 μm away from the SQUID, with the step size of 50 μm in x and y directions. Figure 8.4 (a) shows the field distribution for the in-plane magnetized 15x CFO-PTO composition spread. Here one can see the pure CFO region and the CFO-PTO composition spread region. Even though the entire sample was in-plane magnetized, one can see that pure CFO does not look like it is magnetized in-plane completely. This is because CFO's easy axis is out-of-plane and it does not like to be in-plane magnetized. However, when PTO is added, the anisotropy changes and it becomes easier to magnetize in the in-plane direction. This behavior is discussed later in more details.

Using the inversion technique with the cut-off frequency $k_w = 6$ (which lies in between the upper and lower bounds of the optimal k_w for $z = 150 \mu\text{m}$), I then calculated the magnetic dipole density ρ_m shown in Figure 8.4 (b). To calculate the in-plane magnetization M_{in} I divide the sample into 50 μm strips and integrate ρ_m over each strip.

As discussed in Chapter 6, 50 μm strip is the minimum width of the strip that I can choose, since the step size is 50 μm . It was also shown in Chapter 6 that for z smaller than the sample size, the choice of the integration area does not influence the calculation.

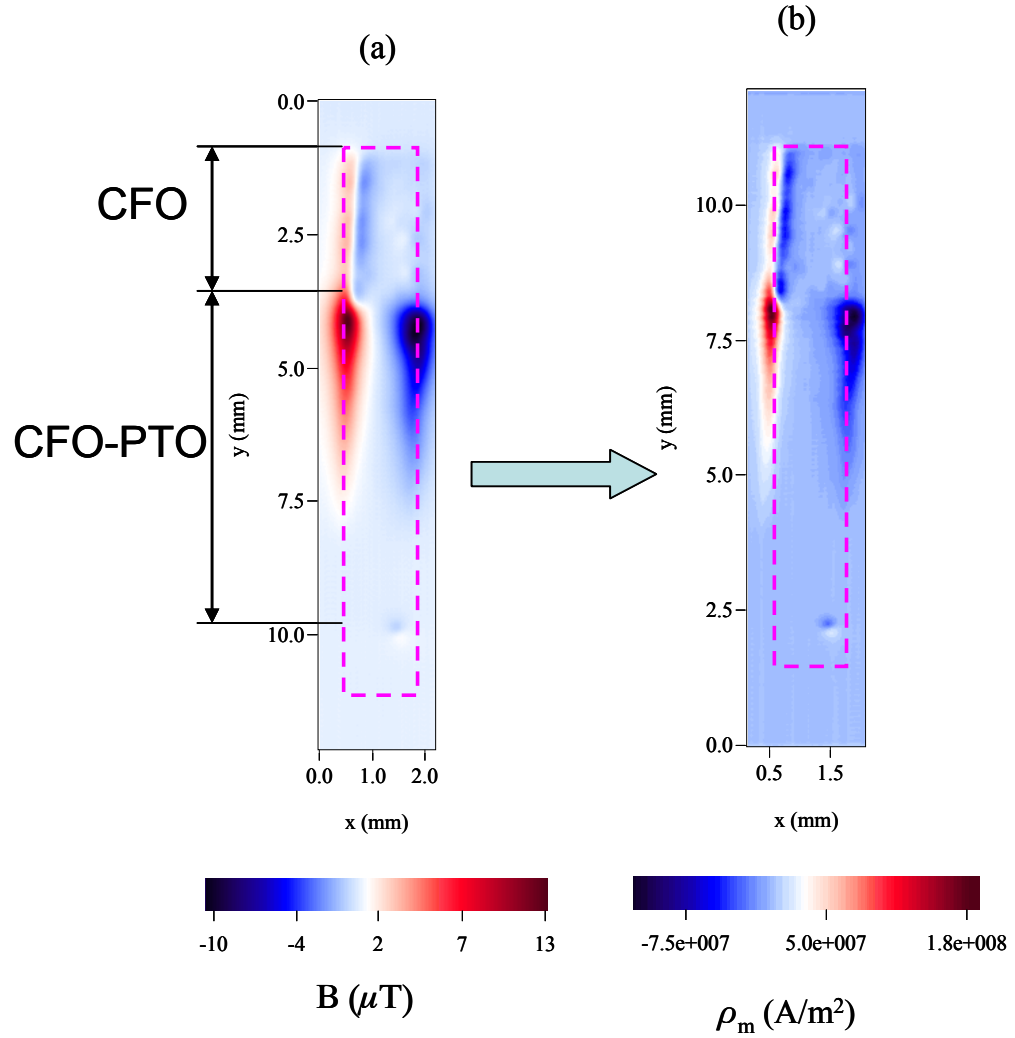


Figure 8.4 CFO-PTO 15x composition spread in-plane magnetized, outlined by a purple dashed line. (a) Two dimensional B field distribution for the sample (b) calculated ρ_m using the inversion technique. In (a) I denoted the regions of the spread and pure CFO.

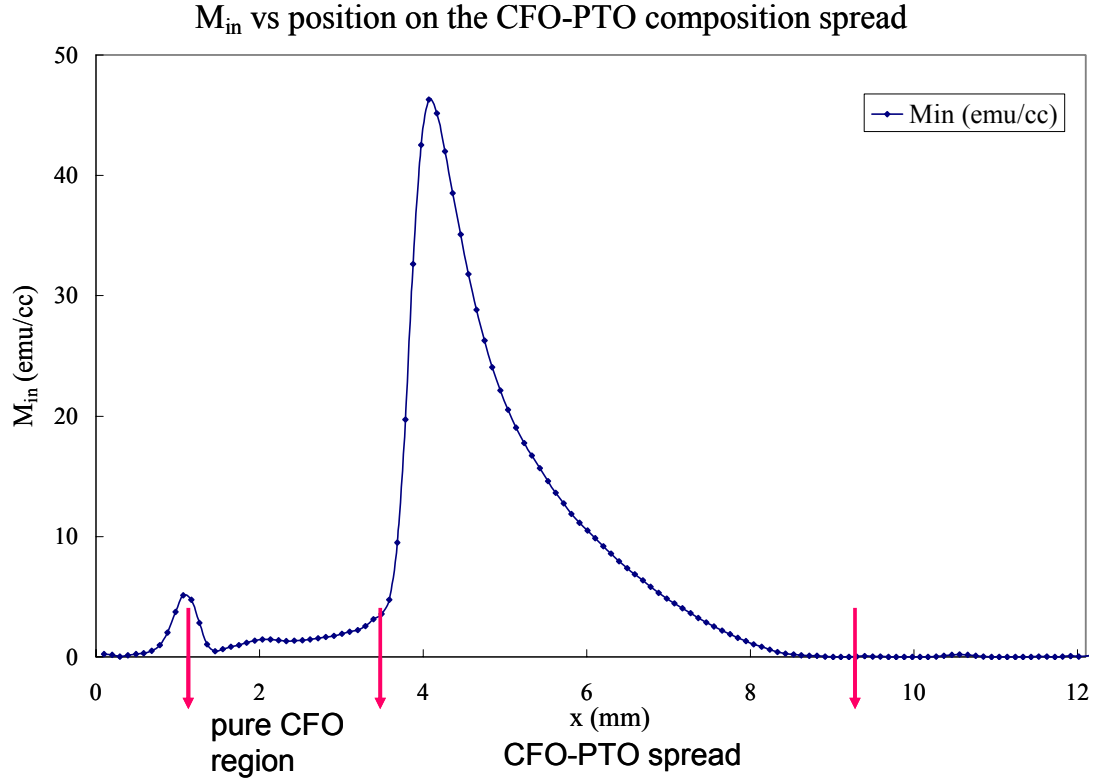


Figure 8.5 M_{in} distribution as a function of position on the CFO – PTO composition spread.

In Figure 8.5, I plot the M_{in} distribution of in-plane magnetized composition spread as a function of position on the scanned chip. Here, one can see the CFO region, and the composition spread region. In addition, there is a maximum in the composition spread region. Once we plot this distribution as a function of average composition, we can explain why this peaking behavior is manifested. This will be explained below.

I also performed the same analysis for the out-of-plane magnetized composition spread. The two dimensional image of the out-of-plane magnetization M_z is shown in Figure 8.6. After integrating the 50 μm strips along the sample, I plot the magnetization distribution as a function of position on the spread.

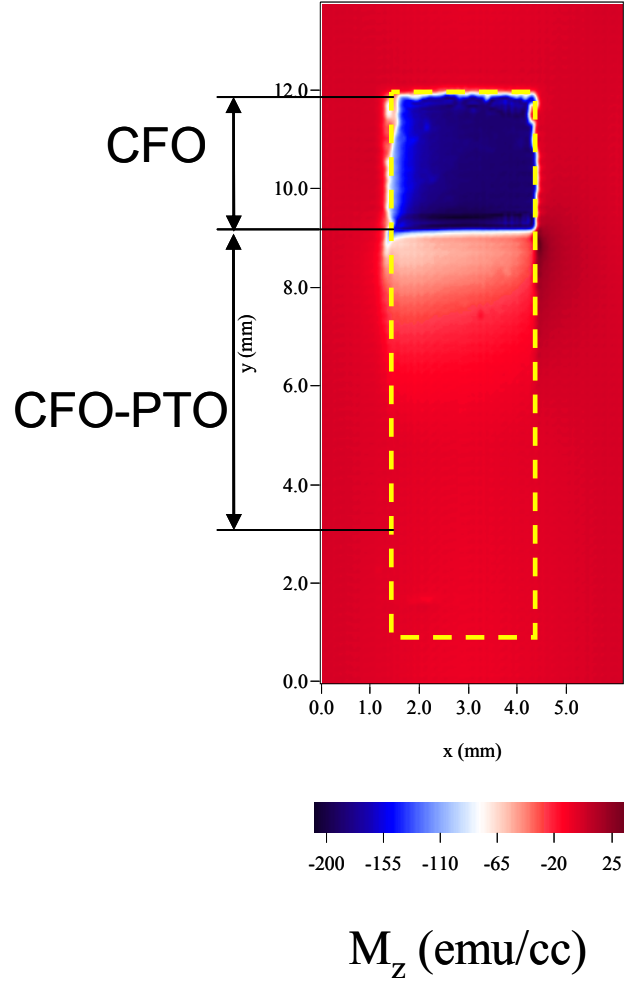


Figure 8.6 CFO-PTO 15x composition spread out-of-plane magnetized, outlined by a yellow dashed line. Shown is the M_z distribution obtained using the inversion technique. Here, I denoted the regions of the spread and pure CFO

Figure 8.7 shows the M_z dependence on the position along the out-of-plane magnetized composition spread sample. Here one can see the pure CFO region (blue) of constant magnetization (which exhibits strong out-of-plane magnetization) and then the magnetization drops.

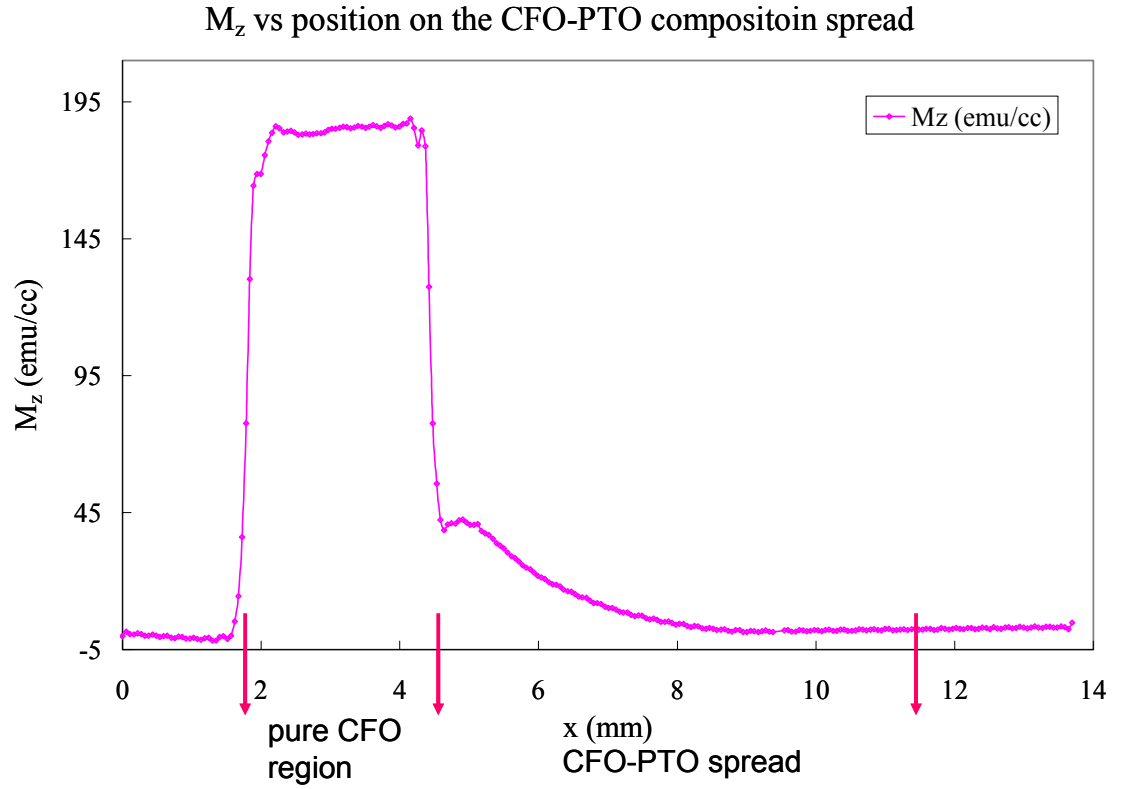


Figure 8.7 M_z distribution as a function of position on the CFO – PTO composition spread.

As the CFO region is finished, the magnetization of the sample drops and then slightly increases as the composition spread starts as shown in Figure 8.7. This dipping effect is possibly an artifact of the inversion technique; as discussed in Chapter 6, when the magnetization distribution changes abruptly the inversion technique gives less precise value for the magnetization. Therefore, in plotting the final magnetization distribution for the out-of-plane magnetized composition spread, I will plot one value for the pure CFO (the average of the CFO region) and the next value is the value at the maximum of the peak after the dip with the corresponding composition.

The goal here is to be able to plot the in-plane and the out-of-plane remanent M distribution as a function of composition. The two distributions of out-of-plane and in-plane magnetization are plotted in Figure 8.8. The remanent magnetization of the individual samples measured with a SQUID magnetometer and the scanning SQUID agree with the reported values of pure CFO films [19].

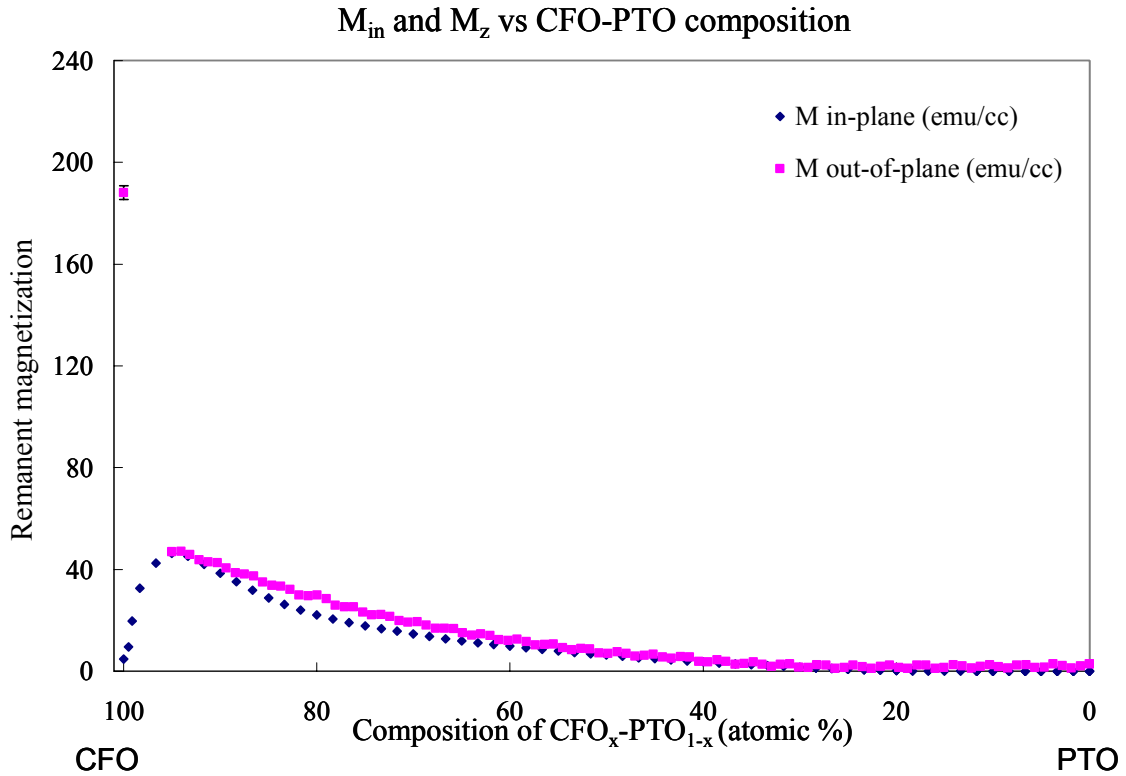
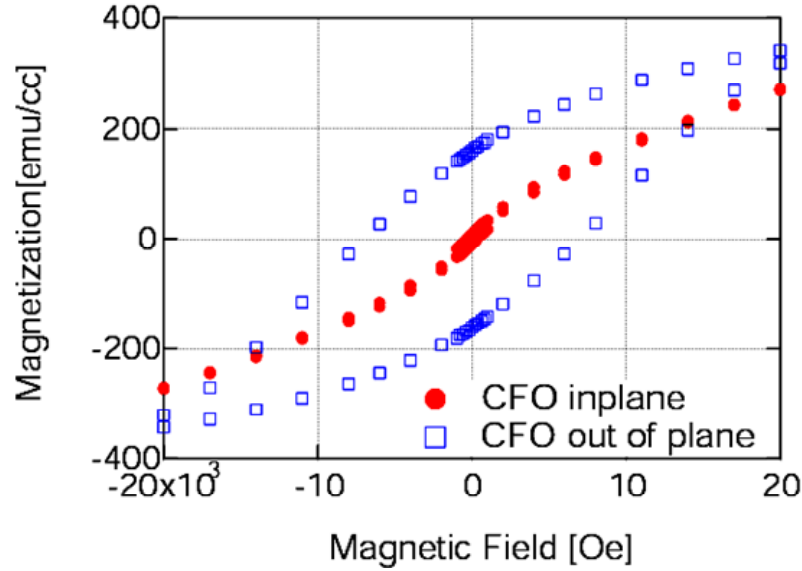


Figure 8.8 Remanent in-plane and out-of-plane M distribution as a function of composition of CFO – PTO composition spread.

It is known that the magnetic easy axis of the CFO is out-of-plane and that it has a large anisotropy [20]. The value of in-plane remanent magnetization of pure CFO is 5-9 emu/cc and that of out-of-plane is 160 emu/cc. Figure 8.9 shows the hysteresis loop in the in-plane and out-of-plane direction for a pure CFO thin film magnetization measured



Pure CFO

Figure 8.9 Hysteresis loop of pure CFO for the in-plane and out-of-plane magnetization measured by the SQUID magnetometer.

by the SQUID magnetometer. As shown in Figure 8.8, as soon as PTO is added, the remanent out-of-plane magnetization decreases and remanent in-plane magnetization increases. The composition where M_{in} is maximal is around 95 % CFO 5% PTO. This indicates that this drop in the out-of-plane magnetization at approximately CFO 95% (composition) appears to be due to the change in the microstructure of CFO. It changes from single phase CFO into a texture interrupted by PTO as revealed by TEM. This is discussed in more detail in Sec. 8.3.3.2. This structural change apparently results in making the material magnetically soft in the in-plane magnetization, and drastically lowers the out-of-plane remanent magnetization. Despite the decaying trend in the magnetization as more PTO is added, it is clear that the material remains magnetic toward the low CFO concentration region. Also, note that low remanent magnetization does not mean that the material is not magnetic.

Figure 8.10 shows the SQUID magnetometer measurement of an out-of-plane magnetization of individual thin film sample with composition $\text{PTO}_{80}\text{-CFO}_{20}$ showing the presence of robust magnetism despite the reduced remanent magnetization at this composition. As will be shown in the next section, this is the composition that we are most interested in to measure the magnetoelectric effect.

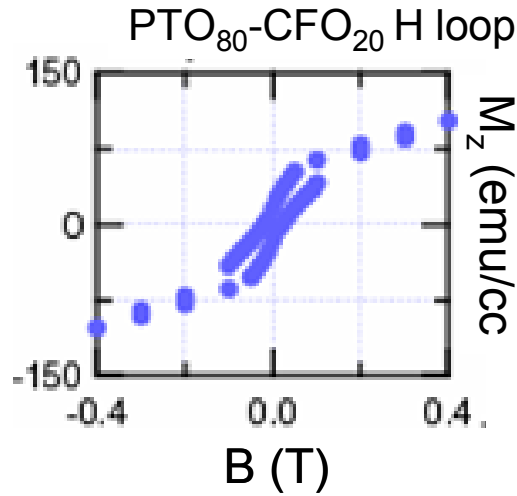


Figure 8.10 Hysteresis loop of the out-of-plane magnetization for the single composition thin film of $\text{PTO}_{80}\text{-CFO}_{20}$.

8.3.2 Dielectric properties

Ferroelectric materials can be characterized by examining the linear and the non-linear dielectric behavior. We used microwave microscope to characterize the linear dielectric constant of the PTO – CFO composition spreads. The near-field scanning microwave microscopy has proven to be a powerful technique for quickly obtaining spatially resolved electrical impedance information non-destructively on a variety of samples [21, 22]. In particular, properties of ferroelectric/dielectric materials are widely

being investigated using microwave microscopy [21, 23, 24]. Quantitative microwave dielectric characterization of thin films using microwave microscopy has been also demonstrated [21, 25]. Previous combinatorial studies with microwave microscopy have been fruitful in identifying novel compositions with improved dielectric properties [26, 27]. In addition, we have modified the microwave microscope with a signal generator and lock-in amplifiers, in order to extract non-linear dielectric signals. Non-linear dielectric signals are a direct reflection of ferroelectricity.

Our microwave microscope is shown in Figure 8.11 (center). It consists of a high- Q $\lambda/4$ coaxial cavity with an STM tip mounted to the center conductor, which protrudes through an aperture in the bottom plate. A sapphire disk with an aperture of the diameter of $100\ \mu\text{m} - 200\ \mu\text{m}$ comparable to the tip is used to shield off the far field.

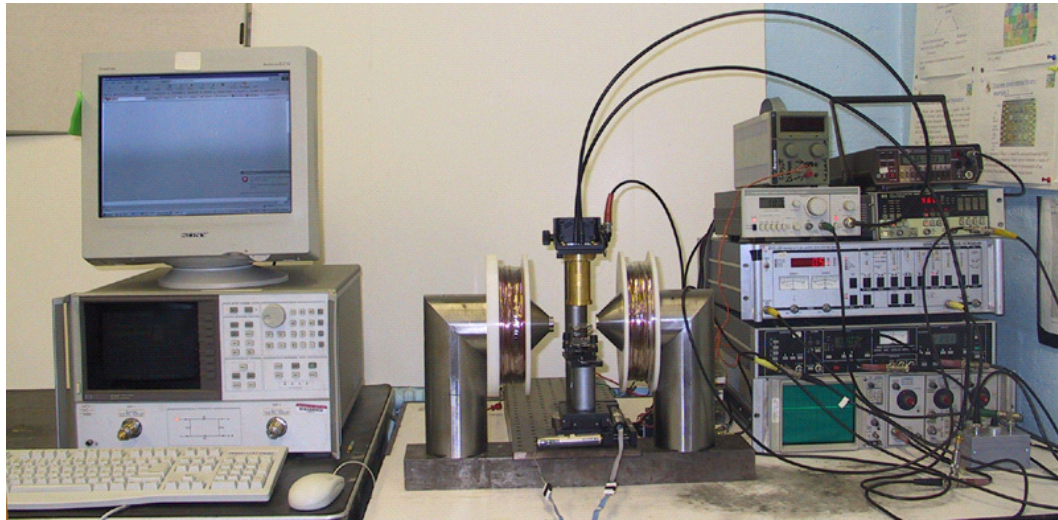


Figure 8.11 A photograph of a scanning tip microwave near-field microscope set-up

The sample under study is placed on the scanning stage. When the tip comes in close proximity to the sample, only the near field, which stays on the tip surface, interacts with

the sample, and we can extract the resonant frequency (f_r) and quality (Q) shifts caused by the local dielectric material. The typical unloaded Q value is ~ 2000 . On the left of the microwave microscope is the network analyzer used to drive the circuit.

Figure 8.12 shows linear dielectric constant at 1 GHz measured across the composition spread. The decaying trend of the linear dielectric constant is as expected, but we also see the unexpected peak at the composition of $(\text{PTO})_{0.8} - (\text{CFO})_{0.2}$.

To measure the non-linear dielectric signal of our samples, microwave microscope was modified. A signal generator was added to apply a low frequency

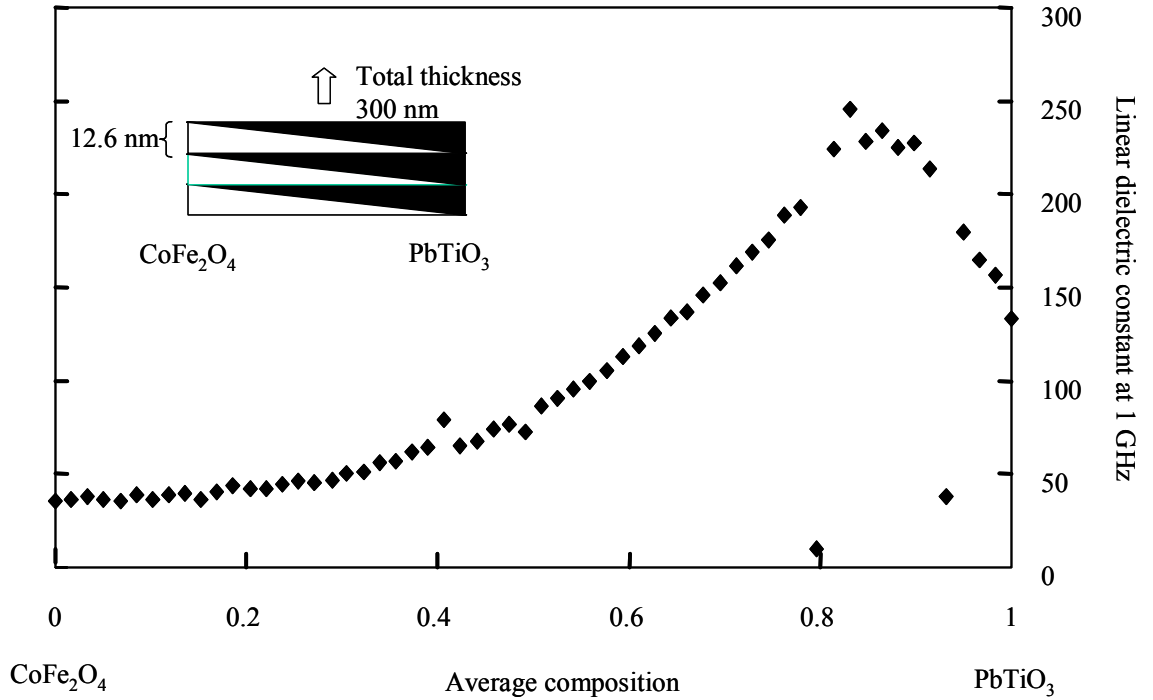


Figure 8.12 Linear dielectric constant measured at 1 GHz as a function of average composition across the spread by the microwave microscope. The thickness of the thick end for each wedge layer is ~ 12.6 nm, which corresponds to the 15x unit cell of CFO and the total thickness is ~ 300 nm (the inset). The highest dielectric constant occurs at the composition of $(\text{PTO})_{0.8} - (\text{CFO})_{0.2}$.

oscillating voltage (1 kHz, 16 V) between the tip and a metallic electrode deposited on the back side of the substrate to modulate the dielectric constant of the sample. A lock-in amplifier was used to modulate the resonant frequency (f_0) (1 GHz) of the microscope resonator, and another lock-in amplifier was used to extract the non-linear dielectric signal when the electric field is applied by a signal generator. Figure 8.13 shows the non-linear dielectric signal at 1 GHz measured across the same spread as the one discussed above (Figure 8.12). As seen in this figure, the non-linear dielectric signal also peaks at the composition of $(\text{PTO})_{0.8} - (\text{CFO})_{0.2}$ and systematically decays toward the two ends. Thus, both linear dielectric constant and non-linear dielectric signal measurements show this peaking behavior.

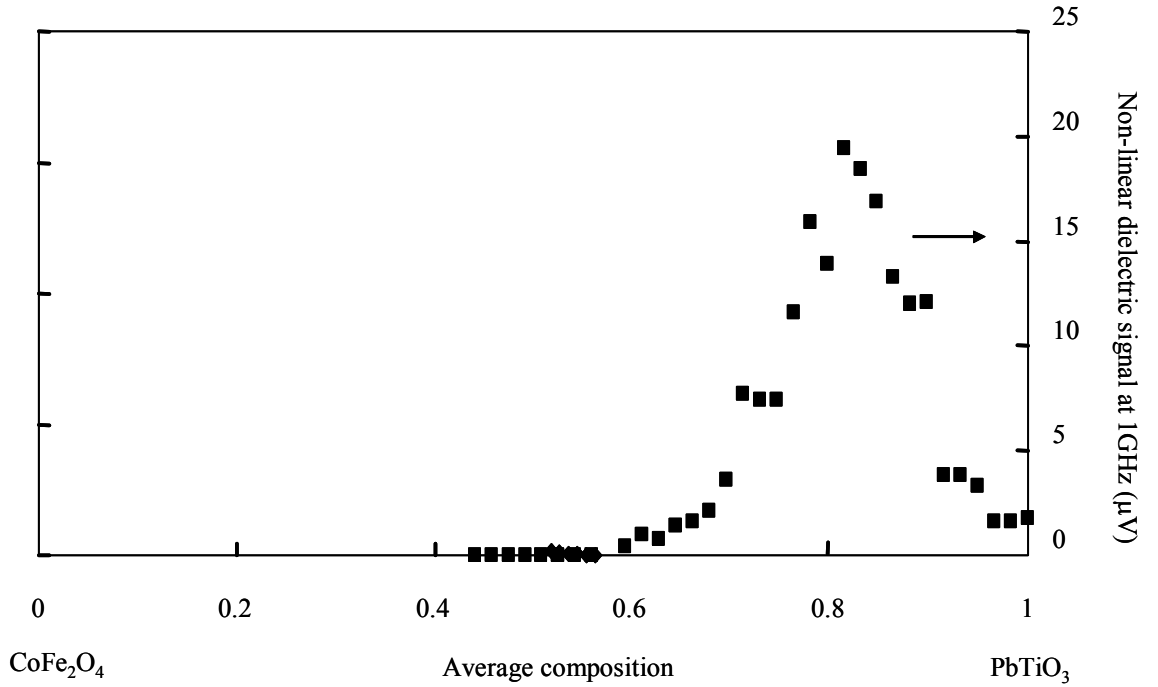


Figure 8.13 The non-linear dielectric signals measured at 1 GHz as a function of average composition across the PTO – CFO spread by the microwave microscope. The sample under study is the same as shown in the inset of Figure 8.12. The highest non-linear dielectric signal also occurs at the composition $(\text{PTO})_{0.8} - (\text{CFO})_{0.2}$.

In order to understand this unexpected peaking behavior in the dielectric constant, we need to understand the microstructure of the composition spread.

8.3.3 Structure

As mentioned before, the crystal structure of CFO is cubic with the lattice constant $a = 0.839$ nm and PTO is tetragonal with $a = 0.390$ nm, $c = 0.415$ nm. To see how CFO and PTO grew together on the MgO substrate and to explore the reasons for the peak in the dielectric constant and the behavior of magnetization, we conducted X-ray and TEM analysis for our 15x composition spreads.

8.3.3.1 X-ray

We performed scanning x-ray microdiffraction using a D8 DISCOVER with GADDS for combinatorial screening by Bruker-AXS (first introduced in Chapter 7). Figure 8.14 (a) shows the x-ray diffraction spectra taken with a $500\ \mu\text{m}$ beam in the 2θ range near the PTO (200) and (002) peaks. The composition range of the spread goes from pure PTO to $\text{PTO}_{70}\text{-CFO}_{30}$ indicating an occurrence of a structural transition. Two peaks of tetragonal PTO (002) and (200) merge when PTO is less than 85%. The continuous shift of (002) tetragonal PTO and (200) tetragonal PTO is observed at $2\theta = 46^\circ$ as the ratio of PTO decreases. The peaks appear to merge at the composition of $\text{PTO}_{80}\text{-CFO}_{20}$. The lattice constant of this composition is in good agreement with the lattice constant of the cubic phase of pure PTO at $\approx 500^\circ\text{C}$.

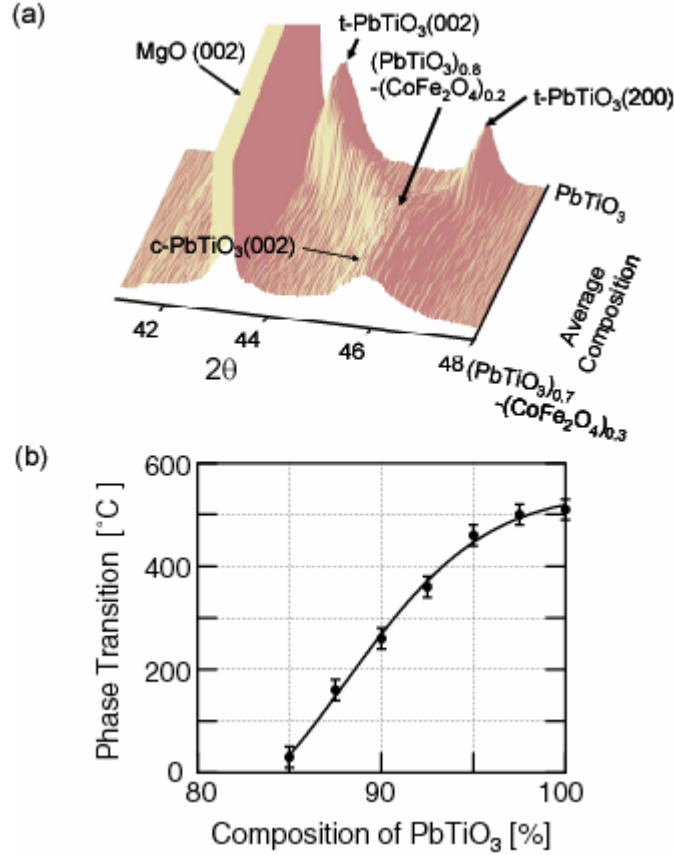


Figure 8.14 (a) X-ray diffraction patterns of the (200) and (002) peaks of PTO–CFO composition spread on MgO substrate. The (002) tetragonal PTO shifts to a higher angle of 46° and the (200) tetragonal PTO shifts to a lower angle of 46° as the ratio of PTO decreases. The two peaks (002) and (200) merge when PTO is less than 85%. (b) Phase transition temperature versus the % of PTO in the composition spread.

We have also performed variable temperature scanning microdiffraction to confirm that indeed the transition temperature (defined to be the temperature at which the tetragonal peaks merge) shifts continuously across the spread in this average composition region (Figure 8.14 (b)). As seen from Figure 8.14 (b), the composition around PTO₈₀-CFO₂₀ has a ferroelectric T_c at room temperature. Thus, the peak in the linear and the non-linear dielectric properties is an indication of the composition where the material is undergoing a ferroelectric transition at room temperature. In addition to the X-ray analysis, we performed TEM on the same sample.

8.3.3.2 TEM

Dr. L.A. Bendersky from NIST in Gaithersburg, MD, has performed cross-sectional high-resolution transmission electron microscopy (HRTEM) at different compositions on the same 15x CFO-PTO composition spread. The images shown in Figure 8.15 (b) and (c) were taken from a spot where the average composition was approximately $\text{PTO}_{80}\text{-CFO}_{20}$. The results shown here are different from what we

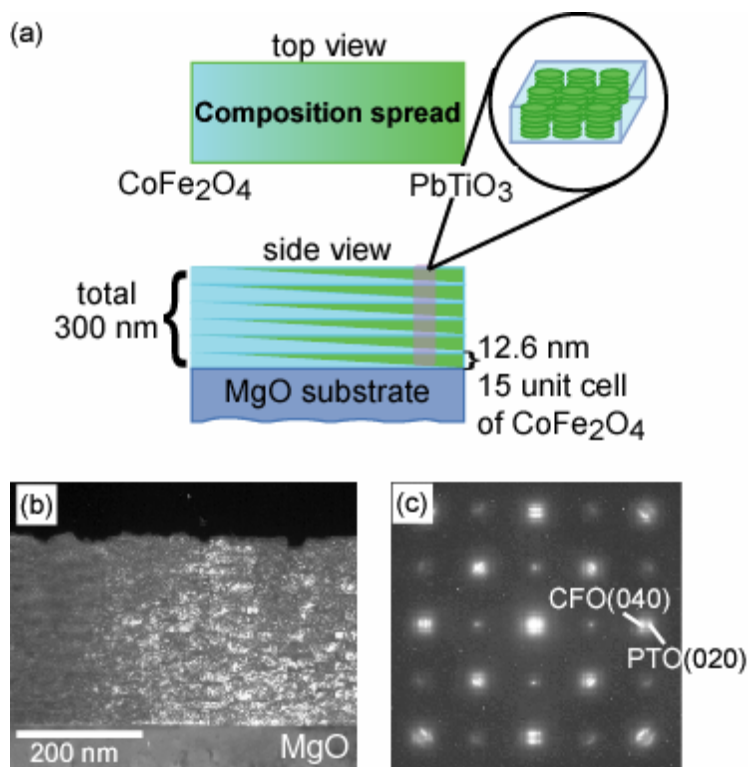


Figure 8.15 (a) A schematic of the composition spread. The thickness of each wedge is 12.6 nm, which corresponds to 15 unit cells of CFO; the total thickness is 300 nm. (b) and (c) show diffraction pattern and an image of cross sectional high-resolution transmission electron micrographs of the $\text{PTO}_{0.8} - \text{CFO}_{0.2}$ film on MgO substrate (incident electron beam is $\langle 100 \rangle$ of MgO).

expected them to be. Here, we see pancake shaped nanograin features of PTO of the order of 30 nm that are embedded in the matrix of CFO. Together they have an overall layered structure. We note that the layered structure is different from the superlattice,

which is what we intended to make originally. Figure 8.15 (c) is an electron diffraction of the same sample as Figure 8.15 (a), taken along the (100) of MgO. Cubic like PTO and CFO are clearly observed to have an epitaxial relationship $\langle 100 \rangle // \langle 100 \rangle$, $\langle 110 \rangle // \langle 110 \rangle$.

Figure 8.16 (a) and (b) shows the cross sectional and electron diffraction TEM of the same sample from a spot where the average composition is $\text{CFO}_{80}\text{-PTO}_{20}$. As discussed in Sec.8.3.1, the magnetic anisotropy of the material is changing as PTO is added to CFO. From TEM, we see that with a small percentage of PTO the layered texture has developed. We attribute the magnetic anisotropy change in CFO to this layering structure, where PTO layer is imbedded into CFO.

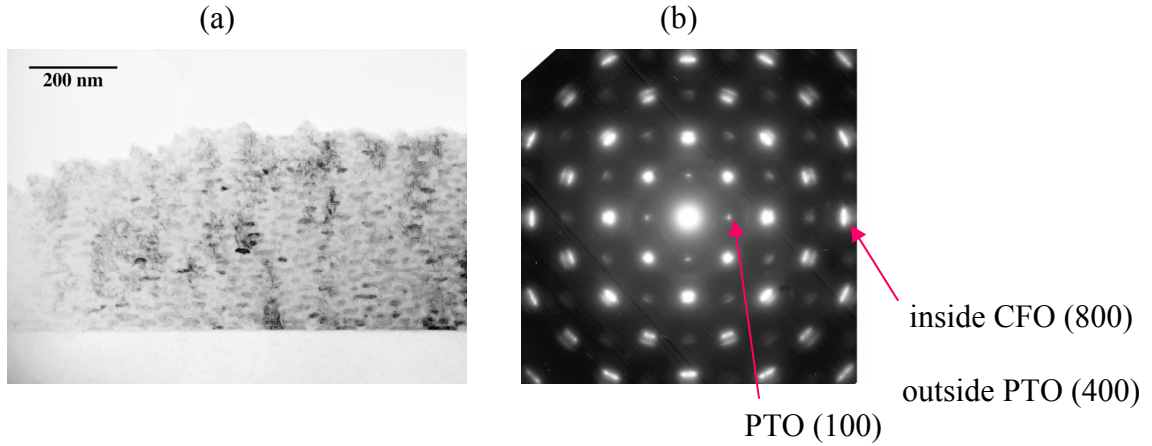


Figure 8.16 (a) and (b) show an image of cross section and a diffraction pattern of high-resolution TEM of the $\text{CFO}_{0.8}\text{-PTO}_{0.2}$ film on MgO substrate (incident electron beam is $\langle 100 \rangle$ of MgO).

The TEM results shown here are still not fully understood, and more investigation is needed. The combination of non-equilibrium laser deposition with diffusion of cations, nucleation of phases, and the eutectic separation are expected to have given rise to the

complex nanostructures observed. The details of the dependence of the formation of nanostructures are still under investigation.

8.3.4 Magnetoelectric effect

Despite the diminished magnetism at the $\text{PTO}_{0.8}$ - $\text{CFO}_{0.2}$ composition, one still sees coexistence of ferromagnetism and ferroelectricity (Figure 8.17). This means that the chance of measuring the magnetoelectric effect is very high. We note that the magnetoelectric effect in the bulk PTO – CFO composites has been reported [13, 28 , 29].

We use the microwave microscope to measure the magnetoelectric effect. Several individual composition samples were made for this purpose. The magnetoelectric coefficient we measure is defined in terms of the change in the non-linear dielectric signal due to an ac voltage applied between the microscope tip and the back of the substrate (16 V) and the equivalent signal induced by the applied magnetic field (ME response signal):

$$\alpha_E = \frac{\partial V_1 / \partial H}{\partial V_2 / \partial V_{film}} \quad \text{Equation 8.3}$$

Here, H is amplitude of the applied AC magnetic field, V_{film} is the voltage drop across the film for the non-linear dielectric measurement, and V_1 and V_2 are ME response signal and the non-linear dielectric signal detected by lock-in amplifiers, respectively [30].

This technique provides a unique method of probing the ME effect in the small region placed underneath the microscope tip without the parallel plate capacitor geometry. For the tip radius of 10 μm , the volume that the tip samples is approximately $60 (\mu\text{m})^3$. The present experiment was carried out at AC 50 Oe at 10 KHz. These

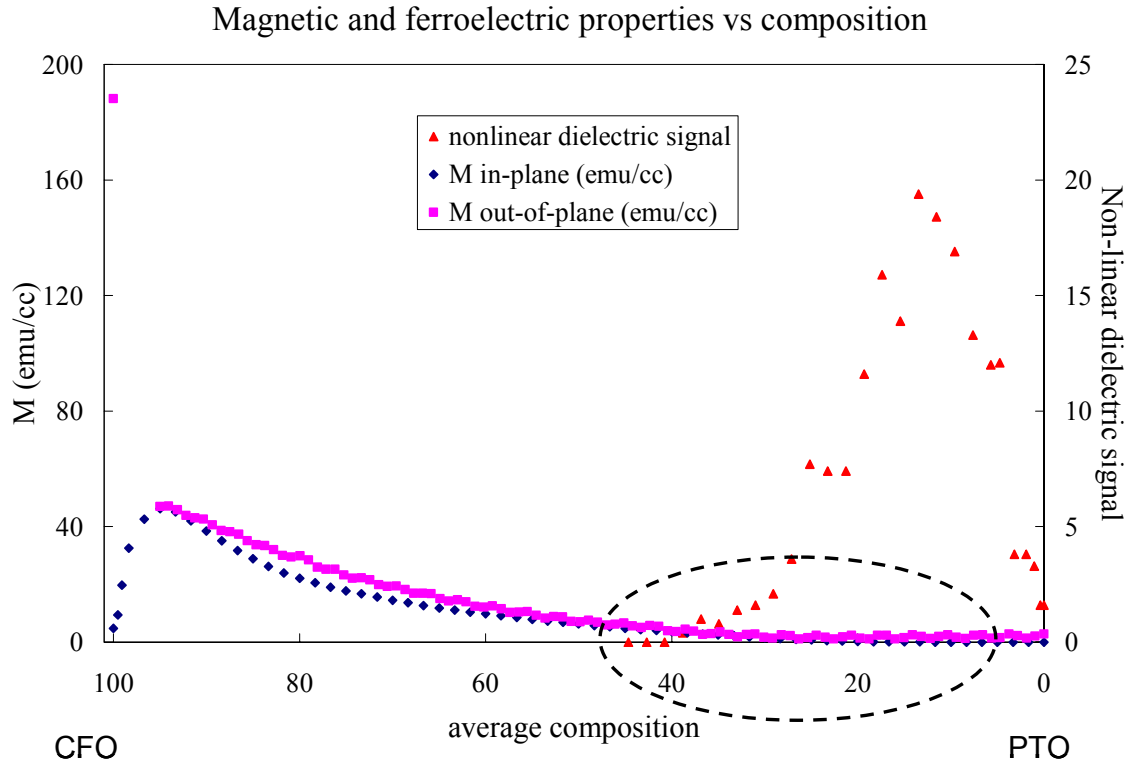


Figure 8.17 Magnetic and ferroelectric properties of the 15x CFO-PTO composition spread. The circled region corresponds to compositions where we expect to measure magnetoelectric effect.

parameters were largely determined by the measurement setup. The value of α_E calculated using Eq. 8.3 for the present nanocomposite $\text{PTO}_{0.8} - \text{CFO}_{0.2}$ composition is 10 – 100 mV/cm Oe. This represents the first time the ME effect is observed in a thin film structure. Harshe et al have predicted that in the present composite configuration with some standard values of physical parameters for CFO and the PTO, the maximum attainable value of α_E is ~ 1 V/cm Oe [28, 31]. Typical reported values of the ME coefficient ranges from 10mV/cm Oe to 1 V/cm Oe. Our measured value is consistent with bulk results.

8.4 Conclusions

We made PTO – CFO composition spreads using the combinatorial PLD flange. I discussed on magnetic characterization of a 15x composition spread, where each alternating layer of CFO and PTO is 12.6 nm thick. Using the optimized parameters of the inversion technique, I calculated in-plane and out-of-plane remanent magnetization distributions for the composition spread. It was shown that as PTO is added to CFO, microstructure of the material changed, CFO's magnetic anisotropy changed. We found that in this spread the compositions between $(\text{PTO})_{0.5} - (\text{CFO})_{0.5}$ and $(\text{PTO})_{0.8} - (\text{CFO})_{0.2}$ exhibit the coexistence of ferroelectricity and ferromagnetism. We have observed the ME effect for a $(\text{PTO})_{0.8} - (\text{CFO})_{0.2}$ sample.

This work represents the first step toward realizing ME thin film devices, which can be operated at room temperature and without the requirement of \sim Tesla field. Such devices can open the door to versatile small smart electronic systems hitherto unexplored whose integrated multifunctionalities can incorporate sensing, actuation and memory capabilities as well as tunable microwave properties.

APPENDICES

Appendix A

Operation of Magma C20

The software, Magma C20 version 3.0, controls the entire scanning SQUID system Magma C20 at Neocera. To start a scan, I load a sample first by taping it to the scanning stage. I run the Acquisition part of the software to start the scan. The first thing that the program does is to tune the SQUID. The flux-locked-loop circuit is different for Magma compared to the scanning SQUID microscope in Prof. Wellstood's lab at the University of Maryland. The electronics (Star Electronics) is of a different design than the Berkeley box. It allows the SQUID to have a larger dynamic range of 20 V than that of the Berkeley box, which is 10 V. The software automatically finds the most suitable setting to have the SQUID working with the best sensitivity and the lowest noise. Figure A.1 shows a panel of all the parameters that the program adjusts before starting the scan. Tuning all the parameters takes about 2-3 minutes. The system checks for the communication with all of its components, the data acquisition board (DAQ) board, the motion control board, all the drivers and motors that drive the stage as well as the motors for the SQUID window, the leveling probe, and the vacuum and temperature control equipment. If there is an error, it will offer options how to fix it.

Then I raise the SQUID window. The window, which is 70 μm to 100 μm away from the SQUID, is raised automatically to a precalibrated position. This distance can be checked accurately (within 1-2 μm) by fitting data from a current carrying wire. This calibration and the calibration between the stage and the window were performed by

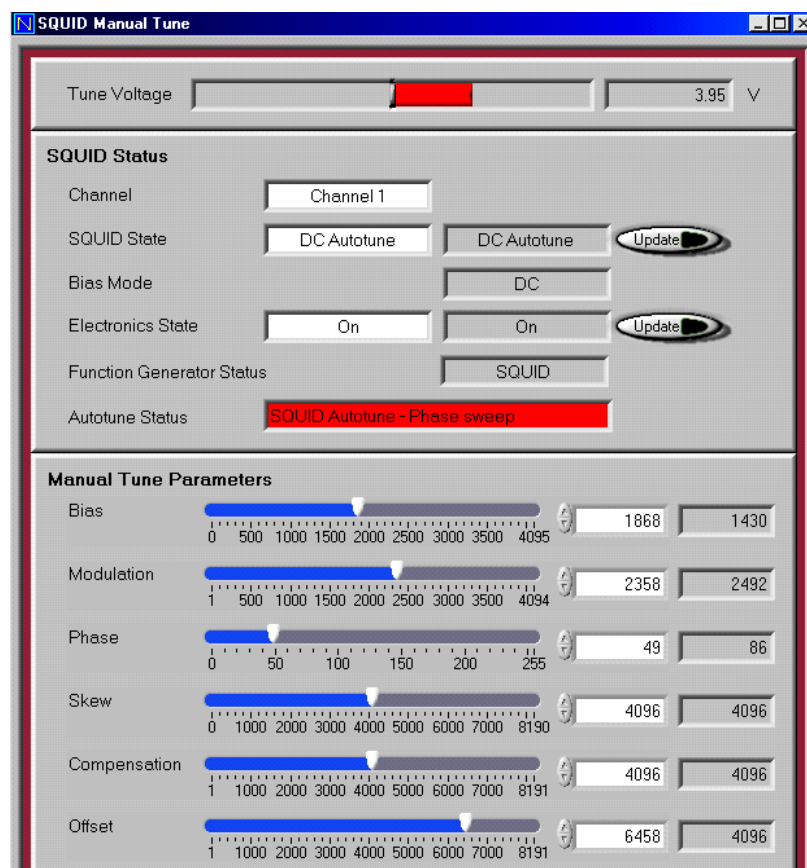


Figure A.1 The panel to tune parameters for the SQUID that are automatically chosen by the software for optimized performance.

a Neocera's engineer using a voltage feedback mechanism and an optical sensor, respectively. After the calibration, the hard stops on the vacuum chamber are set so that even if something goes wrong, the window will not crash into the SQUID. The parameter z , the distance between the SQUID and the sample, is extremely important for accurately calculating magnetization. This is discussed in details in Chapter 6. Previous Magma systems and the university's systems do not have a way to set the distance from the sample to the SQUID. One has to use a micrometer to raise the stage up and down. This can lead to an error larger than $50\text{ }\mu\text{m}$ depending on the backlash of the micrometer. For scanning SQUID systems for which z can not be determined exactly, one can either

approximate the value of z (using an optical microscope) or fit the data from a current carrying wire for each stage setting, which can be very inconvenient and cumbersome.

The next menus are all about preparation of the sample. The sample can be viewed using a CCD camera, which is shown in the zoomed up area in Figure 4.10 of Chapter 4. The sample alignment can be achieved by rotating the scanning stage. The micrometer can be used if the rotation is very small. The sample can also be leveled in this system. There is a leveling probe (Fig 5.10) that records the relative heights of three positions on the sample. From the heights of the three points, the software calculates the sample's tilt. Two knobs located on the stage can be turned in either directions, and the sample tilt is adjusted. This routine of leveling is done until the sample is completely leveled. The accuracy of this leveling is 0.1-0.3 microns in 10 mm in x and y directions. Leveling is another parameter that is extremely important for our measurements. Our combinatorial samples are large in size (3 inch diameter or 10 mm by 10 mm square) compared to small electronic circuit chips. All positions of the compositionally varying samples must be scanned in the same way. Otherwise, one cannot make accurate conclusions about the trend of magnetization.

After setting up the scanning area, the final step is to enter the scanning distance z . As I mentioned, the relative distance from the window to the stage is calibrated but must still be entered. The values of z that I have used range from 150 μm to 300 μm . Unlike in the previous scanning SQUID system, there is no setting of gain here to amplify the signal. The electronics itself adjusts the gain by choosing the right combination of a capacitor and a resistor in the circuit to set a wide dynamic range for the SQUID. The number of lines as well as the step size and the file name to which the data

are saved are entered in the last few menus. The software then calculates the time it takes to scan and starts scanning. The stage positions itself and the data are acquired, displaying the images simultaneously as the sample is scanned.

The SQUID is extremely sensitive I often witnessed sudden changes/jumps in the signal in the data. This happens when the change in the magnetic flux is so large that the operating point of the SQUID shifts to another potential well (Figure 4.2 (c)). When this happens, the SQUID voltage needs to be reset. In such an instance, it is necessary to abort the scan and restart it, and to go back several lines where the jump occurred. Sometimes this jump takes place when a phone rings or someone enters the room. Thus, it is important to monitor the scan closely as it is taking place. Once the data acquisition is complete, I view the two dimensional image of the scan and save the image for future reference. It is helpful to save the image after the scan, since the software that I use to plot the data afterwards (Transform) is different from the software that is used to acquire the data (Labview).

There is a common mistake in plotting the data from scanning probe microscopes. One needs to be careful in correctly orienting the plotted data: it is easy to inadvertently rotate or invert the data. I realized after a few months that the data in Transform was rotated 90° clockwise.

To convert the data in volts that I got from the scan to B field in Tesla correctly, I need to run the SQUID control part of the Magma software. This allows me to calculate the transfer function V/Φ_0 . The data from the SQUID (in volts) are multiplied by the transfer function to obtain the field in the units of micro Tesla.

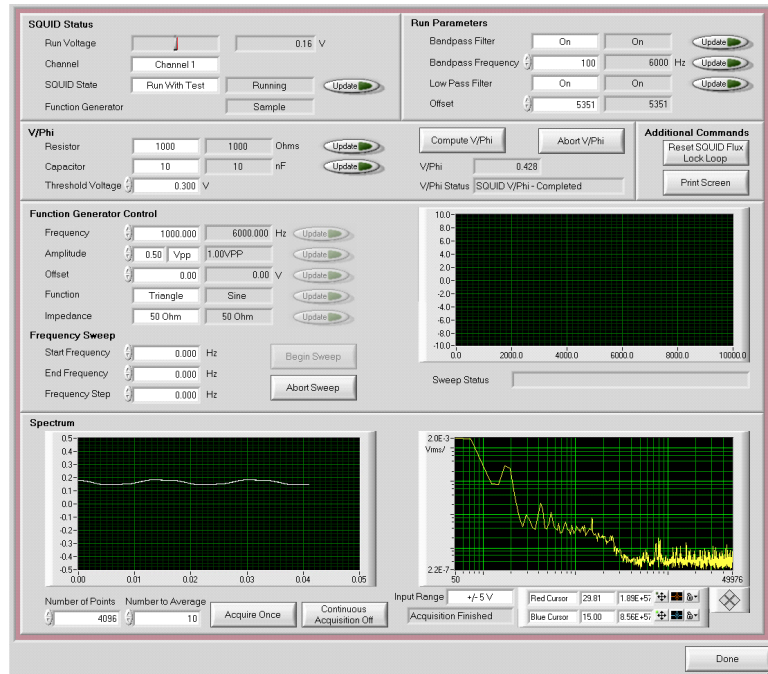


Figure A.2 The SQUID control window from Magma C20 software.

Figure A.2 shows the window where this transfer function is obtained. Also, one can see the frequency sweep of the SQUID.

For more details on operation of Magma C20, one can refer to the manual available at Neocera [1].

Appendix B

Matlab code for calculating magnetization

The file from Transform is saved as a .txt file, in order to be imported into Matlab. The program is shown below. The code is in bold text.

```
[x,y,d,xloc,yloc,m] = readhappyfile('input.txt','output.txt');
```

The main function is named “readhappyfile”

```
function [x,y,d,xloc,yloc,m] = readhappyfile(filename,outfile)
```

where “filename” and “outfile” contain the strings of the input and out file names, respectively. The program reads the input file, which contains the magnetic pole density, ρ_m , and produces the magnetization of a selected area and saves the results in the output file.

```
fid = fopen(filename);  
colstr = fgets(fid);  
c = sscanf(colstr,'%f');  
d = fscanf(fid,'%f',[length(c)+1 Inf]);  
r = d(1,:);  
blah = 1:length(r);  
blah2 = d(:,1);  
d = d(2:length(blah2),:);  
fclose(fid);  
d = d';  
x = c;  
y = r;  
pcolor(x,y,d);  
colormap(hsv);  
shading flat  
colorbar  
disp('Zoom into a place');  
pause
```

It plots the data into a 2 dimensional space; after pressing enter, the crosshair allows the user to select the point from which the grid will be drawn. It finds the uniform spacing in x and y.

```
dx = x(2)-x(1);  
dy = y(2)-y(1);
```

```

dy = abs(dy);
dx = abs(dx);
indx = ceil(1.75/ abs(dx));
indy = ceil(1.75/ abs(dy));
[xr,yr] = ginput(1);
[xind,yind] = findclose(x,y,xr,yr,max(dx,dy));

```

It calls on another function “findclose” to find the shortest distance between the selected point and the next data point in the order it is read into the file. The following code is for the “findclose” function,

```

function [indx, indy] = findclose(x,y,xr,yr,epsilon)
mymin=epsilon^2;
indx = [];
indy = [];
for i=1:length(x)
for j=1:length(y)
    distance = (x(i) - xr).^2 + (y(j)-yr).^2;
    if(distance < mymin)
        indx = i;
        indy = j;
        mymin = distance;
    end
end
end
end

```

Then the program reads the data of the selected area from the input file.

```

fid = fopen(outfile,'w');
lenx = 600;
leny = 600;
for i=-lenx:lenx
    for j=-leny:leny
        % Square definition
        xind1 = floor(xind + indx*i);
        yind1 = floor(yind + indy*j);
        xind2 = floor(xind1 + indx);
        yind2 = floor(yind1 + indy);
        if(xind1<1 | yind1<1 |xind2<1 | yind2<1 | xind2>length(x) |
yind2>length(y) | xind1>length(x) | yind1>length(y))
            continue;
        end
        xr1 = x(xind1);
        yr1 = y(yind1);
        xr2 = x(xind2);
        yr2 = y(yind2);
        line([xr1 xr2],[yr1 yr1]);
        line([xr1 xr2],[yr2 yr2]);
        line([xr1 xr1],[yr1 yr2]);
        line([xr2 xr2],[yr1 yr2]);
        littledata = d([yind1:yind2],[xind1:xind2]);
    end
end

```

```

littlex = x([xind1:xind2]);
littley = y([yind1:yind2]);

```

It defines the square and extends it over the desired area as a grid from the index provided earlier, 1.75 mm x 1.755 mm from the point closest to the selection point; initial starting position is xind and yind.

```

[m(j+leny+1,i+lenx+1)] =
magnetization_out(littlex,littley,littledata);
xloc(i+lenx+1) = (x(xind1) + x(xind2))/2;
yloc(j+leny+1) = (y(yind1) + y(yind2))/2;
fprintf(fid,'%f %f %f\r\n',xloc(i+lenx+1),yloc(j+leny+1),
m(j+leny+1,i+lenx+1));
end
end
fclose(fid);

```

It calls on another function “magnetization” that integrates the area inside each square; a new set of x and y, xloc and yloc, are recorded together with the m value into a file. The following code is for “magnetization” function.

```

function m = magnetization(x,y,data)
x = x*1e-3; % millimeters to meters
y = y*1e-3;
dx = x(2) - x(1);
dy = y(2) - y(1);
l = max(x) - min(x)+dx; %or specify
w = max(y) - min(y)+dy;
%xbar = mean(x);
%ybar = mean(y);
my = 0;
mx = 0;
%mz = 0;
totalpole=0;
for i=1:length(x)
    for j=1:length(y)
        my = my + data(j,i).*x(i).*dx.*dy;
        %my = my + data(j,i).*(x(i) - xbar).*dx.*dy;
        %mz = mz + data(j,i).*dx.*dy;
        mx = mx + data(j,i).*y(j).*dx.*dy;
        %mx = mx + data(j,i).*(y(j) - ybar).*dx.*dy;

        totalpole = data(j,i) + totalpole;
    end
end
m = sqrt(mx.^2 + my.^2);
m=m/(0.00175*0.00175*1000);

```

Appendix C

Transform macros for the inversion technique

As I have mentioned in Chapters 6, 7 and 8, the inversion technique is ideal for calculating magnetization of combinatorial samples. It is quick, convenient, and as shown previously gives an accurate value of M not only for uniformly magnetized thin films, but also for combinatorial libraries and composition spreads whose magnetization is continuously varying in the composition phase space.

The macros that were used to calculate the magnetization density as well as M are written in Transform (Fortner Research LLC) software. Transform allows to perform mathematical functions on the data using macro functions in a built-in notebook page. The data is imported in the form of a 2-dimensional array of voltages obtained from the scanning SQUID microscope. These macros were first used by Guy Chatrathorn [1] and Erin Fleet [2]. I modified some of the parameters and the code to suit to my application. The code is in bold text.

C.1 For converting $B_z(x, y, z)$ to $\rho_m(x, y)$

*** Name of macro: hanning-rho-in**

```
blah1 = extractselection(currentdataset)  
blah = getdatasetname(currentdataset)  
B = var(blah)* 2.143/0.44375*1e-6
```

After selecting the data that one wants to use to calculate ρ_m , the data in volts is converted to field in the units of μT . The constant that is multiplying the data obtained directly from the scanning SQUID is called the transfer function, it has units of $\mu T/V$ and

it is calculated from the area of the SQUID and V/Φ_0 value. $\Phi_0 = h/2e = 2.07 \times 10^{-15} \text{ T} \cdot \text{m}^2$, the area of the SQUID in Neocera varies from $30 \mu\text{m}^2$ - $35 \mu\text{m}^2$, and the value of V/Φ_0 can be obtained from electronics, where it varies from 0.4 to .55.

```
B_r=resamplerows (resamplecols(B,256),256)
xrange=abs(colrange(B_r))
yrange=abs(rowrange(B_r))
B_c = complex(B_r , 0*B_r)
```

For the FFT in Transform the data needs to be resampled into a $2n \times 2m$ matrix. x and y ranges of the data are established. The complex matrix is established.

```
B_fft = fft(B_c,1)
B_fft_re = real(B_fft)
B_fft_im = imag(B_fft)
```

FFT is performed returning a complex matrix for $b(k_x, k_y)$. Then the real and imaginary components are split.

```
kx = c(B_fft_re)
ky = r(B_fft_re)
k = sqrt(ky**2 + kx**2)
```

The k matrices are constructed.

```
kw =10
z=.15
d = 6500*1e-10
pi = acos(-1.)
mu = 4*pi*1e-7
```

All the variables are defined here. The cutoff frequency k_w is in the unit of $1/\text{mm}$, z the SQUID to sample separation in the unit of mm , d the thickness of the film in the unit of m , and μ , the permeability of free space in SI unit.

```
flt = (2/(mu*d))*exp(2*pi*k*z)
filter= zapnan(zapnan((1/flt)*flt,0)*flt,0)
```

The exponential factor of Eq. 5.18 is calculated. Note that in Transform, $k_x = 1/x$ not $2\pi/x$, therefore, the factor 2π must be included wherever k is. This exponential factor can become larger than the software can handle, therefore, Transform will assign a string “Inf”(infinity) to a very large value, which is invalid in further steps. The string “Inf” is eliminated and set to zero, when the value of k is very large.

```
knew = LEmask(k,kw)*k
window = LTmask(0.5*(1 + cos(pi*knew/kw)),1)*0.5*(1 + cos(pi*knew/kw))
```

The Hanning window is defined here in order to eliminate spatial frequencies higher than k_w .

```
Bfft_filter_win_re = B_fft_re*filter*window
Bfft_filter_win_im = B_fft_im*filter*window
rho_k = complex(Bfft_filter_win_re, Bfft_filter_win_im)
rho= rowscales(colscales(real(fft(rho_k,-1)),0,xrange),yrange,0)
graph=interpolated("rho")
```

The complete Eq. 5.21 is reconstructed where $b(k_x, k_y)$, the window and the Fourier of the Green’s function are multiplied. The real and imaginary parts are then put together and the complex $\rho(k_x, k_y)$ matrix is constructed. Inverse FFT is applied and $\rho(x, y)$ is obtained and plotted as a 2 dimensional false color image.

```
user_interactive=false
call close("B")
call close("B_fft")
call close("B_fft_re")
call close("B_fft_im")
call close("ky")
call close("kx")
call close("k")
call close("rho_k")
call close("Bfft_filter_win_im")
call close("Bfft_filter_win_re")
call close("redkx")
```

```

call close("redky")
call close("factor")
call close("flt")
call close("filter")
call close("knew")
call close("window")
call close("B_r")
call close("B_c")
user_interactive=true

```

For convenience all the data sheets except for ρ (x, y) will be closed after the program is ran.

C. 2 For integrating ρ_m (x, y) to obtain M_{in} (x, y)

***Name of macro: mag_in**

```

blah=extractselection(currentdataset)
heeehee=getdatasetname(currentdataset)

```

The data for which M_{in} needs to be calculated is selected; it is either a strip, or a square of all of the data.

```

xarray=c(var(heeehee))*0.001
L = max(xarray)-min(xarray)
deltax=L/cols(var(heeehee))
*newxarray=xarray-mean(xarray)

```

The x values are converted to meters and the length in x and Δx are calculated.

```

yarray=r(var(heeehee))*0.001
w = max(yarray)-min(yarray)
deltay=w/rows(var(heeehee))
*newyarray=yarray-mean(yarray)

```

The y values are converted to meters and the length in y and Δy are calculated

```

dyp = colsum(var(heeehee))*deltay
mx = rowsum(dyp*xarray)*deltax
dyp = rowsum(var(heeehee))*deltax
my = colsum(dyp*yarray)*deltay

```


The summation in x and in y is performed where m_x and m_y are calculated separately.

```
m1 = sqrt(my*my + mx*mx)
m = m1/(L*w*1000)
call prompt("Magnetization in emu/cc is ",mean(m))
```

Then M_{in} is calculated by $\frac{\sqrt{m_x^2 + m_y^2}}{A \times 1000}$. The reason why I divide by 1000 is to convert

M_{in} from A/m to emu/cc. Since all the operations are done with matrices, M_{in} also is a matrix with all of its elements equal to each other.

```
user_interactive=false
call close(heeehee)
call close("dyp")
call close("dyp")
call close("xarray")
call close("yarray")
call close("mx")
call close("my")
call close("m1")
call close("m")
*call close("newxarray")
*call close("newyarray")
user_interactive=true
```

For convenience, all the data sheets will be closed after the user presses OK at the M_{in} prompt.

C.3 For converting $B_z(x, y, z)$ to $m_z(x, y)$

This macro is the same as the macro in 0, except that the Fourier Greens function is different. Also in the end, the matrix that is calculated is $m_z(x, y)$ which is the 2 dimensional distribution of out-of-plane magnetization. To find M_z one must still integrate the data, this is discussed in 0

*** Name of macro: mz-out**

```

blah = extractselection(currentdataset)
blah1 = getdatasetname(currentdataset)
B= var(blah1)* 2.143/0.44375*1e-6

B_r=resamplerows(resamplecols(B,256),256)
xrange=abs(colrange(B_r))
yrange=abs(rowrange(B_r))
B_c = complex(B_r , 0*B_r)

B_fft = fft(B_c,1)
B_fft_re = real(B_fft)
B_fft_im = imag(B_fft)

kx = c(B_fft_re)
ky = r(B_fft_re)
k = sqrt(ky**2 + kx**2)
redkx=zapnan(kx/k,1)
redky=zapnan(ky/k,1)

kw =10
z=.15
pi = acos(-1.)
d = 3000*1e-7
* d is in mm
mu = 4*pi*1e-7
flt = (2/(mu*2*pi*k*d))*exp(2*pi*k*z)
filter=zapnan(zapnan((1/flt)*flt,0)*flt,0)

knew = LEmask(k,kw)*k
window = LTmask(0.5*(1 + cos(pi*knew/kw)),1)*0.5*(1 + cos(pi*knew/kw))
****Hanning window

Bfft_filter_win_re = B_fft_re*filter*window
Bfft_filter_win_im = B_fft_im*filter*window

m_k = complex(Bfft_filter_win_re, Bfft_filter_win_im)

m_1=(rowscales(colscales(real(fft(m_k,-1))),0,xrange),yrange,0))/1000
mout=interpolated("m_1")

user_interactive=false
call close("B")
call close("B_fft")
call close("B_fft_re")

```

```

call close("B_fft_im")
call close("ky")
call close("kx")
call close("k")
call close("m_k")
call close("Bfft_filter_win_im")
call close("Bfft_filter_win_re")
call close("redkx")
call close("redky")
call close("flt")
call close("filter")
call close("window")
call close("B_r")
call close("B_c")
call close("knew")
user_interactive=true

```

C.4 For integrating m_z to obtain M_z

*** Name of macro-Mzout**

```

blah=extractselection(currentdataset)
heeehee=getdatasetname(currentdataset)

```

The data for which M_z needs to be calculated is selected; it is either a strip, or a square or all of the data.

```

xarray=c(var(heeehee))*0.001
L = max(xarray)-min(xarray)
deltax=L/cols(var(heeehee))

```

The x values are converted to meters and the length in x and Δx are calculated.

```

yarray=r(var(heeehee))*0.001
w = max(yarray)-min(yarray)
deltay=w/rows(var(heeehee))

```

The y values are converted to meters and the length in y and Δy are calculated.

```

dyp = colsum(var(heeehee))*deltay
m = rowsum(dyp)*deltax
Mz =m/(L*w)
M_out=mean(Mz)
call prompt("M in emu/cc is ",(M_out))

```

The summation in x and in y is performed where m_z is calculated. The final value is divided by area. Here, I do not need to divide M_z by 1000 in order for the units to be emu/cc, since in the previous program the thickness was in mm.

```
user_interactive=false  
call close(heeehee)  
call close("dyp")  
call close("xarray")  
call close("yarray")  
call close("m")  
call close("Mz")  
user_interactive=true
```

For convenience, all the data sheets will be closed after the user presses OK at the M_z prompt.

Appendix D

Mathematica code using simple models

In Chapters 5, I discussed two simple models that can be used to calculate magnetization of a uniformly unidirectional magnetized sample. For in-plane magnetization calculation, line charge model was used, while, for out-of-plane magnetization the current loop model was used.

The Mathematica (Wolfram Res.) software is used to fit one line of magnetic field data. M is a fitting parameter that is extracted from the fit. The code is in bold text.

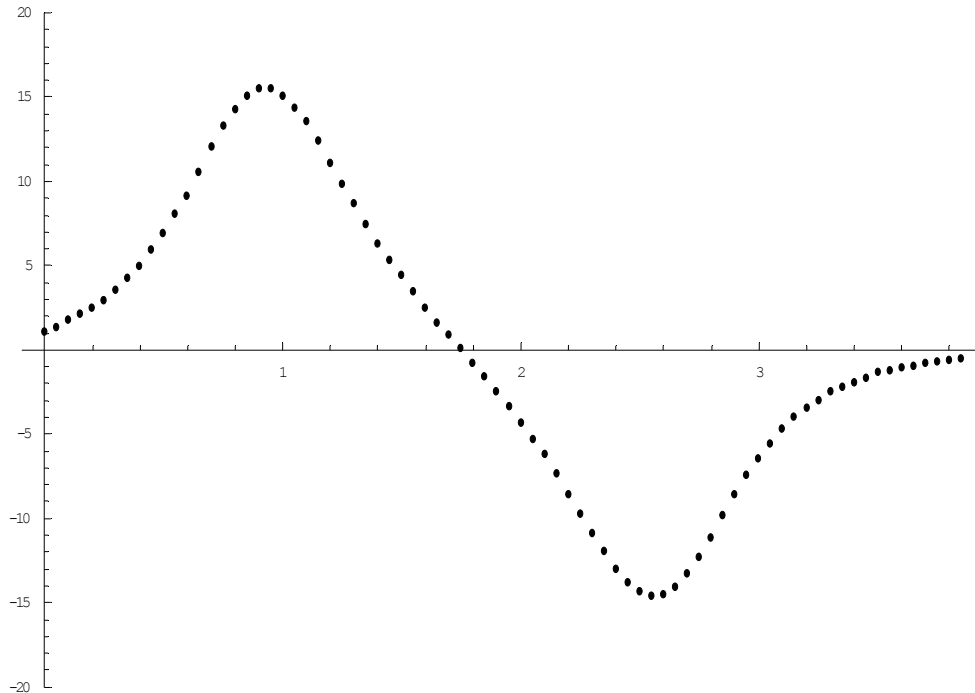
D.1 For in-plane magnetization case

<<Statistics`NonlinearFit`

data=ReadList["minghui.txt",Number,RecordLists→True]

{ {0,1.10914},{0.05,1.38345},{0.1,1.77602},{0.15,2.13828},{0.2,2.47967},{0.25,2.96467},{0.3,3.60272},{0.35,4.31134},{0.4,5.02245},{0.45,5.93182},{0.5,6.97885},{0.55,8.05917},{0.6,9.19962},{0.65,10.5587},{0.7,12.047},{0.75,13.3415},{0.8,14.3016},{0.85,15.0594},{0.9,15.535},{0.95,15.5484},{1,15.1076},{1.05,14.4223},{1.1,13.5532},{1.15,12.4465},{1.2,11.1481},{1.25,9.89035},{1.3,8.70667},{1.35,7.49615},{1.4,6.33334},{1.45,5.3211},{1.5,4.42812},{1.55,3.47054},{1.6,2.48265},{1.65,1.64384},{1.7,0.91633},{1.75,0.1456},{1.8,-0.71558},{1.85,-1.56085},{1.9,-2.41179},{1.95,-3.33737},{2,-4.29842},{2.05,-5.22768},{2.1,-6.18128},{2.15,-7.3267},{2.2,-8.55163},{2.25,-9.71791},{2.3,-10.8141},{2.35,-11.889},{2.4,-12.935},{2.45,-13.755},{2.5,-14.2941},{2.55,-14.5426},{2.6,-14.481},{2.65,-14.0362},{2.7,-13.2834},{2.75,-12.2503},{2.8,-11.074},{2.85,-9.77953},{2.9,-8.52131},{2.95,-7.43801},{3,-6.46055},{3.05,-5.52186},{3.1,-4.6587},{3.15,-3.98436},{3.2,-3.45613},{3.25,-2.93485},{3.3,-2.47137},{3.35,-2.1424},{3.4,-1.89056},{3.45,-1.59713},{3.5,-1.32282},{3.55,-1.1643},{3.6,-1.06541},{3.65,-0.89745},{3.7,-0.7285},{3.75,-0.64849},{3.8,-0.61718},{3.85,-0.50836} }

fig=ListPlot[data,PlotRange→{-20,20}]



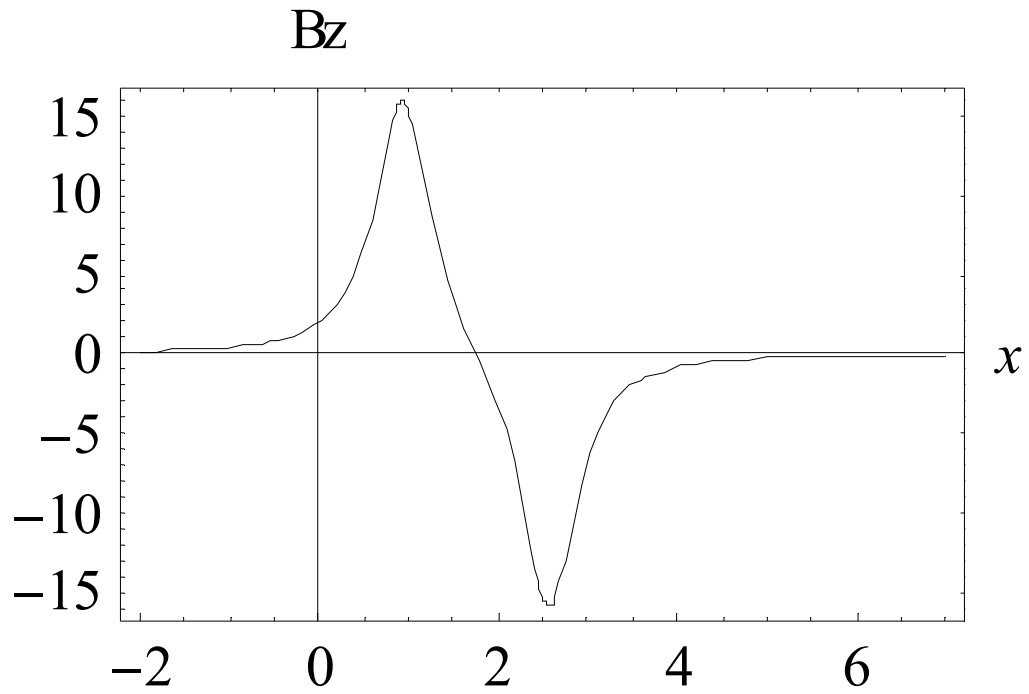
```

-Graphics-
mu0=4*Pi*10^(-7)
      pi
      2500000
z=3.76*10^(-1)
0.376
x0p=.93
0.93
x0m=2.56
2.56
d=1.5*10^(-4)
0.00015
fn=NonlinearFit[data,mu0*M*d/(2*Pi)*z*(1/((x-x0p)^2+z^2) -
1/((x-x0m)^2+z^2)),x,{M}]
2.30779  $\left( -\frac{1}{0.1369 + (-2.56 + x)^2} + \frac{1}{0.1369 + (-0.93 + x)^2} \right)$ 

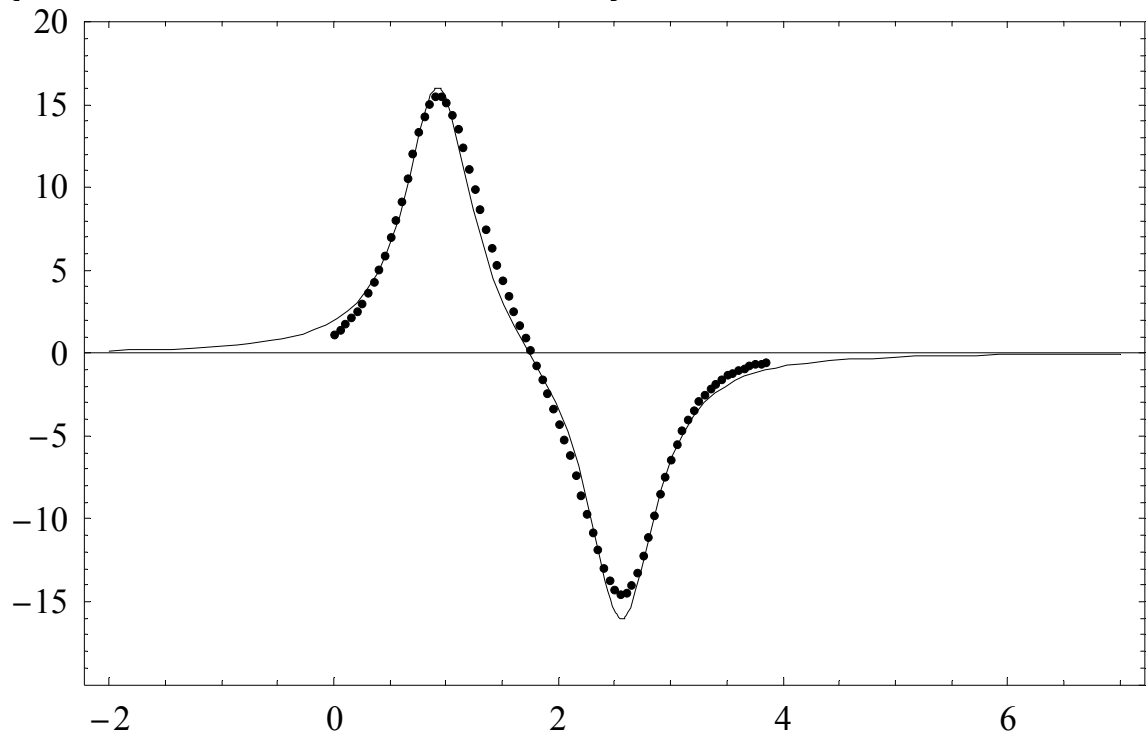
2.3077895343875103`/mu0/d*(2*Pi)/z*10^(-6)/1000
204.591

fg2=Plot[fn,{x,-
2,7},Frame->True,AxesLabel->TraditionalForm/@{x,Bz},TextStyle
->{FontFamily->"Times",FontSize->14}]

```



```
-Graphics-
Show[fig,fg2,Axes→{True,False},Frame→True,TextStyle-
>{FontFamily→"Times",FontSize→22}]
```



```
-Graphics-
```

This is SmCo₅ thin film sample, which is discussed in Chapter 5, Sec. 5.3.1, and the sample is shown in Figure 5.8. The value of M_{in} here is 204.6 emu/cc.

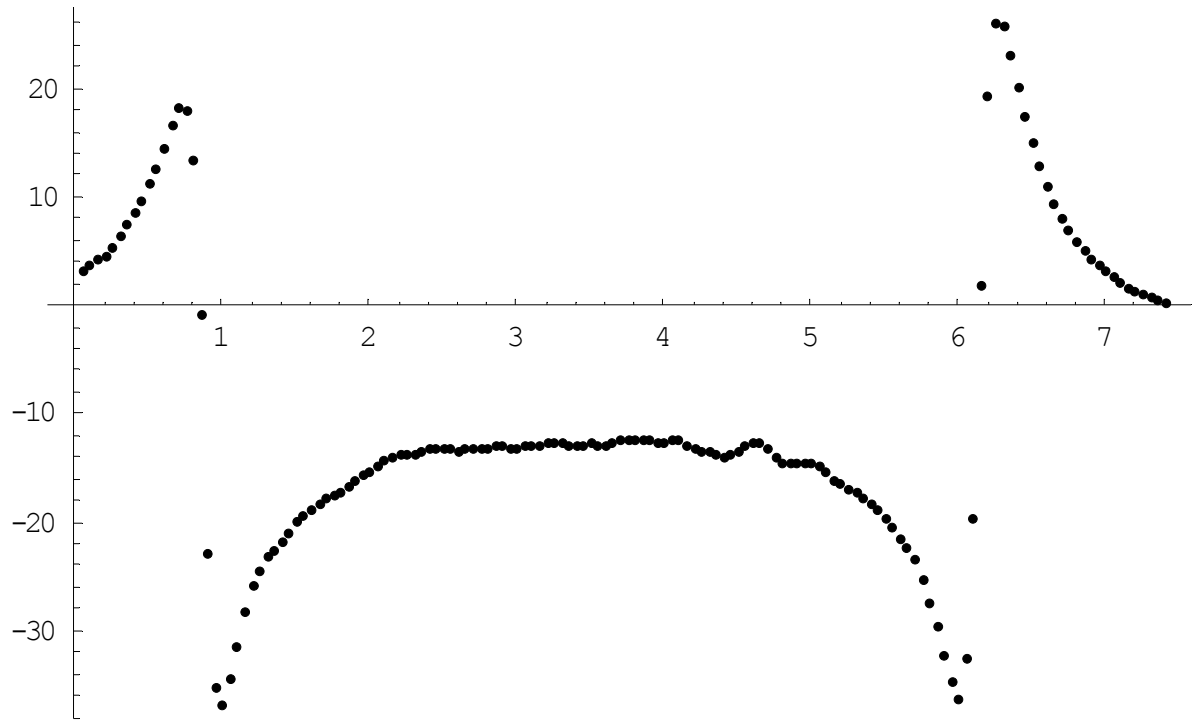
D.2 For out-of-plane magnetization case

```
<<Statistics\NonlinearFit\
```

```
data=ReadList["cfoout-5mm.txt",Number,RecordLists→True]
```

```
{ {0.05,3.284}, {0.1,3.794}, {0.15,4.212}, {0.2,4.677}, {0.25,5.4
47}, {0.3,6.433}, {0.35,7.485}, {0.4,8.567}, {0.45,9.813}, {0.5,1
1.214}, {0.55,12.745}, {0.6,14.555}, {0.65,16.632}, {0.7,18.211}
, {0.75,17.979}, {0.8,13.445}, {0.85,-0.875}, {0.9,-
22.703}, {0.95,-35.297}, {1,-36.659}, {1.05,-34.423}, {1.1,-
31.337}, {1.15,-28.131}, {1.2,-25.9}, {1.25,-24.301}, {1.3,-
23.142}, {1.35,-22.437}, {1.4,-21.737}, {1.45,-20.877}, {1.5,-
19.969}, {1.55,-19.25}, {1.6,-18.742}, {1.65,-18.197}, {1.7,-
17.767}, {1.75,-17.41}, {1.8,-17.043}, {1.85,-16.56}, {1.9,-
16.072}, {1.95,-15.681}, {2,-15.328}, {2.05,-14.85}, {2.1,-
14.304}, {2.15,-13.894}, {2.2,-13.72}, {2.25,-13.638}, {2.3,-
13.594}, {2.35,-13.508}, {2.4,-13.266}, {2.45,-13.025}, {2.5,-
13.039}, {2.55,-13.198}, {2.6,-13.281}, {2.65,-13.256}, {2.7,-
13.237}, {2.75,-13.208}, {2.8,-13.102}, {2.85,-12.986}, {2.9,-
12.986}, {2.95,-13.044}, {3,-13.054}, {3.05,-12.996}, {3.1,-
12.909}, {3.15,-12.822}, {3.2,-12.658}, {3.25,-12.542}, {3.3,-
12.672}, {3.35,-12.875}, {3.4,-12.909}, {3.45,-12.798}, {3.5,-
12.73}, {3.55,-12.788}, {3.6,-12.812}, {3.65,-12.633}, {3.7,-
12.387}, {3.75,-12.344}, {3.8,-12.334}, {3.85,-12.3}, {3.9,-
12.416}, {3.95,-12.6}, {4,-12.508}, {4.05,-12.218}, {4.1,-
12.344}, {4.15,-12.909}, {4.2,-13.227}, {4.25,-13.31}, {4.3,-
13.503}, {4.35,-13.788}, {4.4,-13.908}, {4.45,-13.754}, {4.5,-
13.348}, {4.55,-12.928}, {4.6,-12.653}, {4.65,-12.571}, {4.7,-
13.034}, {4.75,-13.826}, {4.8,-14.372}, {4.85,-14.589}, {4.9,-
14.594}, {4.95,-14.473}, {5,-14.435}, {5.05,-14.787}, {5.1,-
15.41}, {5.15,-16.009}, {5.2,-16.482}, {5.25,-16.849}, {5.3,-
17.265}, {5.35,-17.772}, {5.4,-18.279}, {5.45,-18.883}, {5.5,-
19.631}, {5.55,-20.5}, {5.6,-21.384}, {5.65,-22.311}, {5.7,-
23.441}, {5.75,-25.17}, {5.8,-27.358}, {5.85,-29.604}, {5.9,-
32.115}, {5.95,-34.708}, {6,-36.113}, {6.05,-32.617}, {6.1,-
19.467}, {6.15,1.854}, {6.2,19.337}, {6.25,25.977}, {6.3,25.784}
, {6.35,23.152}, {6.4,20.215}, {6.45,17.506}, {6.5,15.096}, {6.55
,12.918}, {6.6,11.02}, {6.65,9.446}, {6.7,8.07}, {6.75,6.911}, {6
.8,5.983}, {6.85,5.201}, {6.9,4.417}, {6.95,3.665}, {7,3.139}, {7
.05,2.716}, {7.1,2.249}, {7.15,1.754}, {7.2,1.416}, {7.25,1.159}
, {7.3,0.844}, {7.35,0.496}, {7.4,0.269} }
```

```
fig=ListPlot[data]
```

-Graphics-

$\mu_0 = \frac{4 \cdot \pi \cdot 10^{-7}}{\pi}$

2500000

$z = 1.5 \cdot 10^{-1}$

0.15

$x_0p = .82$

0.82

$x_0m = 6.15$

6.15

$y_0p = 5.3$

5.3

$y_0m = 0$

0

$y = 2.65$

2.65

$d = 3 \cdot 10^{-4}$

3

10000

$Bz1[x_, y_, z_] = (M \cdot \mu_0 \cdot d / (4 \cdot \pi)) \cdot (x - x_0m) \cdot ((y - y_0p) / (((x - x_0m)^2 + z^2) \cdot ((x - x_0m)^2 + z^2 + (y - y_0p)^2)^{(1/2)}) - (y - y_0m) / (((x - x_0m)^2 + z^2) \cdot ((x - x_0m)^2 + z^2 + (y - y_0m)^2)^{(1/2)}))$
 $1.59 \times 10^{-10} M (-6.15 + x)$

$Bz3[x_, y_, z_] = ((M \cdot (-1) \cdot \mu_0 \cdot d / (4 \cdot \pi)) \cdot (x - x_0p)) \cdot ((y - y_0m) / (((x - x_0p)^2 + z^2) \cdot ((x - x_0p)^2 + z^2 + (y - y_0m)^2)^{(1/2)}) - (y - y_0p) / (((x - x_0p)^2 + z^2) \cdot ((x - x_0p)^2 + z^2 + (y - y_0p)^2)^{(1/2)}))$
 $(0.0225 + (-6.15 + x)^2) \sqrt{7.045 + (-6.15 + x)^2}$

```

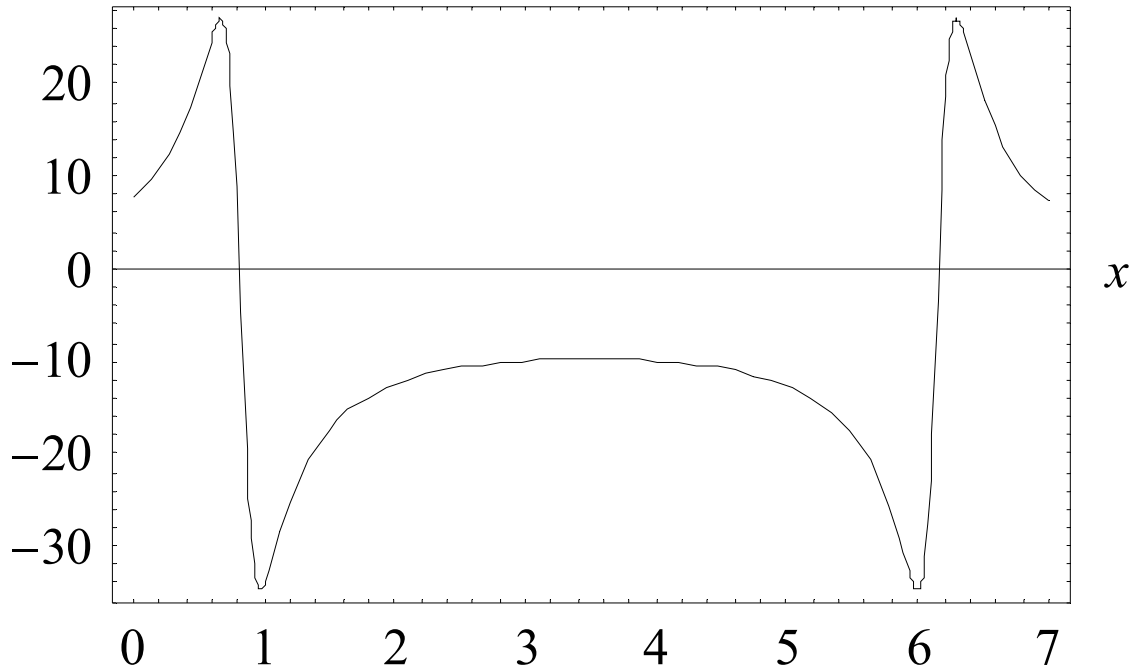
- 1.59 × 10-10 M (-0.82 + x)
(0.0225 + (-0.82 + x)2) √7.045 + (-0.82 + x)2
Bz2[x_,y_,z_]=(M*(-1)*mu0*d/(4*Pi))*(y-y0p)*(((x-
x0p)/(((y-y0p)^2+z^2)*((y-y0p)^2+z^2+(x-x0p)^2)^(1/2))-(x-
x0m)/(((y-y0p)^2+z^2)*((y-y0p)^2+z^2+(x-x0m)^2)^(1/2)))

7.95 × 10-11 M ( - 0.141945 (-6.15 + x) / √7.045 + (-6.15 + x)2 + 0.141945 (-0.82 + x) / √7.045 + (-0.82 + x)2 )
Bz4[x_,y_,z_]=(M*mu0*d/(4*Pi))*(y-y0m)*((x-x0m)/(((y-
y0m)^2+z^2)*((y-y0m)^2+z^2+(x-x0m)^2)^(1/2))-(x-x0p)/(((y-
y0m)^2+z^2)*((y-y0m)^2+z^2+(x-x0p)^2)^(1/2)))
7.95 × 10-11 M ( 0.141945 (-6.15 + x) / √7.045 + (-6.15 + x)2 - 0.141945 (-0.82 + x) / √7.045 + (-0.82 + x)2 )
fn=NonlinearFit[data,Bz1[x,y,z]+Bz2[x,y,z]-Bz3[x,y,z]-
Bz4[x,y,z],x,{M}]

12.2096 ( 0.141945 (-6.15 + x) / √7.045 + (-6.15 + x)2 - 0.141945 (-0.82 + x) / √7.045 + (-0.82 + x)2 ) - 12.2096 ( - 0.141945 (-6.15 + x) / √7.045 + (-6.15 + x)2 + 0.141945 (-0.82 + x) / √7.045 + (-0.82 + x)2 ) +
24.4193 (-6.15 + x) - 24.4193 (-0.82 + x)
(0.0225 + (-6.15 + x)2) √7.045 + (-6.15 + x)2 (0.0225 + (-0.82 + x)2) √7.045 + (-0.82 + x)2
Mz=24.419298639646733 ~ *4*Pi*10-6/(d*mu0*1000)/y0p
153.58

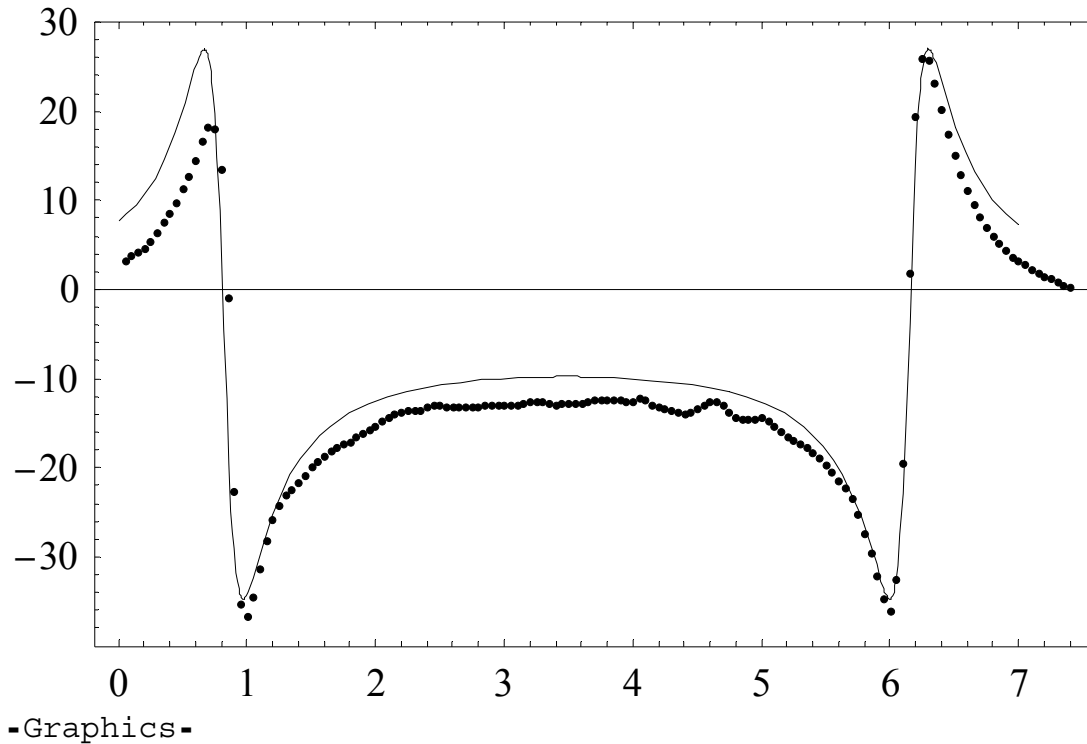
fg2=Plot[fn,{x,0,7},
Frame→True,AxesLabel→TraditionalForm/@{x,Bz},TextStyle-
>{FontFamily→"Times",FontSize→14}]

```



-Graphics-

```
Show[fig,fg2,PlotRange→{-40,30},
Axes→{True,False},Frame→True,TextStyle-
>{FontFamily→"Times",FontSize→22}]
```



This is CoFe_2O_4 thin film sample, which is discussed in Chapter 5, Sec. 5.4.1, and the sample is shown in Figure 5.13. The value of M_z here is 153.6 emu/cc.

Appendix E

The k_w dependence of M_{in} when the scanning area varies

In Sec. 6.2.1 the range of optimal k_w values was obtained as the distance z varied. In this analysis, the scanning area was large enough compared to the sample area. The in-plane magnetization was insensitive to the k_w values in the optimal range. However, when the scanning area becomes smaller, it is understandable that the k_w will be an important factor even if it is within the range.

To this end, I simulated a sample of 3 mm x 850 μm at a distance $z = 150 \mu\text{m}$ and varies the scanning area from 3.35 mm x 3.35 mm to 5 mm x 5 mm as in Sec. 6.2.3. I then used five k_w values to check if there is any dependence of M_{in} on k_w as the scanning area changes. It is important to do this because, as the magnetic field data is being cut off by insufficient scanning area, k_w can not remain the same. The results are presented in Figure E.1. It turns out that as the scanning area approaches the dipole length 3 mm, it becomes more difficult to use higher k_w values. The reason for this is that the magnetic field still remains substantially finite at the edges of the scanning area and thus choosing a higher k_w will generate a large noise due to the apparent discontinuities at the scanning edges. Thus integrating such noisy signal may produce significant error in calculating M_{in} . On the other hand, for a smaller k_w value, even though one can calculate M_{in} with some error, the edge effect can still be seen as well.

Now as one can see in Figure E.1, the sample scanning length (in the x direction) must be at least 1.2 times larger than the sample length l , in order to calculate magnetization accurately with any k_w within the region of optimal values (see Sec. 6.2.1).

Note, however, that when the distance z is larger than the sample size (w) one may need a much larger ratio of the scanning area to the sample area.

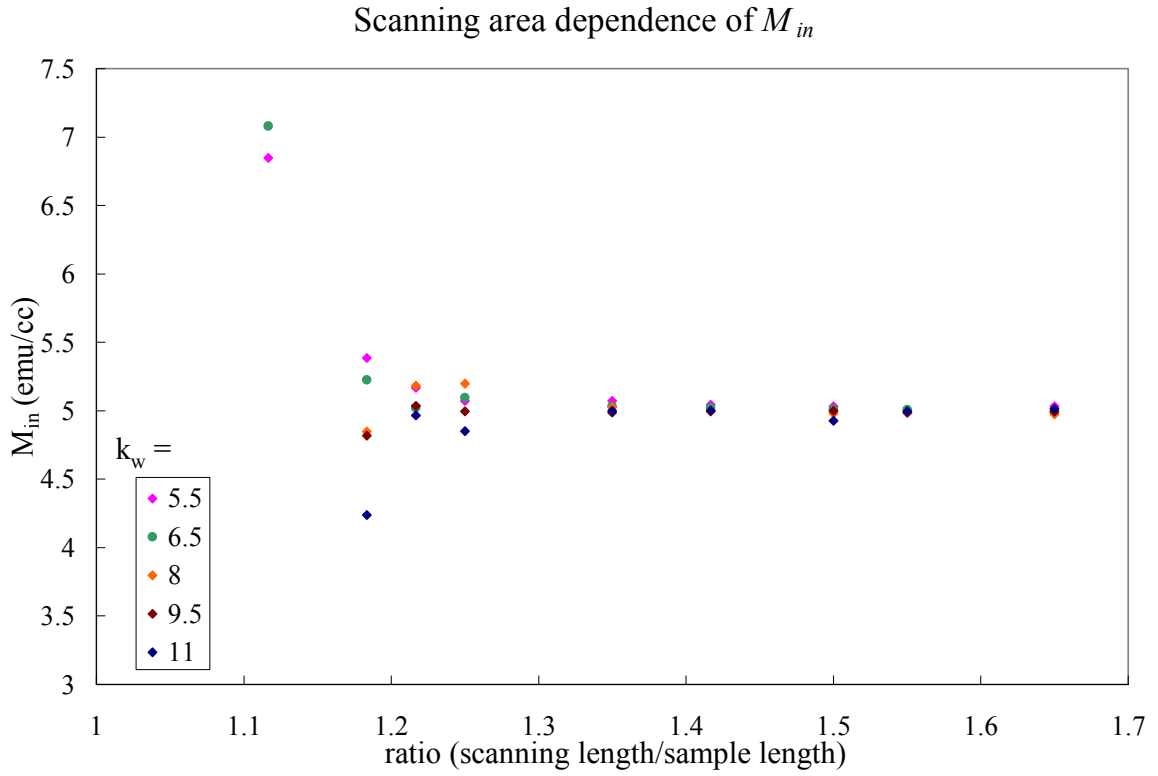


Figure E.1 The dependence of M_{in} on the ratio of scanning length to the sample length for five k_w values.

REFERENCES

Chapter 2

1. H. Koinuma, I. Takeuchi Nature Materials **3**, 429 (2004).
2. X.-D. Xiang, X. Sun, G. Briceno, Y. Lou, K.-A. Wang, H. Chang, W. G. Wallace Freedman, S.-W. Chen, and P. G. Schultz, Science **268**, 1738 (1995).
3. H. Chang, I. Takeuchi, and X.-D. Xiang, Applied Physics Letters **74**, 1165 (1999).
4. I. Takeuchi, H. Chang, C. Gao, P. G. Schultz, X.-D. Xiang, R. P. Sharma, M. J. Downes, and T. Venkatesan, Applied Physics Letters **73**, 894 (1998).
5. J. Wang, Y. Yoo, C. Gao, I. Takeuchi, X. Sun, H. Chang, X.-D. Xiang, and P. G. Schultz, Science **279**, 1712 (1998).
6. H. Chang, C. Gao, I. Takeuchi, Y. Yoo, J. Wang, P. G. Schultz, X.-D. Xiang, R. P. Sharma, M. Downes, and T. Venkatesan, Applied Physics Letters **72**, 2185 (1998).
7. I. Takeuchi, O. O. Famodu, J. C. Read, M. A. Aronova, K.-S. Chang, C. Craciunescu, S. E. Lofland, M. Wuttig, F. C. Wellstood, L. Knauss, and A. Orozco, Nature Materials **2**, 180 (2003).
8. D. A. R. Barkhouse, A. Bonakdarpour, M. Fleischauer, T. D. Hatchard, and J. R. Dahn, Journal of Magnetism and Magnetic Materials **261**, 399 (2003).
9. T. Fukumura, M. Ohtani, M. Kawasaki, Y. Okimoto, T. Kageyama, T. Koida, T. Hasegawa, Y. Tokura, and H. Koinuma, Applied Physics Letters **77**, 3426 (2000).
10. G. Briceno, H. Chang, X. Sun, P. G. Schultz, and X.-D. Xiang, Science **270**, 273 (1995).

11. I. Takeuchi, D. Fukuma, and J. Matsui, *Analytical Chemistry* **71**, 285 (1999).
12. M. Gross, D. C. Muller, H. C. Nothofer, U. sherf, D. Neher, C. Brauchle, and K. Meerholz, *Nature* **405**, 661 (2000).
13. C. H. Reynolds, *Journal of Combinatorial Chemistry* **1**, 297 (1999).
14. S. Sakahara, K. Yajima, R. Belosludoy, S. Takami, M. Kubo, and A. Miyamoto, *Applied Surface Science* **189**, 253 (2002).
15. J. D. Hewes, and L. A. Bendersky, *Applied Surface Science* **189**, 196 (2002).
16. J. C. Phillips, *Physics of High-T_c Superconductors* (Academic Press, New York, 1989).
17. M. A. Aronova, K. S. Chang, I. Takeuchi, H. Jabs, D. Westerheim, A. Gonzalez-Martin, J. Kim, and B. Lewis, *Applied Physics Letters* **83**, 1255 (2003).
18. H. Y. Hwang and S.-W. Cheong, *Science* **28**, 1607 (1997).
19. Y.-K. Yoo, F. Duewer, H. Yang, Y. Dong, J.-W. Li, and X.-D. Xiang, *Nature* **406**, 704 (2000).
20. M. J. Turchinskaya, L. A. Bendersky, A. J. Shapiro, K. S. Chang, I. Takeuchi, A. L. Roytburd, to appear in *Journal of Materials Research*, **19** (2004).
21. A. Stein, S. W. Keller, T. E. Mallouk, **259** 1558 (1993).
22. I. Takeuchi, R. B. van Dover, H. Koinuma, *MRS Bulletin* **27**,301 (2002).
23. C. Y. Chang, S.M. Sze, *ULSI*, McGraw-Hill, Inc., 105 (1996).
24. H. M. Smith and A. F. Turner, *Appl. Opt.* **4**, 147-148 (1965).

25. D. Dijkkamp, T. Venkatesan, X. D. Wu, S. A. Shaheen, N. Jisrawi, Y. H. Min-Lee, W. L. McLean, and M. Croft *Applied Physics Letters* **51**, 619 (1987).
26. D. B. Chrisey, G. K. Hubler, *Pulsed Laser Deposition of Thin Films*, John Wiley & Sons, Inc., (1994).
27. D. M. Bubb, B. R. Ringeisen, J. H. Callahan, M. Galicia, A. Vertes, J. S. Horwitz, R. A. McGill, E. J. Houser, P. K. Wu, A. Piqu'e, and D. B. Chrisey, *Applied Physics A* **73**, 121 (2001).
28. Z. Trajanovic, Ph. D. Thesis, University of Maryland, College Park (1997).
29. O. Auciello, J. Engemann, *Multicomponent and Multilayered Thin Films for Advanced Microtechnologies: Techniques, Fundamentals and Devices*, Kluwer Academic Publishers, 230 (1992).
30. I. Bozovic, *IEEE Transactions on Applied Superconductivity*, **11**, 2686 (2001)
31. Y. Matsumoto, M. Murakami, Z.W. Jin, A. Ohtomo, M. Lippmaa, M. Kawasaki, H. Koinuma, *Japanese Journal of Applied Physics* **38**, L603-L605 (1999).
32. K.-S. Chang, M. A. Aronova, and I. Takeuchi, *Applied Surface Science* **223**, 224 (2004).
33. R. B. van Dover, L. F. Schneemeyer, and R. M. Fleming, *Nature* **392**, 162 (1998).
34. S. Semancik, & R. E. Cavicchi, *Acc. Chem. Res.* **31**, 279–287 (1998).
35. S. Semancik, *Combinatorial Materials Synthesis* (eds X.-D. Xiang, & I. Takeuchi), Ch. 9, Dekker, New York, (2003).

Chapter 3

1. J. Watson, Sensors and Actuators B **5**, 29 (1984).
2. N. Yamazoe, Sensors and Actuators B **5**, 7 (1991).
3. D. Kohl, Sens. and Sens. System for an Electronic Noses, 53 (1992).
4. R. Lalauze, C. Pijolat, S. Vincent and L. Bruno, Sensors and Actuators B **8**, 237 (1992).
5. Y. Shimizu, M. Egashira, MRS Bulletin **24**, 18 (1999).
6. J. Watson, K. Ihokura, MRS Bulletin **14**, 18 (1999).
7. J. Hammond, B. Marquis, R. Michaels, B. Oickle, B. Segee, J. Vetelino, A. Bushway, M. E. Camire, K. D-Dentici, Sensors and Actuators B **84**, 113 (2002).
8. T. Dewettinck, K. Van Hege and W. Verstraete, Water Research., **35**, 2475 (2001).
9. S. Ethrmann, J. Jungst, J. Goschnick, D. Everhard, Sensors and Actuators B **65**, 247 (2000).
10. L. De Angelis, N. Minnaja, Sensors and Actuators B **3**, 197 (1991).
11. G. S. V. Coles, G. Williams, B. Smith, Sensors and Actuators B **3**, 7 (1991).
12. I. Takeuchi, R. B. van Dover, H. Koinuma, MRS Bulletin **27**,301 (2002).
13. J. Tiffany, R. E. Cavicchi, S. Semancik, SPIE Proceedings **4205**, 40 (2000).
14. J. W. Gardner, P. N. Barlett, Sensors and Actuators B **18-19**, 211 (1994).
15. T. A. Dickinson, J. White, J. S. Kauer, D.R. Walt, Tibtech **16**,250 (1998).
16. M. C. Horrillo, J. Getino, L. Ares, J. I. Robla, I. Sayago, F.J. Gutierrez, J.

Electrochemical Society **145**, 2486 (1998).

17. S. E. Stitzel, L. J. Cowen, K. J. Albert, D. R. Walt, Anal. Chemistry **73**, 5266 (2001).

18. M. Bicego, G. Tessari, G. Tecchiolli, M. Bettinelli, Sensors and Actuators B **85**, 137 (2002).

19. P. K. Namdev, Y. Alroy, V. Singh, Biotechnology Progress **14**, 75 (1998).

20. H.T. Nagle, R. Gutierrez-Osuna, S. S. Schiffman, IEEE Spectrum, (1998).

21. J. Goschnick, Micro Engineering **57-58**, 693 (2001).

22. K. Ihokura, New Mater. Proc., **1**, 43 (1981)

23. C. Xu, J. Tamaki, N. Miura, N. Yamazoe, Sensors and Actuators B **3**, 147 (1991).

24. K. D. Schierbaum, U. Weimar, W. Gopel, Sensors and Actuators B **7**, 709 (1992)

25. L. Bruno, C. Pijolat, R. Lalauze, Sensors and Actuators B **18-19**, 195 (1994).

26. B. Gautheron, M. Labeau, G. Delabouglize, U. Schmatz, Sensors and Actuators B **15-16**, 357 (1993).

27. Y. Yasukawa, T. Seki, J-I. Muramatsu, S. Sugie, S. Tasaka, N. Inagaki, Sensors and Actuators B **13-14**, 613 (1993).

28. M. Akiyama, J. Tamai, N. Miura, N. Yamazoe, Chemistry Letters, 1611 (1991).

29. T. Inoue, K. Ohtsuka, Y. Yoshida, Y. Matsuura, Y. Jajiyama, Sensors and Actuators B **24-25**, 388 (1995).

30. T. Nomura, T. Amamoto, Y. Matsuura, Y. Jajiyama, Sensors and Actuators B **13-**

14, 486 (1993).

31. H. Chang, I. Takeuchi, and X.-D. Xiang, "A Low Loss Composition Region Identified from a Thin Film Composition Spread of $\text{Ba}_{1-x-y}\text{Sr}_x\text{Ca}_y\text{TiO}_3$," *Applied Physics Letters*, **74**, 1165 (1999).

32. K-S. Chang, M. A. Aronova, O. Famodu, I. Takeuchi, S. E. Lofland, J. Hattrick-Simpers, H. Chang, *Applied Physics Letters* **79**, 4411 (2001).

33. M. A. Aronova, K. S. Chang, I. Takeuchi, H. Jabs, D. Westerheim, A. Gonzalez-Martin, J. Kim, and B. Lewis, *Applied Physics Letters* **83**, 1255 (2003).

34. K. Persaud, G. H. Dodd, *Nature* **299**, 352 (1982).

35. F. DiMeo, S. Semancik, R.E. Cavicchi, J.S. Suehle, P. Chaparala, N.H. Tea, *MRS Proc.*, **415**, 231-236 (1995).

36. F. DiMeo, S. Semancik, R.E. Cavicchi, J.S. Suehle, P. Chaparala, N.H. Tea, M.D. Vaudin, J.T. Kelliher, *MRS Proc.*, **444**, 203-208 (1997).

37. R. A. Potyrailo, COMBI 2002 - The 4th Annual International Symposium on Combinatorial Approaches for New Materials Discovery, January 23 - 25, San Diego, CA, 2002.

38. H. Breer, *Biosensors Bioelectronics* **9**, 625 (1994).

39. D. E. Clapham, *Nature* **379**, 297 (1996).

40. D. Schild, *Nato ASI Series H: Cell Biology* **39**, (1990).

41. P. N. Bartlett, J. M. Elliott, J. W. Gardner, *Food Technology* **51**, 44 (1997).

42. <http://www.alpha-mos.com/tecprinciple.php>

43 <http://www.almaz.com/nobel/>

Chapter 4

1. J. Bardeen, L.N. Cooper, and J. R. Schrieffer, *Physical Review* **108**, 1175 (1957).
2. R. C. Jaklevic, J. Lambe, A. H. Silver, and J. E. Mercereau, *Physical Review Letters* **12**, 159-160 (1964).
3. G. Bednorz and K. A. Muller, *Z. Phys*, **B64**, 189 (1986).
4. J. E. Zimmerman, P. Thiene, and J. T. Harding, *Journal of Applied Physics* **41**, 1572-1580 (1970).
5. A. M. Chang, H. D. Hallen, L. Harriott, H. F. Hess, H. L. Kao, *Applied Physics Letters* **61**, 1974 (1992).
6. S. Y. Yamamoto, S. Schultz, *Applied Physics Letters* **69**, 3263 (1996).
7. D. Rugar, H. J. Mamin, P. Guethner, S.E. Lambert, J.E. Stern, *Journal of Applied Physics Letters* **68**, 1169 (1990).
8. S. Gotoh, N. Koshizuka, *Physica C* **176**, 300 (1991).
9. L. N. Vu, and D. J. Van Harlingen, *IEEE Transactions on Applied. Superconductivity* **3**, 1918, (1993).
10. A. Mathai, D. Song, Y. Gim, and F. C. Wellstood, *IEEE Transactions on Applied. Superconductivity* **3**, 2609, (1993).

11. C. C. Tsuei, J. R. Kirtley, C. C. Chi, L. S. Yu-Jahnes, A. Gupta, T. Shaw, J. Z. Sun, and M. B. Ketchen, *Physical Review Letters* **3**, 593 (1994).
12. A. Mathai, Y. Gim, R. C. Black, A. Amar, F. C. Wellstood, *Physical Review Letters* **4**, 4523 (1995).
13. L. N. Vu, M. S. Wistrom, and D. J. Van Harlingen, *Applied Physics Letters* **63**, 1693 (1993).
14. R. C. Black, F. C. Wellstood, E. Dantsker, A. H. Miklich, J. J. Kingston, D. T. Nemeth, and J. Clarke, *Applied Physics Letters* **64**, 100 (1994).
15. W. G. Jenks, S. S. H. Sadeghi, J. P. Wikswo Jr., *Journal of Physics D*, **30**, 293 (1997).
16. F. C. Wellstood, Y. Gim, A. Amar, R.C. Black, and A. Mathai, *IEEE Transactions on Applied Superconductivity* **7**, 3134 (1997).
17. S. Chatrathorn, Ph. D. Thesis, University of Maryland, College Park (2000).
18. E. Fleet, Ph. D. Thesis, University of Maryland, College Park (2000).
19. S. Chatrathorn, E. F. Fleet, F. C. Wellstood, L. A. Knauss, and T. M. Eiles, *Applied Physics Letters*, **76**, 2304 (2000).
20. L. A. Knauss, *Superconductor & Cryoelectronics*, pp 16-22, Summer (2000).
21. A. Cochran, J. C. Macfarlane, L. N. C. Morgan, J. Kuznik, R. Weston, Hao Ling, R. M. Bowman, G. B. Donaldson, *IEEE Transactions on Applied Superconductivity* **4**, 128 (1994).
22. L. N. Morgan, C. Carr, A. Cochran, D. McAMcKirdy, G. B. Donaldson, *IEEE Transactions on Applied Superconductivity*, **5**, 3127 (1995).

23. T. S. Lee, Y. R. Chemla, E. Dantsker, and J. Clarke, IEEE Transactions on Applied Superconductivity **7**, 3147 (1997).
24. F. Baudenbacher, N. T. Peters, and J. P. Wikswo Jr., Review of Scientific Instruments **73**, 1247 (2002).
25. J. Dechert, M. Mueck, and C. Heiden, IEEE Transactions on Applied Superconductivity **9**, 4111(1999).
37. D. Li, Y. Ma, W.F. Flanagan, B.D. Lichter and J.P. Wikswo Jr., Tri-Service Conference on Corrosion, Orlando, Florida, (June 21-23 1994).
27. H. Hattori, T. Yamano, T. Tsutada, N. Tsuyuguchi, H. Kawawaki, and M. Shimogawara, Brain & Development, **23**, 528 (2001).
28. D. Embick, M. Hackl, J. Schaeffer, M. Kelepir, and A. Marantz, Cognitive Brain Research **10**, 345 (2001).
29. R. T. Wakai , M. Wang, S. L. Pedron, D. L. Reid, C. B. Martin, Early Human Development, **35**, 15 (1993).
30. G. Stroink, M. J. R. Lamothe, and M. J. Gardner, "SQUID Sensors: Fundamentals, Fabrication and Applications", Kluwer Academic Publishers, p413 (1996).
31. J. Clarke, IEEE Transactions on Magnetics **19**, 288 (1983).
32. B. D. Josephson, Phys. Letters **1**, 251(1962); Advanced Physics **14**, 419 (1965).
33. W. C. Stewart, Applied Physics Letters **12**, 277 (1968).
34. D. E. McCumber, Journal of Applied Physics **39**, 3113 (1968).

35. C. A. Hamilton, R. C. Kautz, R. L. Steiner, and F. L. Loyd, IEEE Electronic Device Letters **EDL6**, 623 (1985).
36. J. Clarke, "SQUIDS Fundamentals, SQUID Sensors: Fundamentals, Fabrication and Applications", Kluwer Academic Publishers, pp. 1-62 , (1996).
37. S. Y. Lee, Ph. D. Thesis, University of Maryland, College Park (2004).
38. M. J. Ferrari, M. Johnson, F. C. Wellstood, J. Clarke, P. A. Rosenthal, R. H. Hammond, and M. R. Beasley, Applied Physics Letters **53**, 695, (1988).
39. <http://superdevices.phys.strath.ac.uk/prgs.html>.
40. A. J. Millar, E. J. Romans, C. Carr, A. Eulenburg, G. B. Donaldson, P. Maas and C. M. Pegrum, Applied Physics Letters **76**, 2445-2447 (2000).
41. J. Beyer, D. Drung, and F. Ludwig, T. Minotani and K. Enpuku, Applied Physics Letters **72**(2), 203 (1998).
42. Earth Chemical Co., Ltd. Inorganic Division, New Awajimahi Bldg. 6F, 3-14, 1-Chome, Awajimachi, Chuo-ku, Osaka 541-0047, Japan.
43. Physics Dept., Electronics Development Group, Work Order # 9539.

Chapter 5

1. I. Takeuchi, O. O. Famodu, J. C. Read, M. A. Aronova, K.-S. Chang, C. Craciunescu, S. E. Lofland, M. Wuttig, F. C. Wellstood, L. Knauss, and A. Orozco, Nature Materials **2**, 180 (2003).

2. S. A. Chambers, and R. F. Farrow, New possibilities for ferromagnetic semiconductors. *MRS Bulletin* **28**, 729–733 (2003).
3. Y. Matsumoto, M. Murakami, T. Shono, T. Hasegawa, T. Fukumura, M. Kawasaki, P. Ahmet, T. Chikyow, S. Koshihara, H. Koinuma, *Science* **291**, 854 (2001).
4. M. Yu, J. H. Simpers, I. Takeuchi, J.P. Liu, S.E. Lofland, S. Tyagic, J.W. Freeland D. Giubertoni, M. Bersani, M. Anderle submitted to *Applied Physics Letters*.
5. K.-S. Chang, M. A. Aronova, C.-L.Lin, M. Murakami, M.-H. Yu, J. Hattrick-Simpers, O. O. Famodu, S. Y. Lee, R. Ramesh, M. Wuttig, and I. Takeuchi, C. Gao, L. A. Bendersky, *Applied Physics Letters* **84**, 3091 (2004);
6. M. Murakami et *al.*, unpublished.
7. www.magnet.fsu.edu/users/facilities/dcfield/magnetometry/mok3/
8. T. P. A. Hase, I. Pape, D. E. Read, and B. K. Tanner, H. Dürr, E. Dudzik, and G. van der Laan C. H. Marrows and B. J. Hickey, *Phys. Rev. B* **61**, 15331–15337 (2000).
9. G. van der Laan, B. T. Thole, G. A. Sawatzky, J. B. Goedkoop, J. C. Fuggle, J.-M. Esteve, R. Karnatak, J. P. Remeika, H. A. Dabkowska, *Physical Review B* **34**, 6529 (1986).
10. G. Schütz, W. Wagner, W. Wilhelm, P. Kienle, R. Zeller, R. Frahm, G. Materlik, *Physical Review Letters* **58**, 737 (1987).
11. http://www.phys.utk.edu/WPWebSite/ewp_workshop_X-Ray_Report.pdf
12. A. Oral, S. J. Bending, M. Henini, *Applied Physics Letters* **69**, 1324 (1996)
13. <http://www.tristantech.com>

14. J. D. Jackson, "Classical Electrodynamics", John Wiley and Sons, New York, p. (1975).
15. B. J. Roth, N. G. Sepulveda, and J. P. Wikswo, Journal of Applied Physics **65**, 361 (1989).
16. S. Chatrathorn, Ph. D. Thesis, University of Maryland, College Park (2000).
17. E. Fleet, Ph. D. Thesis, University of Maryland, College Park (2000).
18. F. J. Harris, Proceedings of the IEEE, **66**, No. 1 (1978).
19. K. S. Chang, Ph. D. Thesis, University of Maryland, College Park (2004).
20. C. L. Lin, M. S. Thesis, University of Maryland, College Park (2004).

Chapter 6

1. F. J. Harris, Proceedings of the IEEE, **66**, No. 1 (1978).
- 2 G. Wolberg, Digital Image Warping, IEEE Computer Society Press, 1990.
3. E. Fleet, Ph. D. Thesis, University of Maryland, College Park (2000).
4. S. Chatrathorn, Ph. D. Thesis, University of Maryland, College Park (2000).

Chapter 7

1. R. E. Newnham, MRS Bulletin **22**, No 5 (1997).
2. www.memory-metalle.de/html/03_knowhow/PDF/MM_04_properties_e.pdf

3. J. D. Harrison, D. E. Hodgson, Shape memory effects in alloys, New York, p. 517 (1975).
4. H. Ohkata, H. Tamura, Materials Research Society Symposium Proceedings **459** p. 345 (1997).
5. H. Kakamoto, K. Uematsu, M. Momota, S. Tanabe, T. Suzuki, T. Endo, U.S. Patent No. 4,925,445 (1990).
6. J. K. Nicholson, R. F. Gattorna, U.S. Patent No. 4,616,656 (1986).
7. M. Wuttig, L. Liu, K. Tsuchiya, R. D. James, Journ. Appl. Phys. **87**, 4707 (2000).
8. M. Wuttig, C. Craciunescu, J. Li, Materials Transactions JIM **41**, 933–937 (2000).
9. S. Miyazaki, Ishida, Mater. Sci. Eng.A **273**, 106–133 (1999).
10. S. J. Murray, M. A. Marioni, A. M. Kukla, J. Robinson, R. C. O'Handley, S. M. Allen, Journal of Applied Physics **87**, 5774–5776 (2000).
11. S. J. Murray, M. A. Marioni, P. G. Tello, S. M. Allen, R. C. O'Handley, Journal of Magnetic Materials **242**, 945–947 (2001).
12. V. A. Chernenko, E. Cesari, V. V. Kokorin, I. N. Vitenko, Scripta Metall. Materials **33**, 1239–1244 (1995).
13. A. N. Vasil'ev, A. D. Bozhko, and V. V. Khovailo, I. E. Dikshtein and V. G. Shavrov V. D. Buchelnikov, M. Matsumoto, S. Suzuki, T. Takagi, and J. Tani, Physical Review B **59**, 1113–1120 (1999).

14. S. I. Patil, Deng Tan, S. E. Lofland, and S. M. Bhagat, I. Takeuchi, O. Famodu, J. C. Read, K.-S. Chang, C. Craciunescu, and M. Wuttig, *Applied Physics Letters* **81**, 1279–1281 (2002).
15. M. Ahlers, *J.Phys. IV* **5**, 71–80 (1995).
16. C. M. Craciunescu, J. Li, M. Wuttig, *Scripta Mater.* **48**, 65–70 (2003).
17. M. Wuttig, L. Liu, K. Tsuchiya, R. D. James, *Journal of Applied Physics* **87**, 4707–4711 (2000).
18. V. A.Chernenko, *Scripta Mater.* **40**, 523–527 (1999).
19. R. M. Bozorth, *Ferromagnetism* **317** (IEEE Press, New Jersey, 1993).
20. H. P. J. Wijn, (ed.) *Data in Science and Technology* **54** (Springer, Berlin-Heidelberg, 1991).
21. E. F. Wassermann, J. Kastner, M. Acet, P. Entel, *Proc. Int. Conf. Solid-State Phase Transitions '99 (JIMIC-3)* 807–814 (1999).
22. A. T. Zayak, , V. D. Buchelnikov, P.A. Entel, *Phase Transit.* **75**, 243–256 (2002).
23. V. V. Godlevsky, K. M. Rabe, *Phys. Rev. B* **63**, 134407–1–5 (2001).
24. W. E. Pickett, J. S.Moodera, *Physics Today* **54**, 39–44 (2001).

Chapter 8

1. L. D. Landau, and E. M. Lifshitz, *Electrodynamics of Continuous Media*, Gostekhizdat, Moscow (1957).

2. D. N. Astrov, Soviet Physics JETP **13**, 729 (1961).
3. Y. F. Popov, A. M. Kadomtseva, S. S. Krotov, D. V. Belov, G. P. Vorobev, P. N. Makhov, and A. K. Zvezdin, Low Temperature Physics **27**, 478 (2001).
4. S. Shetty, V. R. Palkar, and R. Pinto, PRAMANA-Journal of Physics **58**, 1027 (2002).
5. J. Wang, J. B. Neaton, H. Zheng, V. Nagarajan, S. B. Ogale, B. Liu, D. Viehland, V. Vaithyanathan, D. G. Schlom, U. V. Waghmare, N. A. Spaldin, K. M. Rabe, M. Wuttig, and R. Ramesh, Science **299**, 1719 (2003).
6. N. A. Hill, Journal of Physical Chemistry B **104**, 6694 (2000).
7. N. A. Hill, Annual Review of Materials Research **32**, 1 (2002).
8. N. Hur, S. Park, P. A. Sharma, J. S. Ahn, S. Guha , S. W. Cheong, Nature **429**, 392 (2004).
9. J. V. D. Boomgaard, A. M. J. G. Van Run, and J. Van Suchtelen, Ferroelectrics **14**, 727 (1976).
10. J. V. D. Boomgaard, A. M. J. G. Van Run, and J. Van Suchtelen, Ferroelectrics **10**, 295 (1976).
11. J. Van Suchtelen, Philips Research Reports **27**, 28 (1972).
12. J. V. D. Boomgaard, and R. A. J. Born, Journal of Materials Science **13**, 1538 (1978).
13. J. V. D. Boomgaard, D. R. Terrell, R. A. J. Born, and H. F. J. I. Giller, Journal of Materials Science **9**, 1705 (1974).
14. G. Harshe, Ph. D. Thesis, Pennsylvania State University, State College (1991).

15. J. Ryu, A. V. Carazo, K. Uchino, and H.-E. Kim, Japanese Journal of Applied Physics **40**, 4948 (2001).
16. G. Srinivasan, E. T. Rasmussen, J. Gallegos, R. Srinivasan, Y. I. Bokhan, and V. M. Laletin, Physical Review B **64**, 214408-1 (2001).
17. K. Mori, and M. Wuttig, Applied Physics Letters **81**, 100 (2002).
18. S. Dong, J.-F. Li, and D. Viehland, Applied Physics Letters **83**, 2265 (2003).
19. Y. Suzuki, G. Hu, R. B. van Dover, and R. J. Cava, Journal of Magnetism and Magnetic Materials **191**, 1 (1999).
20. L. Horng^{a,*}, G. Chern^b, M.C. Chen^b, P.C. Kanga, D.S. Lee, Journal of Magnetism and Magnetic Materials **270** 389–396 (2004).
21. C. Gao and X.-D. Xiang, Review of Scientific Instruments **69**, 3846 (1998)
22. T. Wei, X.-D. Xiang, W. G. Wallace-Freedman, and P. G. Schultz, Applied Physics Letters **68**, 3506 (1996).
23. Y. Lu, T. Wei, F. Duewer, Y. Lu, N. B. Ming, P. G. Schultz, and X.-D. Xiang, Science **276**, 2004 (1997).
24. D. E. Steinhauer, C. P. Vlahacos, F. C. Wellstood, S. M. Anlage, C. Canedy, R. Ramesh, A. Stanishevsky, and J. Melngailis, Applied Physics Letters **75**, 3180 (1999).
25. J. H. Lee, S. Hyun, and K. Char, Review of Scientific Instruments **72**, 1425 (2001).
26. H. Chang, I. Takeuchi, and X.-D. Xiang, Applied Physics Letters **74**, 1165 (1999).
27. H. Chang, C. Gao, I. Takeuchi, Y. Yoo, J. Wang, P. G. Schultz, X.-D. Xiang, R. P. Sharma, M. Downes, and T. Venkatesan, Applied Physics Letters **72**, 2185 (1998).

28. G. Harshe, J. P. Dougherty, and R. E. Newnham, International Journal of Applied Electromagnetics in Materials **4**, 145 (1993).
29. M. Avellaneda, and G. Harshé, Journal of Intelligent Material Systems and Structures **5**, 501 (1994).
- 30 G. Harshé, J.P. Dougherty and R.E. Newnham International Journal of Applied Electromagnetics in Materials **4** 161-171 (1993).
- 31 . R.E. Eitel, C.A. Randall, T.R. Shrout, P.W. Rehrig, W. Hackenberger and S.-E. Park, Jpn. J. Appl. Phys. **40** 5999 (2001).

Appendix A

1. User manual for Magma C20, Neocera Inc.

Appendix C

- 1 S. Chatraphorn, Ph. D. Thesis, University of Maryland, College Park (2000)
- 2 E. Fleet, Ph. D. Thesis, University of Maryland, College Park (2000).